Dynamics of the Northwestern Atlantic Ocean: A Diagnostic Study

By

Thierry H. Reynaud

Department of Atmospheric and Oceanic Sciences and
Center for Climate and Global Change Research
McGill University, Montréal
June, 1994

A thesis submitted to the Faculty of Graduate Studies and Research
in partial fulfillment of the requirements for the degree of
Doctor of Philosophy.

ISBN 0-612-00130-X

ABSTRACT

New high resolution density fields for the northwestern Atlantic Ocean are calculated from objectively analyzed temperature and salinity fields obtained from archived data. The original data set is the Marine Environment Data Service (MEDS) archived data and is supplemented by a subset of the National Oceanographic Data Centre (NODC) data from J. Reid and by the 1980s additional data of Fukumori and Wunsch (1991). The objective analysis scheme is a modification of that used by Levitus (1982) and uses 37 vertical levels. The scheme is used to calculate the climatological mean (1910-1989) temperature and salinity fields for the summer and the warm and cold seasons. Inverse methods are then applied to these new density fields in order to determine the transport and circulation during these periods. A study of the seasonal and interdecadal variations of the ocean transport and circulation is also presented. The interdecadal analysis is based on temperature and salinity fields analyzed for the warm season of the 1950-1964 and 1965-1981 periods.

RÉSUMÉ

De nouveaux champs de densité à haute résolution ont été calculés, pour le nord ouest de l'océan Atlantique, à partir des champs de temperature et de salinité obtenus par une analyse objective de données archivées. La banque de données originale est composée des données archivées au Marine Environment Data Service (MEDS); elle est complétée par des données du National Oceanographic Data Centre (NODC) et par des données complémentaires pour la période post 1980, de Fukumori and Wunsch (1991), fournies par J. Reid. Le schéma de l'analyse objective est une variante de celui de Levitus (1982) et comprend 37 niveaux verticaux. Ce shéma est utilisé pour calculer les champs climatologiques moyens (1910-1989) de température et de salinité pour l'été et pour les saisons chaude et froide. Puis, des méthodes inverses sont utilisées pour déterminer le transport et la circulation durant ces périodes. Une étude des variations saisonnières et interdécadales du transport et de la circulation océanique est également présentée. L'analyse interdécadale est basée sur des champs de température et de salinité analysés pour la saison chaude des périodes 1950-1964 et 1965-1981.

A Benjamin

et

Marc-André

TABLE OF CONTENTS

ACKNOWLEDGMENTS

It is with deep appreciation that I acknowledge my supervisor Prof. Andrew Weaver for his constant support. His help and advice were always appreciated. After four years under his supervision, I see in Andrew Weaver a friend for whom I have great respect. I share the same gratitude towards my co-supervisor Prof. Richard Greatbatch, from Memorial University, whose complementary vision was very much appreciated. I realize that without their support, I would not have been able to complete this research.

I am also grateful to Jean-Claude Croteau who kindly provided me with computer assistance and to Gus Fanning who provided me with some useful Fortran code and data. I thank you both. I also wish to thank A. Goulding, T. Grose, G. Mellor, R. Ménard, and D. Straub for their comments and assistance. I thank also C. Wunsch who provided some data. The help of K. Biegaj, A. Koziol, R. Lajeunesse and S. Muselet while I was finishing this thesis was also appreciated. I also thank Paul Reynaud for proof reading this thesis.

The work presented in this thesis has been funded by: (i) FCAR, which gave me financial support in the form of a postgraduate fellowship, (ii) the NSERC Collaborative Research Initiative which supports Canadian university activities in the World Ocean Circulation Experiment (WOCE) and (iii) FCAR and DFO/NSERC Subvention grants awarded to A.J.Weaver. I am grateful to all these agencies.

STATEMENT OF ORIGINALITY

The contribution to original knowledge in this thesis are the following:

The summer analysis:

- A new high resolution (1/3°x1/3°) temperature-salinity data set using 37 vertical levels for the climatological mean (1910-1989) summer is calculated for the northwestern Atlantic Ocean;
- The summer transport and the three-dimensional horizontal currents of the northwestern Atlantic Ocean are diagnozed (A research paper, submitted to J. Geophys. Res., is in revision).

The seasonal analysis:

- A new high resolution (1/3°x1/3°) temperature-salinity data set for the climatological mean (1910-1989) warm and cold seasons is calculated for the northwestern Atlantic Ocean;
- A study of the seasonal variability (T-S fields, transport and circulation) of the northwestern Atlantic Ocean is presented.

The interdecadal/interannual analysis:

- A new high resolution (1/2°x1/2°) temperature-salinity data set for the warm season of the 1950-64 and 1965-81 periods is calculated for the northwestern Atlantic Ocean;
- The interdecadal variability (T-S fields and transport) of the northwestern Atlantic Ocean is studied;
- A study of the interannual variability of the T-S fields in the Hamilton Bank and Flemish Cap subregions is presented.

LIST OF TABLES

CHAPTER I: INTRODUCTION

The western North Atlantic was first studied by the US Coast Guard when they decided to improve their knowledge of the iceberg trajectories after the Titanic sank in 1912 (Smith *et al*, 1937). This region, which includes the Labrador Sea and its surrounding waters, is a very important region to Canada for both climatological and economical reasons. Interannual changes in the western North Atlantic affect the fisheries, iceberg trajectories (of importance to shipping and the development of the offshore oil industry) and the renewal of Labrador Sea Water by deep convection (Lazier, 1980) and hence climate. The Labrador Sea is a semi-enclosed basin occupying a region of 10^6 km^2 between Greenland on the east, Labrador and Newfoundland on the west, Baffin Bay on the north and the open North Atlantic on the south (Fig. 1.1). The bottom topography of the Labrador Sea is quite complicated on the shelves with banks and saddles; the maximum depth is about 3500m but reaches 4000-4500m near the southeastern corner of the region.

1.1 Water masses and currents

The waters in the centre of the Labrador Sea are relatively warm and salty compared to those on the neighbouring shelves. A characteristic feature of the region are the shelf breaks currents which mark the boundary between different water masses (eg, the West Greenland Current; the Labrador Current). There are five different water masses

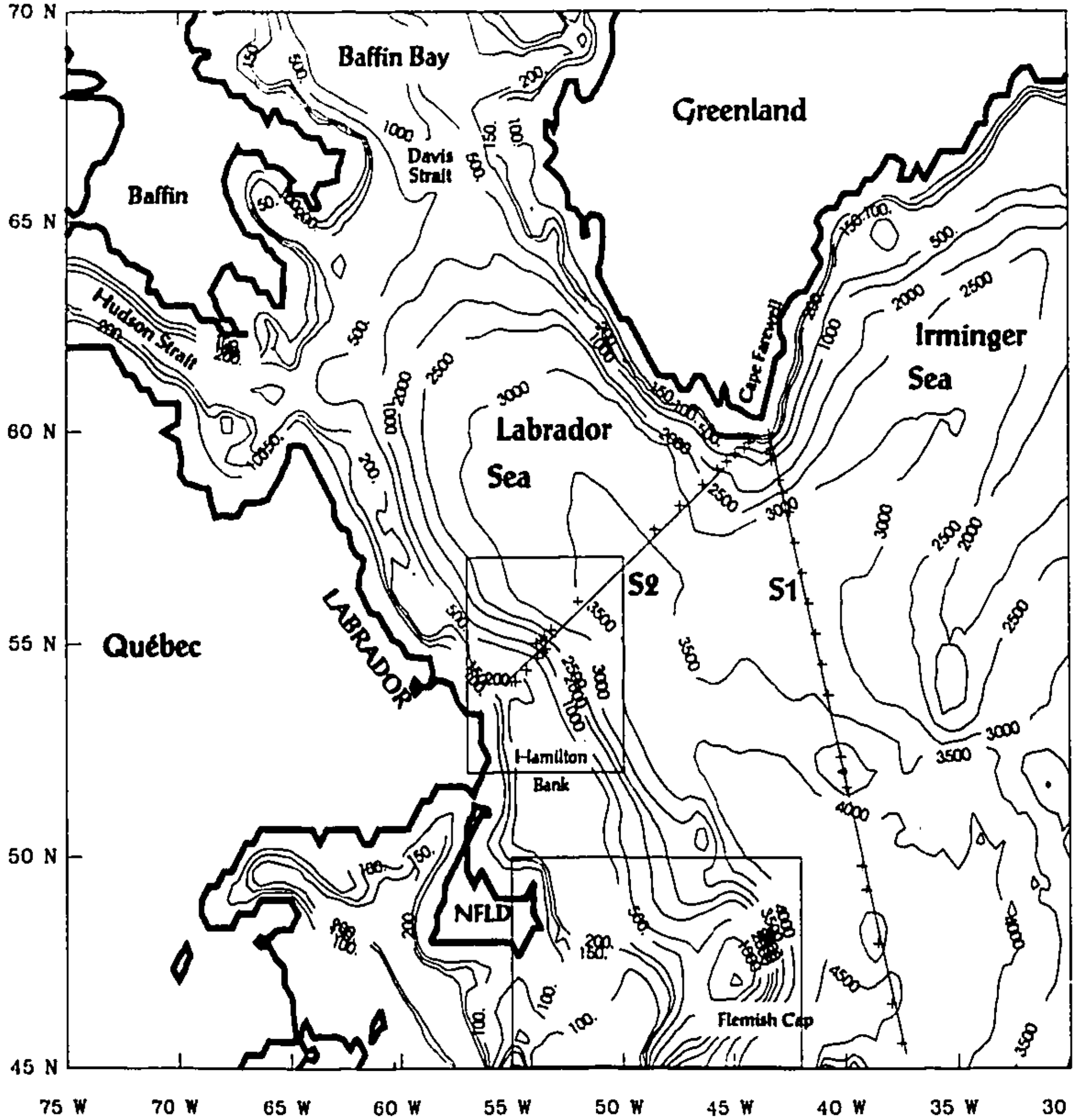

Figure 1.1: Bottom topography (m) of the northwestern Atlantic Ocean. S1 and S2 refer to section 1 and section 2. The Hamilton Bank and Flemish Cap subregions are indicated by boxes.

in the Labrador Sea (Fig. 1.2a, Clarke and Gascard, 1983, and Clarke, 1984): the Denmark Strait Overflow Water (DSOW) (also referred to as the Northwest Atlantic Bottom Water), the North Atlantic Deep Water (NADW), the Labrador Sea Water (LSW), the West Greenland Current (WGC) and the Labrador Current (LC). The WGC carries a mixture

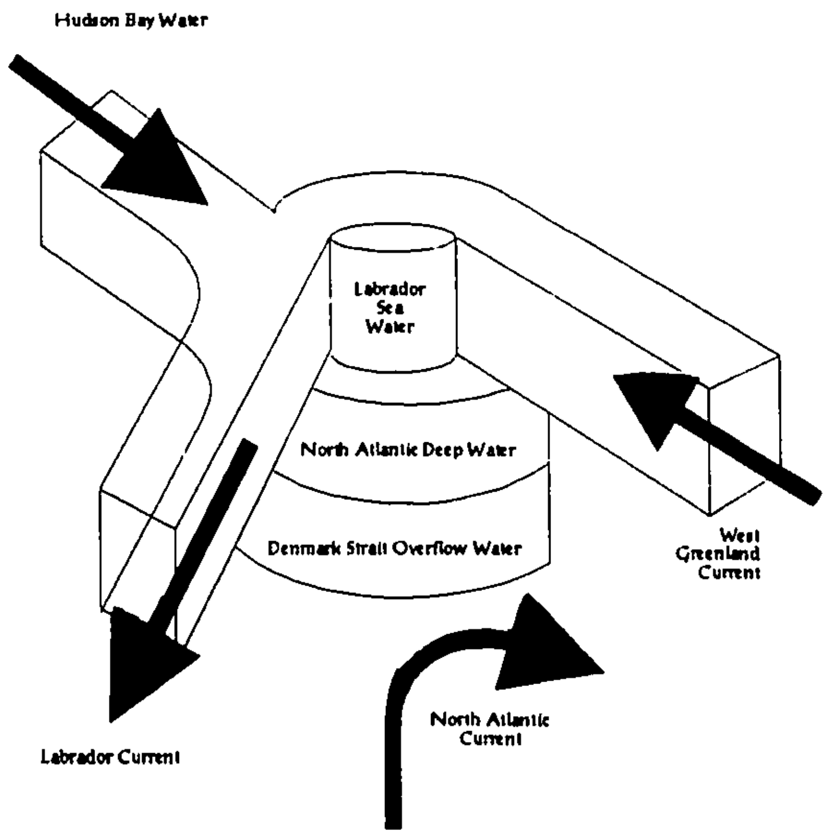

Figure 1.2a: A schematic representation of the water masses in the northwestern Atlantic Ocean.

of waters from the Irminger Current (IC) and the East Greenland Current (EGC, Fig. 1.2b).

On the southeastern side of the Labrador Sea, south of Cape Farewell, the coastal EGC brings cold (~-1.8°C) and low salinity (<34.5 psu) surface waters from the Arctic into the Labrador Sea. Near Cape Farewell and south of the EGC the IC flows westward, and brings a saltier (34.95-35.10 psu) and warmer (4-6°C) water mass into the Labrador Sea. Lee (1968) proposed that a northern branch of the North Atlantic Current turns northward

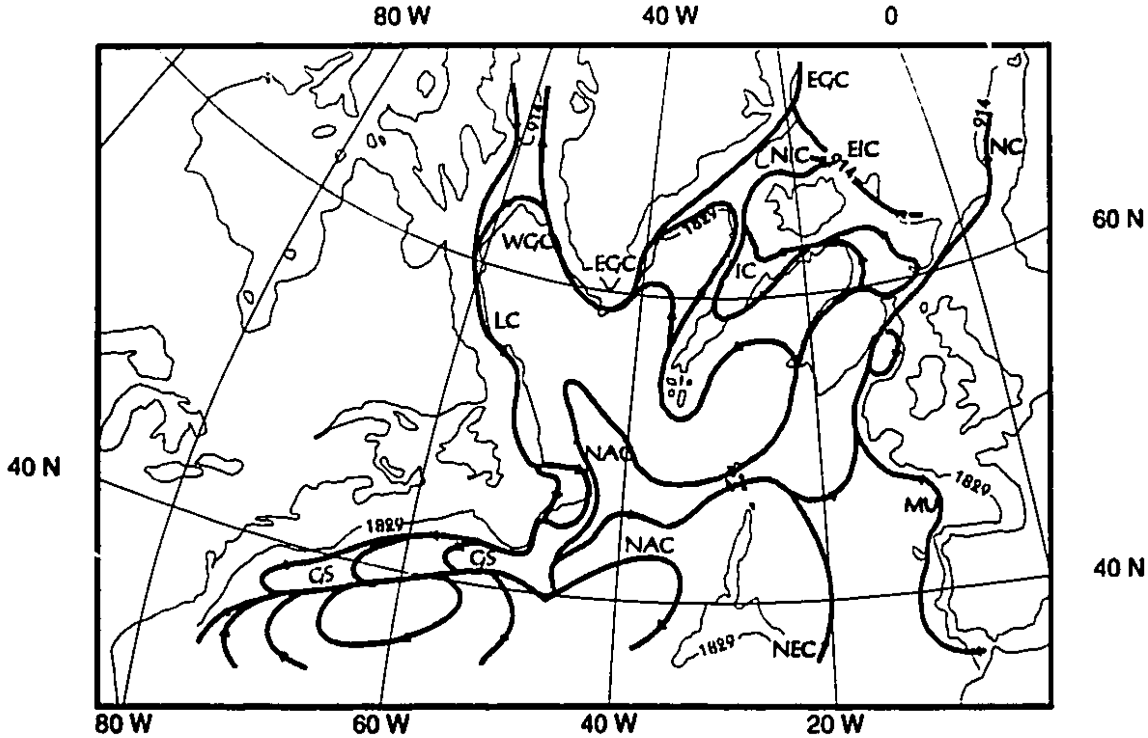

Figure 1.2b: A schematic representation of the shallow circulation of the North Atlantic (from Ivers, 1975). Abbreviations for the currents are as follows: Gulf Stream (GS), North Atlantic Current (NAC), North Equatorial Current (NEC), Mediterranean Undercurrent (MU), Norwegian Current (NC), East Icelandic Current (EIC), North Icelandic Current (NIC), Irminger Current (IC), East Greenland Current (EGC), West Greenland Current (WGC), Labrador Current (LC).

near the mid-Atlantic ridge, then near Iceland a part of the current loops around the Irminger Sea and then flows along the offshore edge of the EGC (see Fig. 19 of Krauss, 1986 and Fig. 1.2b). The water transported by this current is a mixture of the Irminger Sea Water (ISW) formed by winter deep convection and the warmer and saltier water carried from the East.

The WGC flows northward along the western coast of Greenland and splits into two branches: one which goes into Baffin Bay and one which flows cyclonically around the Labrador Sea. On the western side of the Labrador Sea, the southward LC flows over the Labrador shelf carrying a cold and low salinity mixture of waters from Hudson Bay, Baffin Bay, the WGC and the Arctic.

These last two components (WGC and LC) are mostly located over the shelves; the three other water masses are in the central part of the Labrador Sea (Fig. 1.2a). Trapped on the bottom the Deep Western Boundary Undercurrent (DWBU) carries the DSOW (1.4-1.6°C and ~34.9 psu) along the continental slope from Denmark Strait around Cape Farewell. Past Cape Farewell the DSOW flows cyclonically into the Labrador Sea and exits around the north of Flemish Cap. The DWBU flows below the IC and extends up to the 3000m isobath.

The NADW can be found at depths below 1800m , it is characterized by a temperature of ~3.0°C and a salinity of ~34.95 psu. Lee and Ellet (1967) proposed that NADW arises from the Scotland-Iceland overflows out of the Norwegian Sea circulating anticyclonically around the Reyjkanes Ridge, cyclonically around the Irminger Sea and into the Labrador Sea.

The last component, the LSW, is found above the NADW; it is formed by the winter convection in the Labrador Sea (Clarke and Gascard, 1983). Lazier (1973), on the basis of his work on the Labrador Sea in 1960's, defined the LSW as ~3.4°C and ~34.9 psu.

On the south of the Labrador Sea, the North Atlantic Current (NAC) flows northward past Flemish Cap; then it loops westward into the Labrador Sea before turning east near 50°N. The NAC then splits into two branches: one flows around Irminger Sea and the other one flows northeastward around Reykjanes Ridge (Krauss, 1986). Here, the NAC transports the Northeast Atlantic Water (~9.5°C, ~35.35 psu); below the NAC and flowing with it there are portions of recirculating LSW and NADW (Lee, 1968; Worthington, 1976; Clarke, 1984).

The LC carries a fresh and cold mixture made with waters from the WGC, Hudson Bay and from the Arctic (Baffin Bay) and flows along the Labrador shelf and slope. Near Hamilton Bank, the LC splits into two branches: a weak inshore branch, which follows the Newfoundland coast, and a strong offshore branch (Lazier and Wright, 1993) which flows southward through Flemish pass along the Grand Banks slope. Lazier and Wright (1993) also present evidence of what they call the *Deep Labrador Current*, centered onto the 2500m isobath, which flow southward offshore from the shelf break. The annual variations of the LC transport and speed are fully discussed by Lazier and Wright (1993). They found that the inshore and offshore branches show a baroclinic structure while the deep branch is more barotropic. According to Lazier and Wright (1993), Thompson *et al* (1986) and Greatbatch *et al* (1990), it seems that the baroclinic regime on the shelf has a buoyancy driven annual cycle whereas the barotropic regime has a wind driven annual cycle.

1.2 Circulation and transport

All researchers agree on a cyclonic circulation in the Labrador Sea (Ivers 1975, McCartney and Talley, 1982; Talley and McCartney, 1982; Clarke, 1984) but disagreements appear on its estimated transport. The flow field is often calculated from data measurements using a dynamic method with *a deep level of no motion* (~1200m or at the bottom). This assumption and the choice of the level of no motion is mainly responsible for the discrepancies in the estimated transports.

Swallow and Worthington (1969) followed five neutrally buoyant floats for periods of 12-71 hours during field work in the Labrador Sea in 1962. They observed a distinct deep water inflow to the south of Cape Farewell and an outflow on the Labrador side. They estimated (using 1200m as the level of no motion) a deep water inflow to the south of Cape Farewell of between 9.7 and 15.8 Sv (1 Sverdrup= 10^6 m^3/s). On average they observed a cyclonic deep transport in the Labrador Sea of the order of 10 Sv relative to the 1200m reference level. But Swallow and Worthington also concluded that they could not assume that 1200m is a level of no motion everywhere and at all times in the Labrador Sea. Clarke (1984), using current meter data collected in the Labrador Sea south of Cape Farewell in early 1978 (see Fig. 1 in Clarke 1984), observed a ~25 cm/s bottom-trapped current which extended across the continental slope from the 1900m to the 3000m isobath. Clarke used a reference velocity, obtained from current meter measurements, added to the geostrophic velocity for each station pair to improve current and transport estimates (more details are given in Clarke 1984). Clarke's results (see Fig. 1.3) suggest

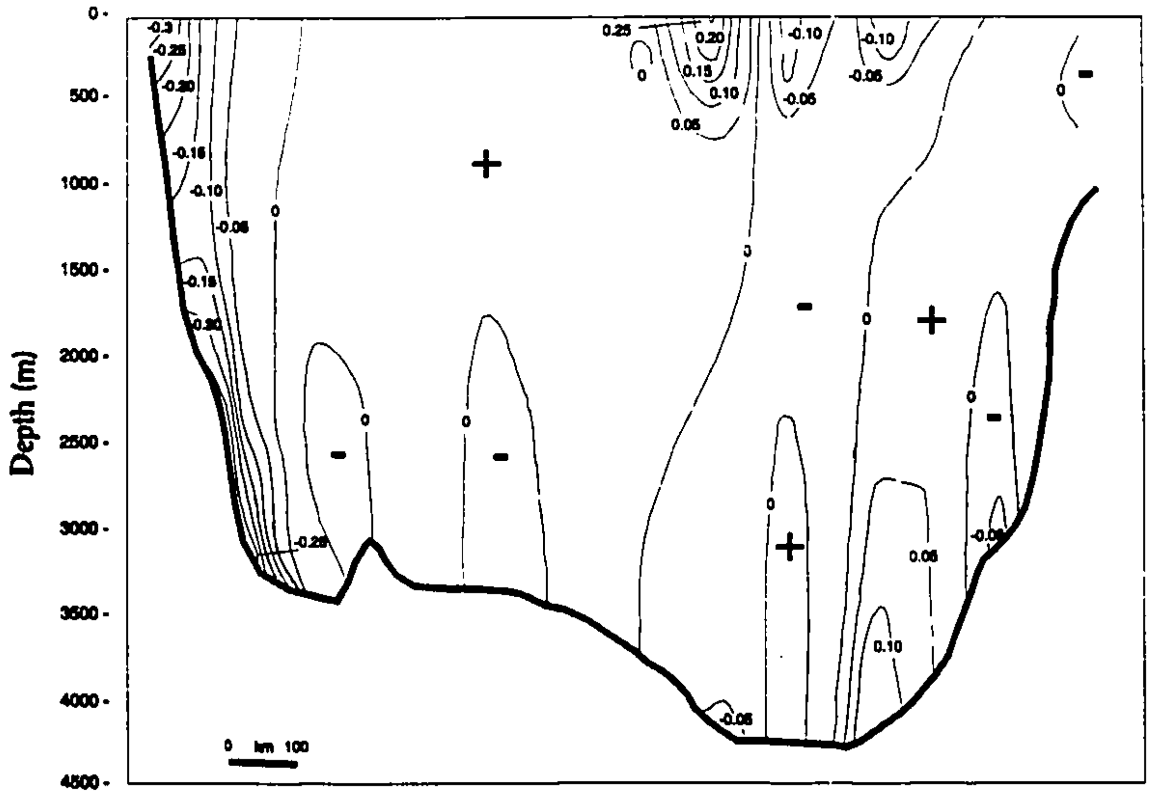

Figure 1.3: Geostrophic velocity for the Cape Farewell-Flemish Cap section (Redrawn from Clarke, 1984).

that there is likely a strong current on the slope at depth of 1200-1500m. But, as mentioned earlier, this level has often been considered to be a level of no motion. Consequently, the traditional geostrophic estimates of current and transport might have been underestimated. Dickson *et al* (1990) also observed strong currents on the slope in deep waters. The problem is that in order to successfully describe the absolute current structure and transport from the density field, either the surface pressure or a reference velocity are needed. The difficulty, as in all inverse calculations, is to find realistic values for these variables.

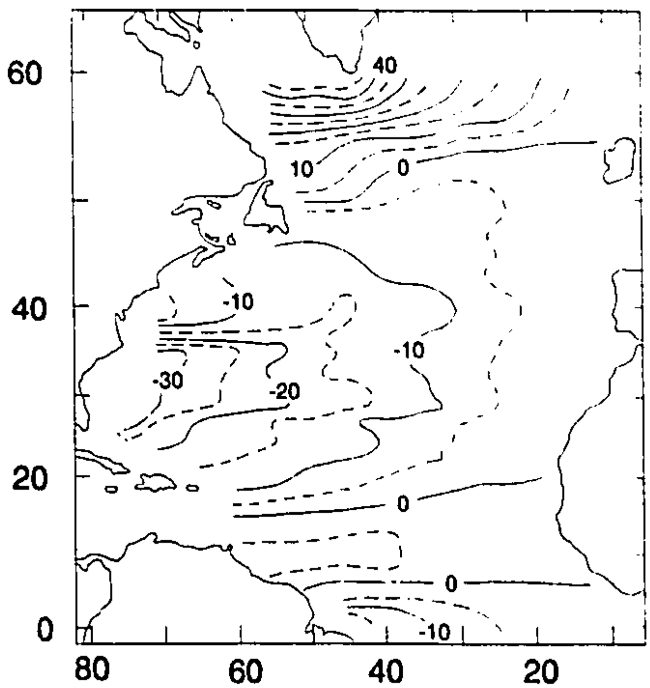

Figure 1.4: contours of the annual mean sverdrup mass transport (from Leetmaa and Bunker, 1978). Units are 10^{12} g/sec (= 1 Sv).

Leetmaa and Bunker (1978) used the Bunker (1976) estimation of the annual wind stress and estimated a maximum volume transport for the subpolar gyre of the order of 40 Sv (see Fig. 1.4). Ivers used what he called the *Method of qualitative constraints* which consists of determining the reference velocities based on information like: current measurements, ship drift data, consideration of continuity with other regions etc. Ivers estimated the transport across a section parallel to Cape Farewell-Cape Flemish section to be 53 Sv. He stated that this value was likely an overestimate.

Provost and Salmon (1986) used a variational inverse technique to determine the currents in the Labrador Sea. The method used by Provost and Salmon allows the determination of a velocity field which is consistent with data and dynamical constraints to within prescribed misfits (never equal to zero). The misfits represent errors in the data and dynamics, and are estimated from scaling analysis. They were able to reproduce Ivers' results using the conservation of the potential density as a dynamical constraint. Their technique has three disadvantages: (1) they did not use the *no flow through condition* and, consequently, this sometimes leads to streamlines intersecting the coast; (2) they did not introduce wind-stress as a dynamical constraint- they argued that its effects were included in the T-S data; (3) the data used to determine the circulation in the Labrador Sea were collected during a two-month cruise in the spring of 1966 and may not show the mean circulation.

1.3 The governing equations

In this section, some useful relations for describing the circulation of a fluid over a variable bottom topography will be derived. The governing equations are:

$$\frac{d\vec{v}_h}{dt} + f\hat{k}\times\vec{v}_h = -\frac{1}{\rho}\nabla_h p + \frac{1}{\rho}\frac{\partial\vec{\tau}}{\partial z} \qquad (1.1)$$

$$\frac{\partial p}{\partial z} = -\rho g \qquad (1.2)$$

$$\frac{d\rho}{dt} + \rho\nabla.\vec{v} = 0 \qquad (1.3)$$

where $\vec{v}_h$, $\vec{v}$, p, ρ, $\vec{\tau}$, g, ∇_h, dF/dt are, respectively, the horizontal velocity, the three dimensional velocity, the pressure, the density, the stress, the acceleration due to gravity, the horizontal gradient operator and the total rate of change of any variable F (see Eq. 1.5 below). Equations 1.1, 1.2 and 1.3 are respectively the *conservation of momentum*, the *hydrostatic approximation* and the *continuity equation*. If the fluid is Boussinesq then the continuity equation can be rewritten as:

$$\nabla.\vec{v} = 0 \tag{1.4}$$

as ρ can be replaced by a constant reference density ρ_0. The total derivative, d/dt, is defined as:

$$\frac{d}{dt} = \frac{\partial}{\partial t} + u\frac{\partial}{\partial x} + v\frac{\partial}{\partial y} + w\frac{\partial}{\partial z} \tag{1.5}$$

where u, v, w are the eastward, northward and vertical components of the velocity vector $\vec{v}$. Then, by using Eq. 1.5, neglecting the higher order terms (small Rossby number) and imposing the Boussinesq approximation, the Eq. 1.1 is written as:

$$\frac{\partial u}{\partial t} - fv = -\frac{1}{\rho_0}\frac{\partial p}{\partial x} + \frac{1}{\rho_0}\frac{\partial \tau^x}{\partial z} \tag{1.6a}$$

$$\frac{\partial v}{\partial t} + fu = -\frac{1}{\rho_0}\frac{\partial p}{\partial y} + \frac{1}{\rho_0}\frac{\partial \tau^y}{\partial z} \tag{1.6b}$$

The hydrostatic approximation (Eq. 1.2) and the continuity equation (Eq. 1.4) are now added to the Eqs. 1.6a-b:

$$\frac{\partial p}{\partial z} = -\rho g \tag{1.6c}$$

$$\frac{\partial u}{\partial x} + \frac{\partial v}{\partial y} + \frac{\partial w}{\partial z} = 0 \qquad (1.6d)$$

and the set of equations 1.6 is obtained. This system is unfortunately incomplete as there are 5 unknowns but only 4 equations. For completeness, equations for the conservation of salinity and heat can be added. Notice that in this section, the conservation of salinity and heat will not be involved. Following Mertz and Wright (1992), the rigid lid approximation is used, and equations 1.6a and 1.6b are depth averaged:

$$\frac{\partial}{\partial t}\frac{1}{H}\int_{-H}^{0} u\,dz - f\frac{1}{H}\int_{-H}^{0} v\,dz = -\frac{1}{\rho_o}\frac{1}{H}\int_{-H}^{0}\frac{\partial p}{\partial x}dz + \frac{1}{\rho_o}\frac{1}{H}\int_{-H}^{0}\frac{\partial \tau^x}{\partial z}dz \qquad (1.7a)$$

$$\frac{\partial}{\partial t}\frac{1}{H}\int_{-H}^{0} v\,dz + f\frac{1}{H}\int_{-H}^{0} u\,dz = -\frac{1}{\rho_o}\frac{1}{H}\int_{-H}^{0}\frac{\partial p}{\partial y}dz + \frac{1}{\rho_o}\frac{1}{H}\int_{-H}^{0}\frac{\partial \tau^y}{\partial z}dz \qquad (1.7b)$$

The streamfunction is defined by:

$$\begin{aligned} -\psi_x &= \int_{-H}^{0} v\,dz \\ \psi_y &= \int_{-H}^{0} u\,dz \end{aligned} \qquad (1.8)$$

which, once substituted in Eq. 1.7, leads to:

$$\frac{\partial}{\partial t}\left[\frac{\psi_y}{H}\right] + \frac{f}{H}\psi_x = -\frac{1}{\rho_o}\frac{1}{H}\int_{-H}^{0}\frac{\partial p}{\partial x}dz + \frac{1}{\rho_o}\frac{1}{H}(\tau_s^x - \tau_b^x) \qquad (1.9a)$$

$$\frac{\partial}{\partial t}\left[-\frac{\psi_x}{H}\right] + \frac{f}{H}\psi_y = -\frac{1}{\rho_o}\frac{1}{H}\int_{-H}^{0}\frac{\partial p}{\partial y}dz + \frac{1}{\rho_o}\frac{1}{H}(\tau_s^y - \tau_b^y) \qquad (1.9b)$$

where τ_s^x and τ_s^y are respectively the x and y component of the surface wind stress and

τ_b^x and τ_b^y are the x and y component of the bottom friction stress. Equation 1.10 is then obtained by cross differenciating (1.9a) and (1.9b):

$$-\nabla.\left[\frac{1}{H}\nabla\psi_t\right] - J[\psi,\frac{f}{H}] = -\frac{1}{\rho_o}[\partial_x\frac{1}{H}\int_{-H}^{0}p_y dz - \partial_y\frac{1}{H}\int_{-H}^{0}p_x dz] + \text{curl}_z\frac{\vec{\tau}_s - \vec{\tau}_b}{\rho_o H} \tag{1.10}$$

Now, from Leibnitz's theorem:

$$\begin{aligned}\int_{-H}^{0}p_\alpha dz &= \frac{\partial}{\partial\alpha}\int_{-H}^{0}p dz - p\,\Big|_{z=-H}\frac{\partial H}{\partial\alpha} \\ &= \frac{\partial}{\partial\alpha}\int_{-H}^{0}p dz - p_b\frac{\partial H}{\partial\alpha}\end{aligned} \tag{1.11}$$

and through integration by parts:

$$\begin{aligned}\int_{-H}^{0}p dz &= (zp)\,\Big|_{z=-H}^{z=0} + g\int_{-H}^{0}\rho z dz \\ &= Hp_b + \rho_o\phi\end{aligned} \tag{1.12}$$

Eq. 1.10 can be rewritten as a function of a quantity termed the available potential energy (Φ):

$$-\nabla.\left[\frac{1}{H}\nabla\psi_t\right] - J[\psi,\frac{f}{H}] = \text{curl}_z\frac{\vec{\tau}_s - \vec{\tau}_b - \rho_o\nabla\phi}{\rho_o H} \tag{1.13}$$

where J is the Jacobian operator: $J(A,B)=A_xB_y-A_yB_x$; the available potential energy is defined by Eq. 1.14:

$$\phi = \frac{g}{\rho_o}\int_{-H}^{0} \rho z dz \tag{1.14}$$

For a steady state flow with weak bottom friction, this equation is then reduced to:

$$-J[\psi, \frac{f}{H}] = \text{curl}_z \frac{\vec{\tau}_s - \rho_o \nabla\phi}{\rho_o H} \tag{1.15}$$

which can be rewritten as:

$$-J[\psi, \frac{f}{H}] = \text{curl}_z \frac{\vec{\tau}_s}{\rho_o H} + J[\phi, \frac{1}{H}] \tag{1.16}$$

Eq. 1.16 is equivalent to Eq. 20 of Mellor *et al* (1982). In terms of the depth integrated current **V**, Eq. 1.16 becomes:

$$\mathbf{V} . \nabla \frac{f}{H} = \text{curl}_z \frac{\vec{\tau}_s}{\rho_o H} + J[\phi, \frac{1}{H}] \tag{1.17}$$

The last term on the right hand side of Eq 1.17 is the *Joint Effect of Baroclinicity and Relief* (JEBAR) term. These three last equations are a vorticity balance where the transport across planetary vorticity (f/H) contours is forced by the surface wind stress and by the JEBAR term (see Eq. 1.17). JEBAR enters in the vorticity balance as a baroclinic forcing which vanishes under homogeneous conditions. Furthermore, if no local surface stress is applied the flow should be parallel to the f/H contours.

JEBAR was independently discovered by Sarkisyan and Ivanov (1971), and Holland and Hirschman (1972), this effect was found to be responsible for motions over a variable topography (Huthnance, 1984). A detailed description of JEBAR can be found in Mertz and Wright (1992). This derivation is similar to that of Mellor *et al* (1982) except for the fact that Mellor *et al* (1982) used the spherical coordinates without the rigid lid approximation.

1.4 The Bottom Pressure Torque versus JEBAR

Holland (1973) tried to understand why theories did not explain the strength of western boundary currents like the Gulf Stream for which the observed transport is twice the theoretical Munk (1950) value. Holland used the Bryan (1969) primitive equation ocean general circulation model (see Cox (1984) for detailed description of this model). Combining the governing equations of this model, he ended up with the equation Eq. 1.18 for the vorticity conservation:

$$-\beta\frac{m}{a}\psi_\lambda - \frac{m}{a}\left(\frac{\tau_\lambda}{m}\right)_\theta + J[P_b,H] + \frac{m}{a}[F^\theta_\lambda - (\frac{F^\lambda}{m})_\theta] = 0 \qquad (1.18)$$

where: θ is the latitude, λ is the longitude, ψ is the horizontal transport stream function, a is the Earth's radius, β is defined as $\partial f/\partial y$ (f is the Coriolis parameter), τ_t is the zonal wind-stress, $\rho_o P_B$ is the bottom pressure, H is the bottom depth, and F is the lateral friction term. In Eq. 1.18 the terms are respectively the planetary vorticity tendency, the wind stress, the bottom pressure torque and friction. If the bottom pressure term is zero then this equation corresponds to that obtained using Munk's theory. Holland assumed that the distributions of zonal wind stress surface salinity and temperature varied only in the latitudinal direction. Notice that Holland used a sign convention for his streamfunction which is opposite to that described by Eq. 1.8 (ie. positive ψ values are, here, associated with an anticyclonic circulation). He ran his model under three different conditions: with stratification and constant depth (E1), with topography and no stratification (E2) and with both stratification and topography (E3). In the first simulation (E1) the bottom pressure torque was zero everywhere and the total northward transport in the western boundary current was about 20 Sv, a value which depended on the wind stress distribution. In the second simulation (E2) the streamlines tended to follow the f/H lines (conservation of potential vorticity) and the maximum northward transport was about 12 Sv. In the last simulation (E3) there was a single but very intense gyre over the topographic slope region for which the northward transport was about 40 Sv. Figure 1.5 shows the distribution of the four terms of Eq. 1.18. For E1, the friction balanced the advection of planetary vorticity near the western boundary while in offshore regions the wind-stress curl balanced the advection of planetary vorticity (Fig. 1.5a). For E2, the friction term was not playing an important role except near the western boundary where it was balanced by the wind-stress curl; the advection of planetary vorticity was balanced by the bottom torque over the slope and, in offshore regions, by the windstress curl (Fig. 1.5b). For E3, the very large negative planetary vorticity advection near the western boundary was compensated by a very large friction; the planetary vorticity advection became positive over the slope and was balanced by the bottom pressure torque; again, the windstress curl offshore balanced the advection of planetary vorticity (Fig. 1.5c). The increased northward current on the western boundary in E3 was due to the combined increase of the bottom pressure (northward) and depth (eastward) leading to a negative bottom pressure torque which was

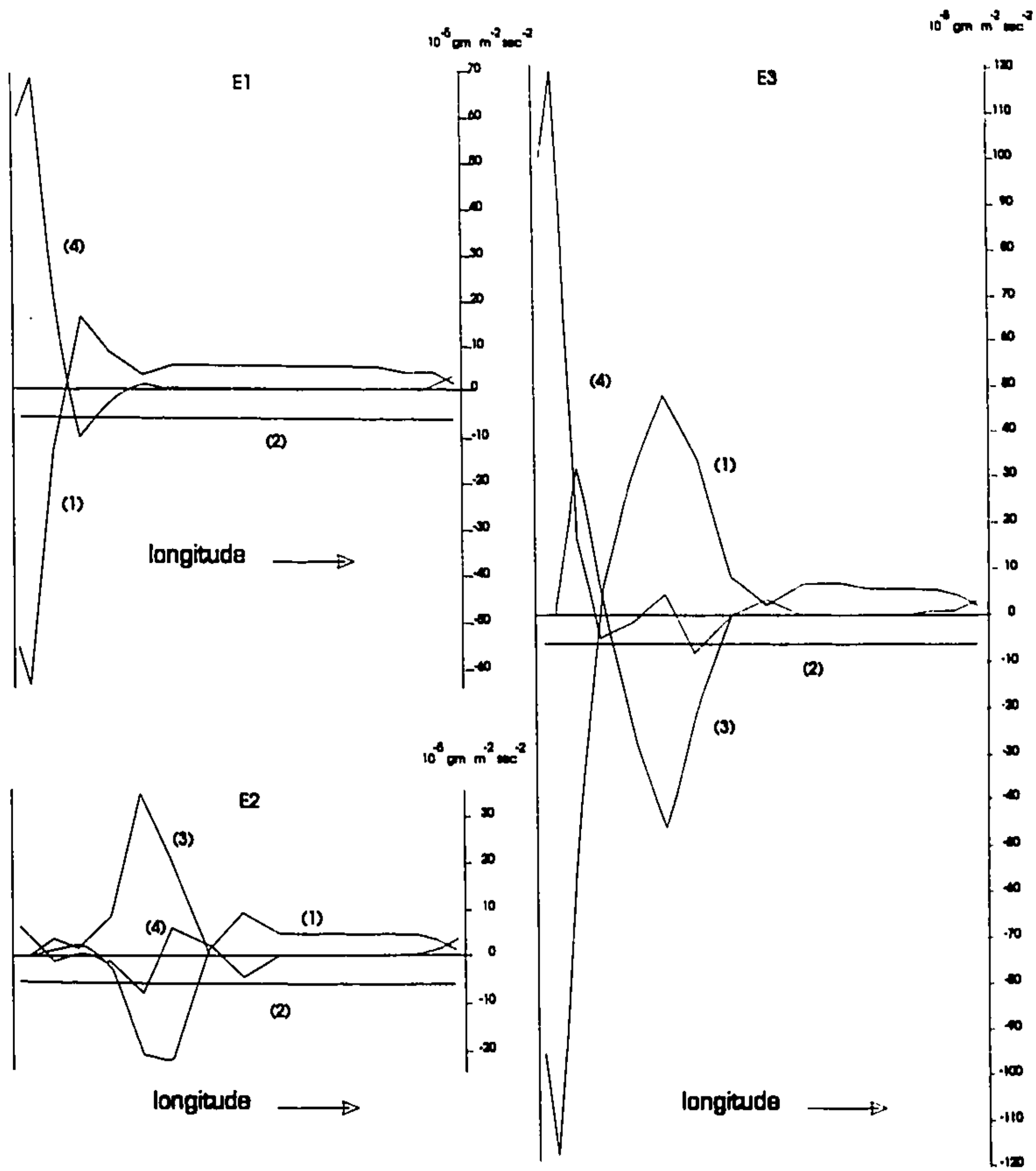

Figure 1.5: The east-west distribution of terms in the vorticity Eq. (1) at the latitude of the maximum (negative) wind-stress curl, about 34°N. The vertical scale is the same on all graphs. Term (1) is the planetary vorticity tendency, term (2) is the wind-stress curl, term (3) is the bottom pressure torque and term (4) is the frictional term (redrawn from Holland, 1973).

balanced by positive planetary vorticity advection; hence, by a southward flow. This increased southward flow required, by continuity, an increased northward flow on the shelf near the western boundary. The Holland (1973) paper gives a good picture of the contribution of the bottom pressure torque to the circulation, but the choice of a meridionally dependant depth is not appropriate fcr the Labrador Sea, where banks and saddles found on the Labrador shelf introduce both a longshore and offshore dependence in the topography.

As both the bottom pressure torque and JEBAR were introduced in the present section and section 1.3, it is now important to differentiate these two mechanisms. Following Greatbatch *et al* (1991) and Mertz and Wright (1992), the hydrostatic equation (Eq. 1.6c) can be vertically integrated:

$$\begin{aligned} &\int_{p(-H)}^{p(z)} dp = -\int_{-H}^{z} \rho g dz \\ \Leftrightarrow \quad & p(z) - p(-H) = -g\int_{-H}^{z} \rho dz \end{aligned} \tag{1.19}$$

and then depth integrated throughout all the water column:

$$\int_{-H}^{0} \left(p(z) - p(-H)\right) dz = -g\int_{-H}^{0}\int_{-H}^{z} \rho dz' dz \tag{1.20}$$

The left hand side of Eq. 1.20 can be rewritten as:

$$H(\bar{p} - p_b) = -g\int_{-H}^{0}\int_{-H}^{z} \rho dz' dz \tag{1.21}$$

where the depth average pressure, $\bar{p}$, is defined as:

$$\bar{p} = \frac{1}{H}\int_{-H}^{0} p\,dz \qquad (1.22)$$

By using Eq. 1.13, Eq. 1.22 is rewritten as:

$$\begin{aligned} \int_{-H}^{0} \rho g z\,dz &= -g\int_{-H}^{0}\int_{-H}^{z} \rho\,dz'dz \\ \Leftrightarrow \quad \rho_o\phi &= -g\int_{-H}^{0}\int_{-H}^{z} \rho\,dz'dz \end{aligned} \qquad (1.23)$$

Equation 1.24 is obtained by combining Eqs. (1.21) and (1.23) together:

$$\begin{aligned} H(\bar{p} - p_b) &= \rho_o\phi \\ \Leftrightarrow p_b &= \bar{p} - \frac{1}{H}\rho_o\phi \end{aligned} \qquad (1.24)$$

Using Eq. 1.24, the bottom pressure torque, $J(p_b,H)$, can be expressed in terms of the depth averaged pressure torque and JEBAR (see Eq. 1.25).

$$\begin{aligned} J[p_b,H] &= J[\bar{p},H] - \rho_o J[\frac{\phi}{H},H] \\ &= J[\bar{p},H] + \rho_o H J[\phi,\frac{1}{H}] \end{aligned} \qquad (1.25)$$

From this last equation, JEBAR appears as the difference between the depth averaged pressure torque and the bottom pressure torque. The first term on RHS of Eq. 1.25 is also referred as the density compensation term (see Greatbatch *et al*, 1991). It is clear from Eq. 1.25 that under homogeneous conditions the JEBAR term is equal to zero, whereas the bottom pressure torque term is still there.

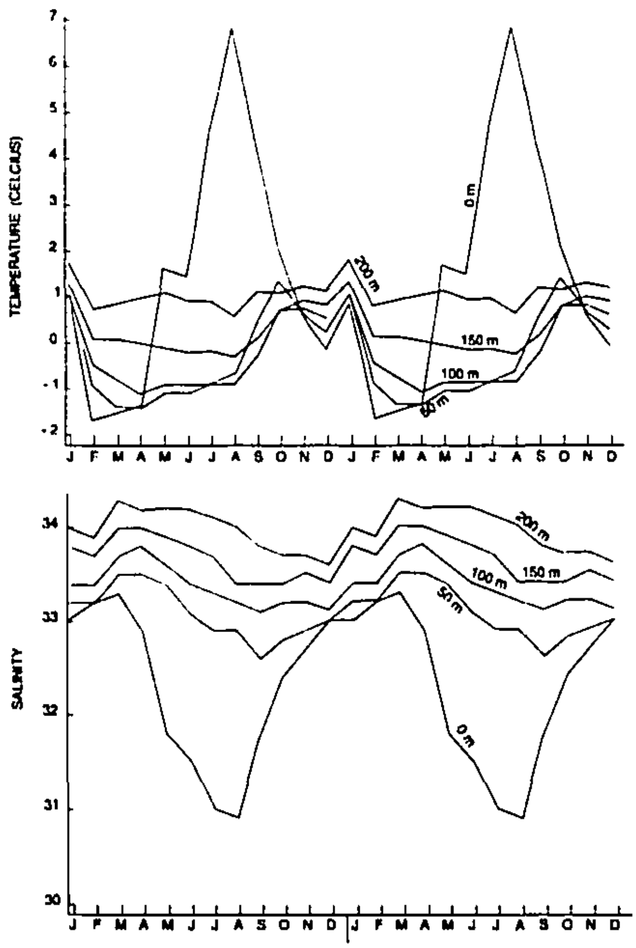

Figure 1.6: Temperature and salinity on the Labrador shelf (Redrawn from Lazier, 1982).

1.5 Seasonal, interannual and interdecadal variabilities

A problem associated with data analysis is that temperature, salinity and wind stress are subject to variability on various time scales, and hence so is the circulation. The seasonal variability of the oceanic data is well observed but not necessarily well understood. For example, Lazier(1980) reported that the salinity annual cycle is not directly connected with the seasonal precipitation cycle. Figure 1.6 shows temperature and salinity time series for different depths (data have been collected over the Labrador shelf). Both Fig. 1.6a and 1.6b show an annual cycle: the temperature is maximum at the surface in July and January at 200m, the surface salinity is maximum in March and is minimum in August (later in deeper water). There is an 8.5°C difference between the summer and winter surface temperatures and a 2.5 psu seasonal variation in salinity. At 50m, the seasonal variations are smaller (2°C for temperature and 1 psu for salinity). The seasonal variations are observed in the whole Labrador Sea, but they depend strongly on the offshore distance (over the shelf stronger variations would be expected due to the WGC and the LC). Lazier (1980) reports an annual cycle of 0.25°C at 1500m. The seasonal variability of the temperature can be easily interpreted in terms of heating; thermal stratification is established in the upper layer in the spring and the summer and then is rapidly removed by fall and winter storms.

Lazier (1980), in analyzing oceanic data collected at the Ocean Weather Station Bravo (56°30'N,51°00'W) located in the center of the Labrador Sea from 1964 to 1974, observed interannual variability in the salinity signal. He observed a density decrease, induced by a salinity freshening, in the top 200m between the winter of 1967-68 and the winter of 1971-72 (Fig. 1.7). At 10m, the minimum salinity value in the summer was 34.6 psu for the 1964-67 period but decreased to 33.9 psu for the 1967-71 period. The decrease in salinity diminished with depth to 0.1 psu at 200m from 1967 to 1971. The average salinity above 1500m showed a net decrease in salinity of 0.04 psu. This decrease in salinity is explained by the advection of the *Great Salinity Anomaly* (Dickson et *al*, 1988). Briefly, during the sixties, a high atmospheric pressure anomaly was established over Greenland leading to a stronger northerly wind component over the Greenland Sea.

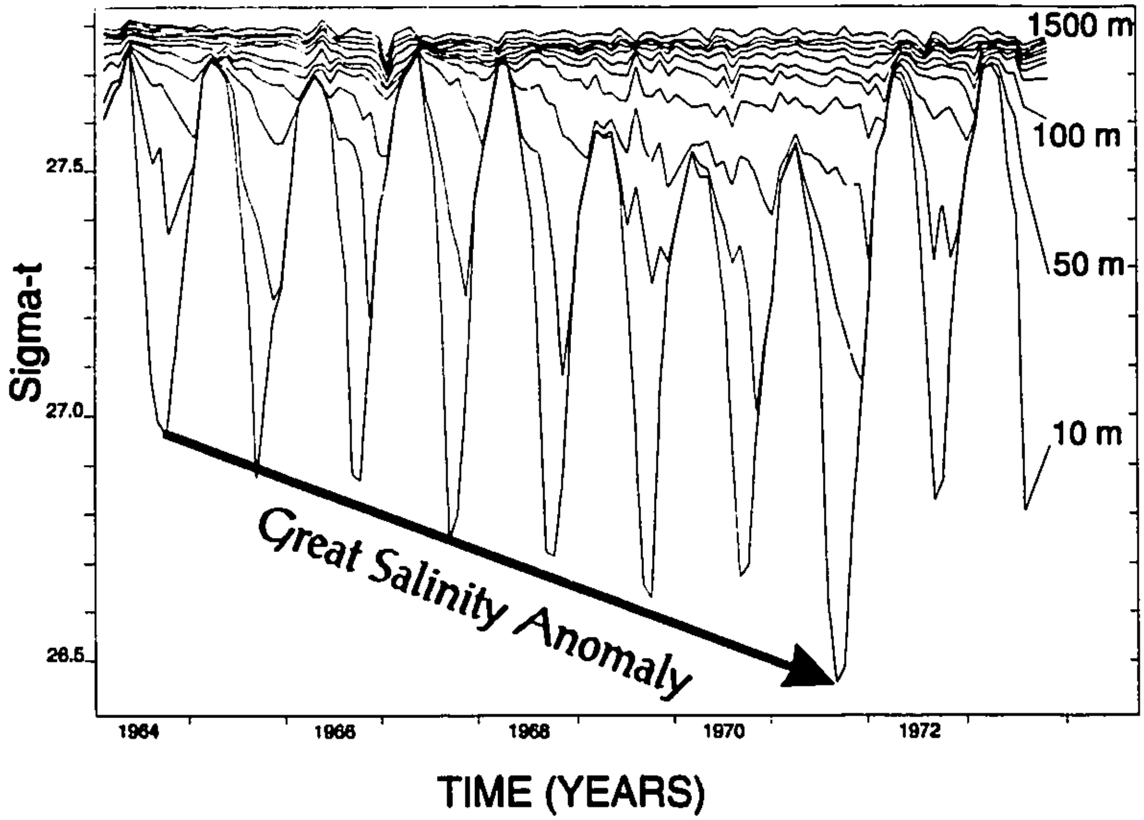

Figure 1.7: Sigma-t at Ocean Weather Station Bravo (Redrawn from Lazier, 1980).

Consequently, the East Greenland Current and the East Icelandic Current became fresher and colder due to an increasing proportion of Polar waters being brought south to the seas north of Iceland. Dickson *et al* (1988) proposed that this salinity anomaly was then advected around the Labrador Sea and from there to the East-Atlantic and all around the subpolar gyre at a speed of 2-5cm/s. The relationship between these salinity anomalies and the North-Atlantic air-ice-ocean system is the subject of much recent interest (e.g. Mysak and Manak, 1989; Ikeda, 1990; Mysak *et al*, 1990).

The atmosphere is the main source of ocean forcing (heat exchange, wind, evaporation and precipitation, atmospheric pressure). The atmospheric circulation over the North

Atlantic, including the Labrador Sea, is governed by the Icelandic Low-Azores High pressure system. In the winter, the Icelandic Low is deep, leading to strong north-westerly winds across the Labrador Sea. The Icelandic Low weakens in the spring, and, accordingly, the wind speed decreases, but the direction stays approximately the same (see Fig. 6.7). The Azores High also gets stronger in the spring. In the summer, the Icelandic Low weakens still further and, hence, the winds are weaker. The deepening of the Icelandic Low restarts in the fall. A useful measure of the North Atlantic atmospheric circulation is given by the North Atlantic Oscillation (NAO) index, which is defined as the pressure difference between the Azores High and the Icelandic Low. Myers *et al* (1989) report another example of interannual variability: the baroclinic transport throughout the upper layer of the Labrador Sea decreases in the summers following strong mid-latitude westerlies. In other words, they observed that the baroclinic transport relative to 100m is negatively correlated with the strength of the winter westerlies at mid-latitudes (represented by the NAO index). They also report a positive correlation between the ice cover and the NAO index.

The renewal of the LSW is done through deep convection which mixes the top 1500m of the water column (2000m in severe winters). Deep convection can occur only in the winter because the surface waters in the summer are warmer and fresher (stronger stratification, Fig. 1.6). In the winter season the fresher surface waters lose their heat to the atmosphere, getting denser and sinking: convection occurs. The variability observed in the LSW properties (T and S) may be due to variability in the water masses (LC, WGC, NADW) that make up the Labrador Sea and/or to the convection process. Lazier (1980) reports that the depth of convection was around 200m from 1968 to 1971, and 1200-1500m for 1967 and 1972. He also states that the heat loss to the atmosphere was stronger in the winters of 1967 and 1972 ($2.8\text{-}4.5 \times 10^9$ J/m^2) than in the winters of 1968 to 1971 ($1.6\text{-}1.9 \times 10^9$ J/m^2). The effect of the low salinity anomaly (mentioned earlier), at least in sofar as the mild winters are concerned, was to increase the stratification and hence limit convection to the top 200m (see Fig. 1.7). Lazier proposed that the main areas for deep convection are regions of greatest heat loss and where the water column is least stable. The offshore side of the Labrador Current is a good example of such an area due to the proximity of the North American continent where the air is colder in the winter. The wind is also another atmospheric agent which plays an important role in deep convection processes: Lazier reports that the heat loss may be driven by strong (20 m/s) and cold (-20°C) northwesterlies; during the 1978 winter the winds blew predominantly from the east or the northeast over the Labrador Sea-consequently the heat loss was smaller and the convection was relatively shallow (400m).

At longer time scales, the ocean temperature and salinity seem to be subject to interdecadal varibilities (see Levitus, 1989a, b, c; 1990; Kushnir, 1994; and Deser and Blackmon, 1993). Kushnir (1994) compared the sea surface temperature (SST) of the North Atlantic for four 15-year-long periods: 1900-1914, 1925-1939, 1950-1964 and 1970-1984 (see Fig. 1.8). He observed that the SST of the 1900-1914 and 1970-1984 periods where colder than the SST of the 1925-1939 and 1950-1964 periods. Kushnir looked at

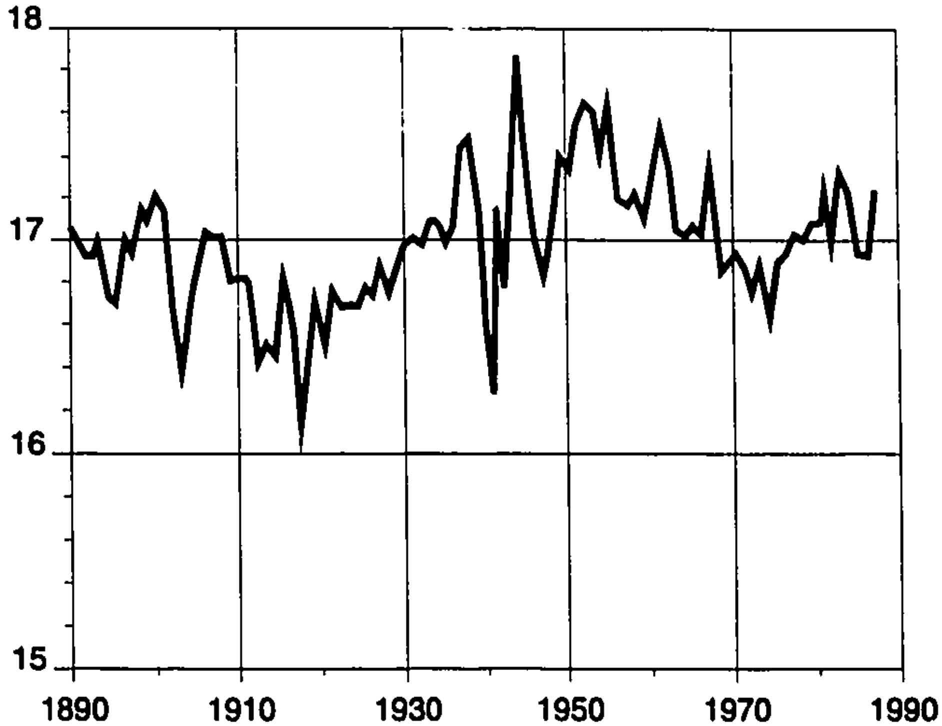

Fig. 1.8: mean SST of the 30-50°N latitude band (redrawn from Kushnir, 1994)

the corresponding spatial structures of the SST interdecadal variability and he found that the Labrador Sea and Greenland Sea are the regions where the variations of SST between the cold and warm periods are strongest. These regions, as mentioned earlier, are sources of deep water. He suggested that the SST interdecadal variabilities are most likely due to changes in the thermohaline circulation. This idea is supported by numerical results (see Weaver and Sarachik, 1991) and by the fact that Kushnir found that the related interdecadal variability of the sea level pressure (SLP) and surface wind are due to a reaction of the lower atmosphere to the ocean temperature anomaly. Since interdecadal variations of temperature and salinity should affect the circulation, Greatbatch *et al* (1991) applied the Mellor *et al* (1982) diagnostic method to the salinity and temperature data of Levitus (1989a, b, c; 1990) for the pentads 1955-59 and 1970-74. They diagnosed the subtropical gyre to be ~30 Sv weaker for the pentad 1970-74 than during the pentad 1955-59, and found that this weakening was due to a decrease in the bottom pressure torque forcing.

1.6 The aim of this study

Although the qualitative description of the circulation of the Labrador Sea is generally known, there is still much work left for improving the quantification of this circulation. Most of the data analyzed (eg: Clarke, 1984; Lazier, 1973; Lazier and Wright, 1993) offer an *instantaneous* description of what the currents were during a specific cruise. Still, because of the variabilities described in the previous section, one might wonder how representative these short time series of observations are of the mean currents. The widely used Levitus (1982) data are an attempt at describing the seasonal and mean temperature-salinity values for all the oceans with a relatively coarse resolution of 1°x1°. As will become clear later, the Levitus data are not suitable for analysing the circulation of the northwestern Atlantic Ocean as the parameters used in his analysis overly-smoothed and hence eliminate some important features of the region (eg: temperature and salinity gradients associated with the West Greenland-Labrador Current system are too weak, the T-S signature of the Deep Western Boundary Undercurrent is not visible).

Evaluating the currents from hydrographic data is not an easy task and has been the subject of much research. The reference level method is the easiest and most commonly used technique. Usually this method works well for estimating surface currents but fails, as mentioned earlier, in regions where there are strong currents at the reference level. Hence, it does not work well for estimating the volume transport (eg: a 0.5 cm/s bottom currents across a section 1000 km wide leads to a volume transport of 15 Sv). The β-spiral technique (Schott and Stommel, 1978) was developed for the purpose of estimating the reference level currents. Killworth and Bigg (1988) compared three inverse technique. the β-spiral technique, the Bernoulli method (Killworth, 1986) and the Box inverse method (Wunsch, 1978), and concluded that in most regions the two last techniques gave more accurate results. All the inverse methods mentioned above assumed a perfect density field without taking into account errors in the T-S values. The next improvement, by Mercier (1986, 1989 and 1992), was to correct the density field using theoretical information, current meter data, Lagrangian float data, etc. Bogden *et al* (1992) also optimized their density field by minimizing the mixing at a depth of 1000m.

In this thesis, I seek to improve the density field using a modified, high resolution version of the Levitus objective analysis scheme, in order to get a better representation of the distribution of the water masses found in the northwestern Atlantic Ocean. The purpose of this study is also to describe the seasonal and interdecadal variability of the temperature and salinity fields, and the associated changes in the circulation. Interannual varibility cannot be studied in detail as the amount of observations restricts such an analysis. The circulation is diagnosed using inverse techniques (reference level of no motion, Bernoulli technique and the Mellor *et al* (1982) method).

CHAPTER 2: THE OBJECTIVE ANALYSIS

2.1 The description of the data set

The temperature and salinity data used are from the Marine Environment Data Service (MEDS), Ottawa, Canada, supplemented by a subset of the National Oceanographic Data Centre (NODC) data from Joe Reid, together with the 1980s additional data of Fukumori and Wunsch (1991). The combined data set covers a 79 year period starting in 1910. Most of the comments made by Levitus (1982) about the data set that he used are also true for this combined data set. The number of temperature observations are always higher than the number of salinity observations due to the use of XBTs for sampling the upper-ocean temperature (Tables 2.1 and 2.2). Also, the number of observations is influenced by the world economic and political situtations: the drop in 1925-1929 (see Fig. 2.1) is associated with an economic crisis and the 1940-1944 drop is a consequence of the World War II. The number of observations is always higher in the summer (July-August-September) than in any other season (Table 2.1 and 2.2). About 52,000 salinity and 145,000 temperature vertical profiles were made over the 79 year period but, a large number of these profiles were obtained in the second half of the century (see Fig. 2.1). Although, the number of observations available seems to be very large, it should be noted that this number drops rapidly (see Table 2.3) with increasing depth. However, what is most important is not the total number of observations but their horizontal distribution. It should also be mentioned that the salinity measurements taken during the *Great Salinity Anomaly* (see Dickson *et al*, 1988), which was advected into the

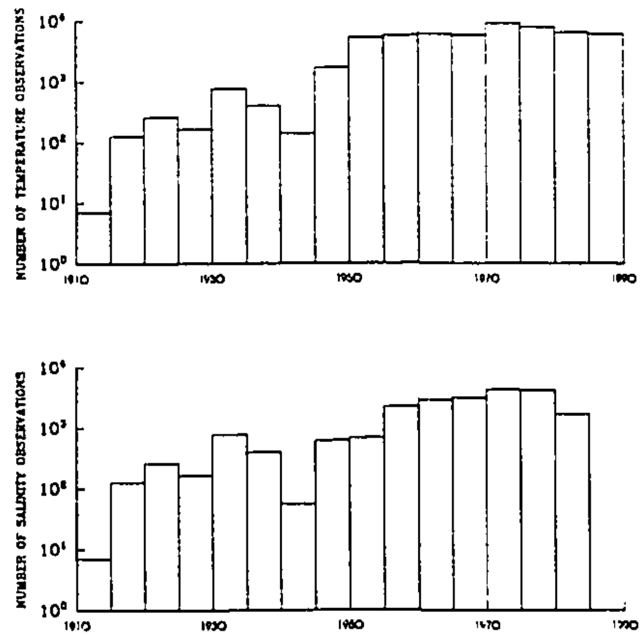

Figure 2.1: Time distribution of salinity and temperature summer data.

northwestern Atlantic ocean in 1970-1974 (see Lazier, 1980), represent about 15% of the total number of observations.

As the purpose of this analysis is to study the climatological mean as well as the variablility of the northwestern Atlantic Ocean, the combined data set was divided into three parts: the summer season (July-August-September), the warm season (June-November) and the cold season (December-May). As the analysis also attempts to determine the interdecadal variability of the northwestern Atlantic Ocean, an objective analysis for the warm season during the 1950-1964 and 1965-1981 periods will also be carried out. It is not possible to examine earlier periods (1900-14 and 1925-39) as there is a lack of data (see Tables 2.1 and 2.2). The same reason also restricts the analysis to

Table 2.1: Time distribution of salinity observations

	1900-14	1925-39	1950-64	1965-81	1910-89
January	0	4	230	1296	1531
February	0	3	386	579	972
March	0	45	489	1366	1968
April	0	156	1739	3229	5237
May	0	252	1682	4111	6245
June	0	406	2403	4098	7223
July	7	687	2944	5531	9591
August	0	327	2636	4671	8070
September	0	315	1179	2850	4566
October	0	66	862	1692	2806
November	0	6	706	2029	2843
December	0	1	109	412	545
Summer	7	1329	6759	13052	22227
Cold	0	461	4635	10993	16498
Warm	7	1807	10730	20871	35099

Table 2.2: Time distribution of temperature observations

	1900-14	1925-39	1950-64	1965-81	1910-89
January	0	4	770	2798	4820
February	0	6	916	2047	6045
March	0	50	1242	2845	6169
April	0	156	2165	4634	9907
May	0	261	2971	8891	16644
June	0	409	5757	8707	19544
July	7	694	6445	10019	21424
August	0	330	6773	10422	21983
September	0	319	4096	6207	13306
October	0	74	2706	4371	10743
November	0	6	2644	4624	12003
December	0	1	449	1163	2999
Summer	7	1343	17314	26648	56713
Cold	0	8513	8513	22378	46584
Warm	7	28421	28421	44350	99003

Table 2.3: Vertical distribution of the summer (July-August-Septembre) temperature and salinity observations for the 1910-89 period.

Level	Depth (m)	SALINITY	TEMPERATURE
1	0	20764	49616
2	10	16084	48814
3	20	15782	47543
4	30	14919	44559
5	40	14232	42156
6	50	13549	39739
7	75	11810	33799
8	100	10437	29622
9	125	9357	26211
10	150	8484	22985
11	200	6914	18983
12	250	5824	14373
13	300	4892	10129
14	400	3709	7235
15	500	3132	4915
16	600	2625	3844
17	700	2424	3447
18	800	2267	2760
19	900	2163	2596
20	1000	2049	2426
21	1100	1824	1999
22	1200	1757	1917
23	1300	1651	1795
24	1400	1578	1720
25	1500	1408	1543

TABLE 2.3: cont ...

Level	Depth (m)	SALINITY	TEMPERATURE
26	1750	1031	1154
27	2000	881	1000
28	2250	716	727
29	2500	590	599
30	2750	504	508
31	3000	387	393
32	3250	265	274
33	3500	149	151
34	3750	88	88
35	4000	63	65
36	4250	35	36
37	4500	10	10

the warm season of the 1950-1964 and 1965-1981 periods.

2.2 The description of the objective analysis scheme

The objective analysis scheme used to grid the data is a modification of the *Method of Successive Corrections* (hereafter MSC) that was used in Levitus and Oort (1977) and later by Levitus (1982) to successfully map the world oceans' properties. For a detailed discussion of the MSC, see Cressman (1959), Daley (1991) and Seeman (1983). The data were first vertically interpolated using a cubic spline onto 37 standard vertical levels and then objectively analyzed onto a grid with a horizontal resolution of 1/3° by 1/3° for all vertical levels. The standard levels used (see Table 2.3) are the same as those used by Levitus (1982) for the upper 1500m; below this depth, the standard levels are those used by Fukumori and Wunsch (1991) and Fukumori *et al.* (1991); their finer resolution (250m as compared to Levitus' 500m) will help improving the DWBU signature. The total number of summer temperature and salinity observations for all standard levels is shown in Table 2.3. The scheme is described by equations 2.1-2.3:

$$S = S_{guess} + \frac{\sum WQ}{\sum W} \tag{2.1}$$

$$Q = S_{guess} - S_i \tag{2.2}$$

$$W = 0 \qquad\qquad r>R \tag{2.3a}$$

$$W = e^{-\frac{4r^2}{R^2}} \qquad r \leq R \tag{2.3b}$$

where r is the spatial distance between the observation, S_i, and the gridpoint. This scheme behaves as follows: an initial guess, S_{guess} is corrected by the weighted mean (2nd term on the right hand side of 2.1) of the difference between that value and all measurements, S_i, that are within a given influence radii, R. This corrected value, S, is then used as a new initial value and corrected by the same procedure using a smaller influence radius. Levitus (1982) used four iterations with decreasing influence radii of 1500 km to 800 km. The question of setting values for the influence radii is a subtle problem where one should consider the spatial density of observations as well as the grid resolution. Three iterations with influence radii of 800, 500 and 200 km are used in this analysis.

As mentioned earlier, there are very well defined fronts along the shelf break in the northwestern Atlantic Ocean. The use of the same scheme as Levitus (Eqs. 2.1-2.3), even with relatively small influence radii, spreads these frontal regions over too large an area. The original Levitus (1982) scheme is modified here in such a way that only observations located over a range of isobaths are used. A modified spatial distance, r, is defined by:

$$r = d + R * \delta \tag{2.4a}$$

where d is the real spatial distance between the observation and the gridpoint (see Fig. 2.2), R is the influence radius and δ is defined by:

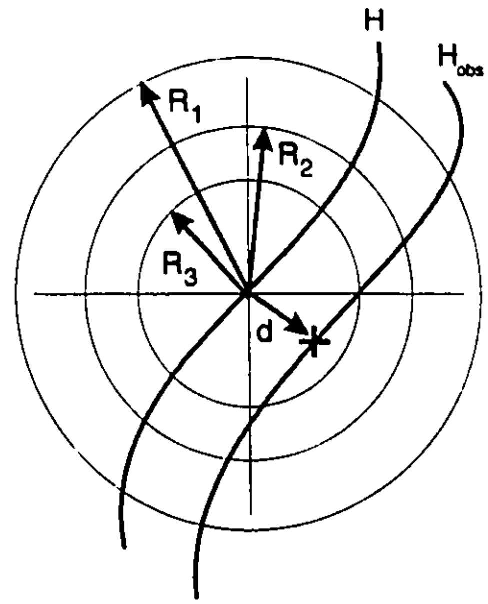

Figure 2.2: A schematic representation of the parameters used in the objective analysis.

$$\delta = 0 \quad \text{if} \quad |H - H_{obs}| \leq \delta h \tag{2.4b}$$
$$\delta = 1 \quad \text{if} \quad |H - H_{obs}| > \delta h$$

Here H_{obs} is the ocean depth at the data location and δh is defined by the function:

$$\delta h = 900 - 600\, e^{-\left(\frac{H}{5261}\right)^2} \tag{2.5}$$

where H is the ocean depth at the gridpoint location. Equation 2.5 implies a larger δh in deep ocean which is justified as offshore water masses occupy a larger area than nearshore water masses. In equation 2.5, several functions were tried: constant (δh=300m), linear, exponential; the Gaussian Function was finally chosen because it allows δh to be small in both the shelf and the slope regions such that the DWBU signature could be captured. The choice of 900, 600 and 5261 in Eq. 2.5 was obtained such that: i) in shelf region δh~300m, ii) δh~500m near h~3300m and iii) δh~900m in interior regions. It should be noticed that the modified analysis scheme preserves the location of fronts in coastal and slope regions which is very important for the northwestern Atlantic Ocean.

If, for a given gridpoint, there were no data within the area defined by the influence radius, then the gridpoint value was flagged and the iteration was stopped. These *no data* gridpoints and the number of data used in the last iteration were saved in separate files.

2.3 The horizontal data distribution

In spite of the strong decrease in the number of observations in deeper water, the number of undetermined gridpoints, discussed in the previous section, depends much more on the horizontal distribution. A rather small number of observations (e.g. 4000) but well distributed could give good results. Figures 2.3-2.5 show the positions of the salinity observations for summer, the warm and the cold seasons, respectively. An example of a relatively sparse horizontal distribution is shown in Fig. 2.7a for the salinity observations taken during the 1965-1981 warm season at 10m. Figure 2.6a shows the positions of the salinity observations at 10m for the 1950-1964 warm season; although the number of observations is comparable to that of Fig. 2.7a, their horizontal distribution is far better as large areas without data can be seen in the Irminger and Labrador Seas in Fig. 2.7a. The temperature data positions are not shown as the data coverage for temperature is always better than for salinity. The 1965-81 period was considered rather than the 1970-84 period of Kushnir (1994) for a purely technical reason: the data coverage for 1970-84

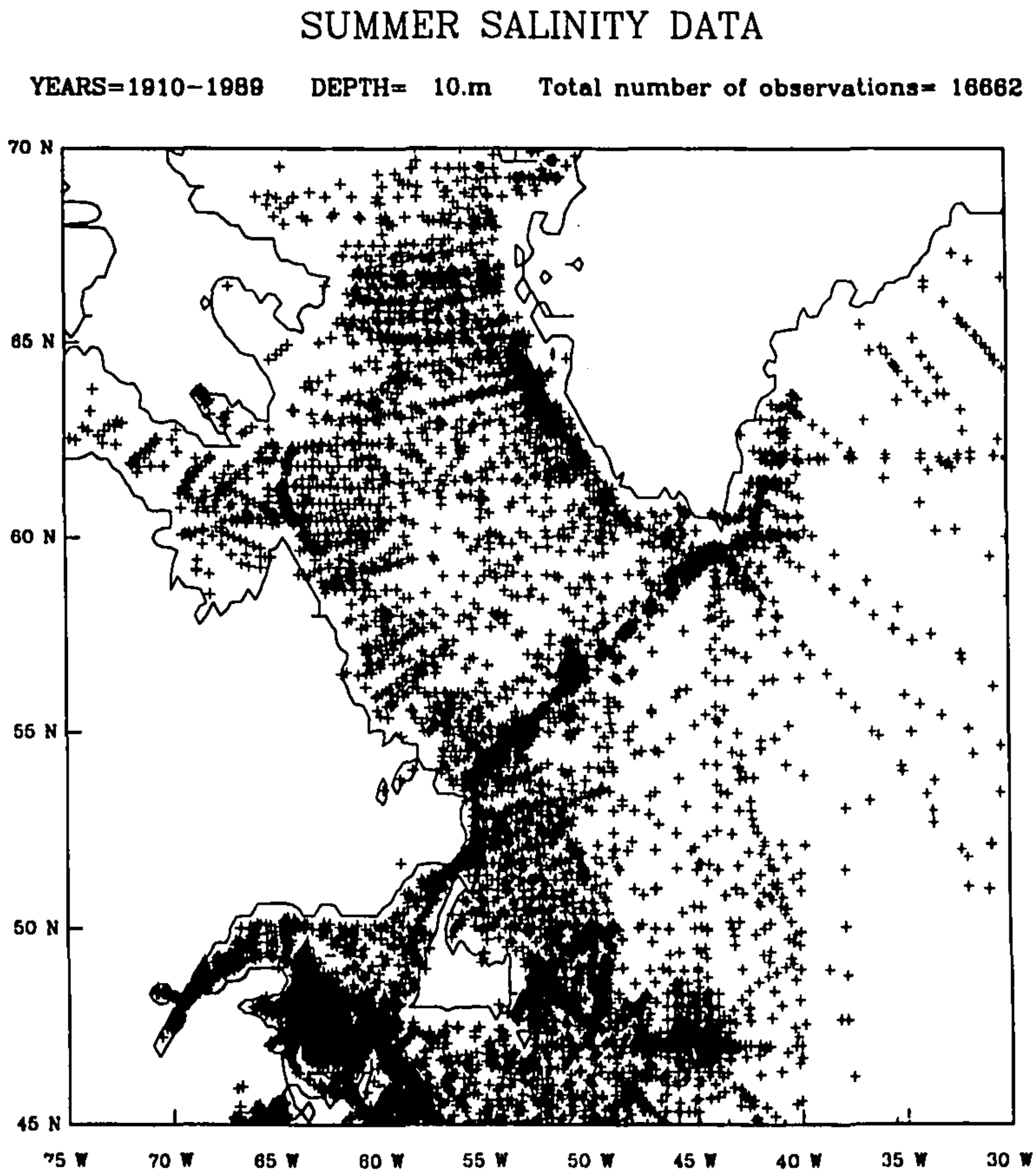

Figure 2.3: Horizontal distribution of salinity observations for the 1910-89 summer season at a) 10m,

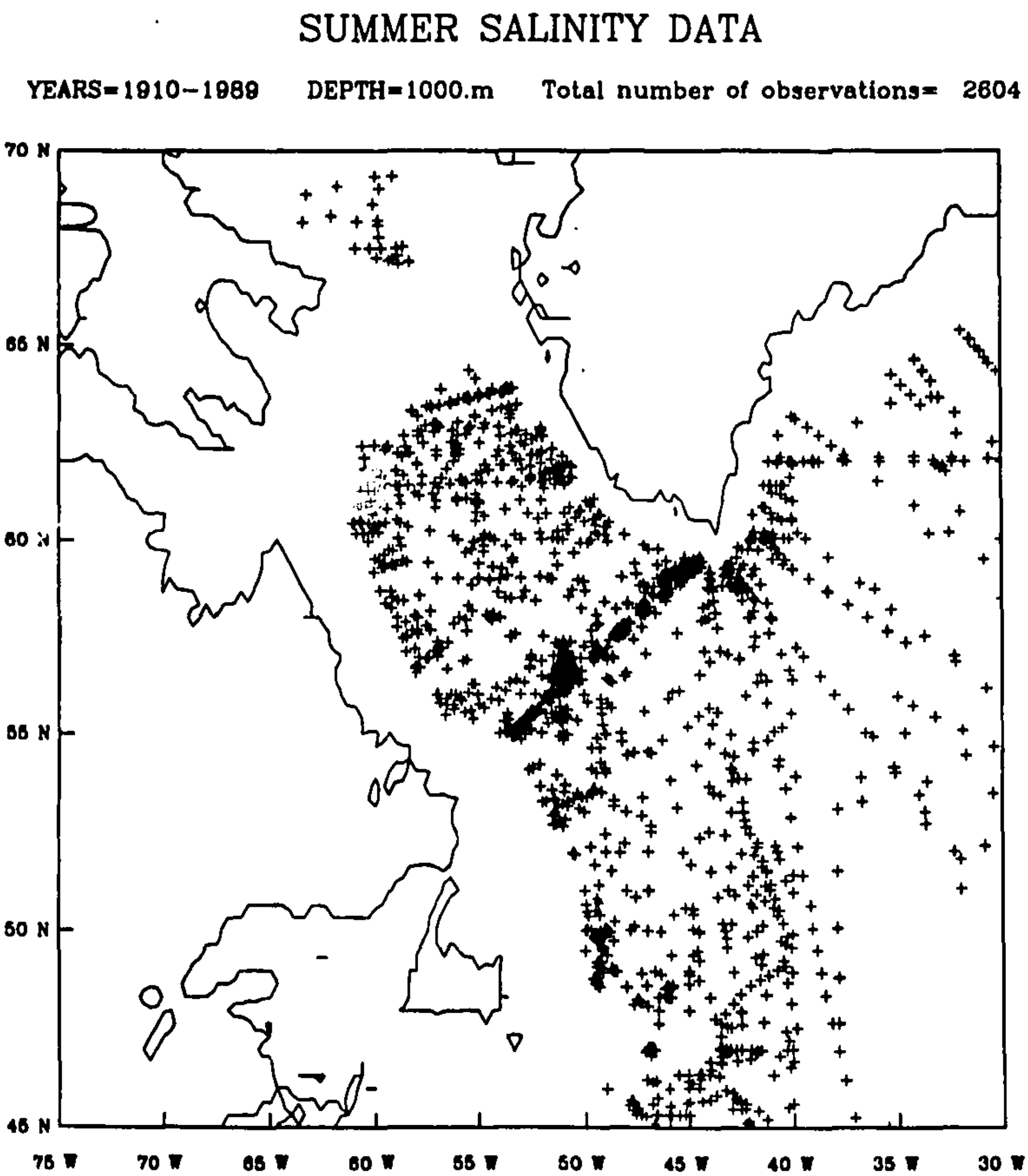

Figure 2.3 cont: b) 1000m,

SUMMER SALINITY DATA

YEARS=1910-1989   DEPTH=3250.m   Total number of observations= 271

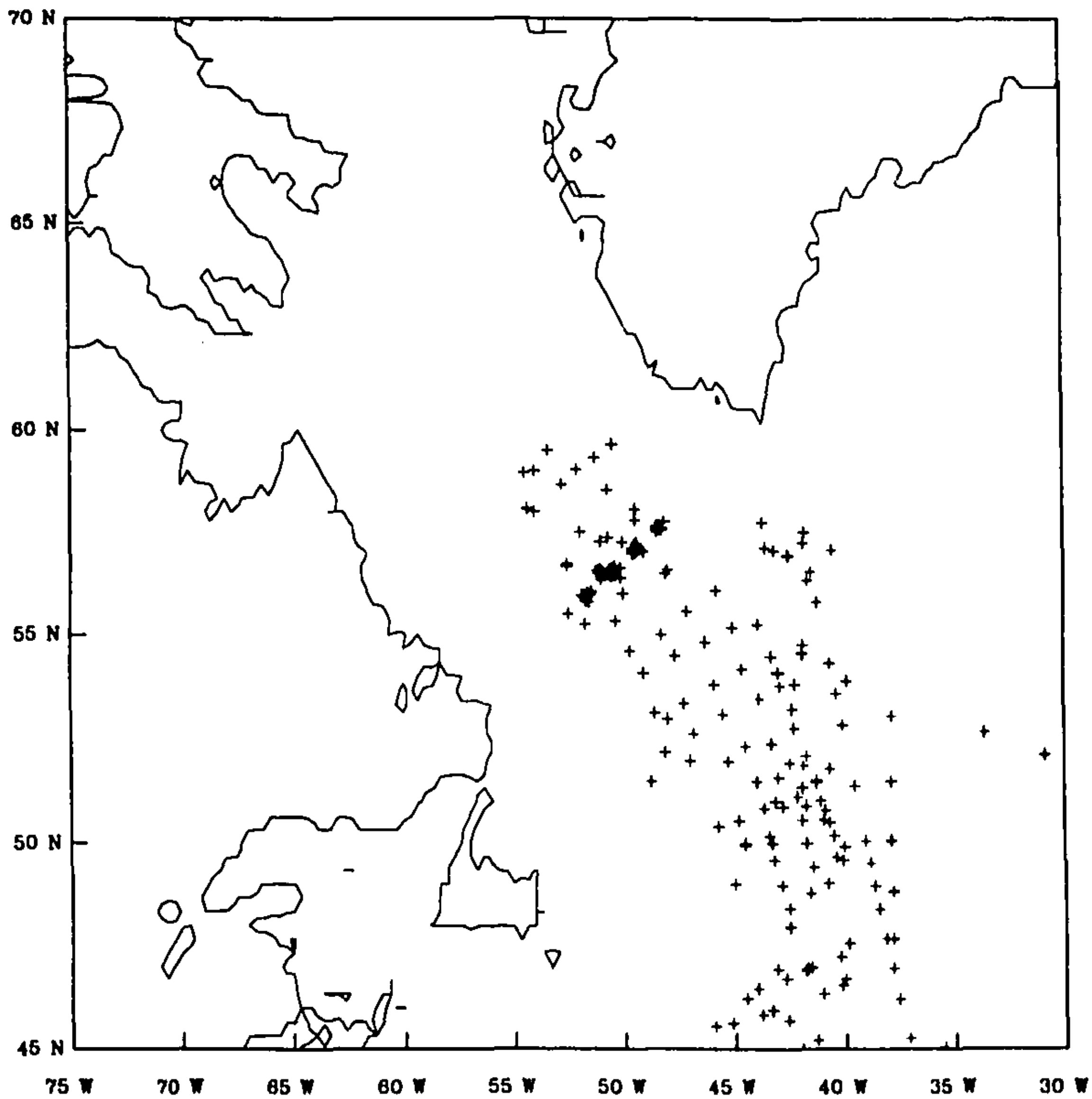

Figure 2.3 cont: and c) 3250m.

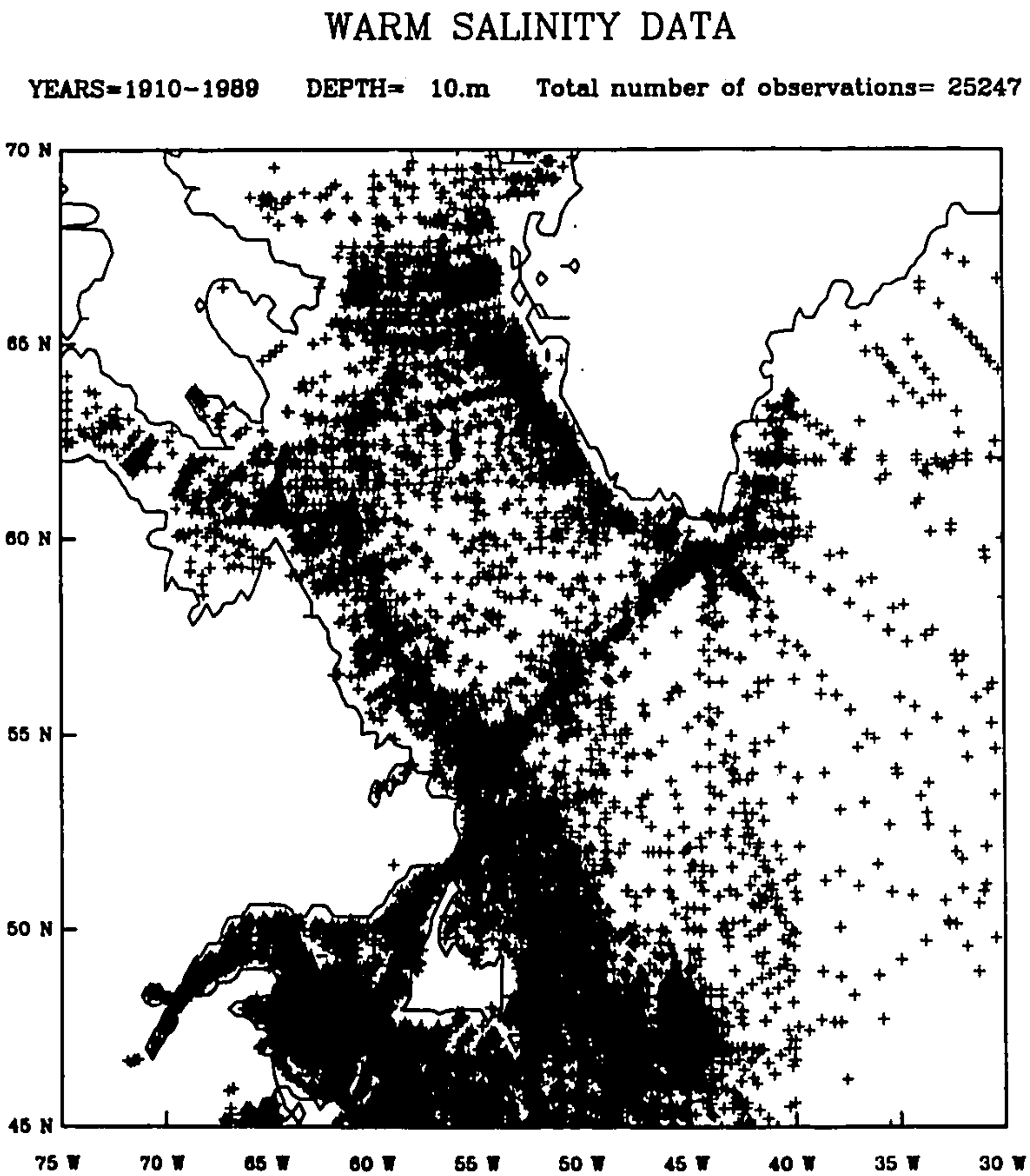

Figure 2.4: Horizontal distribution of salinity observations for the 1910-89 warm season at a) 10m,

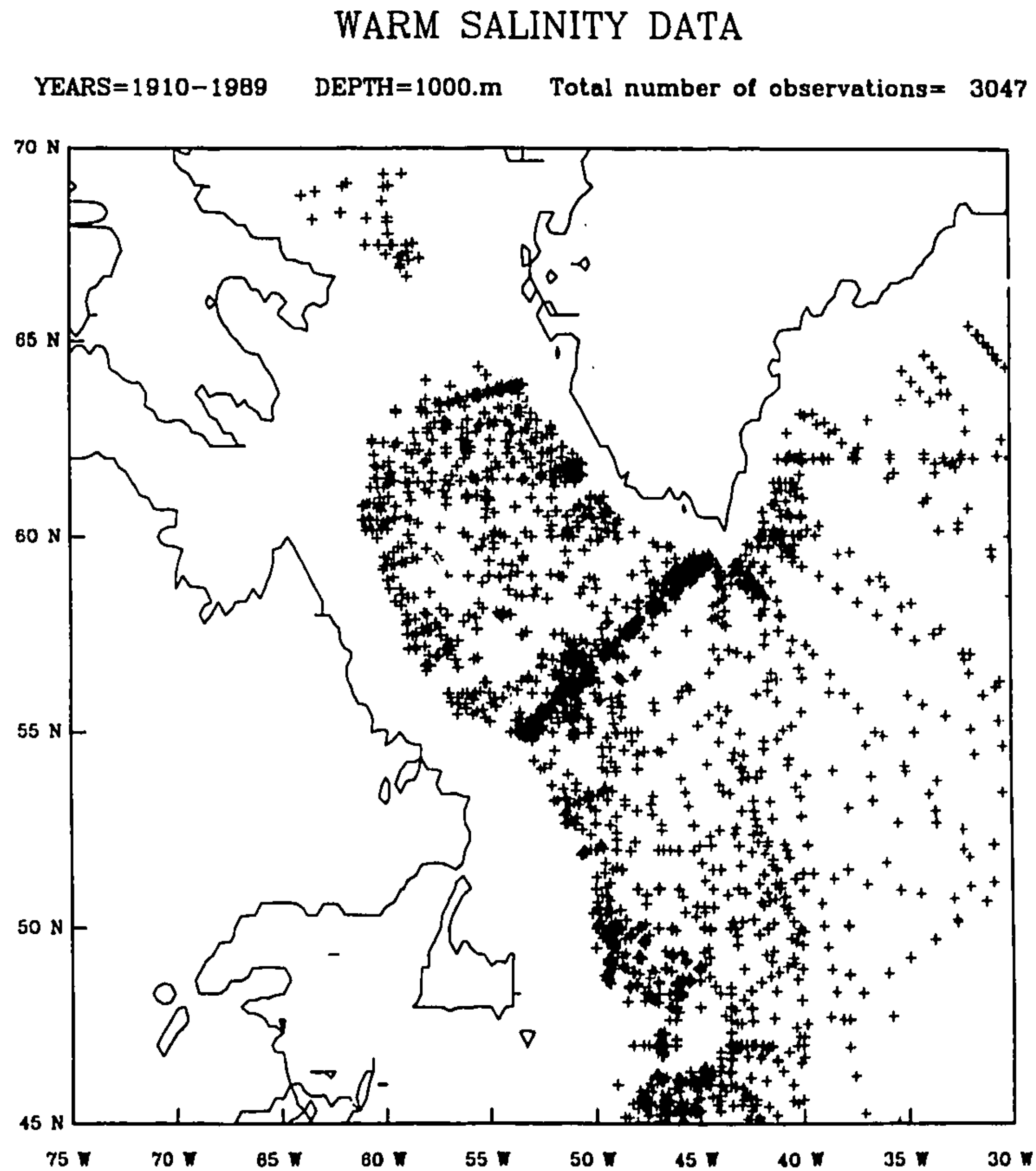

Figure 2.4 cont: b) 1000m,

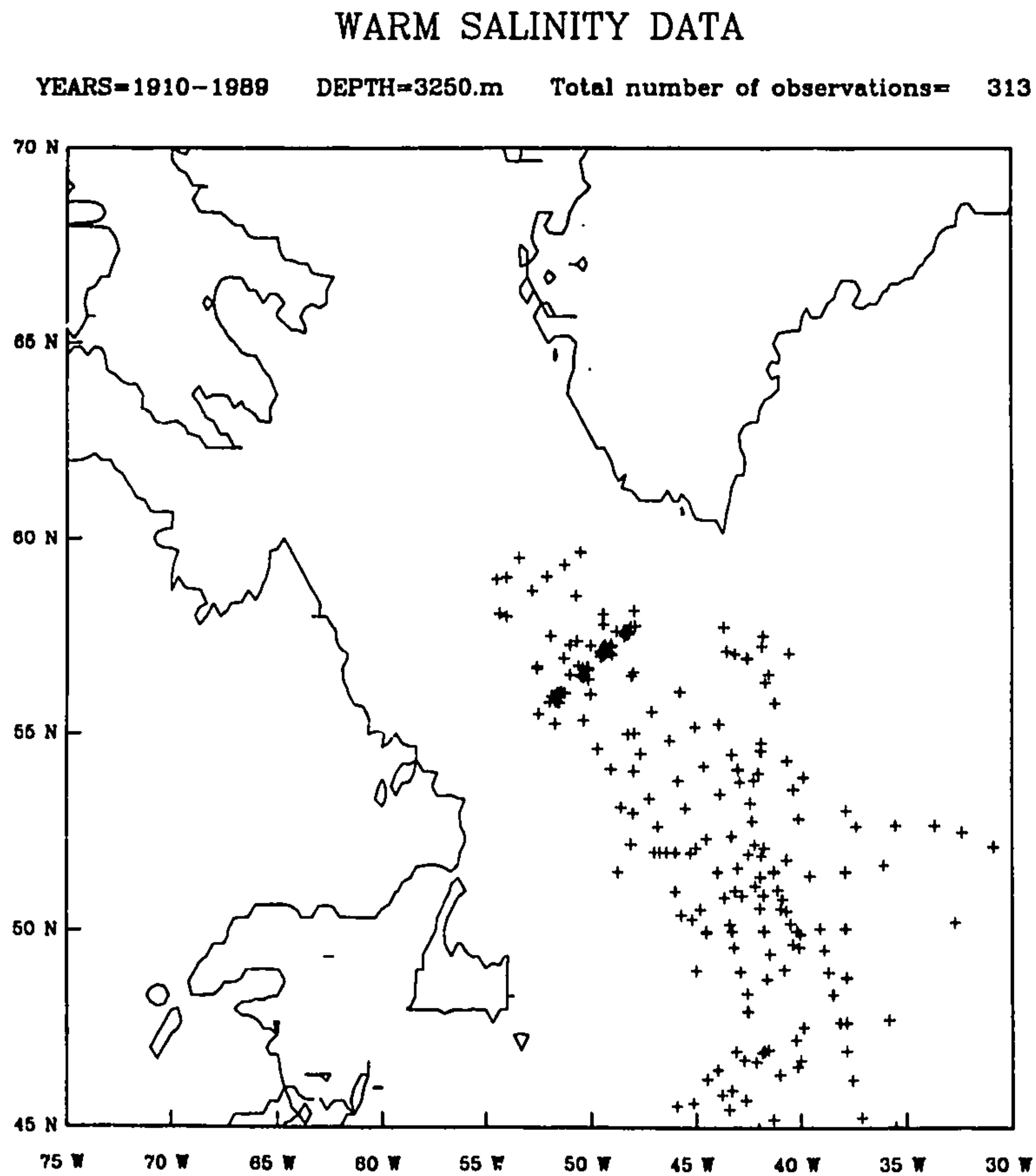

Figure 2.4 cont: and c) 3250m.

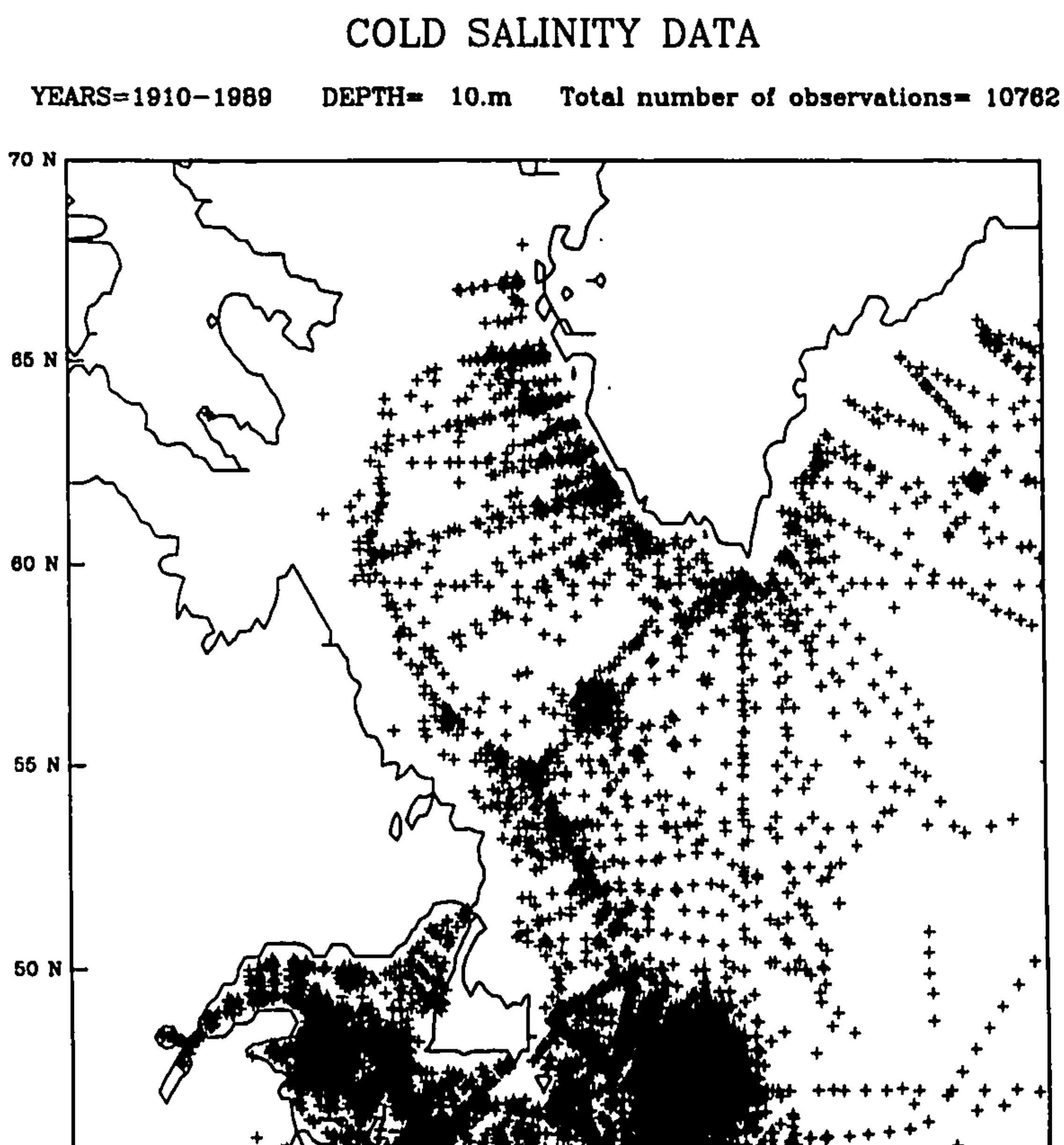

Figure 2.5: Horizontal distribution of salinity observations for the 1910-89 cold season at a) 10m,

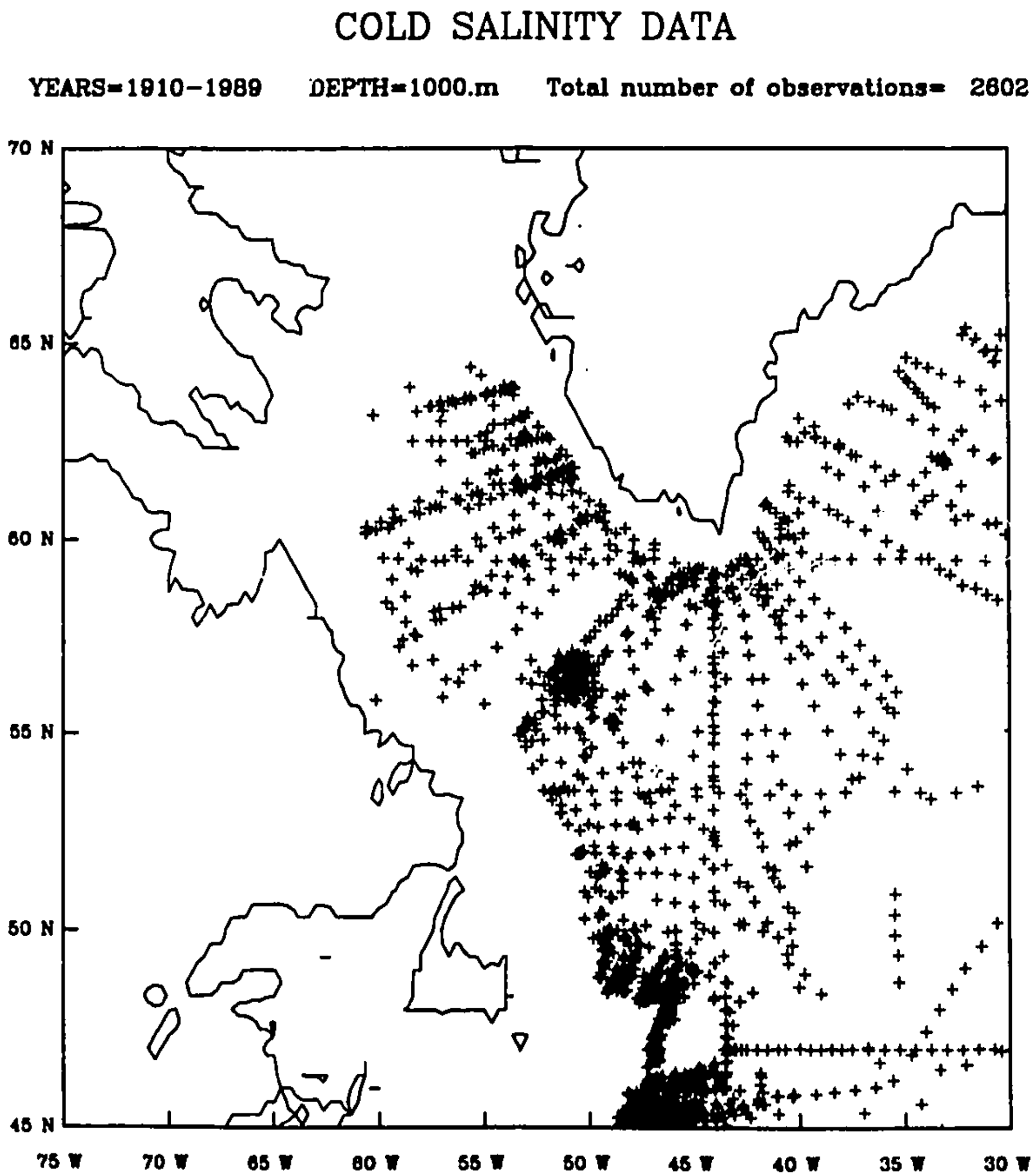

Figure 2.5 cont: b) 1000m.

COLD SALINITY DATA

YEARS=1910-1989 DEPTH=3250.m Total number of observations= 316

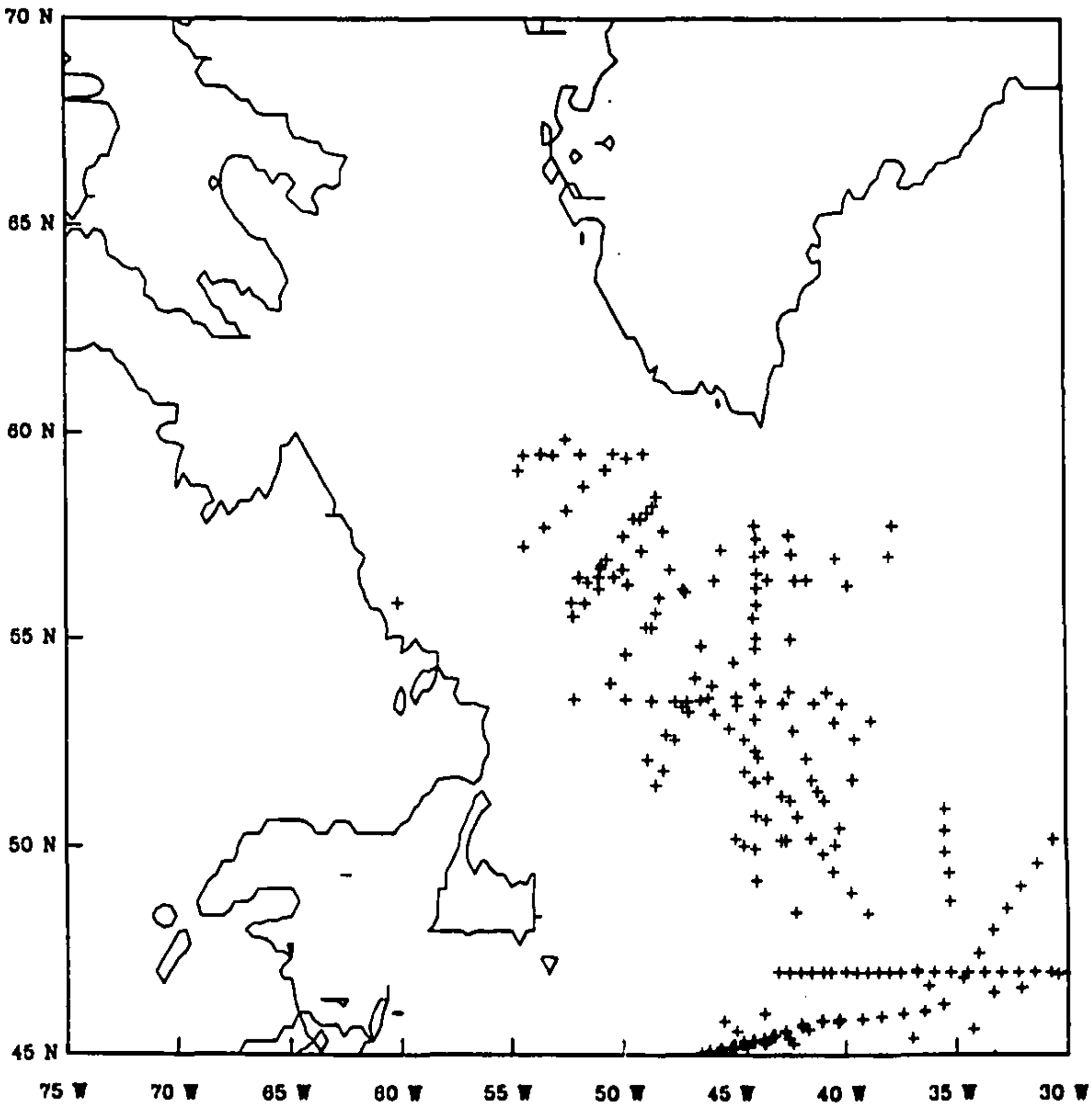

Figure 2.5 cont: and c) 3250m.

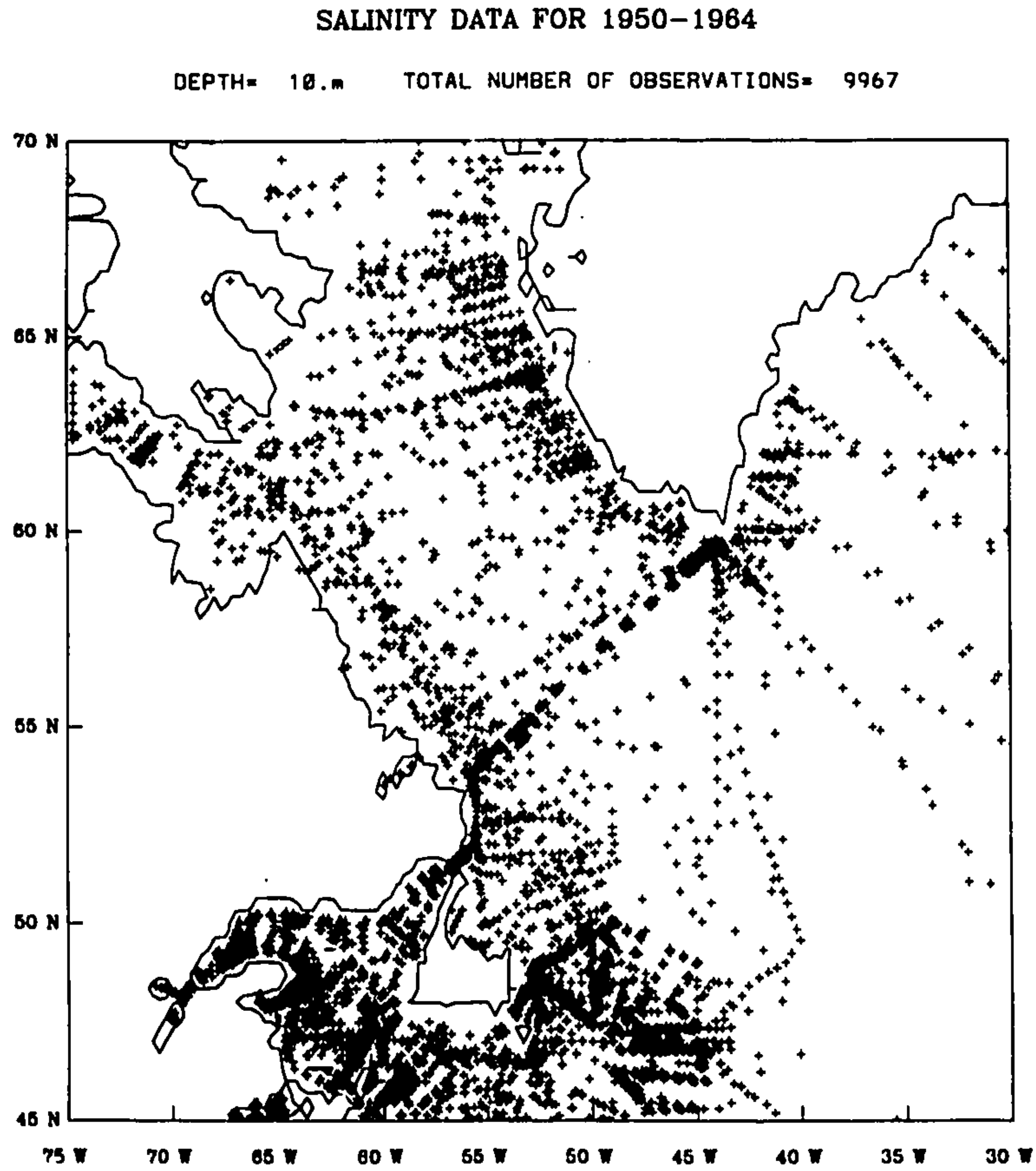

Figure 2.6: Horizontal distribution of salinity observations for the 1950-64 warm season at a) 10m,

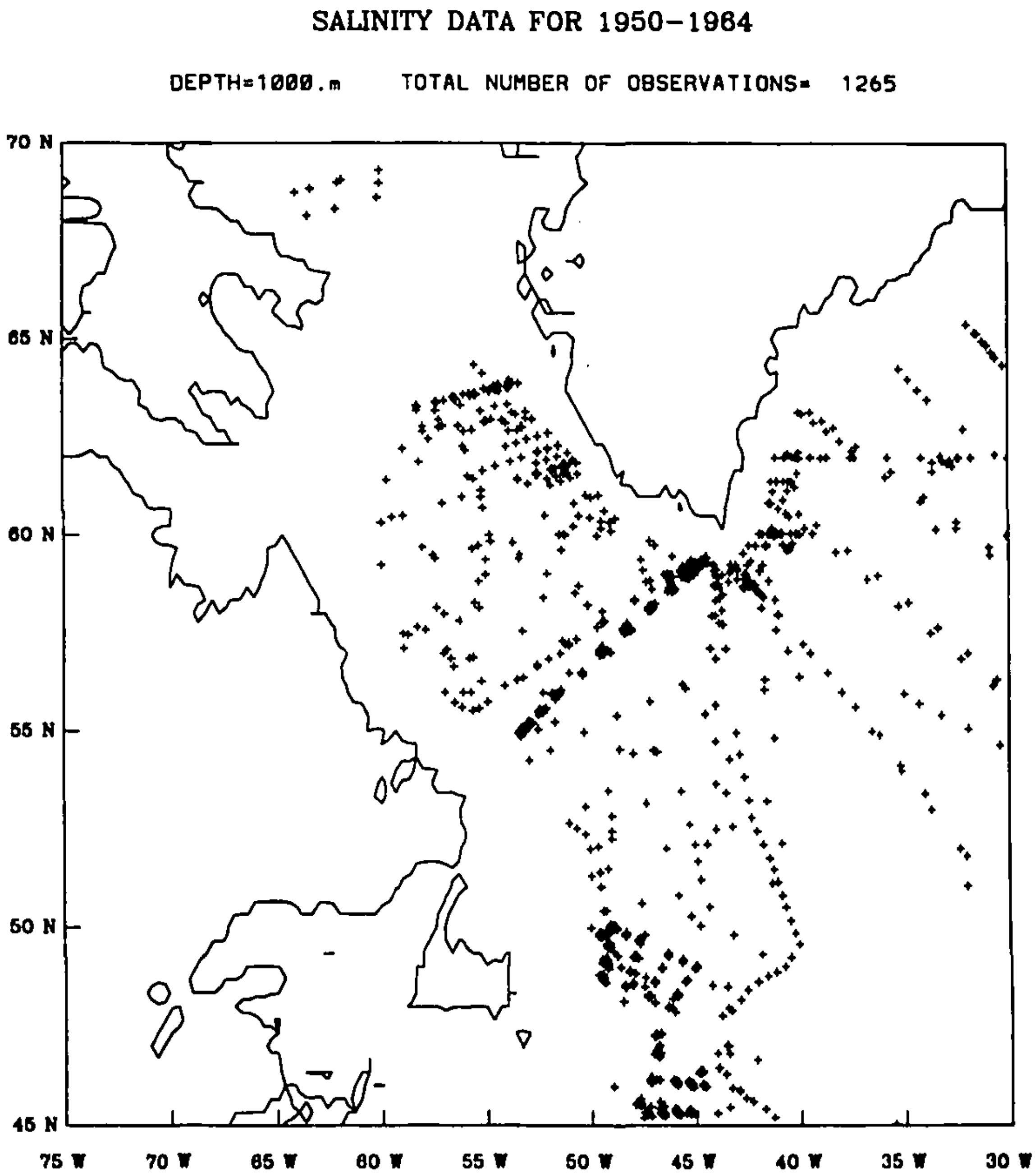

Figure 2.6 cont: b) 1000m,

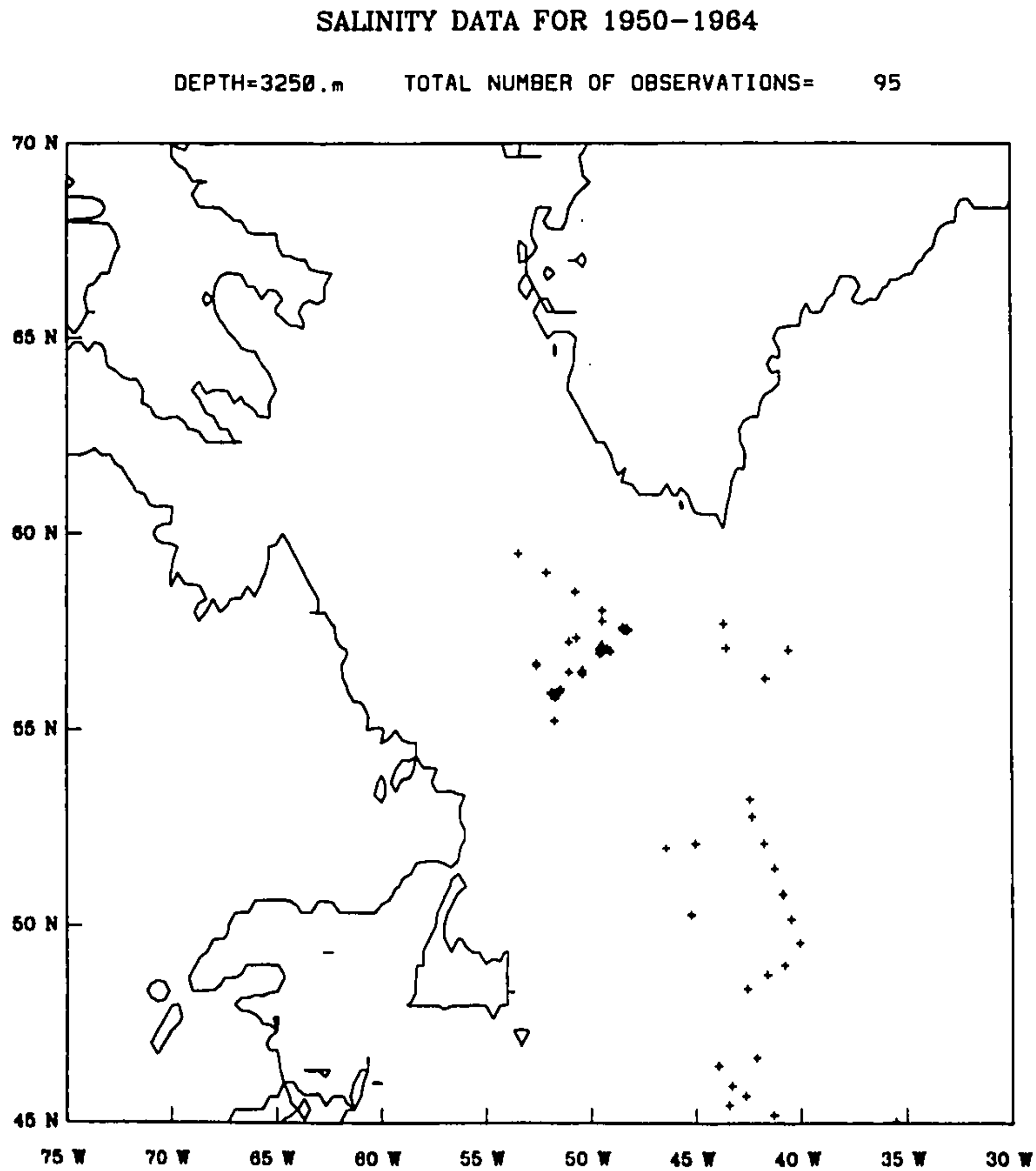

Figure 2.6 cont: and c) 3250m.

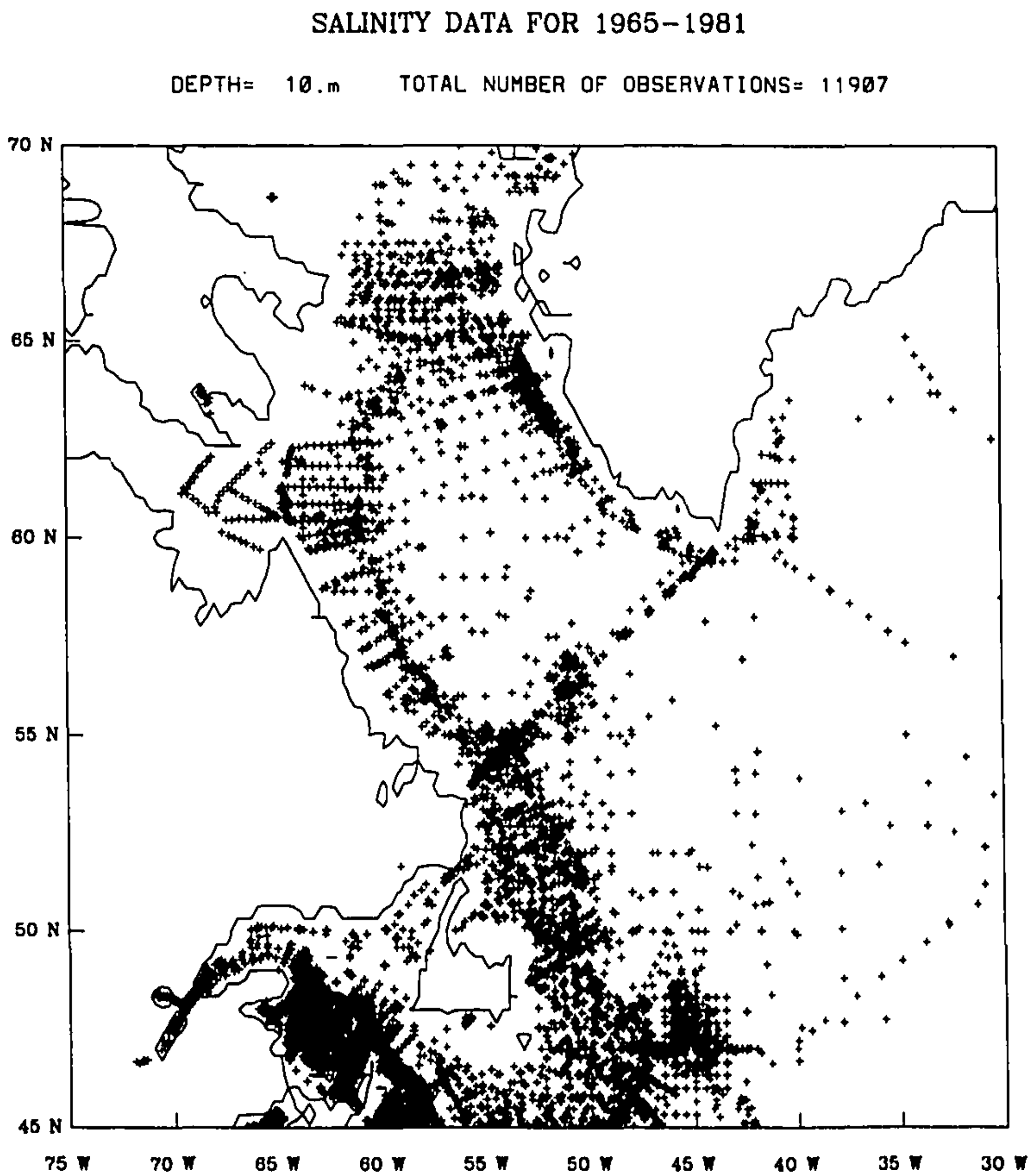

Figure 2.7: Horizontal distribution of salinity observations for the 1965-81 warm season at a) 10m,

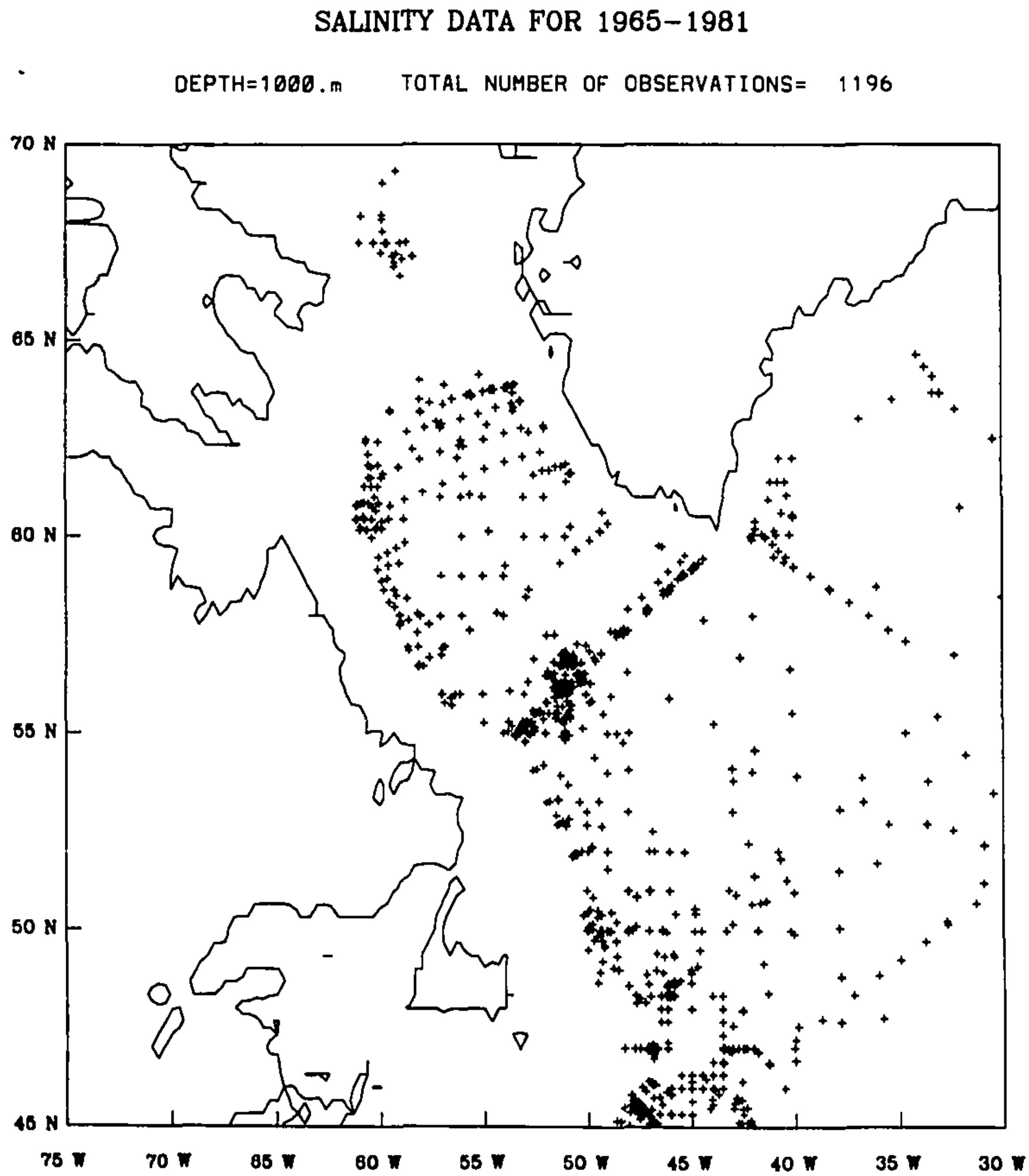

Figure 2.7 cont: b) 1000m.

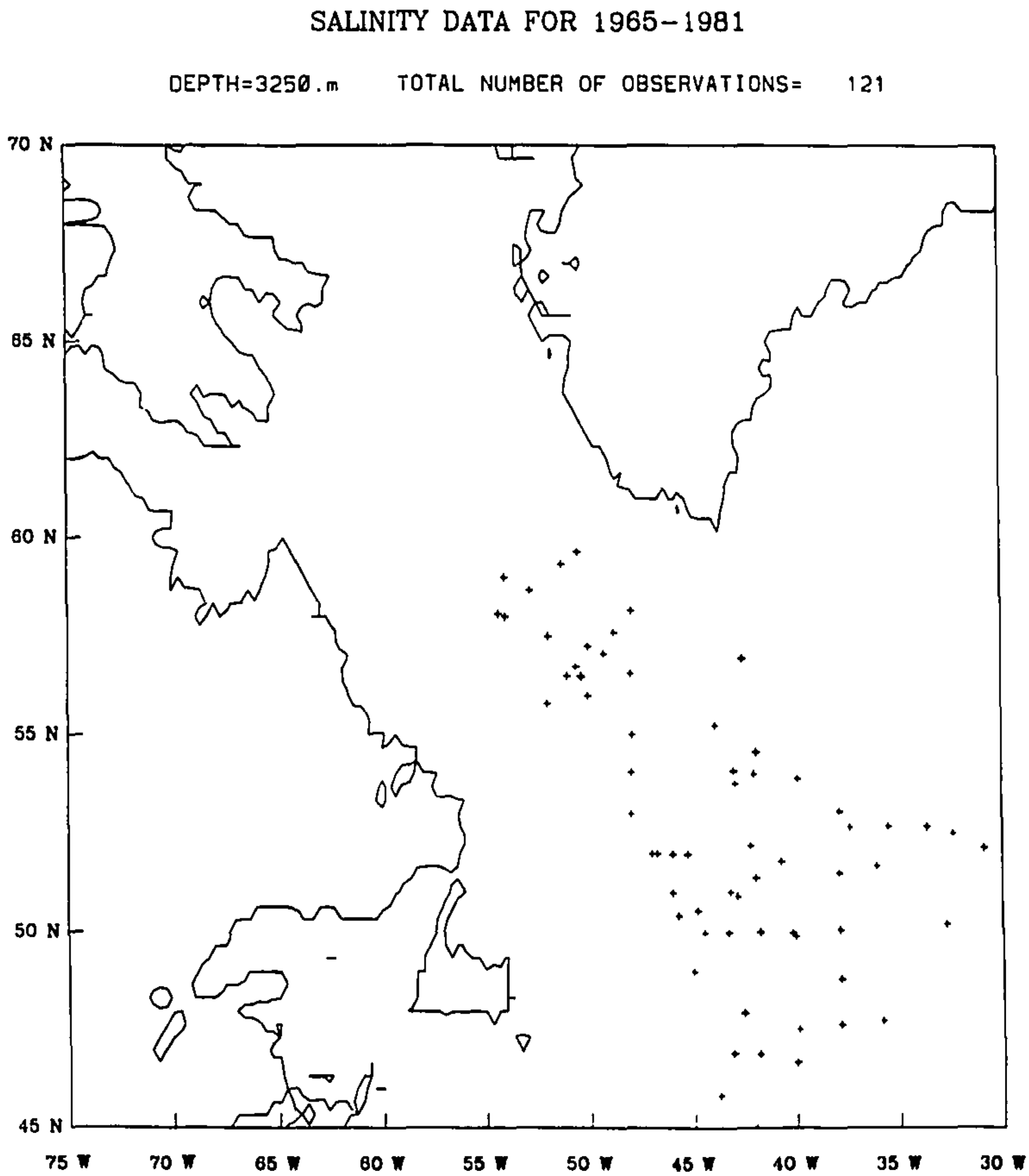

Figure 2.7 cont: and c) 3250m.

period was too sparse with very few stations in central Labrador Sea. As the Labrador Sea was the subject of an intense sampling activity during the sixties, the period was shifted toward 1965.

It seems that during the warm season the southeastern corner of the region of interest was poorly sampled (see Figs. 2.3 and 2.4). Figures 2.5 show that the eastern region of the domain was also poorly sampled during the cold season. The Hudson and Davis Straits as well as the Baffin Bay region were not sampled at all during the cold season presumably because of harsh winter conditions that occur in these regions (ice, icebergs, etc). Some *in land* temperature values were also observed in the data set! These values probably came from either gross errors in the boat position or lake samplings and were not used in the objective analysis.

2.4 The quality control

Any data set contains suspicious values, which could come from many sources: measurements obtained in an eddy (then the question of the representativeness of these values arises), seasonal and interdecadal variabilities or gross errors (calibration problems, broken equipment, manipulation, etc). In this section, it will be shown how the gross errors were treated as the combined data sets contained many of them; e.g. low salinity values like 7, 14, 0.6 psu were recorded in deep waters, very high salinity values were also *measured* (e.g. 40 psu) and unacceptable temperature values such -10, -46, -52, -34°C were also found within the data set.

An other error, found in the post-1970 data set, is that the depth of measurement in many of the vertical profiles was set to zero for the entire profile. As only the surface value for each profile could be used, the number of observations between the first and second level during the 1965-1981 warm season dropped considerably- from 41538 to 34959 for the temperature and from 19478 to 11987 for the salinity.

In order to find other gross errors, a statistical check was performed before proceeding with the objective analysis. The mean and standard deviation, at each gridpoint location (at each vertical level), were calculated using the data located within a 200 km radius of that gridpoint and for which the isobath range did not exceed the limit allowed by Eq. 2.5. Then, the mean (at each gridpoint location) was reavaluated by not using data outside of two standard deviations. But an *n standard deviation* (n=2, 3, 4...) criteria cannot be blindly used in the objective analysis because gross errors, like those mentioned earlier, created large standard deviations, which reduce the efficiency of the filtering. Furthermore, it should be noted that as the number of observations decreases near the eastern limit of the domain, an *n standard deviation* quality criteria may fail. The localisation of the gross errors was determined by plotting the mean and standard deviation fields for both salinity and *in situ* temperature at every level. Errors could be easily recognized in these plots as they created bulls eyes in the standard deviation plots which were often associated with correponding bull eyes in the mean field plots (see Figs. 2.8 and 2.9). The artificial structures in Figs. 2.8 and 2.9 are due to a 0.618 psu salinity value recorded on October 26, 1983 and an *in situ* temperature value of 32.641°C obtained

a)

b)

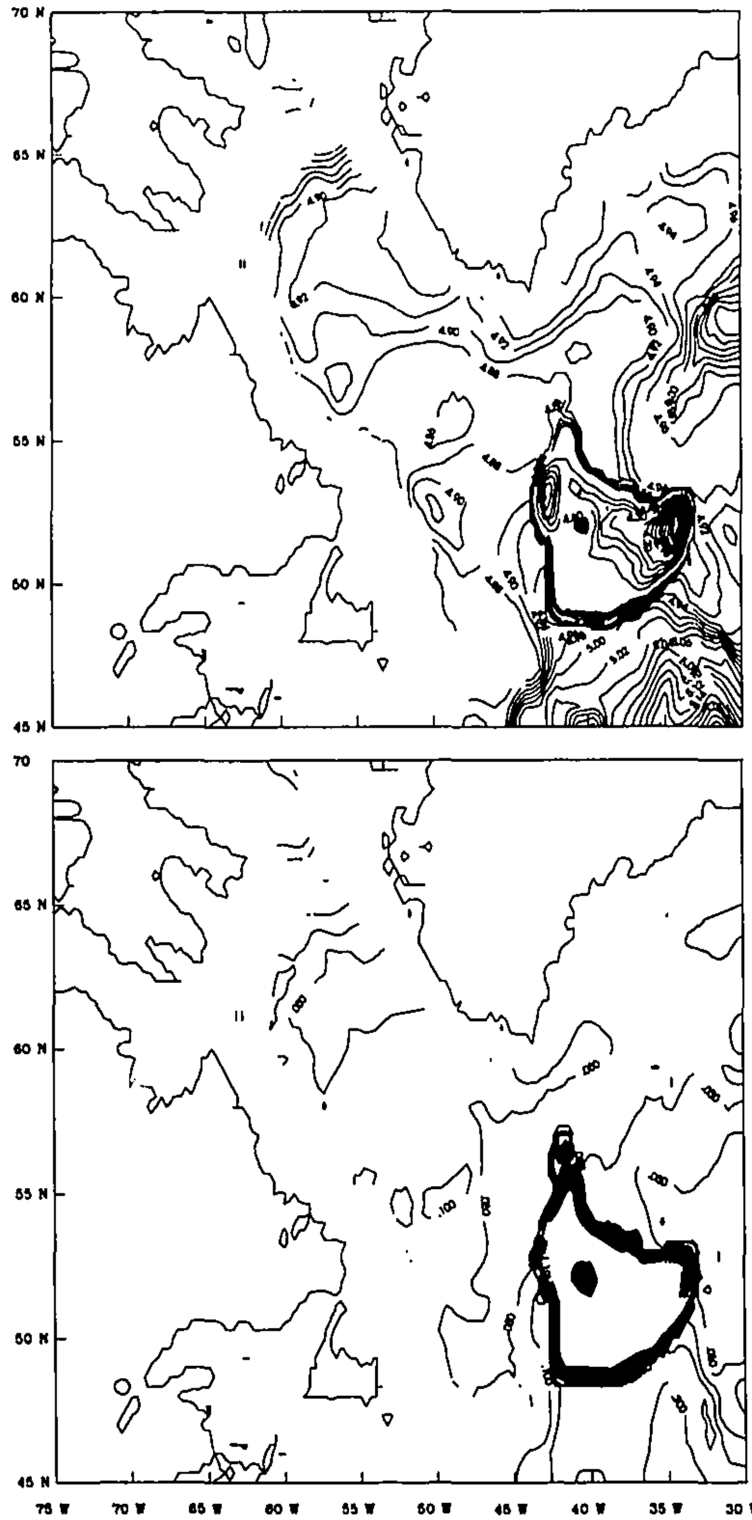

Figure 2.8: Summer salinity a) mean and b) standard deviation at 600m (units are psu, in a) real value=30+value).

a)

b)

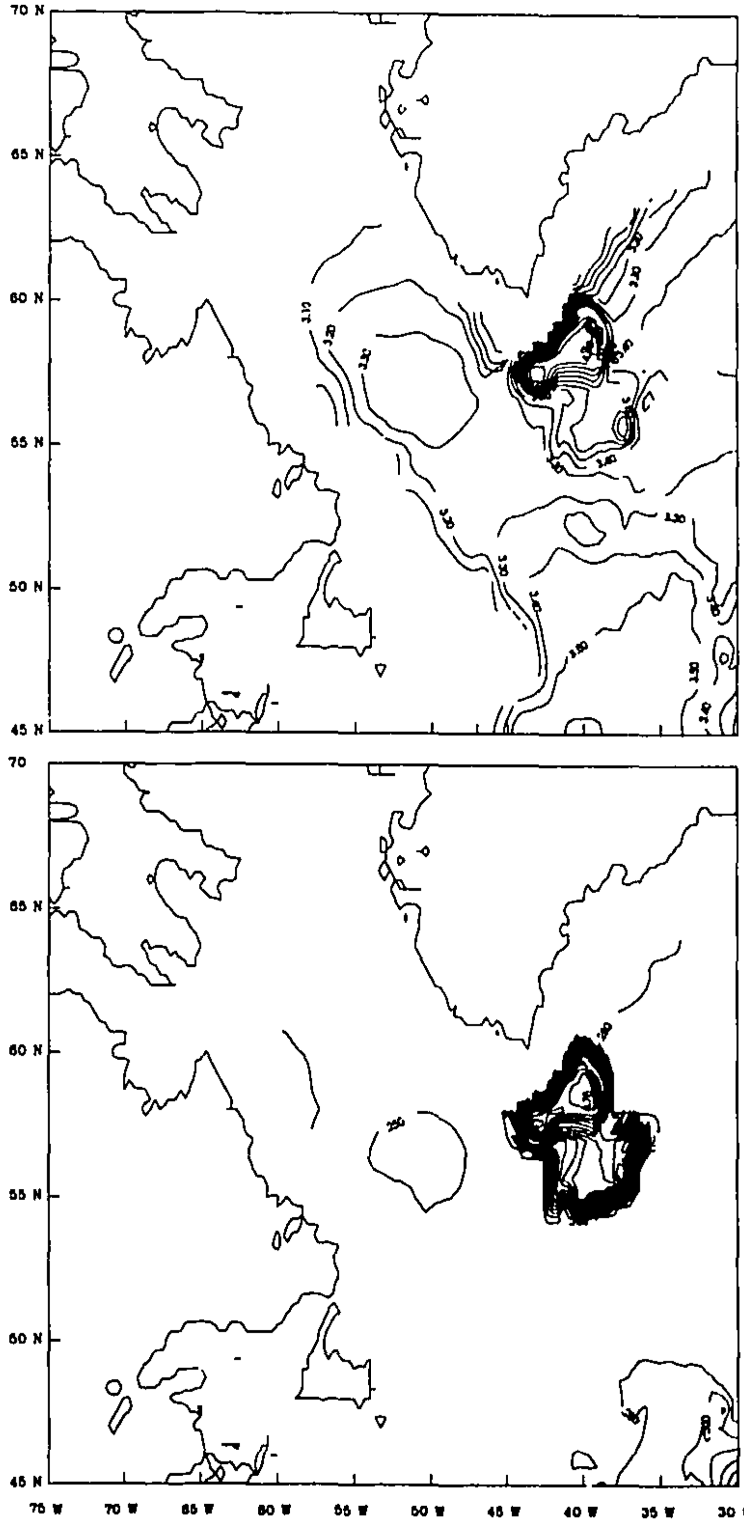

Figure 2.9: Summer *in situ* temperature a) mean b) standard deviation at 2000m (units are °C).

a)

b)

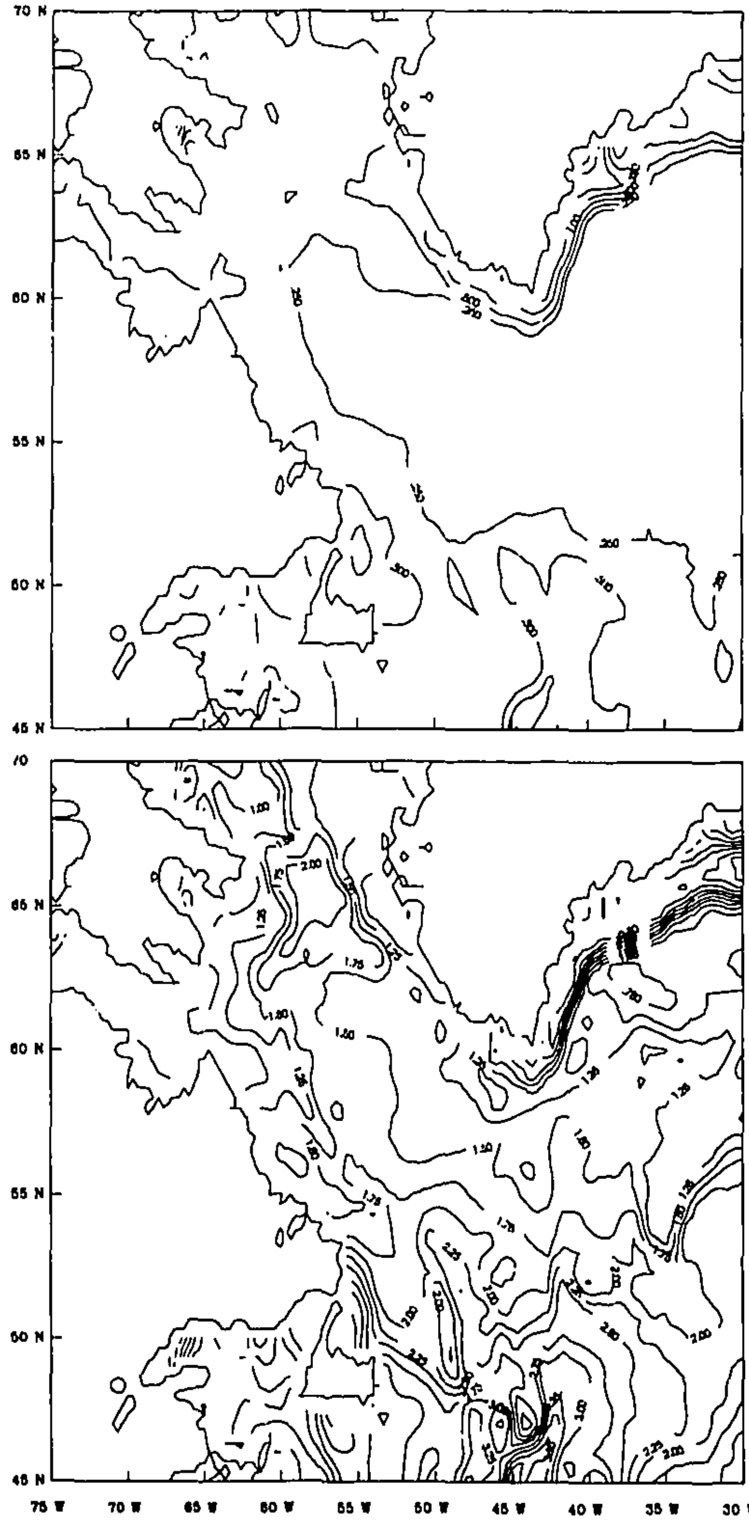

Figure 2.10: Summer standard deviation fields a) for salinity (psu) and b) for *in situ* temperature (°C) at 30m.

on July 13, 1961. In order to get rid of such values, only data within a prescribed range could be used in the objective analysis. For the salinity analysis, the conditions on the salinities were: i) $5.0 \leq S \leq 37.0$ psu for $z < 1750$m and ii) $34.8 \leq S \leq 35.2$ psu for $z \geq 1750$m. The $S \geq 10$ psu for $z \geq 50$m condition was further added for the salinity seasonal analysis. For the temperature analysis, the conditions on the *in situ* temperatures were: i) $-2.0 \leq T \leq 25.0$°C for $z < 500$m, ii) $0.0 \leq T \leq 25.0$ °C for $500\text{m} \leq z < 1750$m, iii) $0.0 \leq T \leq 15.0$ °C for $z \geq 1750$m and iv) the $T \leq 20.0$ °C at all depths condition was further added for latitudes greater than 60.0°N.

In summary, for each gridpoint (and for each vertical level), corrected mean and standard deviation values were produced sequentially by: removing the gross errors, evaluating the mean and standard deviations, filtering out the data which were outside two standard deviations from the mean and then re-estimating the mean and standard deviation on the filtered subset. The corrected *in situ* temperature and salinity mean fields were then used as the first guess (S_{guess} in Eqs. 2.1 and 2.2) of the objective analysis. Some corrected standard deviation fields are shown in Figs. 2.10 for the summer salinity and *in situ* temperature at 30m. These standard deviation fields represent the cumulative effect of observational and background errors. Although the background errors, due to both the climatological bias and variances, could be separated from the observational errors (see Daley, 1991, chapter 4), this was not done in the present analysis. The larger standard deviations along the eastern Greenland coast likely arise from the δh parameter used (see Eq. 2.5) which, in shallow waters, is around 300m. This means that data on the 500m isobath are used in estimating the mean and standard deviation values for the salinity and *in situ* temperature in near coastal regions (e.g. for h = 200m). As the 500m isobath on the eastern side of Greenland goes quite far offshore (see Fig. 1.1), data from different water masses are used and consequently the standard deviation is relatively large.

It should be noted that the combined data set was corrected for another reason. Between 1945 to 1974, the Ocean Weather Ship (hereafter OWS) Bravo (56.5°N, 51.0°W) was used to collect oceanographic data for the top 1500m. A problem arises since, contrary to Levitus (1982) analysis, the data were not binned prior to start the objective analysis. As this large amount of data was biasing the objective analysis, the OWS Bravo data were averaged in such a way that only one value per month be allowed. All data within 56.3 to 56.7°N and 50.5 to 51.5°W were considered as OWS Bravo data.

During the objective analysis, a statistical check was performed at every iteration (radius of influence) for all gridpoints such that only observations that were within two standard deviations of the mean for the given radius of influence were used. Data which did not meet this criterion were kept for the next iteration; this was because of the large temperature and salinity variations in coastal regions. Levitus (1982) used a five standard-deviation criterion for surface and coastal region waters and a three standard-deviation criterion otherwise; these are both considerably larger than the criteria that have been used here.

2.5 The topographic data set

The topographic data set used in this study is the 1/12° x 1/12° U.S. Navy's bathymetry obtained from MEDS. This raw data was then smoothed slightly onto the 1/3°x1/3° grid by applying the original Levitus (1982) objective analysis scheme (not modified) with one iteration using a 20 km influence radius and an initial guess from the raw data set. The result is shown in Fig. 1.1.

CHAPTER 3: THE OBJECTIVELY ANALYZED T-S FIELDS

3.1 The undetermined gridpoints

The scheme described in the previous chapter was applied to the area between 45°N and 70°N and between 75°W and 30°W (see Fig. 1.1) which, for a resolution of 1/3°x1/3°, represents 136x76 gridpoints. The undetermined gridpoints, for which the MSC was unable to estimate temperature or salinity values, were obtained through interpolation using the IMSL interpolation scheme of Akima (1978). The advantage of this scheme is that it preserves the gradient structure. Some of these gridpoints are shown in Figs. 3.1. For the summer analysis, the undetermined gridpoints were located around Baffin Island, within Baffin Bay and along the eastern border of the domain (see Fig. 3.1a). Although a smaller amount of these gridpoints were obtained for the warm analysis, they were all located in the same regions as for the summer analysis (Figs 3.1b and 3.1d). The largest number of these gridpoints were found for the cold season analysis (Fig. 3.1c) where the whole of Hudson and Davis straits and Baffin Bay was unresolved. Some missing data was also found near the southeastern corner. However some gridpoints were left unknown: all gridpoints west of 70°W and north of 67°N as well as all the gridpoints in the Davis and Hudson straits in the cold season analysis.

3.2 The summer results

The results for several levels are shown in Figs. 3.2 and 3.3. On the eastern side of Greenland (Fig. 3.2a), fresh (< 34.5 psu) surface waters are transported by the EGC

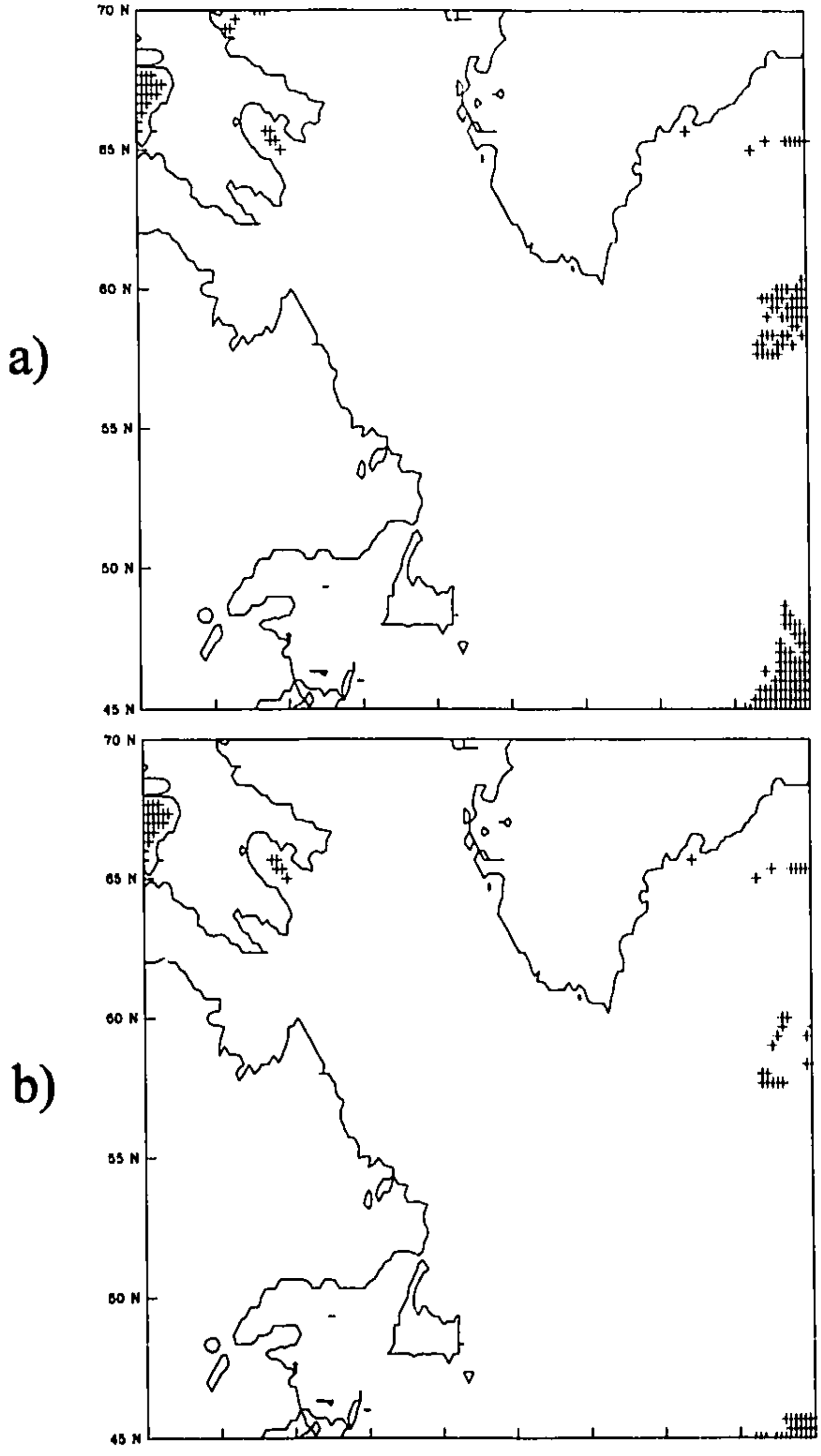

Figure 3.1: Undetermined gridpoints from the objective analysis: a) for the summer season salinity at 10m, b) for the warm season salinity at 10m,

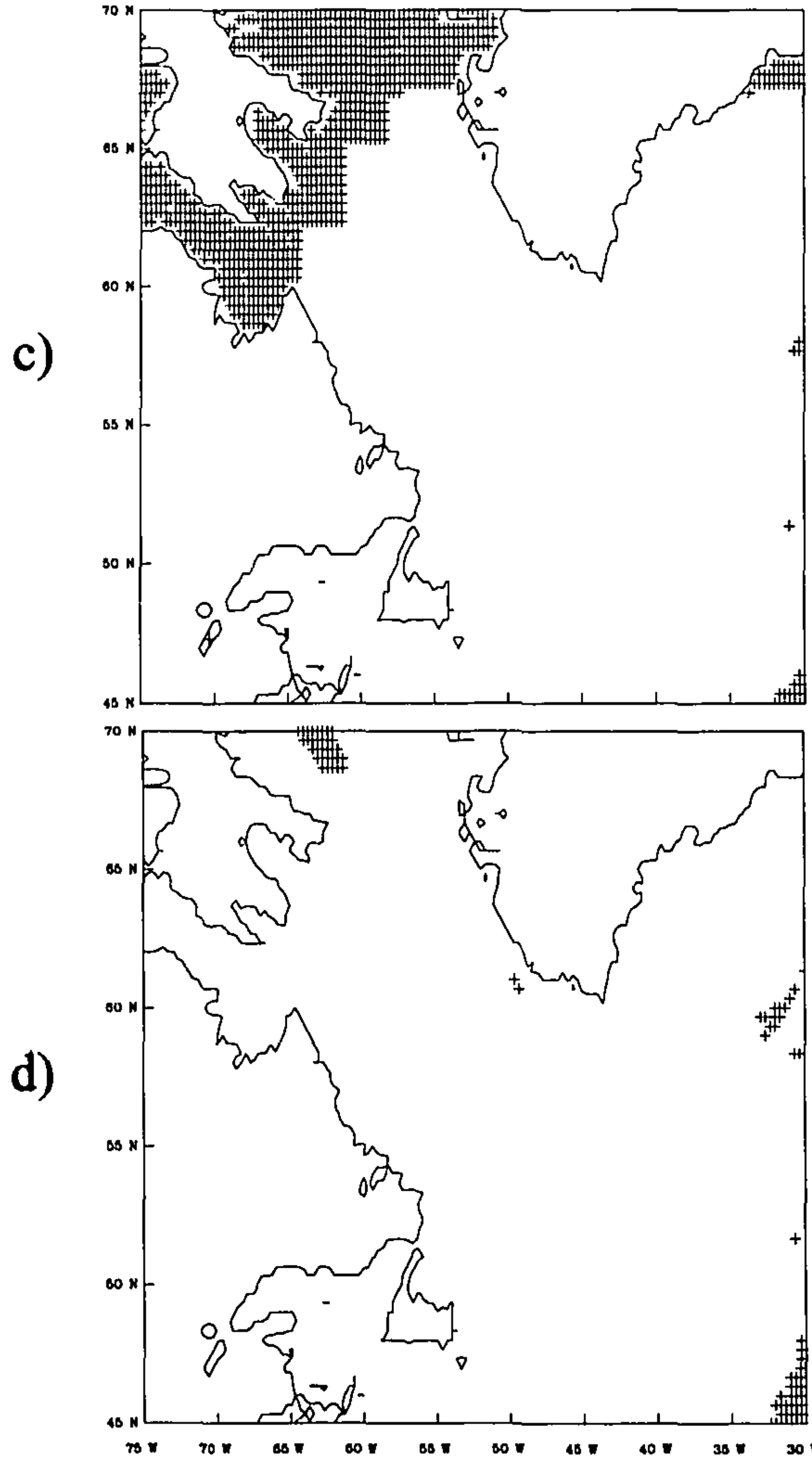

Figure 3.1 cont: c) for the cold season salinity at 10m and d) for the warm season temperature at 1750m.

a)

b)

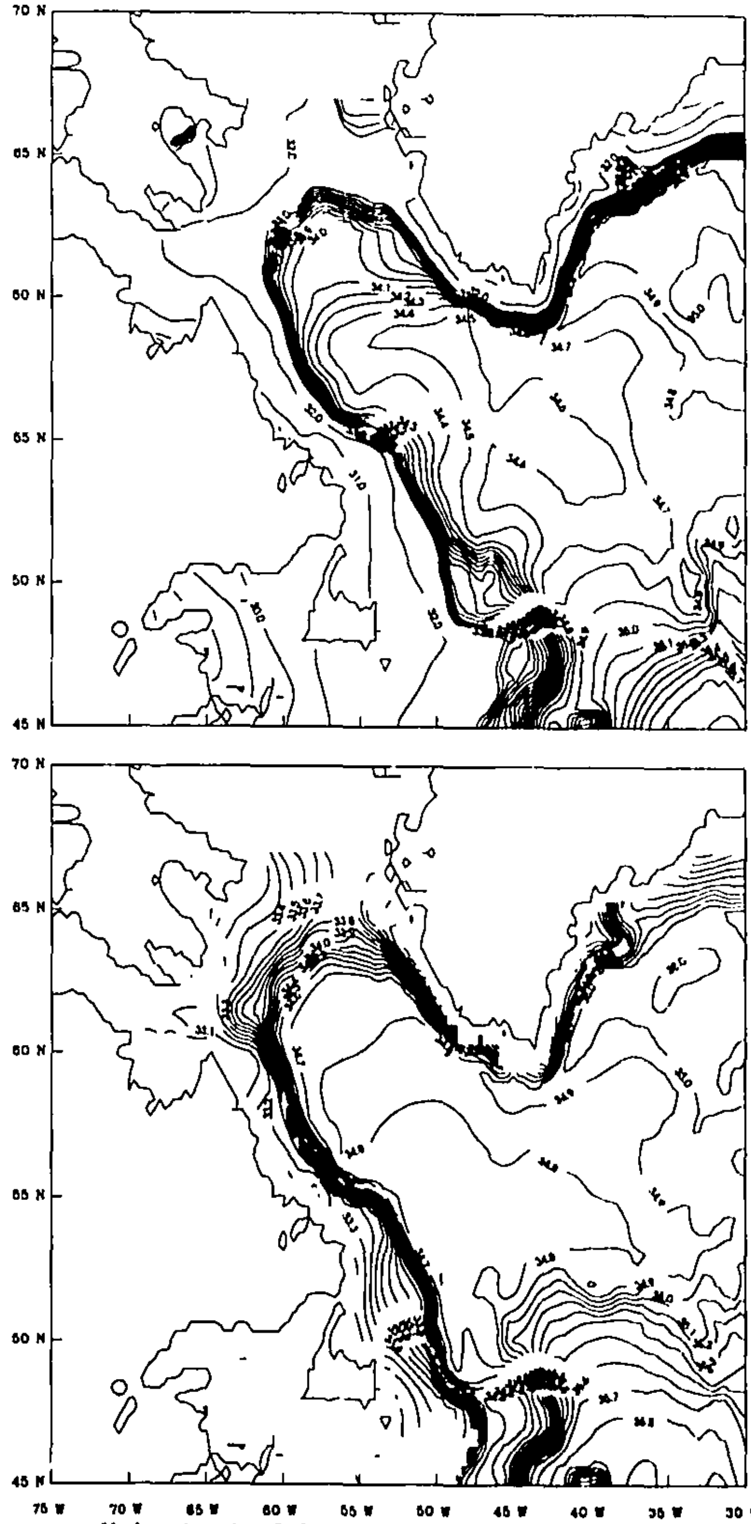

Figure 3.2: Summer salinity (psu) of the northwestern Atlantic Ocean at a) 0m, b) 100m,

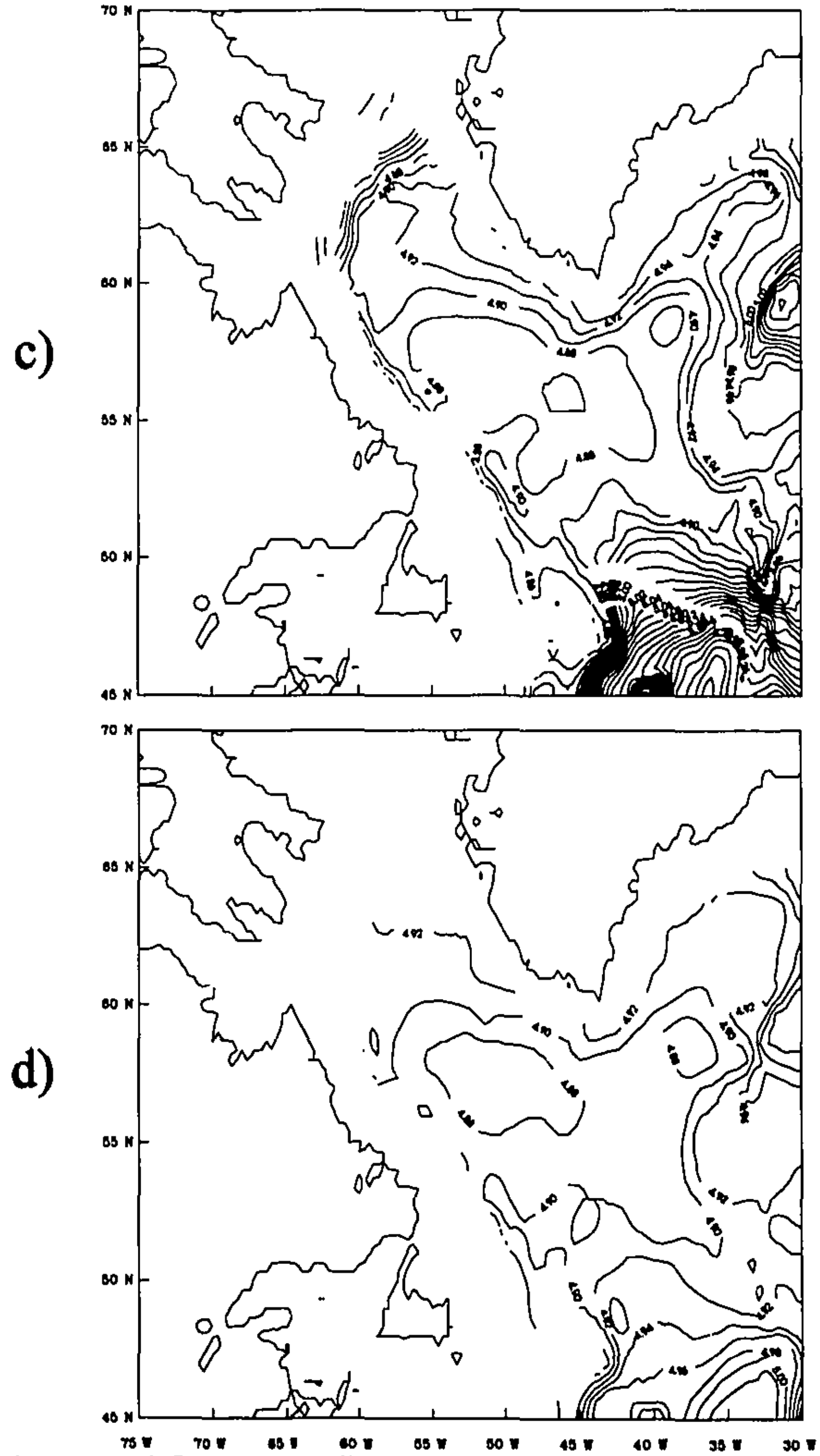

Figure 3.2 cont: at c) 500m (true salinity= 30 + reported salinity, at d) 1000m (true salinity= 30 + reported salinity),

e)

f)

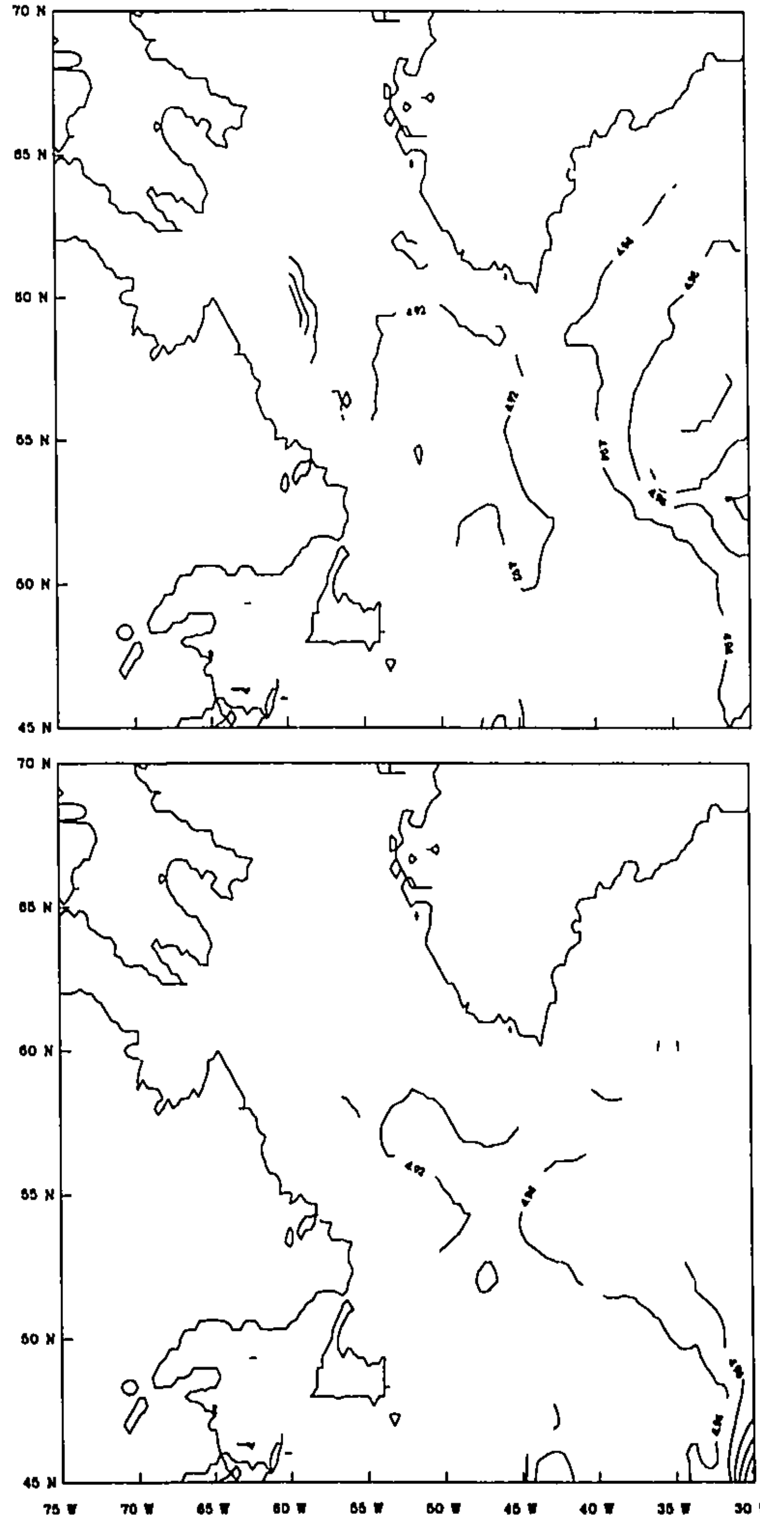

Figure 3.2 cont: at e) 2000m (true salinity= 30 + reported salinity and at f) 3000m (true salinity= 30 + reported salinity).

a)

b)

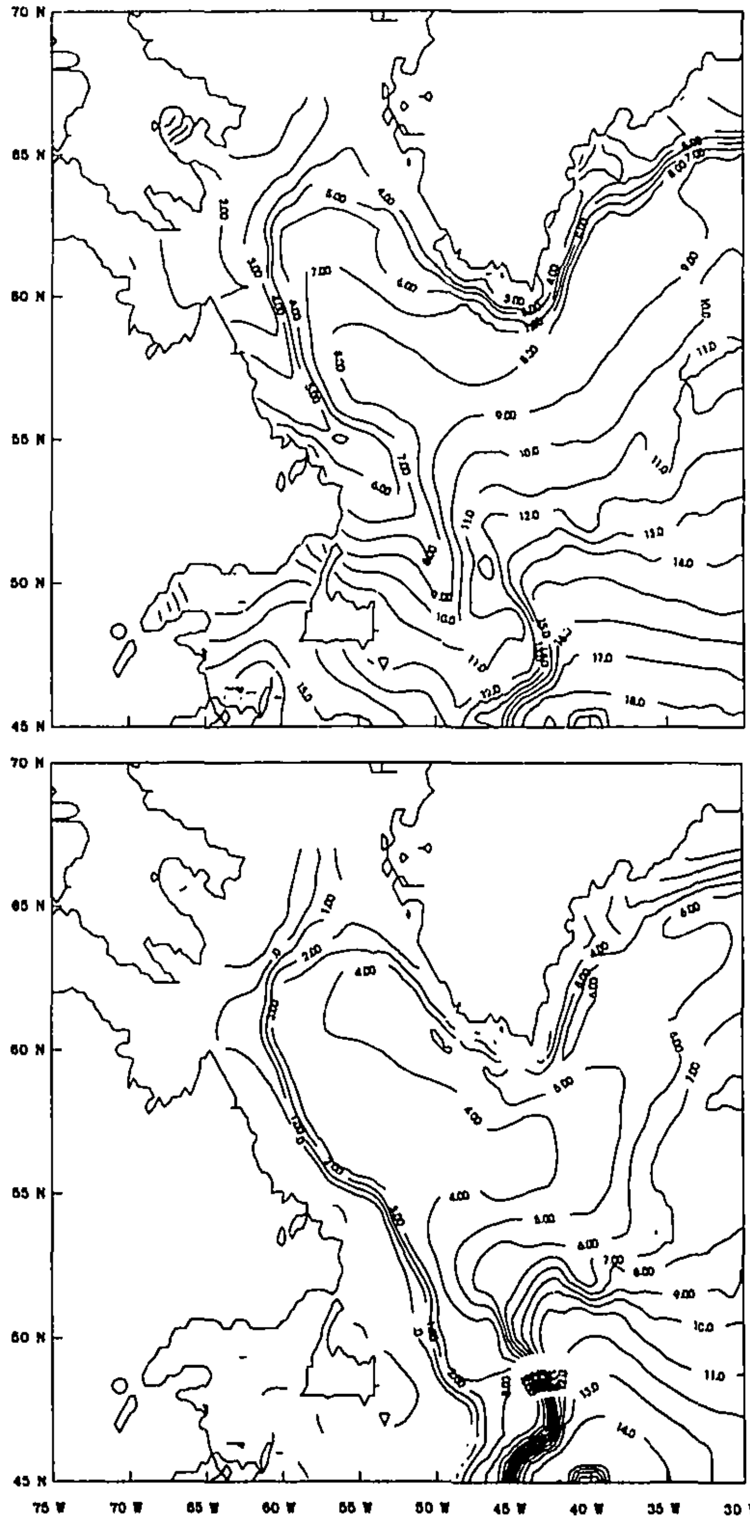

Figure 3.3: Summer *in situ* temperature (°C) of the northwestern Atlantic Ocean at a) 0m, b) 100m,

c)

d)

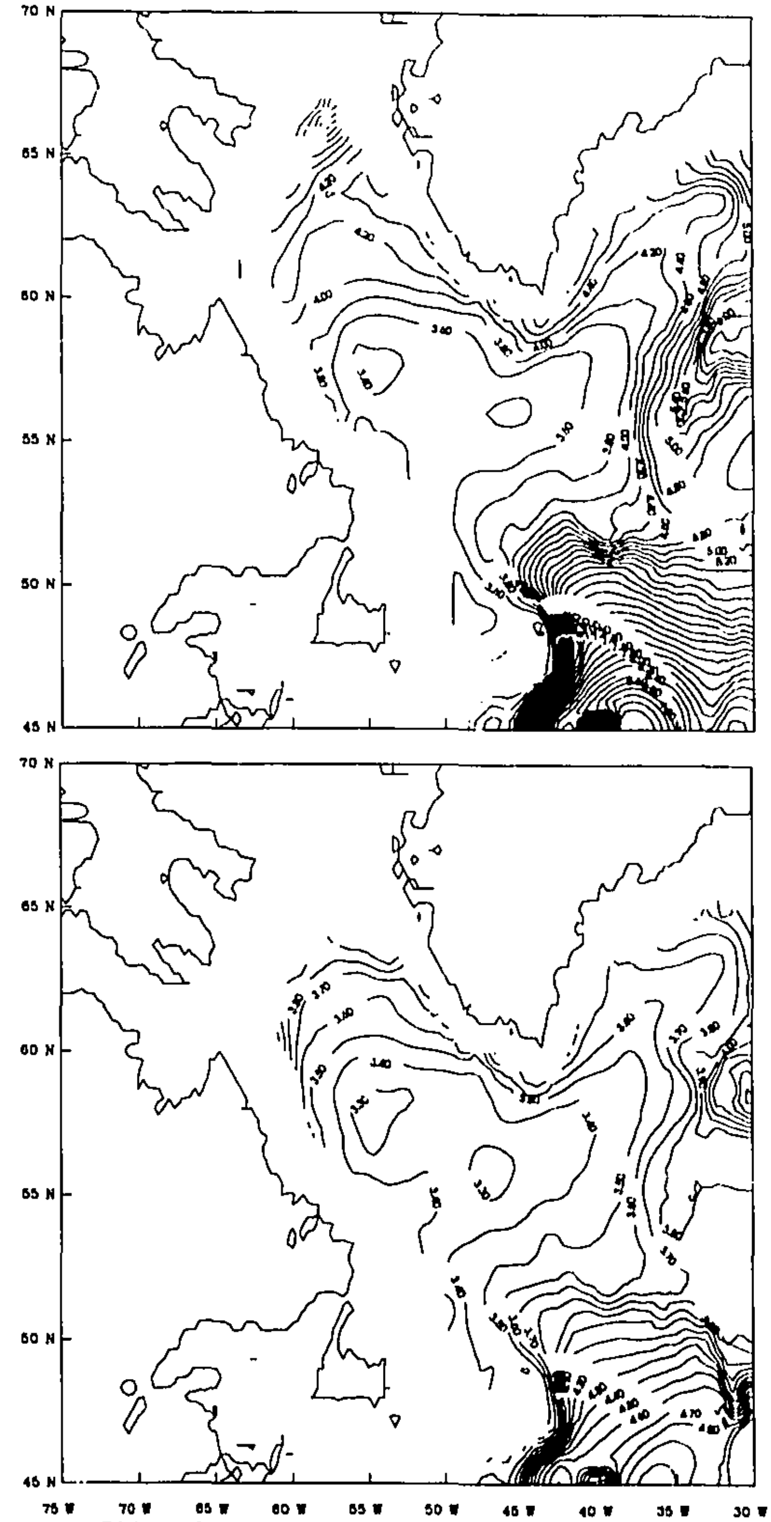

Figure 3.3 cont: at c) 500m, d) 1000m,

e)

f)

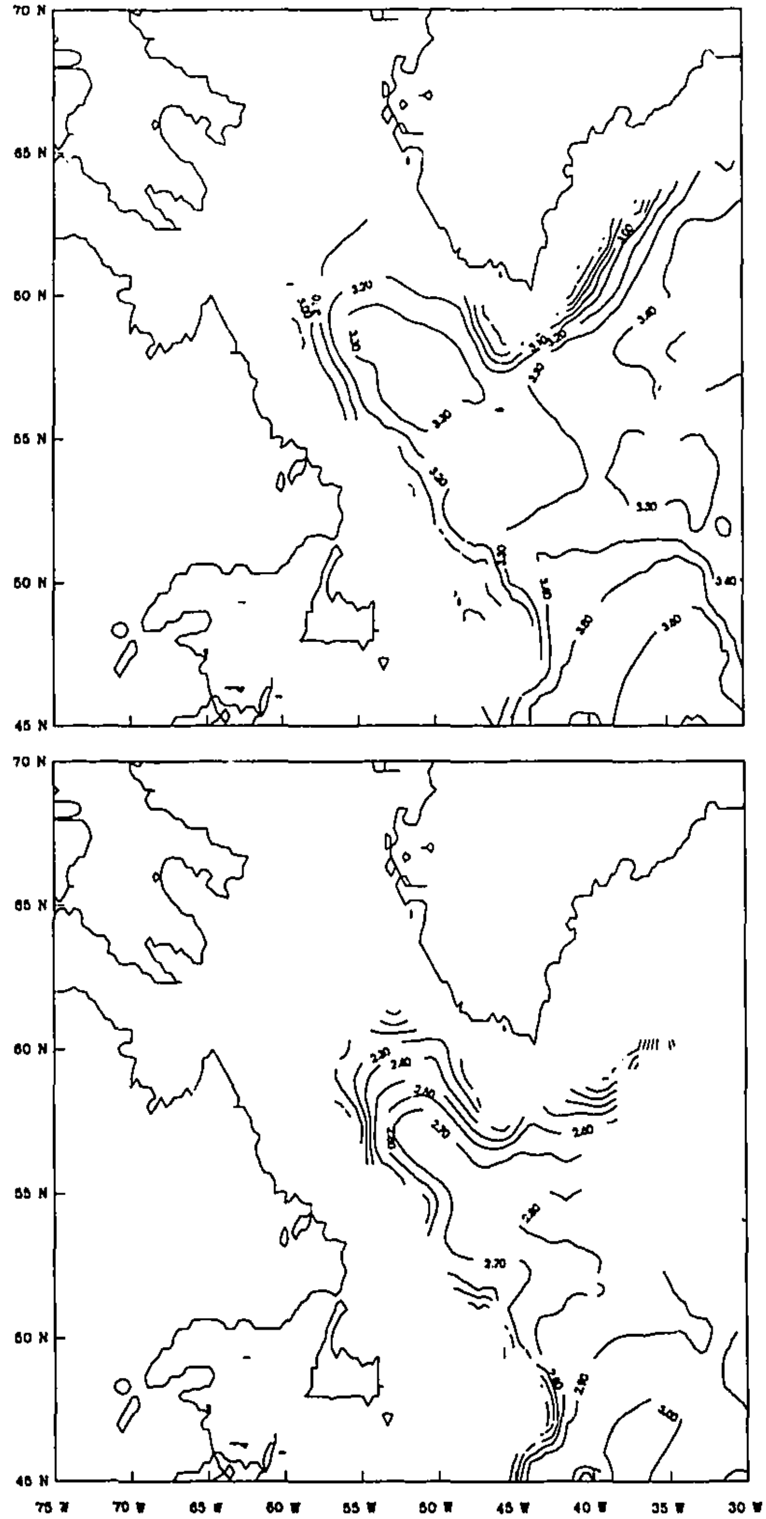

Figure 3.3 cont: at e) 2000m and at f) 3000m.

which Clarke (1984) characterized as having typical temperature values of -1.8°C using data collected in February-April 1978. Temperatures extracted from the original data set exhibited surface values of 1-6°C , in agreement with Fig. 3.3a, and ~-1°C values for subsurface waters. However the objective analysis results for the subsurface waters (Fig. 3.3b) show a minimum temperature within the range of 2 to 3°C. This difference likely comes from the δh parameter used and is associated with the large standard deviations shown in Figs. 2.10a and b. The Irminger Current salinity and temperature values, obtained from the objective analysis and shown in Figs. 3.2b and 3.3b, are 34.9-35.0 psu and 6-8°C. Figures 3.4a-3.9a show vertical sections of salinity, potential temperature and potential density along the 43.67°W meridian and across the LS (S2 on Fig. 1.1). Figures 3.4b-3.9b, which show values extracted from the original data set, will be used in section 3.4. The EGC and the IC are visible on the left-hand-side of Figs. 3.4a and 3.5a and on the right-hand-side of Figs. 3.7a and 3.8a. The potential temperatures of Figs. 3.5 were estimated using the Bryden's (1973) polynomial expansion (Eq. 4.7) and the densities of Figs 3.8 were calculated using the UNESCO equation of state (1981, see also Gill, 1982).

In the slope regions of the Labrador Sea, the strong temperature and salinity gradients observed in Figs. 3.2a-d and Figs. 3.3a-d are associated with the WGC-LC system. The Baffin branch of the WGC is barely observable in the temperature and salinity fields (Figs. 3.2 and 3.3), but can be seen in the velocity field (Fig. 6.9). On the western side of the Labrador Sea, the southward LC flows over the Labrador shelf carrying a cold and low salinity mixture of waters from Hudson Bay, Baffin Bay, the

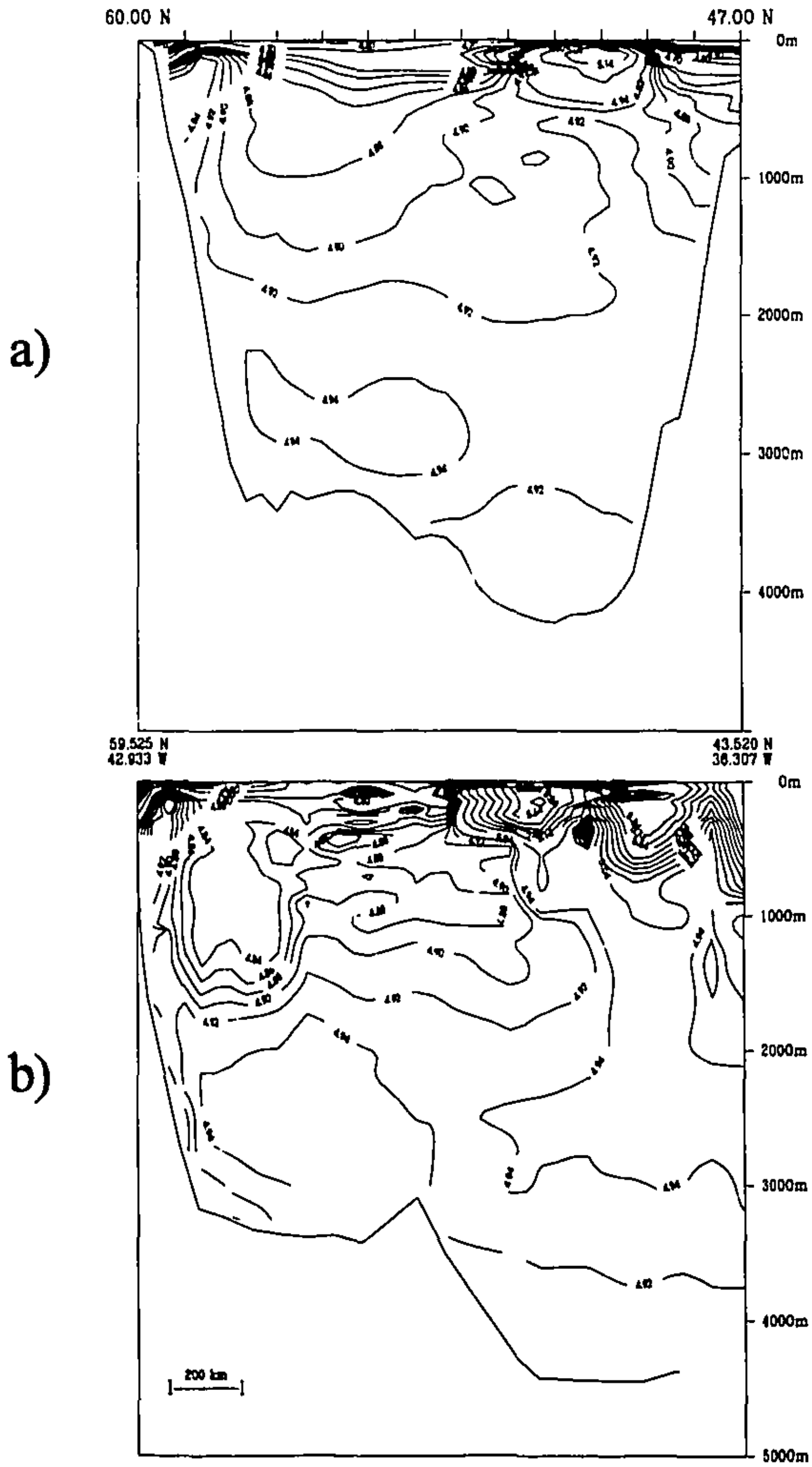

Figure 3.4: Salinity (psu) sections: a) objectively analyzed summer results along 43.67°W and b) Section 1 data (24/07 to 30/07 1983). True salinity = 30 + reported value.

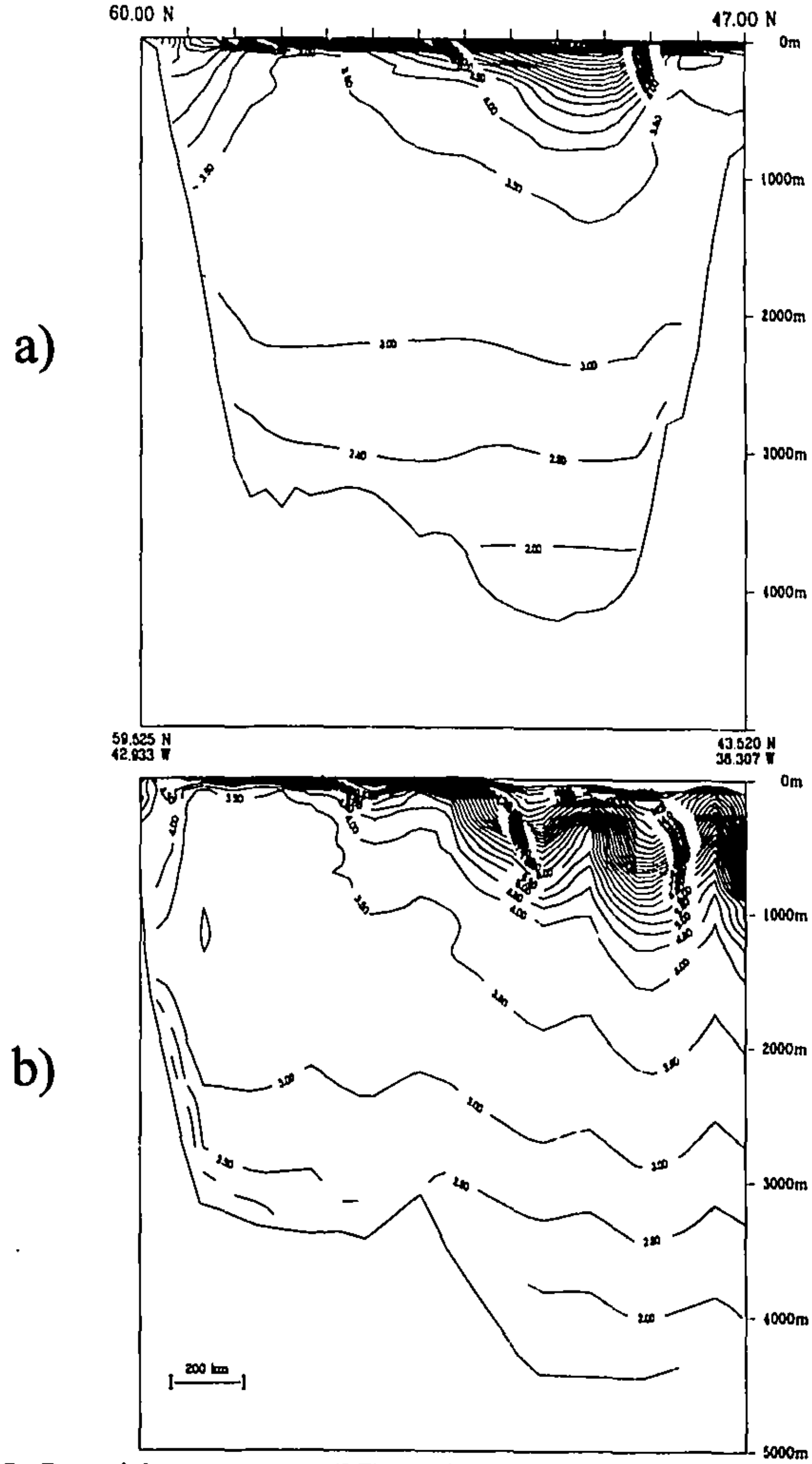

Figure 3.5: Potential temperature (°C) sections: a) objectively analyzed summer results along 43.67°W and b) Section 1 data (24/07 to 30/07 1983).

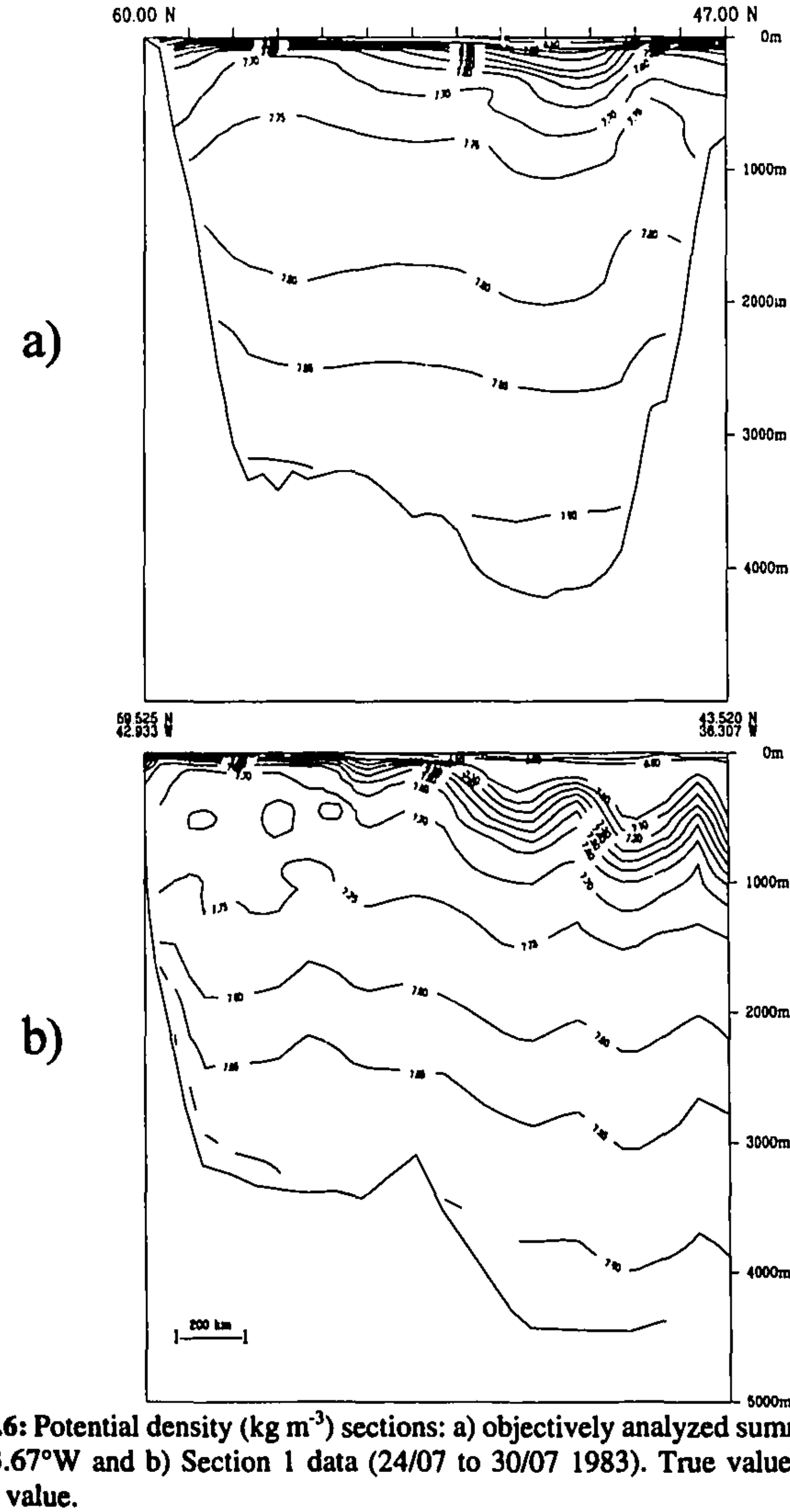

Figure 3.6: Potential density (kg m^{-3}) sections: a) objectively analyzed summer results along 43.67°W and b) Section 1 data (24/07 to 30/07 1983). True value = 1020 + reported value.

a)

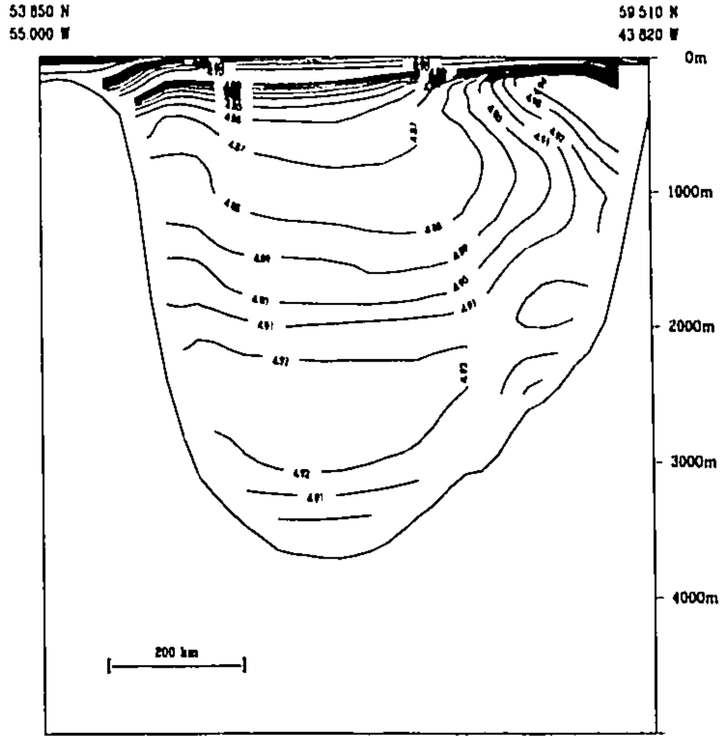

b)

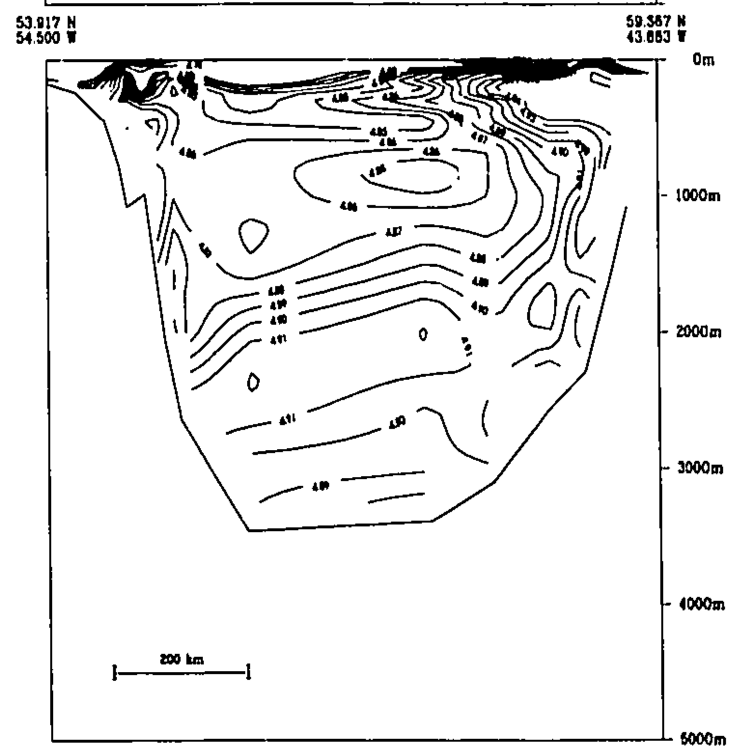

Figure 3.7: Salinity (psu) sections: a) objectively analyzed summer results along Section 2 and b) Section 2 data (8/07 to 1/08 1961). True salinity = 30 + reported value.

a)

b)

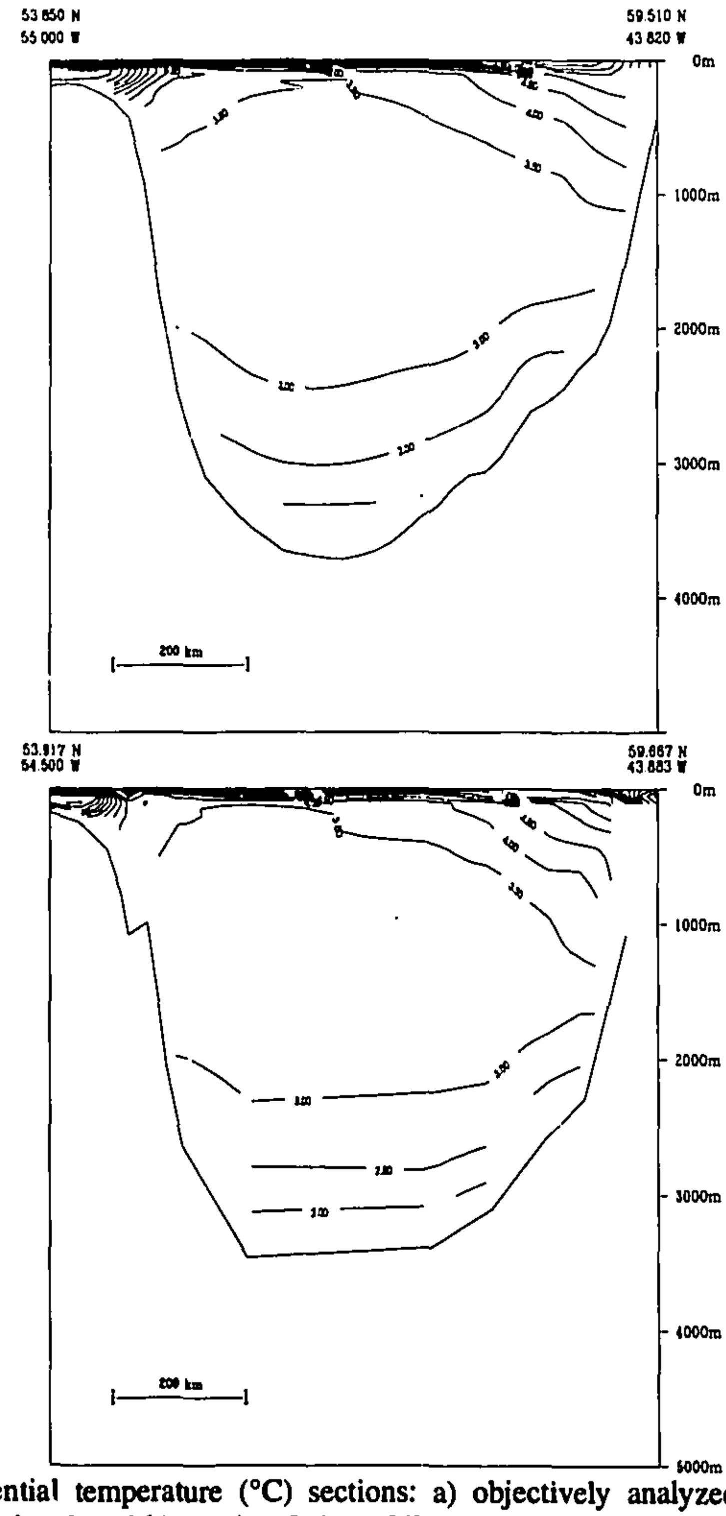

Figure 3.8: Potential temperature (°C) sections: a) objectively analyzed summer results along Section 2 and b) Section 2 data (8/07 to 1/08 1961).

a)

b)

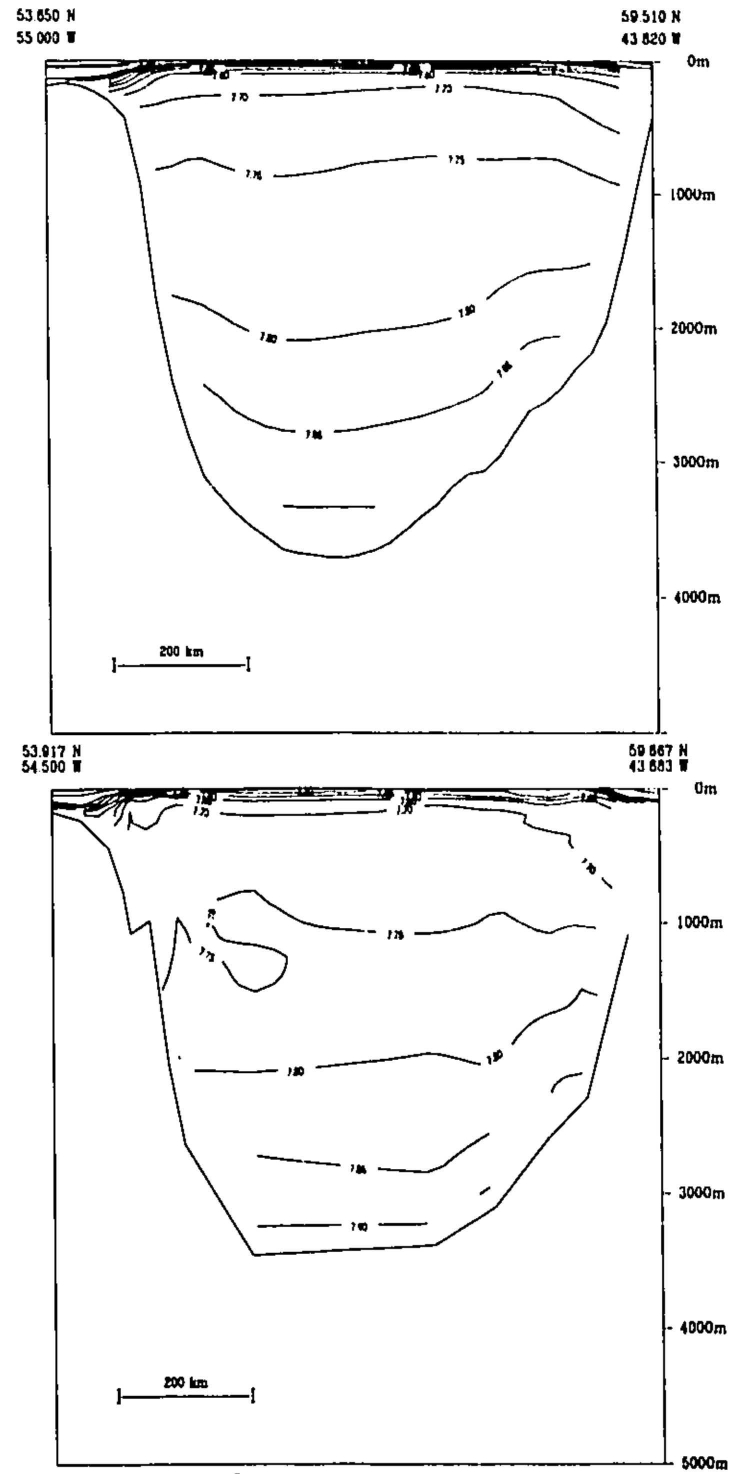

Figure 3.9: Potential density (kg m^{-3}) sections: a) objectively analyzed summer results along Section 2 and b) Section 2 data (8/07 to 1/08 1961). True value = 1020 + reported value.

WGC and the Arctic.

As mentioned in Chapter 1, the Deep Western Boundary Undercurrent (DWBU) which carries the DSOW along the continental slope from Denmark Strait around Cape Farewell is found trapped at the bottom of the ocean. The DWBU flows below the IC and extends up to the 3000m isobath. Typical values of 1.4-1.6°C and ~34.9 psu are assigned to the potential temperature and salinity of this current (Clarke and Gascard, 1983). The strong horizontal temperature gradient around the edge of Labrador Sea in Figs. 3.3e-f is due to the DWBU with a minimum value for the potential temperature of around 2°C. The tilt of the 2.5°C and 3.0°C isoterms in Fig 3.5a and 3.8a is also due to the DWBU. The NADW which is characterized by a potential temperature of ~3.0°C and a salinity of ~34.95 psu can be seen in Figs. 3.2e, 3.3e, 3.4, 3.5, 3.7 and 3.8 as well. The LSW, found above the NADW is defined as ~3.4°C and ~34.9 psu. These values correspond quite well to those found in Figs. 3.2d and 3.3d. The last component, the NAC, is found in the southeastern corner of Figs. 3.2 a-d and Figs. 3.3 a-d as well as in Figs. 3.4a and 3.5a.

A feature which was initially found to be suspicious was the circular structure of the isohalines in Central Labrador Sea (Figs. 3.2b-d) which is responsible for cross-shelf flow (Chapter 6). Two reasons were hypothesized in attempting to account for this structure: (i) it seemed that the radius of the feature was close to the value of the third influence radius used in the objective analysis and (ii) perhaps the large number of observations at OWS Bravo were responsible for its existence. This latter point was found

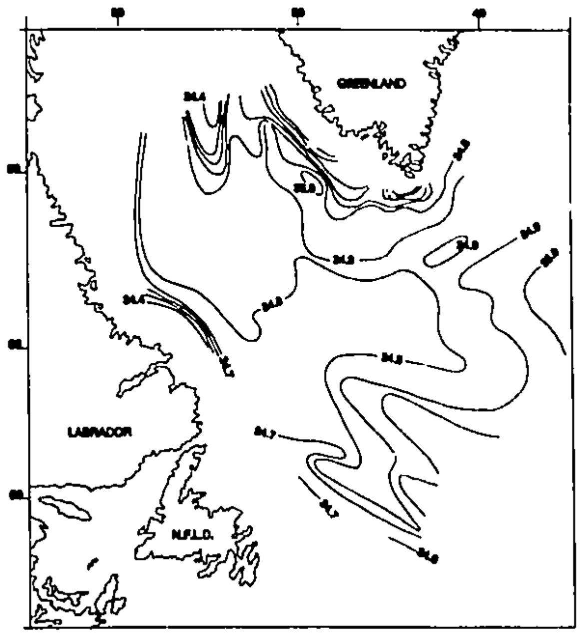

Figure 3.10: Salinity at 50m with contours every 0.1 psu for 34.4 < S < 35.0 psu. The stations were occupied from March 15 to May 15 1966 (redrawn from Lazier, 1973).

to be irrelevant as the circular feature was seen even after correcting the data set by reducing the amount of OWS Bravo data used in the analysis. While the circular appearance is partially related to the value of the third influence radius, it is deduced that these cross-isobath isohalines are real since Lazier (1973) also found evidence of isohalines crossing the isobaths near the same location (Fig. 3.10).

3.3 The warm and cold season results

The seasonal cycle in the Labrador Sea was discussed in Lazier (1980 and 1982) and some of Lazier's results were discussed in section 1.5 of this thesis. Briefly, the upper water column temperature is warmer during the warm season because of stronger local

a)

b)

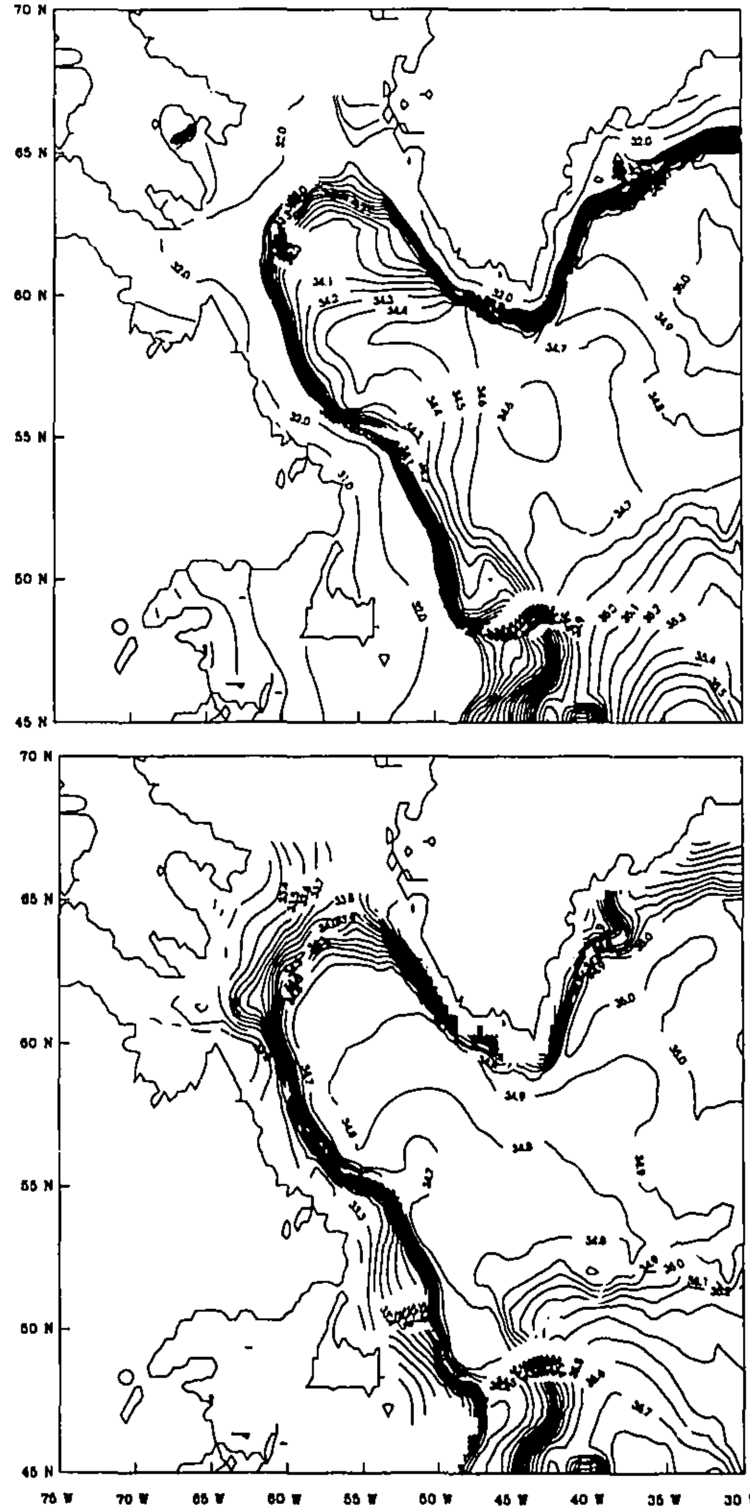

Figure 3.11: Warm season salinity (psu) of the northwestern Atlantic Ocean at a) 0m, b) 100m,

c)

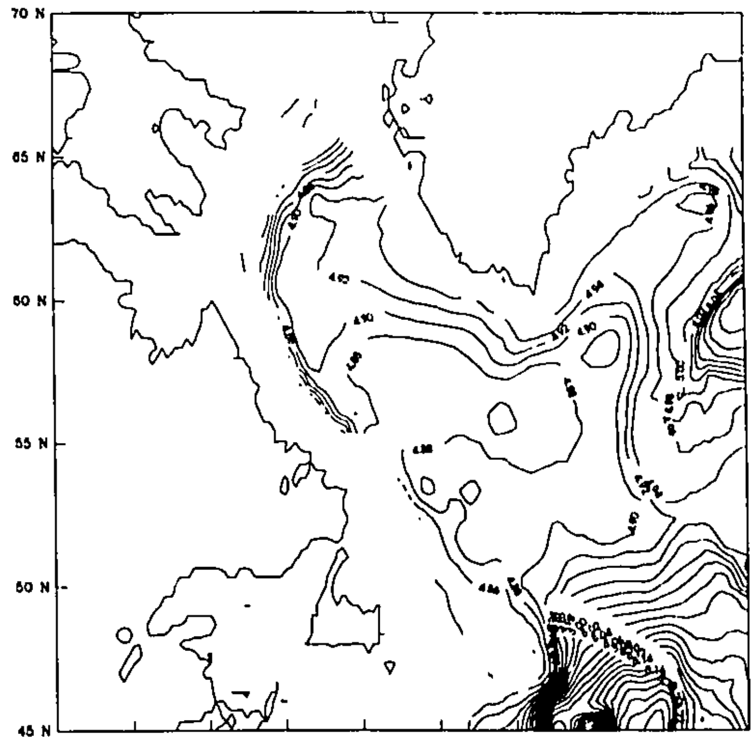

d)

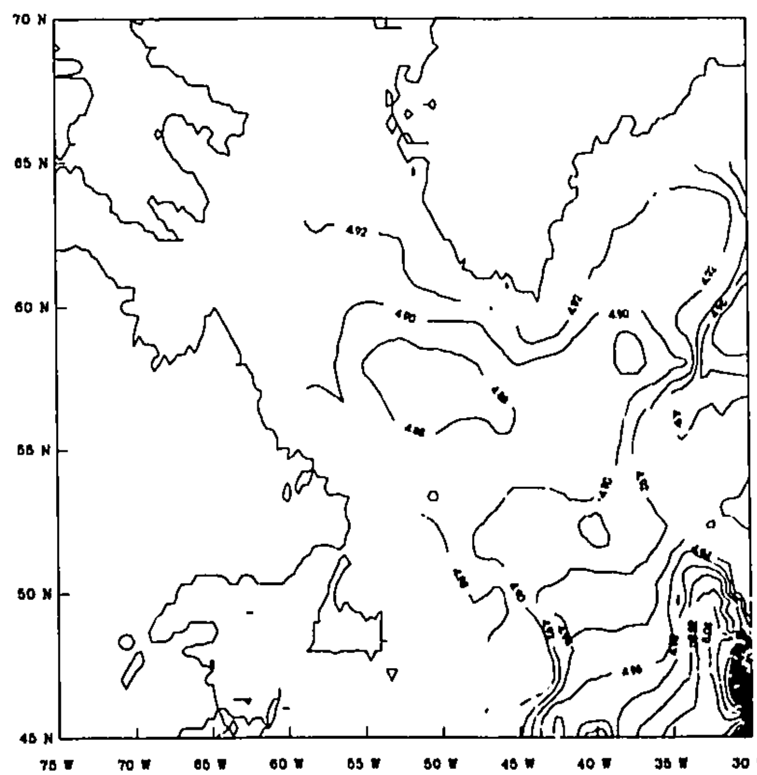

Figure 3.11 cont: at c) 500m (true salinity = 30 + reported salinity), at d) 1000m (true salinity = 30 + reported salinity),

e)

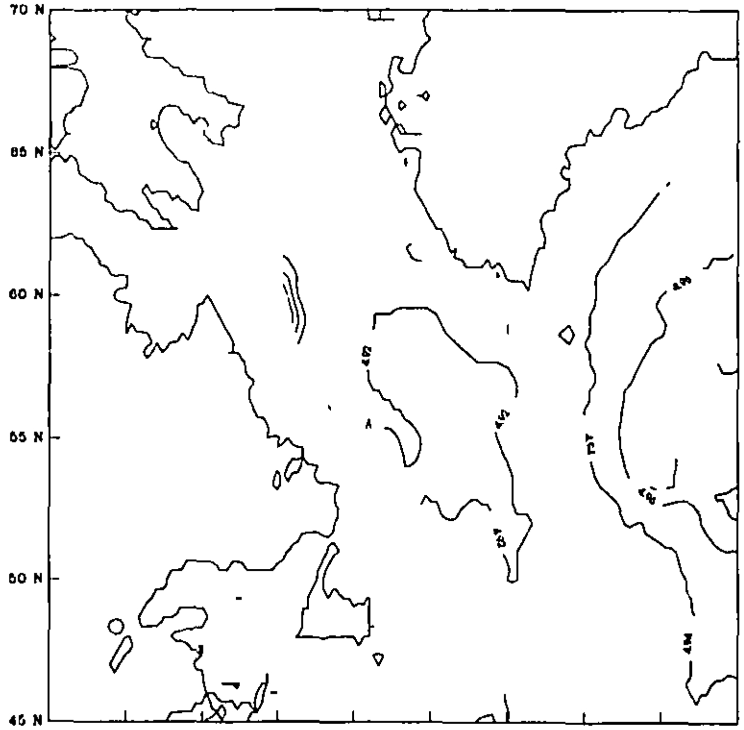

f)

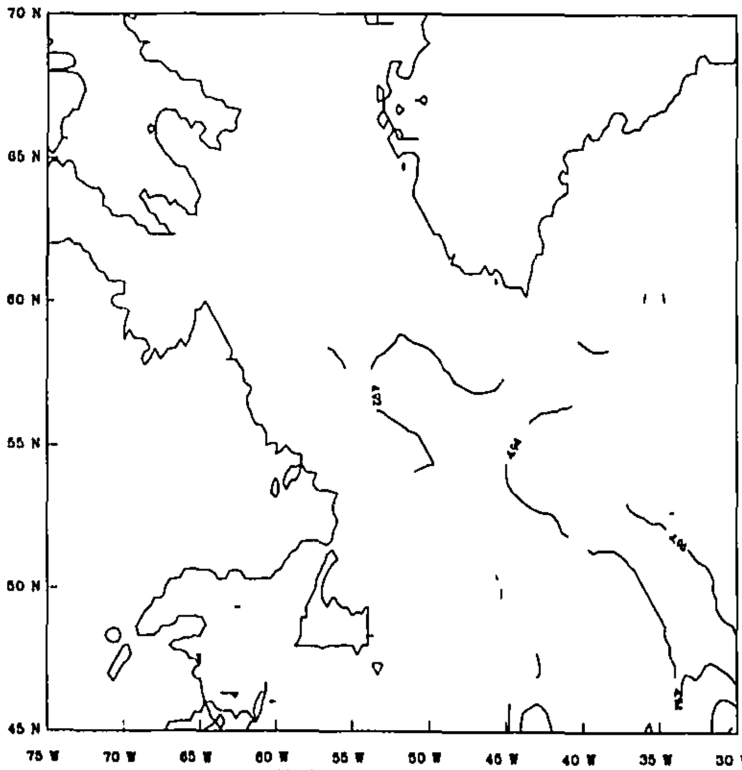

Figure 3.11 cont: at e) 2000m (true salinity = 30 + reported salinity) and at f) 3000m (true salinity = 30 + reported salinity).

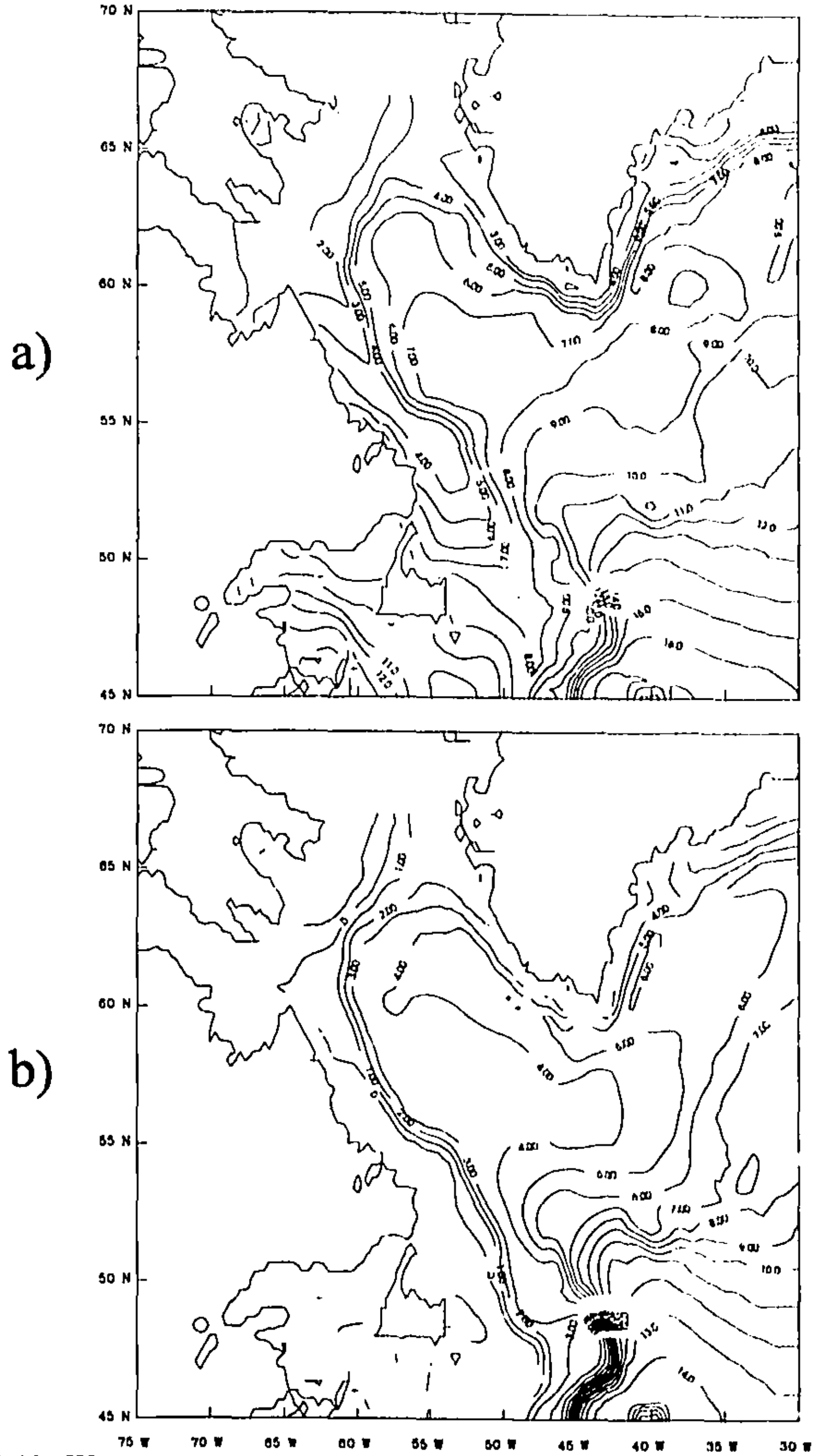

Figure 3.12: Warm season *in situ* temperature (°C) of the northwestern Atlantic Ocean at a) 0m, b) 100m,

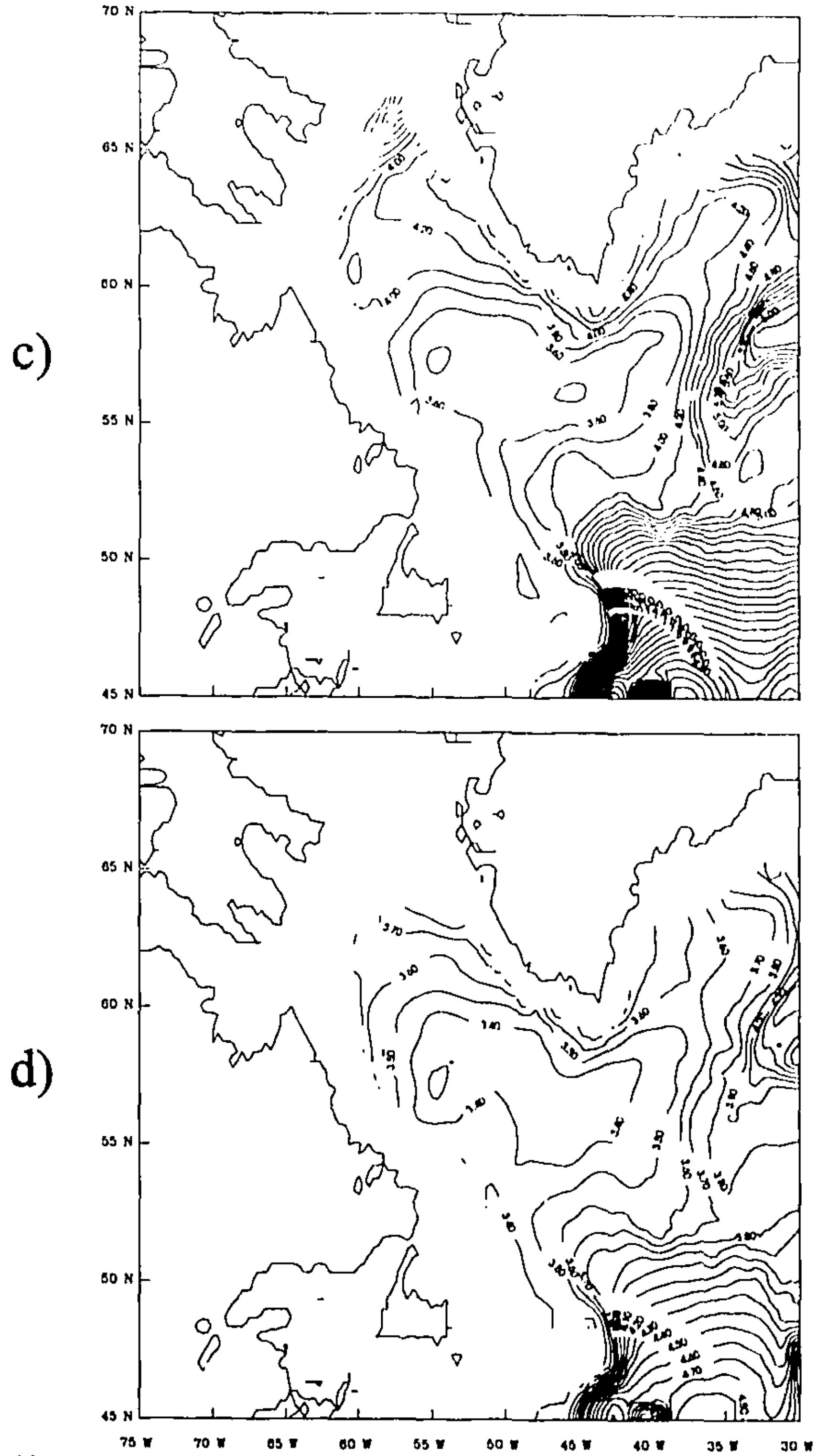

Figure 3.12 cont: at c) 500m, d) 1000m,

e)

f)

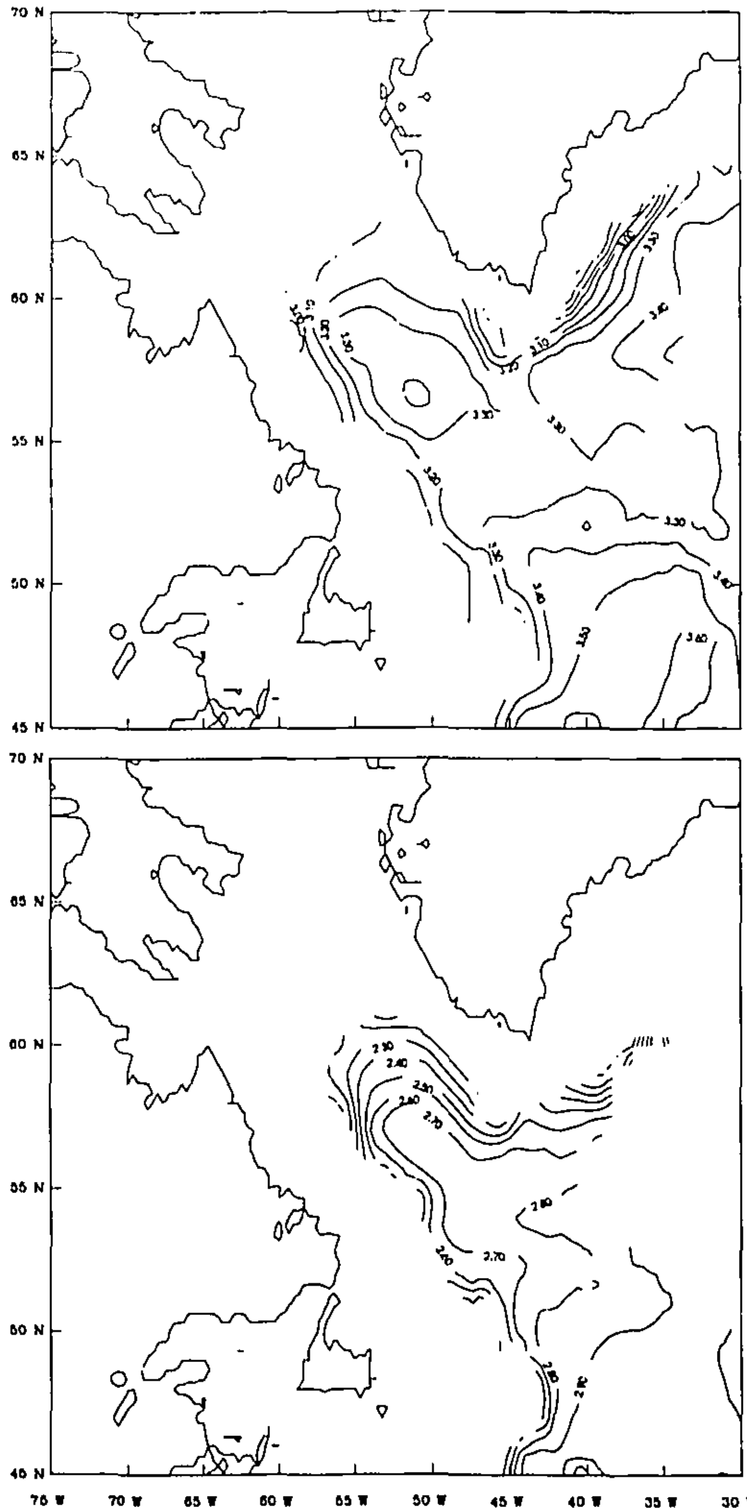

Figure 3.12 cont: at e) 200m and at f) 3000m.

a)

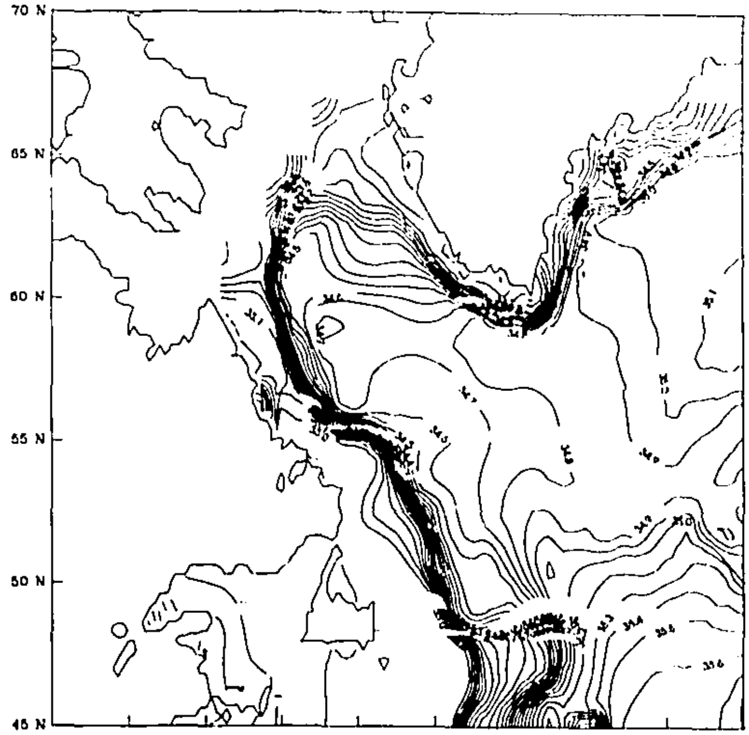

b)

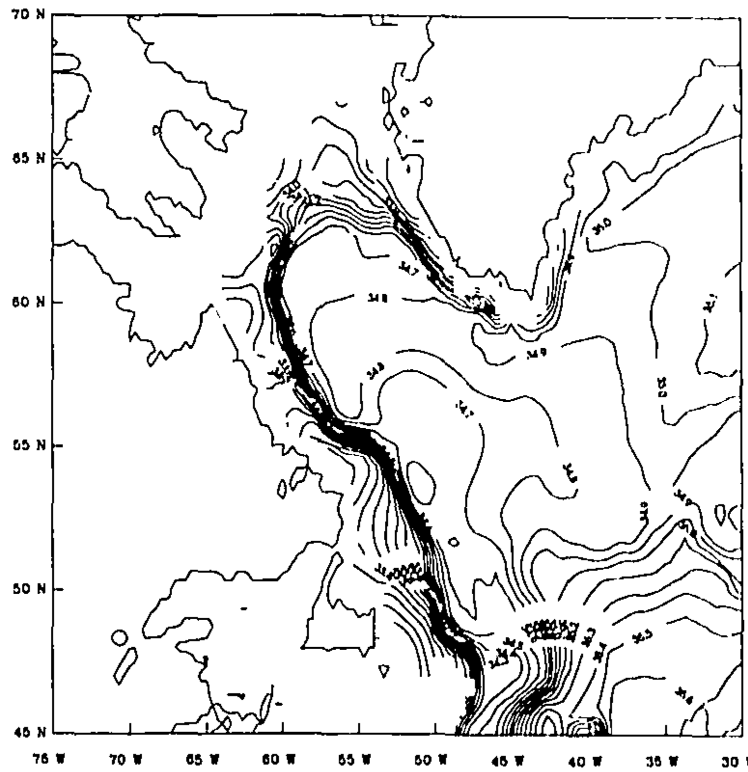

Figure 3.13: Cold season salinity (psu) of the northwestern Atlantic Ocean at a) 0m, b) 100m,

c)

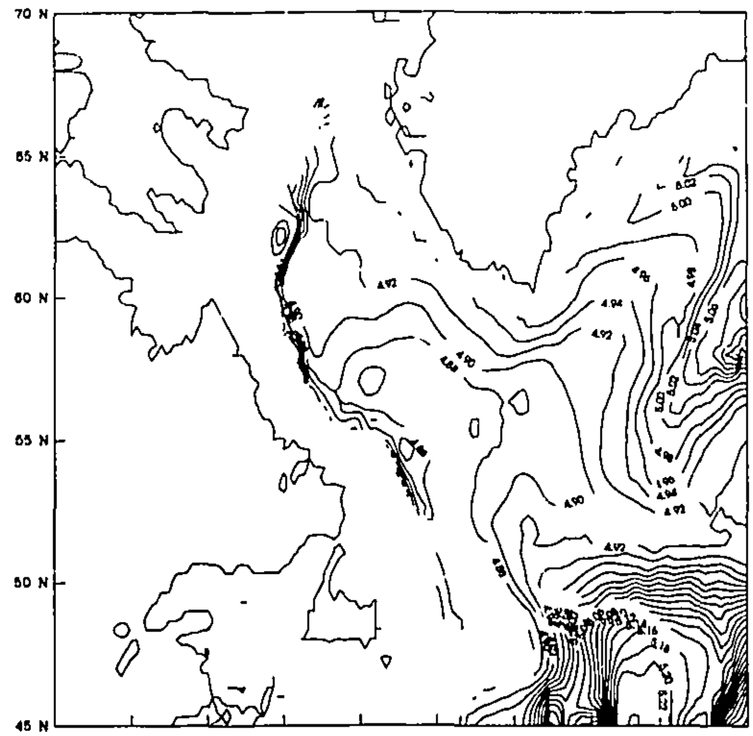

d)

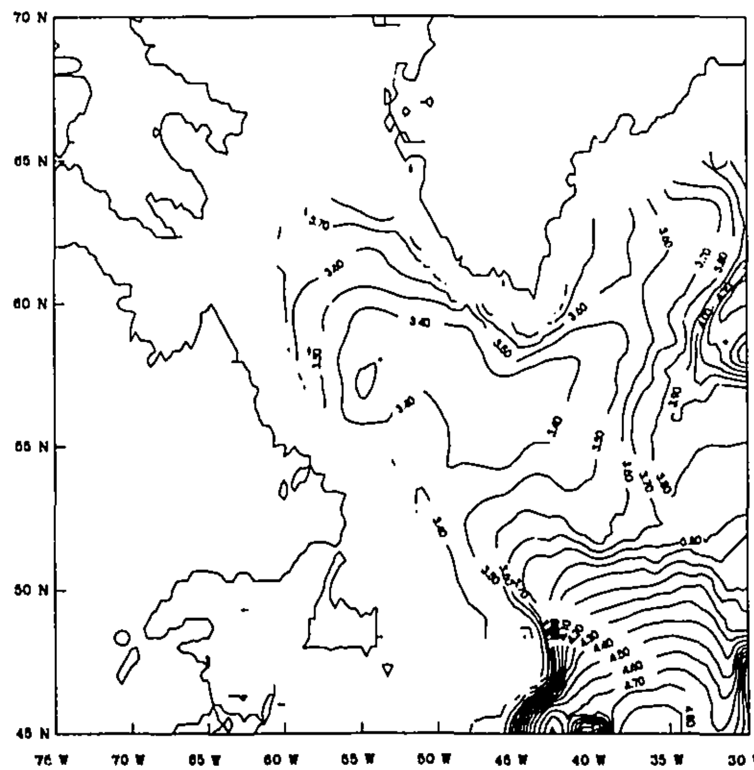

Figure 3.13 cont: at c) 500m (true salinity = 30 + reported value), at d) 1000m (true salinity = 30 + reported value),

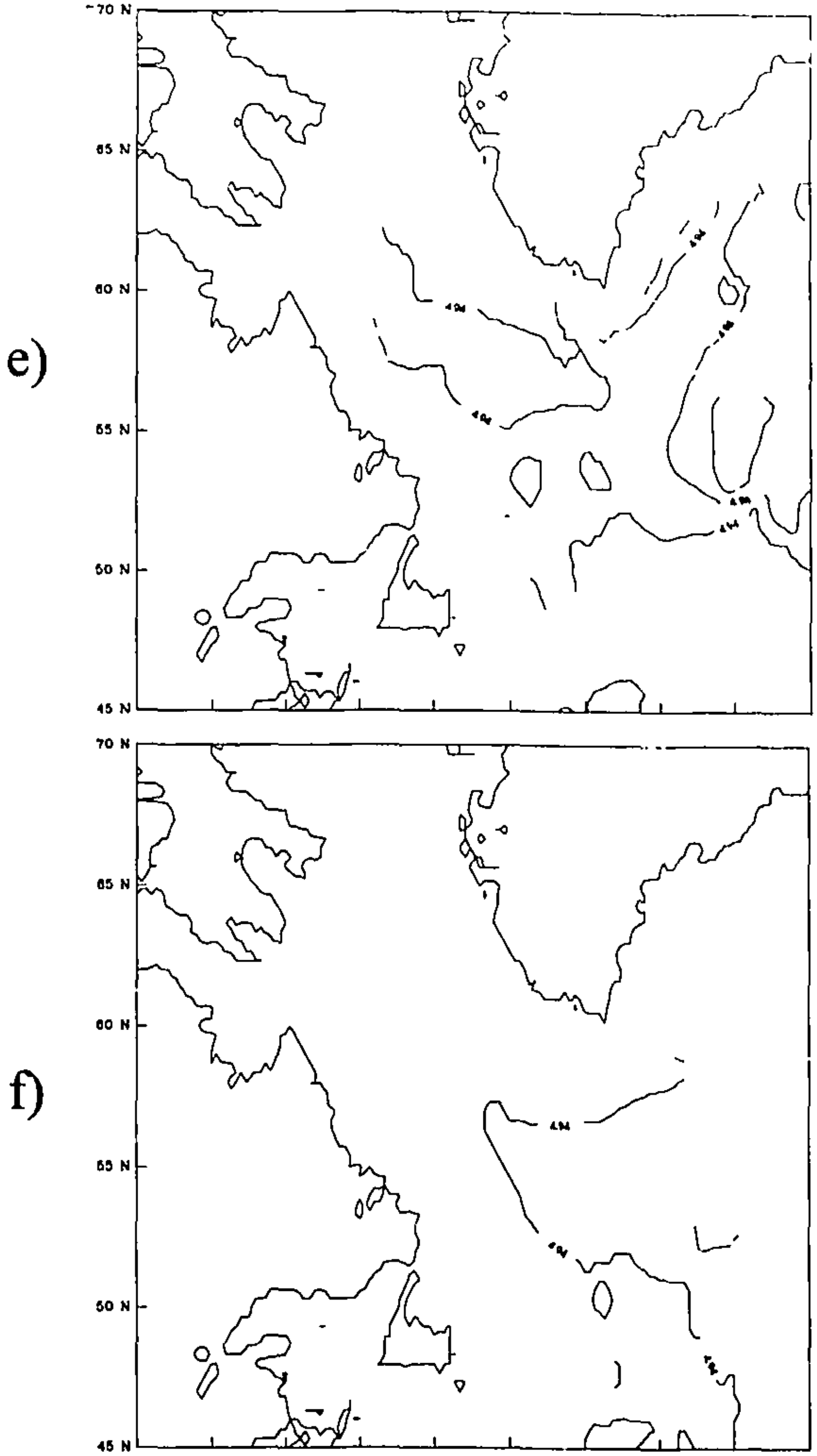

Figure 3.13 cont: at e) 2000m (true salinity = 30 + reported value) and at f) 3000m (true salinity = 30 + reported value).

a)

b)

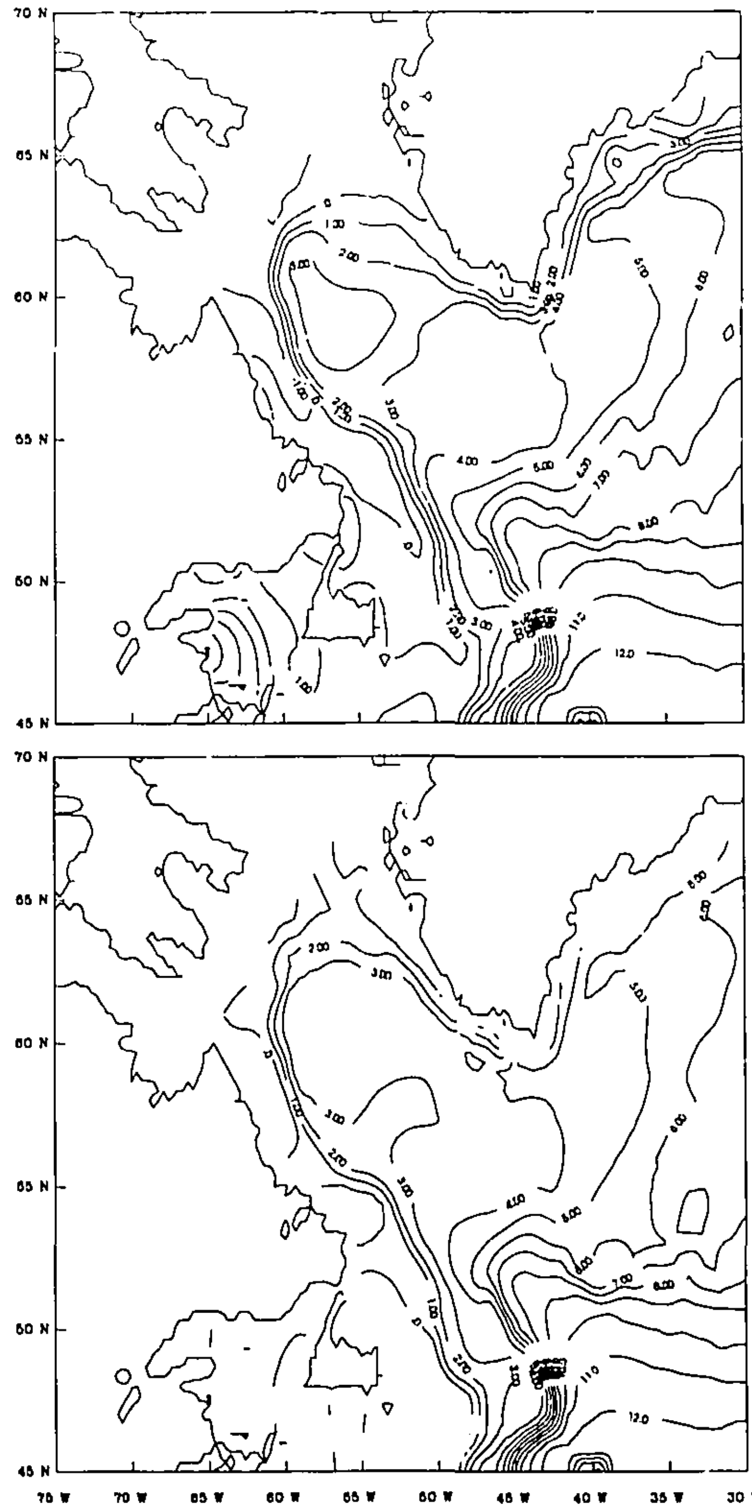

Figure 3.14: Cold season *in situ* temperature (°C) of the northwestern Atlantic Ocean at a) 0m, b) 100m,

c)

d)

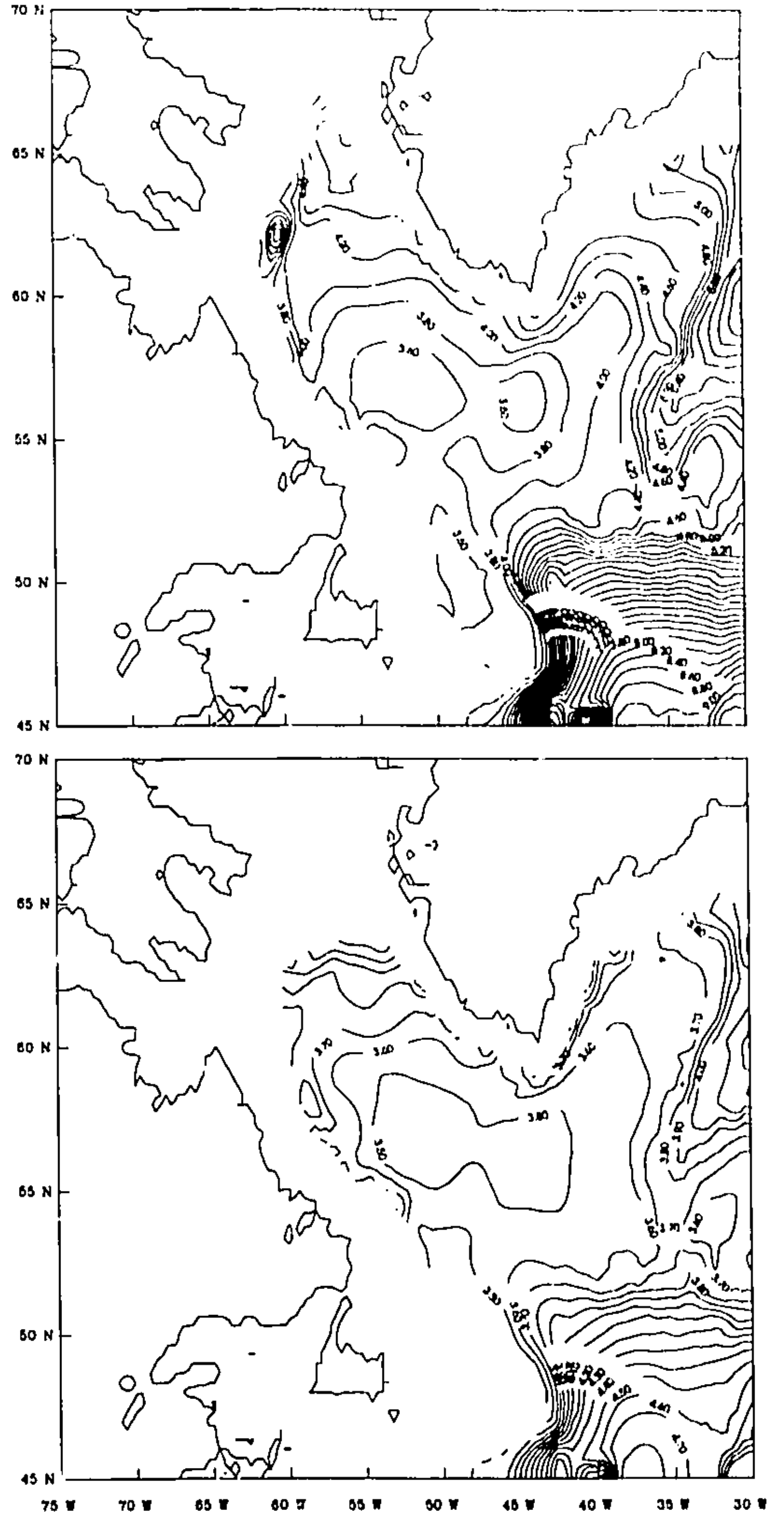

Figure 3.14 cont: at c) 500m, d) 1000m,

e)

f)

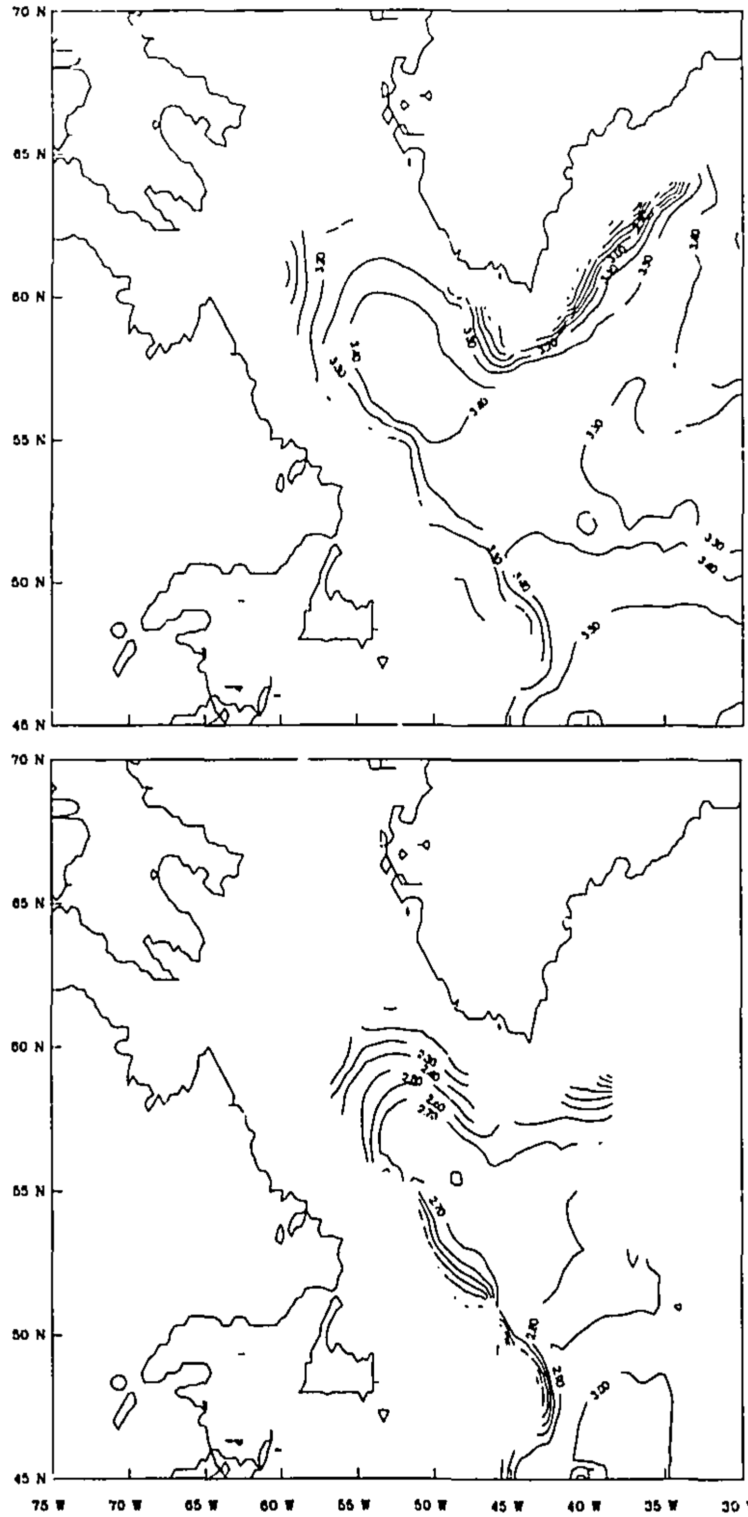

Figure 3.14 cont: at e) 2000m and at f) 3000m.

heating. The salinity seasonal cycle is not directly linked to the precipitation cycle since, as reported by Lazier (1982), most of the precipitation occurs during the cold season when the salinity is at its highest. Lazier (1982) suggested that the advection of fresh water from Hudson and Baffin Bays to the central Labrador Sea is responsible for the decrease in salinity observed during the warm season. Also, ice growth along the borders of the Labrador Sea in the cold season (and hence generate brine rejection), together with ice melt during the warm season contributes to the seasonal cycle of the salinity in the region. Furthermore, seasonal variations in the transport of freshwater by the EGC/WGC is also important. The question now is whether the objectively analyzed results can account for these features.

Seasonal results are shown in Figs. 3.11 and 3.12 for the warm season (June-November) analysis and in Figs. 3.13 and 3.14 for the cold season (December-May) analysis. The levels shown are the same as in the case of the summer analysis. In the coastal region, the summer surface results (Figs. 3.2a and 3.3a) show slightly fresher salinities and roughly 2°C warmer temperatures than those of the warm season (Figs. 3.11a and 3.12a). This temperature difference, again, is due to the local heating which is stronger in the summer. In the offshore regions, the summer salinity surface field (Fig. 3.2a) is similar to the warm season surface salinity field (Fig. 3.11a) and the summer surface temperature is ~1°C warmer. At a depth of 500m, the differences between the summer and the warm season results are almost insignificant (Figs. 3.2c, 3.3c, 3.11c and 3.12c).

The seasonal results show that during the warm season the surface coastal waters are ~1.0-2.0 psu fresher (Figs. 3.11a and 3.13a) and ~2-7°C warmer (Figs. 3.12a and 3.14a) than during the cold season. These values are in agreement with Lazier's (1982) observations reproduced in Fig. 1.6. The maximum seasonal salinity variability of 2.0 psu occurs along the eastern coast of Greenland (Figs. 3.11a and 3.13a). In offshore regions, a ~0.1-0.4 psu (Figs. 3.11a and 3.13a) and a ~3-5°C (Figs. 3.12a and 3.14a) seasonal variability can be found between the warm and cold season surface waters. At a depth of 100m, the differences between the warm and cold season salinities and temperatures are smaller: a 0.1-0.4 psu variability can be found near coastal regions (Figs. 3.11b and 3.13b) and there is a 0.5-2.0°C variability over most of the domain (Figs. 3.12b and 3.14b). Notice that the highest temperature variability occurs in the NAC region.

At depth greater than 500m, the seasonal cycle in salinity disappears. The difference between seasonal fields are not significant in so far as the precision of the salinity values used (which is around 0.03 psu; see Lazier, 1980) is concerned. The temperature seasonal cycle shows a complex structure, where, in the case of water levels above ~300m, the warm season temperature is higher than the cold season temperature-whereas, when the water level is below ~300m the cold season temperature is higher than the warm season temperature (Figs. 3.15a, b and d). This feature is found as deep as ~2000m over most of the domain (the only exception being along the southern border between 35°W and 45°W). Now, the question is whether or not the pattern exhibited here has some degree of reality. Lazier (1980) estimated the instrumental errors on temperature

a)

b)

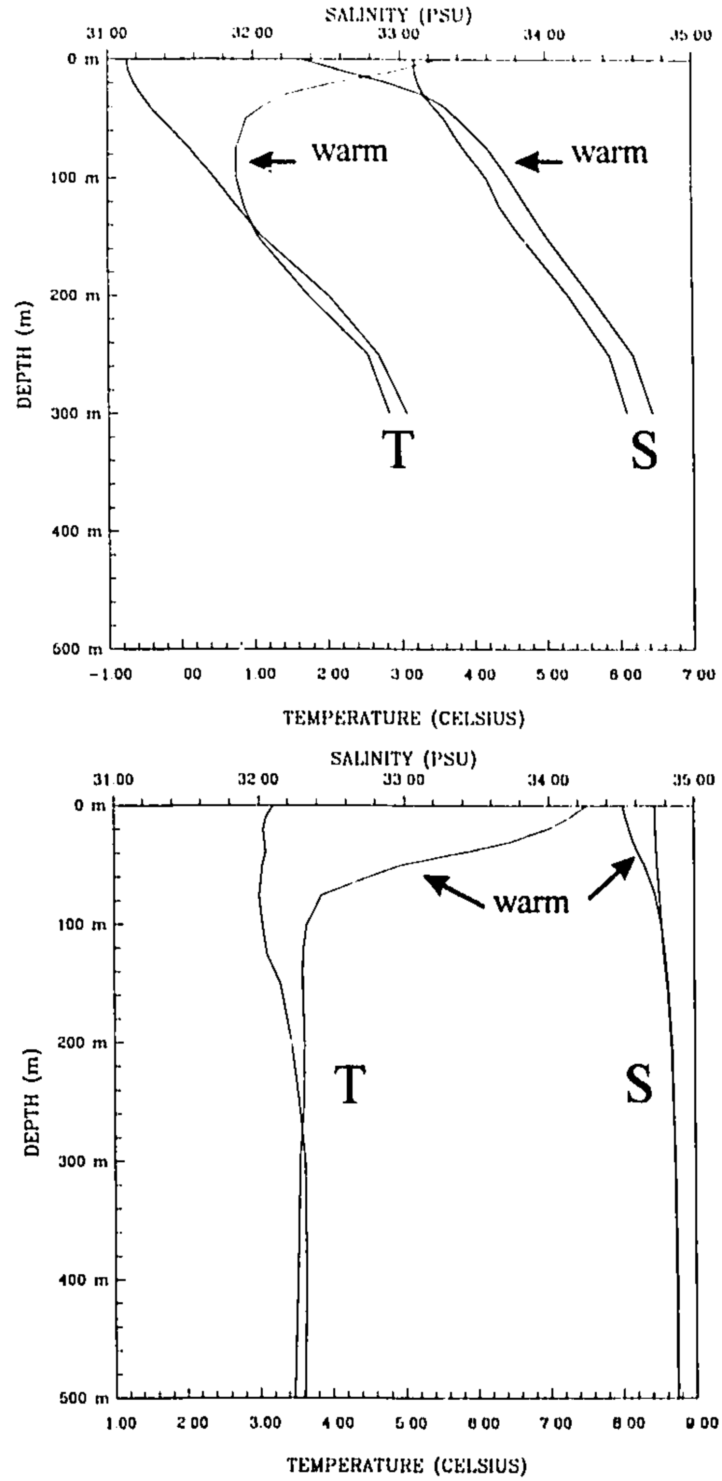

Figure 3.15: Vertical temperature and salinity profiles for the cold and warm seasons at a) 55.00°N and 55.00°W (southern Labrador shelf), b) 58.00°N and 50.00°W (central Labrador Sea),

c)

d)

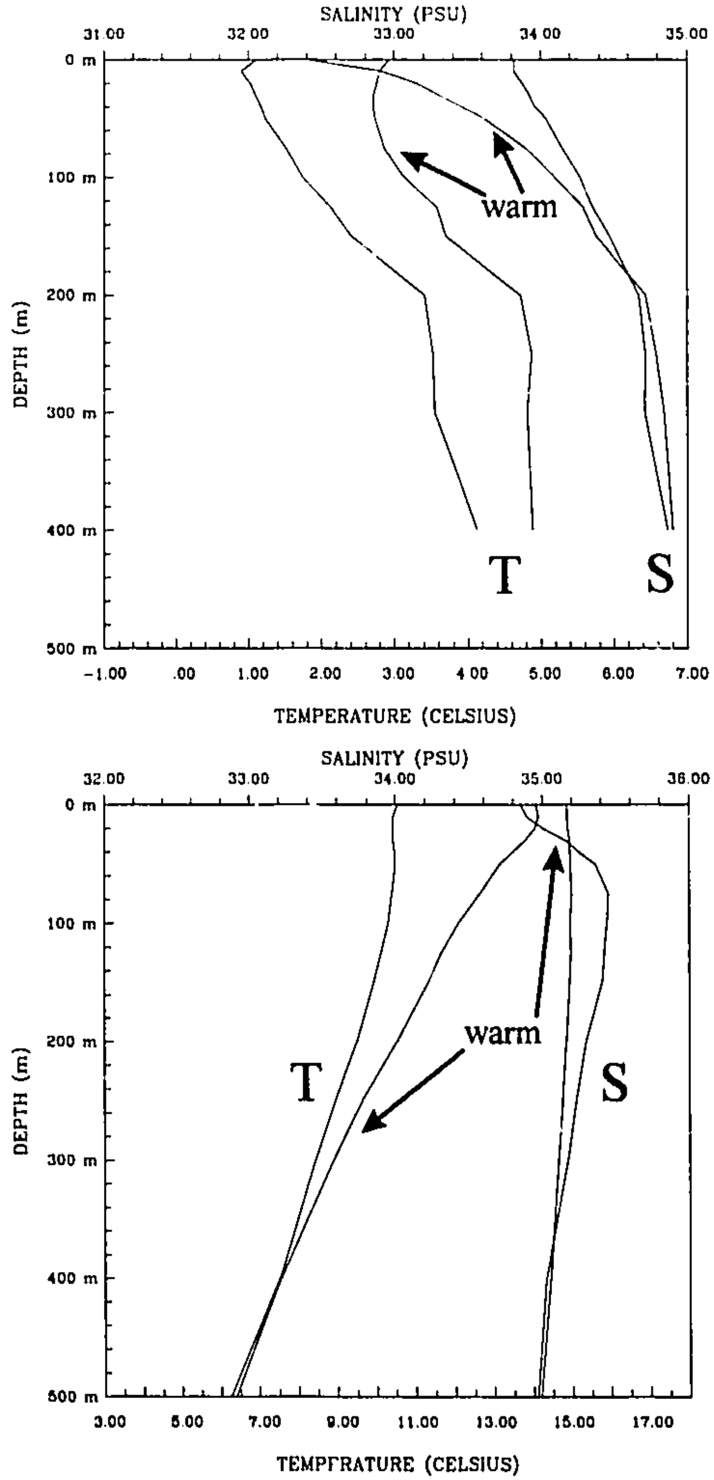

Figure 3.15 cont: c) 60.00°N and 46.33°W (west Greenland shelf) and at d) 50.00°N and 40.00°W (North Atlantic Current region). The warm profiles are indicated on the figures with arrows.

values to be 0.02°C which is about 10 times smaller than the feature under discussion; consequently is it likely to be real. Accounting for this sign inversion is rather difficult but, two reasons could be mentioned: (1) the downward vertical diffusion of heat stored during the warm season in near surface waters, and (2) the advection of LSW formed through deep convection in winter in the Labrador Sea. Both may explain this temperature anomaly.

There is another feature which should be commented on: in northern Labrador Sea, a low temperature anomaly can be found in the cold season field at a depth of 500m (Fig. 3.14c). This structure is due to some low temperature values, obtained in December 1981, which were not detected during the statistical check. Also, the strength of the structure is explained by the higher weights used in the objective analysis due to their smaller spatial distances (see Eq. 2.3b). This feature is not interpreted as real and is a result of data aliasing.

Some temperature and salinity vertical profiles (from the objectively analyzed results) are shown in Figs. 3.15 for four different sites: on the southern part of the Labrador shelf (Fig. 3.15a), in the central Labrador Sea (Fig. 3.15b), on the west Greenland shelf (Fig. 3.15c) and near the North Atlantic Current region (Fig. 3.15d). On the southern Labrador shelf, the diagnosed cold season surface temperature is ~-1.0°C and increases up to ~3.4°C during the warm season, whereas the salinity drops to ~32.4 psu but reaches 33.10 during the cold season. Fig. 3.15a also shows, in comparison with near surface waters, an out-of-phase seasonal cycle in waters below 140m. In the central Labrador Sea, the warm season temperature obtained is ~7.4°C, and this drops to ~3.1°C during the cold season. The salinity seasonal cycle of this region is very weak, a salinity maximum of ~34.7 psu is found during the cold season, which drops to ~34.5 psu during the warm season. Notice that below a depth of 260m the temperature and salinity are almost uniform although the weak reverse seasonal temperature cycle, discussed earlier, can be observed below that depth. On the Greenland shelf (Fig. 3.15c) the temperature and salinity profiles show warmer and saltier water masses than on the Labrador shelf presumably due to the Irminger Current. The last profile (Fig. 3.15d), which is for the North Atlantic Current region, shows that the seasonal cycle can be observed up to a depth of ~400m. The warm and cold season salinity profiles, in that region, show an interesting vertical structure, where the upper 30m waters are fresher during the warm season and the 30-380m waters are saltier during the warm season.

Petrie *et al* (1991) analyzed the temperature and salinity cycle on the eastern shelf of Newfoundland. Figure 2 in Petrie *et al* (1991) shows the average temperature and salinity over depth and time. The warm and cold season results (Figs. 3.11-3.14) are in relatively good agreement with Petrie *et al* (1991). At the surface, the seasonal results for the salinity show a annual cycle of ~0.8 psu with a minimum value of ~31.6 psu reached during the warm season and a maximum value of ~32.4 psu found during the cold season. Comparing these values with those found in the Figure 2 of Petrie *et al* (1991), it seems that 31.6 psu is a good estimate of average surface conditions for the warm season while the cold season value of 32.4 psu seems a bit high. At the surface, the objectively analysed results for temperature show an annual cycle of ~7.5°C, with a maximum temperature of 8.5°C during the warm season and a minimum temperature of ~1°C during the cold season. Again the warm season estimate seems to be in good agreement with Petrie *et al* (1991) while the cold season value seems to be biased toward the April-May conditions. The Newfoundland shelf is also characterized by subsurface waters with a temperature colder than 0°C. This feature can be found in both the warm and cold seasons results (Figs. 3.12b and 3.14b). The 0°C isotherm is found, in the objectively analysed results on the eastern Newfoundland shelf, at a depth of ~30m and ~60m for the cold and warm season, respectively. The value of 30m for the cold season tends, again, to show that the cold season temperature field, at least for the eastern Newfoundland shelf, is slighly biased toward the conditions that occur in April-May (see also Table 2.1).

3.4 A comparison with the raw data set

Although the water masses discussed in the introduction are found within the objectively analyzed results, the question of how much smoothing is done by the objective analysis scheme is important and should be discussed. In order to examine this, two hydrographic sections along S1 and S2 (Fig. 1.1), which are a subset of the total data set, are compared with the objectively analyzed results presented in the previous section. The section 1 (S1) data (see Figs. 3.4b, 3.5b and 3.6b) were obtained in July 1983. The shape of the isohalines and isotherms shown in Figs. 3.4b and 3.5b are similar to those of Figs. 3.4a and 3.5a with minor differences in that the DWBU temperature and salinity gradients are slightly weaker in the objectively analyzed results, and the slope of the isotherms and isohalines associated with the NAC are smaller, probably because the meridional section (Fig. 3.4a-3.6a) is located westward of S1. The section 2 (S2) data (see Figs. 3.7b, 3.8b and 3.9b) were taken during summer 1961. Again, many similarities exist between Figs. 3.7a and 3.8a and Figs. 3.7b and 3.8b, but some features such as the fresh water pool at 1000m deep and the slope of the isohalines near a depth of 2000m are not seen in the objectively analyzed results. However, the general similarity of the objectively analyzed results and the observation section data do indicate that the along-isobath objective analysis technique, discussed in Chapter 2, did not overly smooth the data.

Some selected temperature and salinity profiles extracted from the original data set are presented in Figs. 3.16-3.18. The southern Labrador Shelf profiles, presented in Fig. 3.16a, clearly show the high variability of characterisitic T-S values in that region. The variability is especially obvious in near surface waters where a difference of ~2°C and 1.4 psu can be observed at the sea surface on the two July profiles (profiles 1 and 2 in Fig. 3.16a). Also, notice the negative temperature values on the July profiles for sub-surface waters which are not found on the warm season profiles of Fig. 3.15a, although the cold sub-surface temperature signature is obtained. As the objectively analyzed results represent the averaged conditions over a 6 month-period, the profiles of Fig. 3.15 should not be identical to those of Figs. 3.16-3.18. The profiles shown in Figs. 3.17 were obtained by averaging together all OWS Bravo data obtained during a month of a specified year (see section 2.4), e.g. September 1964. These profiles (Figs. 3.17a and b) are very similar to

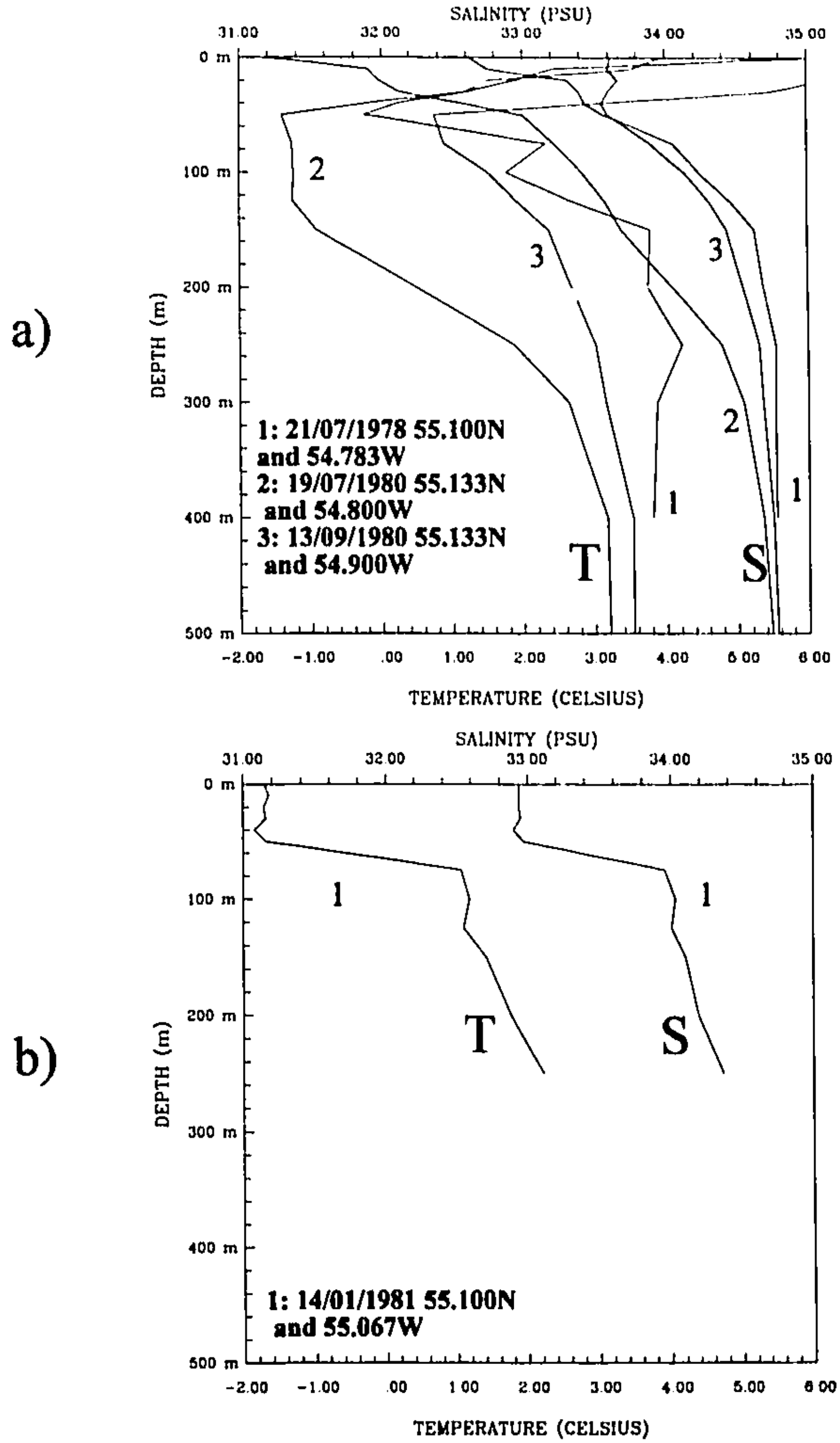

Figure 3.16: Selected temperature and salinity profiles on the southern Labrador shelf from the original data set for a) the warm season and b) the cold season.

a)

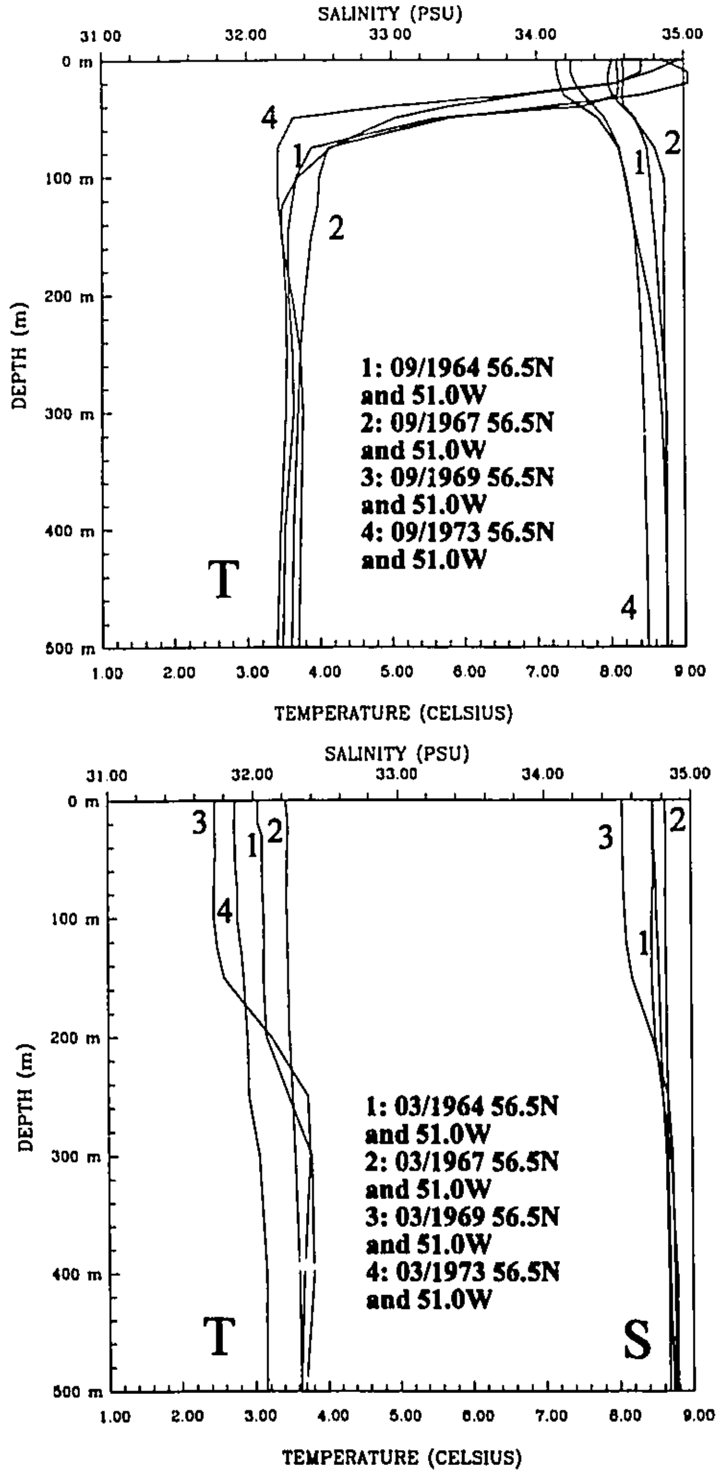

b)

Figure 3.17: Selected temperature and salinity profiles in central Labrador Sea from the original data set for a) the warm season and b) the cold season.

a)

b)

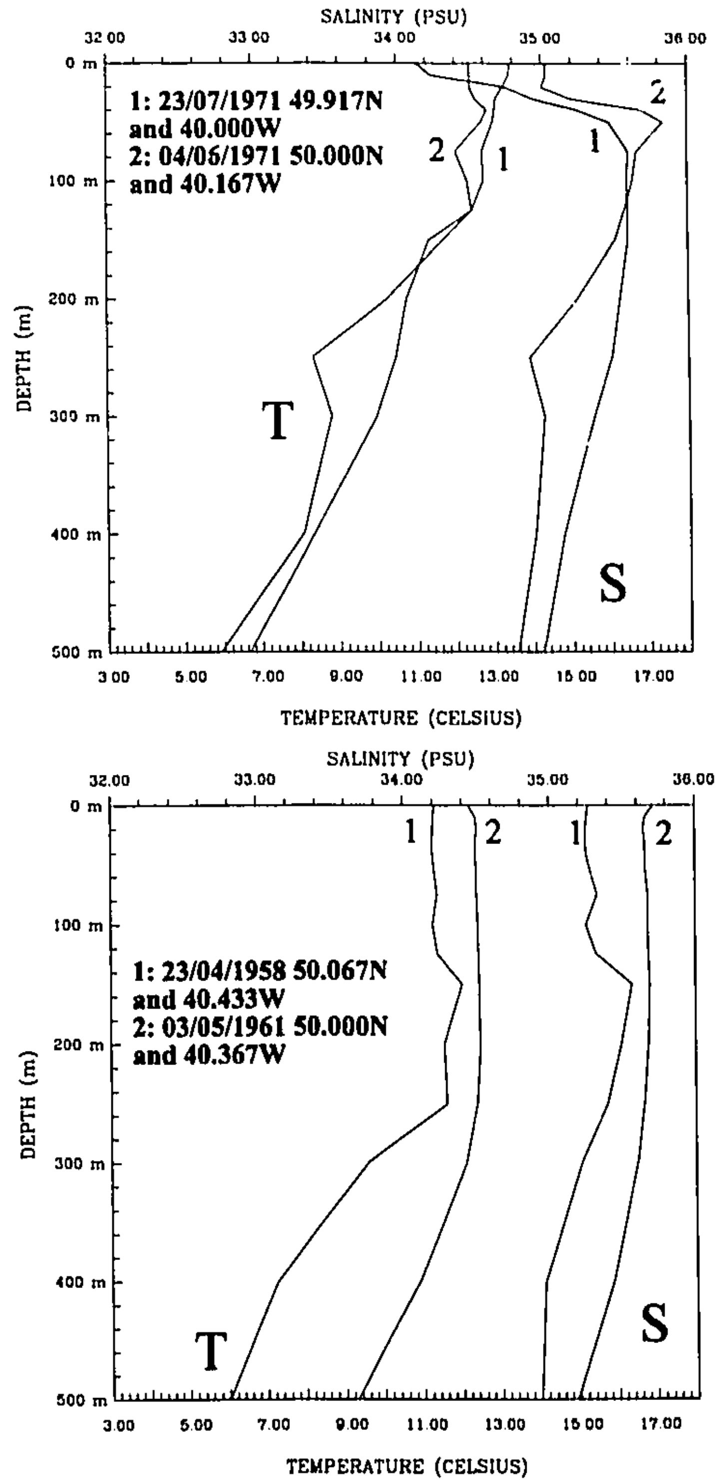

Figure 3.18: Selected temperature and salinity profiles in the North Atlantic Current region from the original data set for a) the warm season and b) the cold season.

those of Fig. 3.15b. The low surface salinity values on profiles 3 and 4 of Figs. 3.17 are associated with the *Great Salinity Anomaly* (*G.S.A*) discussed in the introduction. Since the warm and cold season profiles (Fig. 3.15b) are rather similar to the 1964-67 profiles of Figs. 3.17b (profiles 1 and 2), this seems to show that the objectively analyzed results are not too biased by the data obtained during the *G.S.A*. years. The profiles of Figs. 3.18 are from stations occupied within the North Atlantic Current region. Although Figs. 3.18 are generally similar to Fig. 3.15d, some differences are found. The warm season objectively analyzed surface waters (Fig. 3.15d) are a little warmer and saltier than those of the stations (see Fig. 3.18a) and the sub-surface salinity maxima is also weaker in Fig. 3.15d. The top 300m waters from the cold season results (Fig. 3.15d) are fresher and colder than on the T-S station profiles of Fig. 3.18b.

As surface waters are colder than sub-surface waters in the Labrador Sea during the cold season (Figs 3.15 a and b), the question of static stability of the water column arises as an unstable density profile is very unlikely as a mean state. In order to address this problem, the *in situ* density profliles are presented in Figs. 3.19 for the cold and warm seasons on the Labrador shelf (Fig. 3.19a) and in the central Labrador Sea (Fig. 3.19b). During the warm season the question of stability is not a problem as the fresh surface waters prevent any instability. In the cold season, as the salinity compensates for the colder surface temperature, the density profile are still stable although nearly homogeneous conditions are found in the central Labrador Sea (Fig. 3.19b). In the winter, the colder surface temperature is responsible for instability and deep water formation.

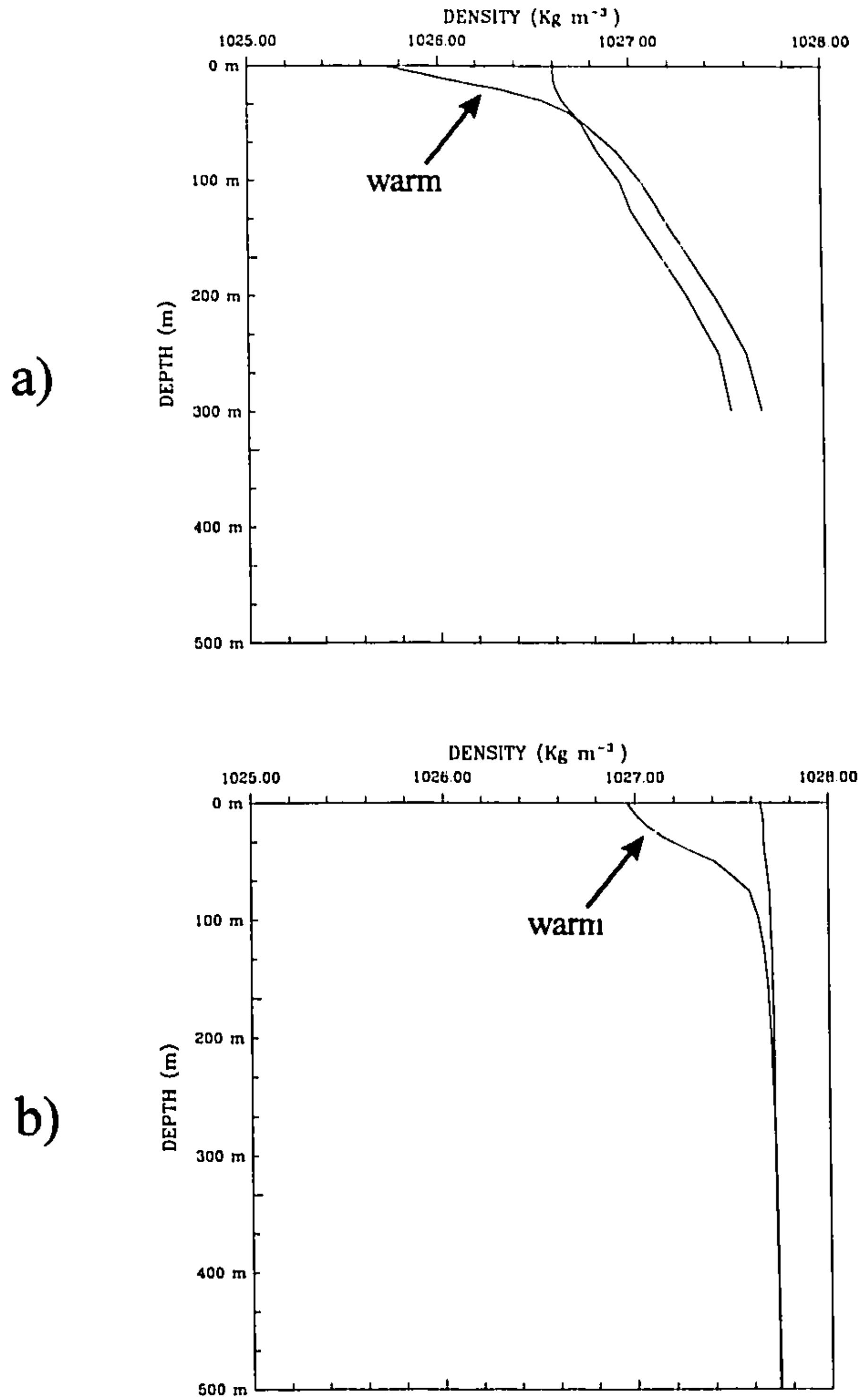

Figure 3.19: Cold and warm season *in situ* density profiles for the top 500m at a) 55.00°N and 55.00°W and b) 58.00°N and 50.00°W.

a)

b)

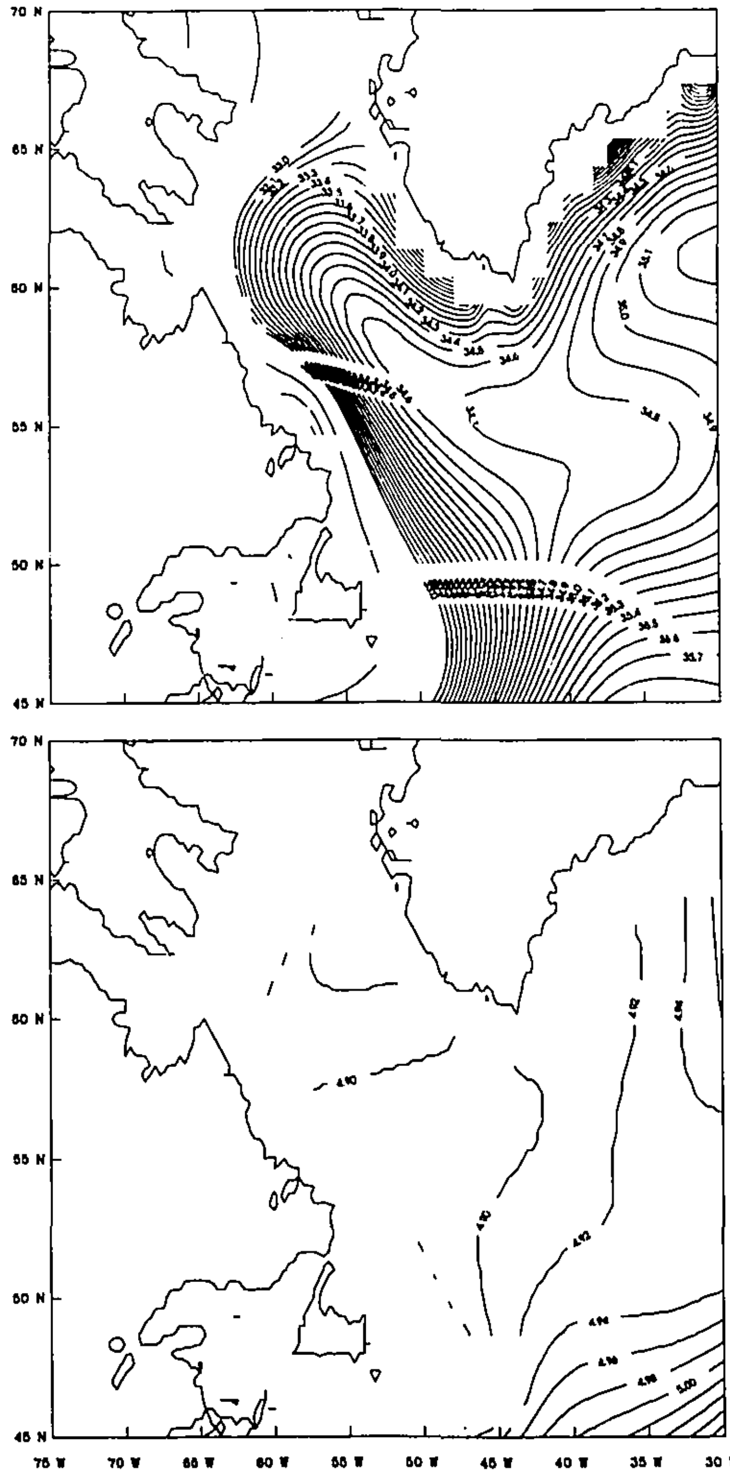

Figure 3.20: The annual mean Levitus (1982) salinity (psu) and *in situ* temperature (°C); a) salinity at 0m, b) salinity at 1000m (true value = 30 + reported value),

c)

d)

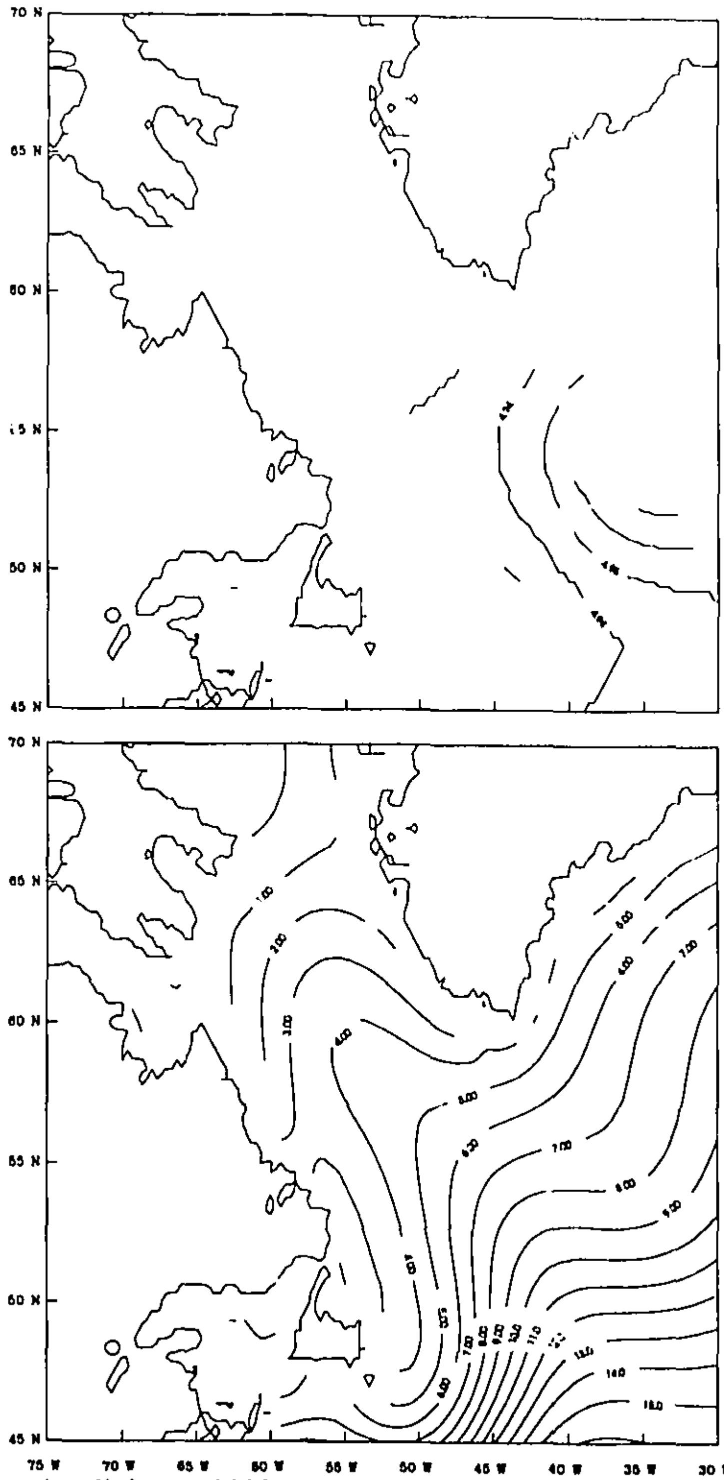

Figure 3.20 cont: c) salinity at 3000m (true value=30+reported value), d) in situ temperature at 0m,

e)

f)

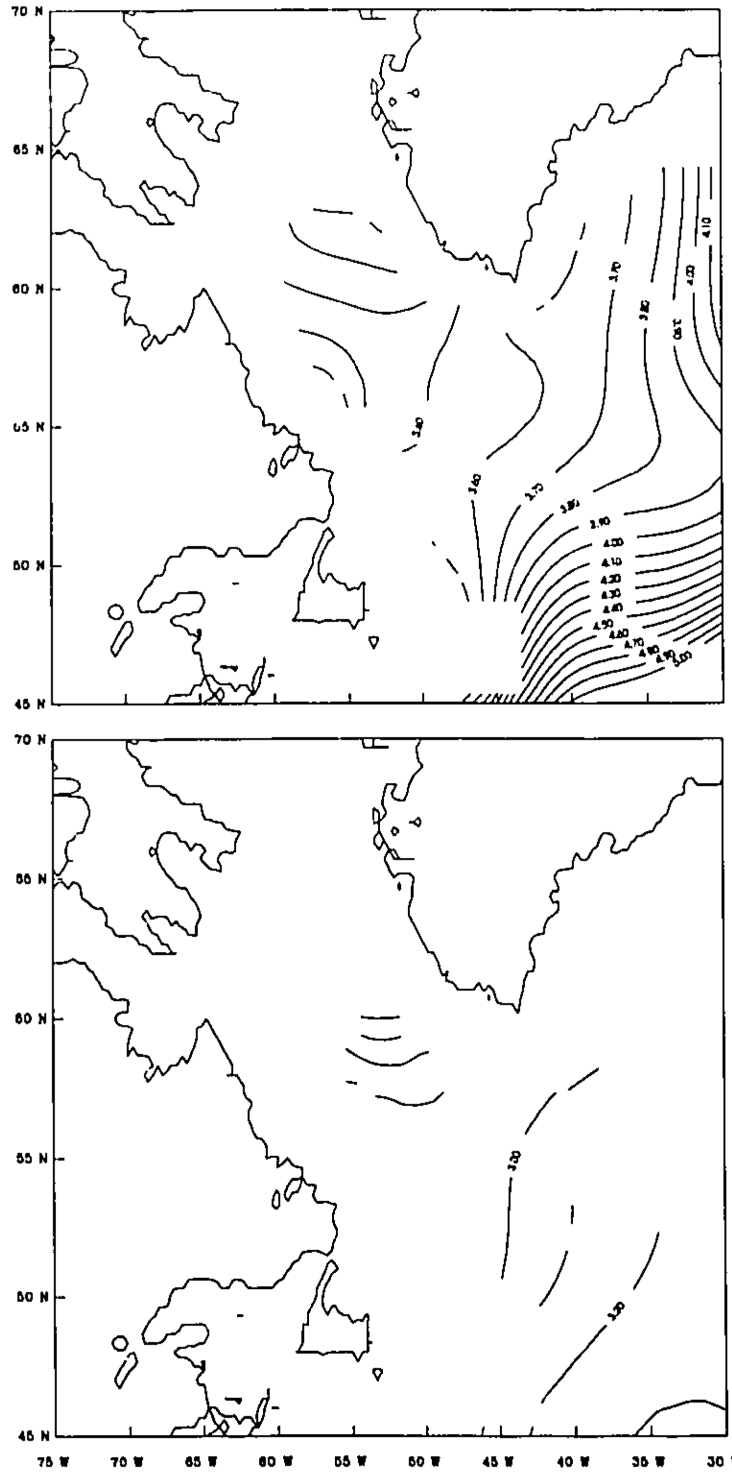

Figure 3.20 cont: e) *in situ* temperature at 1000m and f) *in situ* temperature at 3000m.

3.5 A Comparison with the Levitus (1982) data

As the scheme used in this analysis is similar to that used by Levitus (1982), it is appropriate to compare the new objectively analyzed temperature and salinity fields with those from the analysis of Levitus. The Levitus annual mean *in situ* temperature and salinity for several levels are shown in Fig. 3.20. At the surface, the T-S gradients of the WGC-LC system are too weak (compare Fig. 3.2a with Fig. 3.20a and Fig 3.3a with Fig 3.20d). At greater depth, the isotherms and isohalines are no longer parallel to the isobaths (compare Fig. 3.2d with Fig. 3.20b and Fig 3.3d with Fig 3.20e). Finally, the DWBU cannot be seen in the Levitus data (compare Fig. 3.3f with Fig. 3.20f). The main benefit of the analysis in this thesis is that the isotherms and isohalines were forced to follow the isobaths more closely and hence preserve the fronts near shelf breaks which is a characteristic feature of the northwestern Atlantic Ocean.

CHAPTER 4: THE INVERSE TECHNIQUES

Determining the ocean circulation is still a problem as direct measurements of currents are only available in limited quantity. On the other hand, temperature and salinity data are available in much larger quantities and can be used for estimating the circulation. But evaluating the currents from hydrographic data is not an easy task and has been the subject of much research. The general class of models which determine the horizontal velocity field from the horizontal density gradients are called either *diagnostic* or *inverse methods*. Some commonly used inverse techniques are: the level of no-motion calculation, variational inverse techniques (e.g. Provost and Salmon, 1986), the β-spiral (Stommel and Schott, 1977), the Box (Wunsch, 1978), the Bernoulli (Killworth, 1986), and the Mellor *et al* (1982) method.

The β-spiral, Box and Bernoulli methods were compared in Killworth and Bigg (1988) using an eddy-resolving Ocean General Circulation Model. Their results showed that in most regions the Box and Bernoulli methods gave a more accurate current estimation and that in regions of strong current shear, like in the Labrador Sea, the Bernoulli method was more appropriate. In this chapter the level of no motion and the Bernoulli methods are described. The Mellor *et al* (1982) method will be discussed in a separate chapter.

4.1 The level of no motion method

This method consists of combining geostrophy and hydrostatic relationships:

$$f\vec{k} \times \vec{v}_h = -\frac{1}{\rho} \nabla_h p \tag{4.1}$$

$$\frac{\partial p}{\partial z} = -\rho g \tag{4.2}$$

$\vec{v}_h$, p, ρ, f, g and $\vec{k}$ are the horizontal velocity, the pressure, the *in situ* density, the Coriolis parameter, the acceleration due to gravity and the unit vector in the vertical direction, respectively. The thermal wind equation (Eq. 4.3) is obtained by substituting Eq. 4.2 in the vertical derivative of Eq. 4.1:

$$f \frac{\partial \rho \vec{v}_h}{\partial z} = g \nabla p \times \vec{k} \tag{4.3}$$

The thermal wind equations can be vertically integrated to give:

$$\vec{v}_h(z) = \frac{f \rho(z_{ref})\, \vec{v}_h(z_{ref}) + g \int_{z_{ref}}^{z} (\nabla p \times \vec{k})\, dz}{\rho(z)\, f} \tag{4.4}$$

Equation 4.4 shows that, by providing the currents at a reference level and the density profile, the horizontal current can be determined for the whole water column. But the reference velocity is almost always unknown; the β-spiral inverse method was introduced as a means of estimating $\vec{v}_h(z_{ref})$. The easiest assumption consists of setting the reference velocity to zero (a level of no-motion) at depth of typically 1200m or at the bottom (Eq. 4.5):

$$\vec{v}_h(z) = \frac{g \int_{z_{ref}}^{z} (\nabla p \times \vec{k})\, dz}{\rho(z)\, f} \tag{4.5}$$

Usually this method works well for estimating surface currents. It does, however, fail where there are strong currents at the reference level and also in estimating the volume transport (eg: a 0.5 cm/s bottom current across a 1000 km section leads to a volume transport of 15 Sv).

4.2 The potential density

In this section, it will be shown how the potential density is evaluated since this quantity is used in the Bernoulli method considered in section 4.3. The potential density (ρ_θ)is defined as the density of a parcel of fluid if it is moved adiabatically (no heat exchange) to a reference pressure level (p_{ref}) without losing or gaining salt:

$$\rho_\theta = \rho(p_{ref}, S, \theta) \tag{4.6}$$

where S is the salinity and θ the potential temperature. The reference pressure level is often chosen as 10 dbars (1 atmospheric pressure). The potential temperature is evaluated from Bryden's (1973) polynomial expansion:

$$\theta = T - \sum_{i=1}^{3} \sum_{j=0}^{1} \sum_{k=0}^{3} A_{ijk} P^i (S-35)^j T^k \tag{4.7}$$

where T, S and P are the *in situ* temperature (°C), the salinity (psu) and pressure (dbars). The none zero coefficients are given in Table 4.1 below:

TABLE 4.1: Coefficients for the potential temperature

A_{100} =	0.36504×10^{-4}	A_{210} =	-0.41057×10^{-10}
A_{101} =	0.83198×10^{-5}	A_{200} =	0.89309×10^{-8}
A_{102} =	-0.54065×10^{-7}	A_{201} =	-0.31628×10^{-9}
A_{103} =	0.40274×10^{0}	A_{202} =	0.21987×10^{-11}
A_{110} =	0.17439×10^{-5}	A_{300} =	-0.16056×10^{-12}
A_{111} =	-0.29778×10^{-7}	A_{301} =	0.50484×10^{-14}

The potential temperature polynomial expansion above has an accuracy of ~0.002°C, and is valid for $30 \le S \le 40$ psu, $-2 \le T \le 30$°C and $0 \le P \le 10{,}000$ dbars. In all this manuscript the potential temperatures were estimated using the surface as reference level even though Eq. 4.7 was obtained for a reference level at 10m. This minor difference has no influence on the analysis as the compressibility effect over 10m depth is negligible.

4.3 The Bernoulli method

This method is based on the assumptions that the ocean is geostrophic (Eq. 4.1) and hydrostatic (Eq. 4.2) and that the Boussinesq approximation is valid. The geostrophic balance and continuity equation (1.3) can then be rewritten as:

$$f\vec{k}\times\vec{v}_h = -\frac{1}{\rho_o}\nabla_h p \tag{4.8}$$

$$\frac{\partial u}{\partial x} + \frac{\partial v}{\partial y} + \frac{\partial w}{\partial z} = 0 \tag{4.9}$$

where ρ_o is the constant Boussinesq reference density. The hydrostatic equation is rewritten in term of the potential density (ρ_θ):

$$\frac{\partial p}{\partial z} = -\rho_\theta g + Eg \tag{4.10a}$$

where

$$E = \rho_\theta - \rho \tag{4.10b}$$

and ρ is the *in situ* density. The Bernoulli method uses the fact that both potential temperature and salinity are conserved:

$$\frac{d\theta}{dt} = 0 \tag{4.11}$$

$$\frac{dS}{dt} = 0 \tag{4.12}$$

Equations 4.11 and 4.12 can be combined together to give the conservation of potential density:

$$\frac{d\rho_\theta}{dt} = 0 \tag{4.13a}$$

Equation 4.13a, under steady state conditions, is rewritten as:

$$u\frac{\partial \rho_\theta}{\partial x} + v\frac{\partial \rho_\theta}{\partial y} + w\frac{\partial \rho_\theta}{\partial z} = 0 \tag{4.13b}$$

Equation 4.14 is obtained by taking the vertical derivative of Eq. 4.13b:

$$\frac{\partial \vec{v}}{\partial z}.\nabla \rho_\theta + \vec{v}.\nabla\frac{\partial \rho_\theta}{\partial z} = 0 \tag{4.14}$$

where $\vec{v}$ is the three dimensional velocity vector. The combination of Eqs. 4.8, 4.9, 4.10 and 4.14 yields:

$$\frac{dq}{dt} = \frac{g}{\rho_o^2}J[\rho_\theta, E] \tag{4.15}$$

where J is the Jacobian operator and q, the potential vorticity, is defined as:

$$q = \frac{f}{\rho_o}\frac{\partial \rho_\theta}{\partial z} \tag{4.16}$$

Equation 4.15, using Eq. 4.10b, can also be rewritten as:

$$\frac{dq}{dt} = -\frac{g}{\rho_o^2}J[\rho_\theta, \rho] \tag{4.17}$$

By adding the extra term on the RHS of the hydrostatic equation (Eq. 4.10), the potential vorticity is not exactly conserved. If the compressional effects are small or if the potential isopycnals are nearly parallel to the *in situ* isopycnals then Eq. 4.17 becomes:

$$\frac{dq}{dt} \approx 0 \tag{4.18}$$

The Bernoulli function, B, is defined as:

$$B = p + \rho_\theta g z \tag{4.19}$$

Under steady state conditions and using Eqs. 4.8, 4.10 and 4.13, the following equation for the conservation of the Bernoulli function (Eq. 4.18) is obtained :

$$\frac{dB}{dt} = \vec{v}.\nabla B = Ewg \tag{4.20}$$

or, using Eq. 4.13, as:

$$\frac{dB}{dt} = -\frac{g}{f}\frac{\rho_\theta - \rho}{\rho_o}\frac{1}{\partial\rho_\theta/\partial z}J[p,\rho_\theta] \tag{4.21}$$

under the assumptions that the compressional effects are small or the vertical velocity is small, Eqs. 4.20 and 4.21can be rewritten as:

$$\frac{dB}{dt} = \vec{v}.\nabla B \approx 0 \tag{4.22}$$

Notice that the Bernoulli function is not uniquely defined and any *pseudo*-Bernoulli function (Eq. 4.23) is also conserved (because of Eqs. 4.18 and 4.22),

$$B_{pseudo} = F(q, B, \rho_\theta) \tag{4.23}$$

where F can be any function.

All inverse techniques encounter the problem of determining either the surface pressure field or the reference level velocities, and hence so does the Bernoulli method. However, it will be shown that, because of the conservation of the potential density, potential vorticity and Bernoulli function on a streamline, the Bernoulli function may be evaluated. Once the Bernoulli function is known, the surface pressure field can be evaluated (see Eq. 4.19) which because of geostrophy allows for the determination of the velocity field.

a)

b)

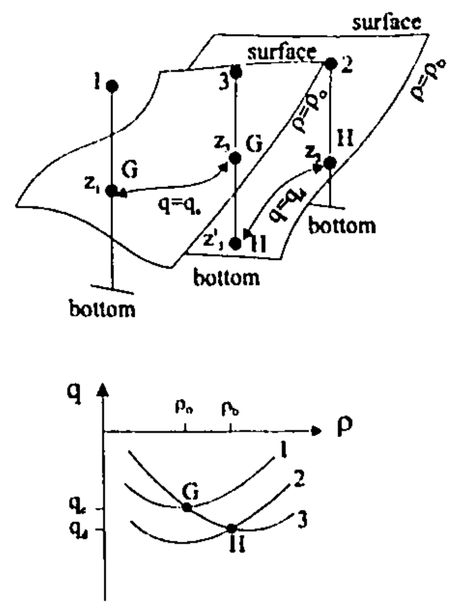

Figure 4.1: a) A schematic representation of 3 stations with 2 isopycnal surfaces and b) the potential density-potential vorticity diagram.

The vertical derivative of the Bernoulli function (Eq. 4.24) is used in this method rather than Eq. 4.19:

$$\frac{\partial B}{\partial z} = zg\frac{\partial \rho_\theta}{\partial z} + Eg \qquad (4.24)$$

The integrated form of Eq. 4.24 is:

$$B_n = \tilde{B}_n + g\int_0^z z(d\rho_n/dz)dz + g\int_0^z E\,dz \qquad (4.25)$$

where n is the station number (gridpoint location) and ρ_n is the potential densiy at station n. B_n can be evaluated at all depths save for an unknown additive constant B_n which is the surface pressure at the gridpoint location. In the Bernoulli method, the problem consists of finding a way to evaluate these surface pressure values. The procedure is the following: if, for a pair of stations n and m (e.g. 1 and 3 on Fig. 4.1), the same values for q and ρ are found at two depths z_n and z_m (e.g. z_1 for station 1 and z_3 for station 3 on Fig. 4.1a), then a crossing is found and the values of the Bernoulli function B_n and B_m (e.g. B_1 and B_3) are the same at these depths (a consequence of Eq. 4.22). Equation 4.26 can then be obtained:

$$\begin{aligned}&\left(\bar{B}_n + g\int_0^{z_n} z\left(d\rho_n/dz\right)dz + g\int_0^{z_n} E\,dz\right) - \\ &\left(\bar{B}_m + g\int_0^{z_m} z\left(d\rho_m/dz\right)dz + g\int_0^{z_m} E\,dz\right) = 0\end{aligned} \tag{4.26}$$

where z_n and z_m are evaluated from the vertical profiles of q and ρ. Equation 4.26 can be rewritten as:

$$\begin{aligned}\bar{B}_n - \bar{B}_m = &+g\int_0^{z_m} z\left(d\rho_m/dz\right)dz - g\int_0^{z_n} z\left(d\rho_n/dz\right)dz \\ &+ g\int_0^{z_m} E\,dz - g\int_0^{z_n} E\,dz\end{aligned} \tag{4.27}$$

In this analysis, the author follows Killworth (1986) and the correction term (E) is set to zero in Eq. 4.23. Taking all pairs of stations, a linear system of equations is obtained for which the complete determination of the Bernoulli function leads to an overdetermined problem. This is solved by either singular value decomposition or through a least-squares error solution. It should be noted that the introduction of the Bernoulli function replaces the determination of the reference velocities. This technique is less accurate in homogeneous water conditions such as may occur in winter.

4.4 Results

In order to apply the Bernoulli method, the whole domain was subdivided into 80 sub-regions because of the large numbers of equations which had to be solved. For example, the maximum number of unknowns in each subregion was 124 (this correponds to a sub-region where there are no land gridpoints) and the maximum number of equations was nearly 35,000. It was empirically observed that the number of equations was roughly proportionnal to the square of the number of unknowns. The summer currents obtained from the Bernoulli method are shown in Fig. 4.2 and those derived using a level of no-motion at 1200m and at the bottom of the ocean are presented in Figs. 4.3 and 4.4, respectively.

The Bernoulli method currents at all levels are weaker and noiser than those from the level of no-motion method. According to the Bernoulli calculation, in the southern section of the domain, the top 250m of the ocean flows northward near 40°W and then eastward near 52°N (Fig. 4.2a). Below this depth, the currents flow in an opposite direction (Figs. 4.2b,c and d). A similar structure is obtained using a 1200m level of no motion although the current reversal occurs in deeper waters (Figs. 4.3b and c) whereas the bottom level of no motion results did not show any current reversal (Figs. 4.4 a,b and c). Although the surface current field (Fig. 4.2a), derived from the Bernoulli method, is reasonable (see Fig. 6.9a), the vertical current structure is thought to be highly suspicious as currents changed direction twice at ~100m and at ~2100m. The surface (Fig. 4.2a) and deep (Fig. 4.2d) currents flow cyclonically, while the intermediate currents (Figs. 4.2b and c) flow anticyclonically around the Labrador Sea. Notice that a current direction reversal is also obtained in the results derived with a bottom level of no-motion (Fig. 4.4c). The vertical current structure from the Bernoulli method contradicts the description of the circulation in the Labrador Sea presented in section 1.2.

This highly baroclinic structure is very unlikely as small potential density differences between the surface and bottom can be found in the summer results (see Figs. 3.6a and 3.9a). In the northwestern Atlantic Ocean, although the T-S characteristics are distinct, the fresher water masses are compensated by colder temperature, and saltier water masses are compensated by warmer temperature such that the density differences are not large. Under nearly homogeneous conditions Killworth and Bigg (1988) found that the Bernoulli method was less accurate than the other inverse methods compared in their analysis. In practice, under such conditions it is more difficult to evaluate an accurate value for the vertical intersection z_n used in Eqs. 4.22 and 4.23. The large number of equations that need to be solved, for so few unknowns, could also be responsible for the poor Bernoulli method results. Although the number of equations was already reduced, by imposing the criterion that the vertical intersection (z_n) from both the potential density and potential vorticity should not be different by more than 0.5m and by breaking the domain into 80 subregions, this number needed to be reduced still further. Perhaps another way of reducing the number of equations is be to verify, for each crossing, whether or not salinity and potential temperature are conserved; if not then the crossing should not be used.

The potential vorticity equation (Eq. 4.16) used in the Bernoulli method is a simplification of Eq. 4.28 (see Eq. 2.5.9 of Pedlosky, 1979):

$$q = \frac{2\Omega + \nabla \times \vec{v}}{\rho_o} . \nabla \rho_\theta \tag{4.28}$$

where $\nabla\times$ is the curl operator and Ω is the planetary angular velocity. After neglecting the terms from the scalar product of the horizontal components, Eq. 4.28 is rewritten as:

$$q = \frac{1}{\rho_o}\left[f + \left(\frac{\partial v}{\partial x} - \frac{\partial u}{\partial y}\right)\right]\frac{\partial \rho_\theta}{\partial z} \tag{4.29}$$

Neglecting the relative vorticity term in Eq. 4.29 was shown to be valid through the estimation of this quantity using the Mellor *et al* (1982) diagnosed current fields (see chapters 5 and 6). It was found that the relative vorticity was one or two orders of magnitude smaller than the planetary vorticity. Consequently, Eq. 4.16 is valid and neglecting the relative vorticity contribution to the total vorticity was not responsible for the poor results of the Bernoulli method. Although the E term in Eq. 4.27 was neglected, this is probably not the reason which explains why the Bernoulli method fails. The poor Bernoulli method results are more likely due to the approximate equivalent barotropy of the currents in the region of interest.

In this chapter, the summer circulation was estimated using level of no motion calculations and the Bernoulli method. Although the surface current fields obtained through the use of a level of no motion look reasonable, the transport associated with it is too weak as the cyclonic circulation in the Labrador Sea is found only in near surface waters. As the Bernoulli did not give better results, for the reasons mentioned earlier, another more reliable method is needed for estimating the circulation and transport in the northwestern Atlantic Ocean. This method will be introduced in the next section.

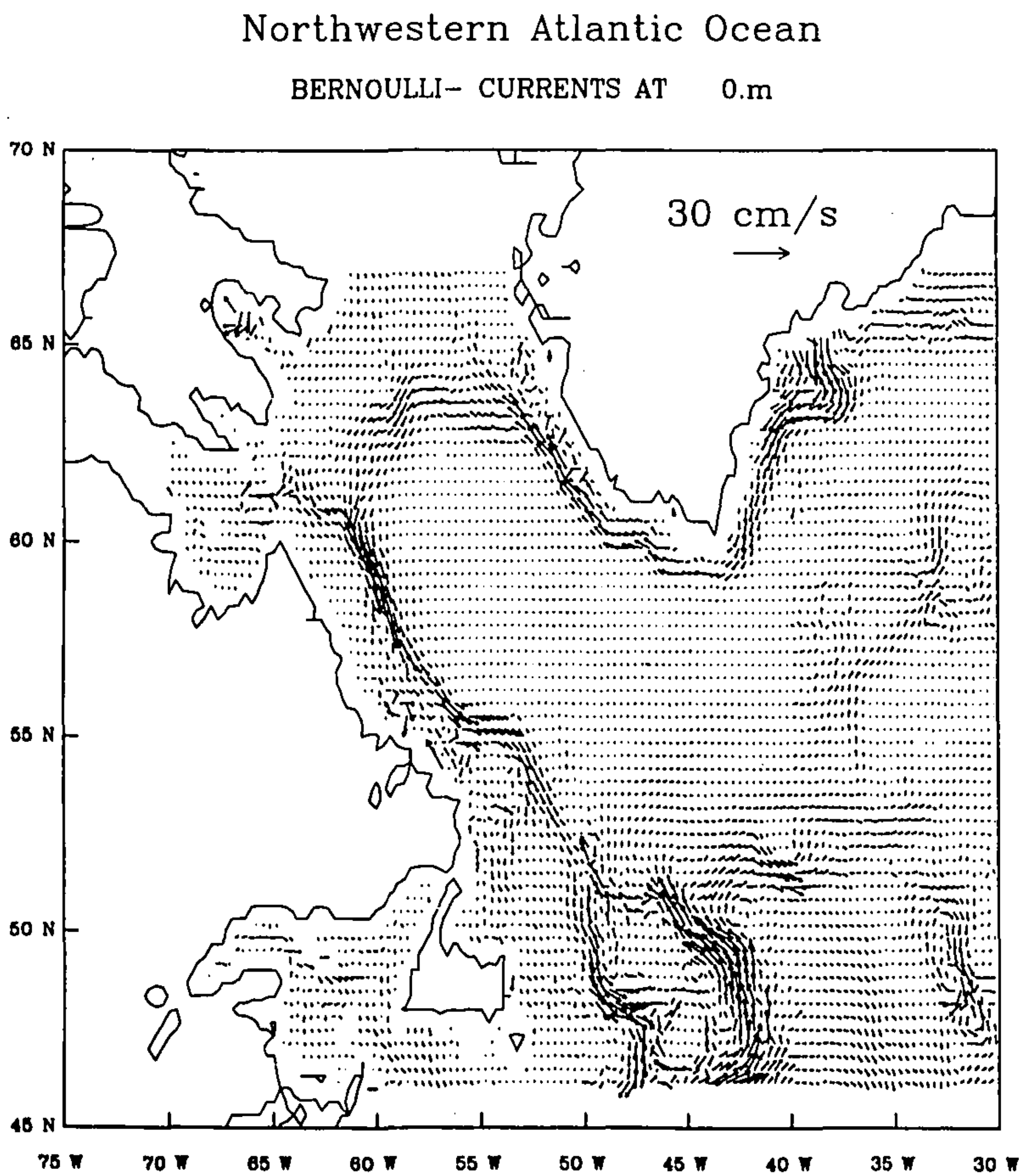

Figure 4.2: Northwestern Atlantic Ocean horizontal currents for summer (1910-89), derived using the Bernoulli method, at a) 0m,

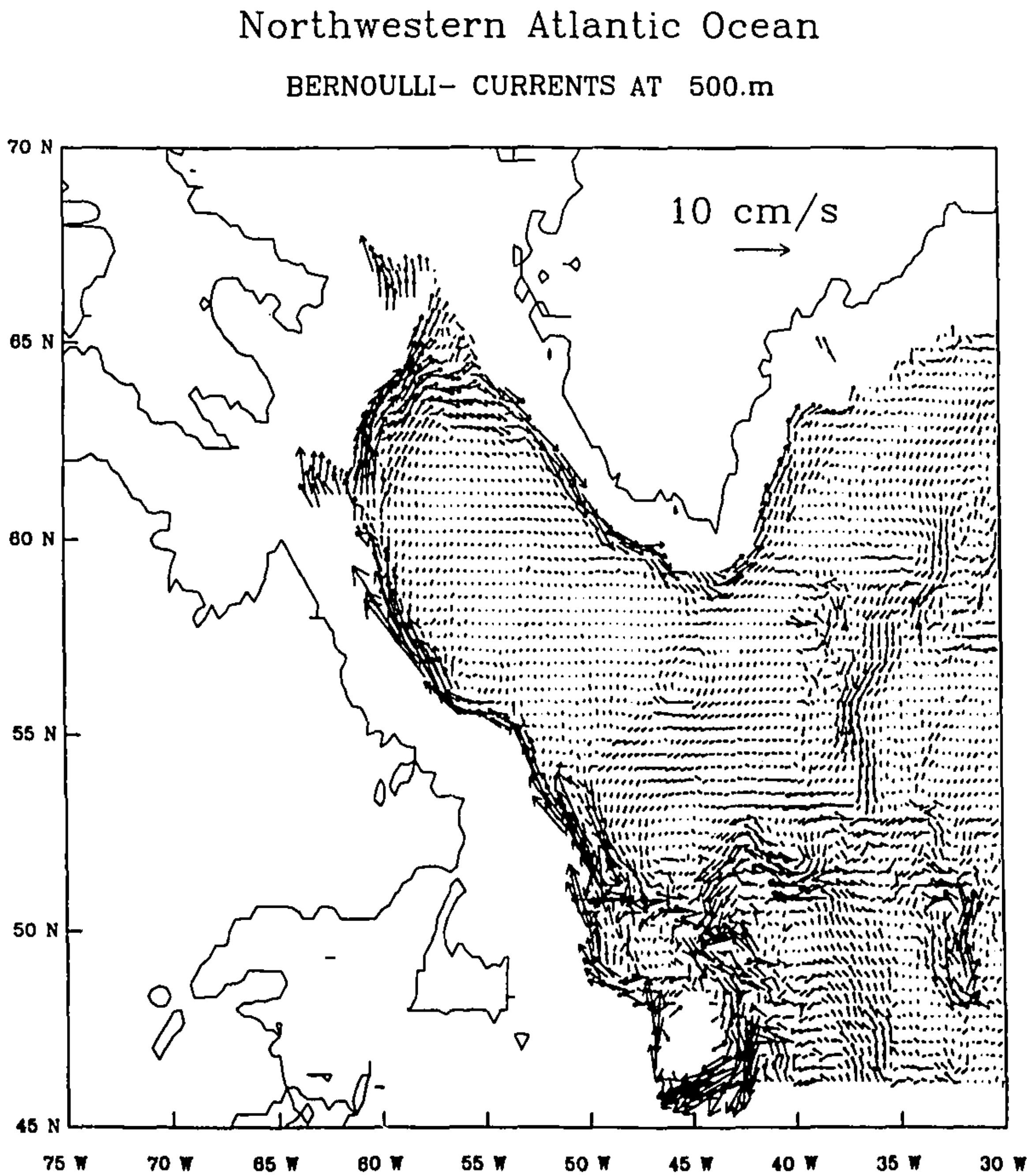

Figure 4.2 cont: b) 500m,

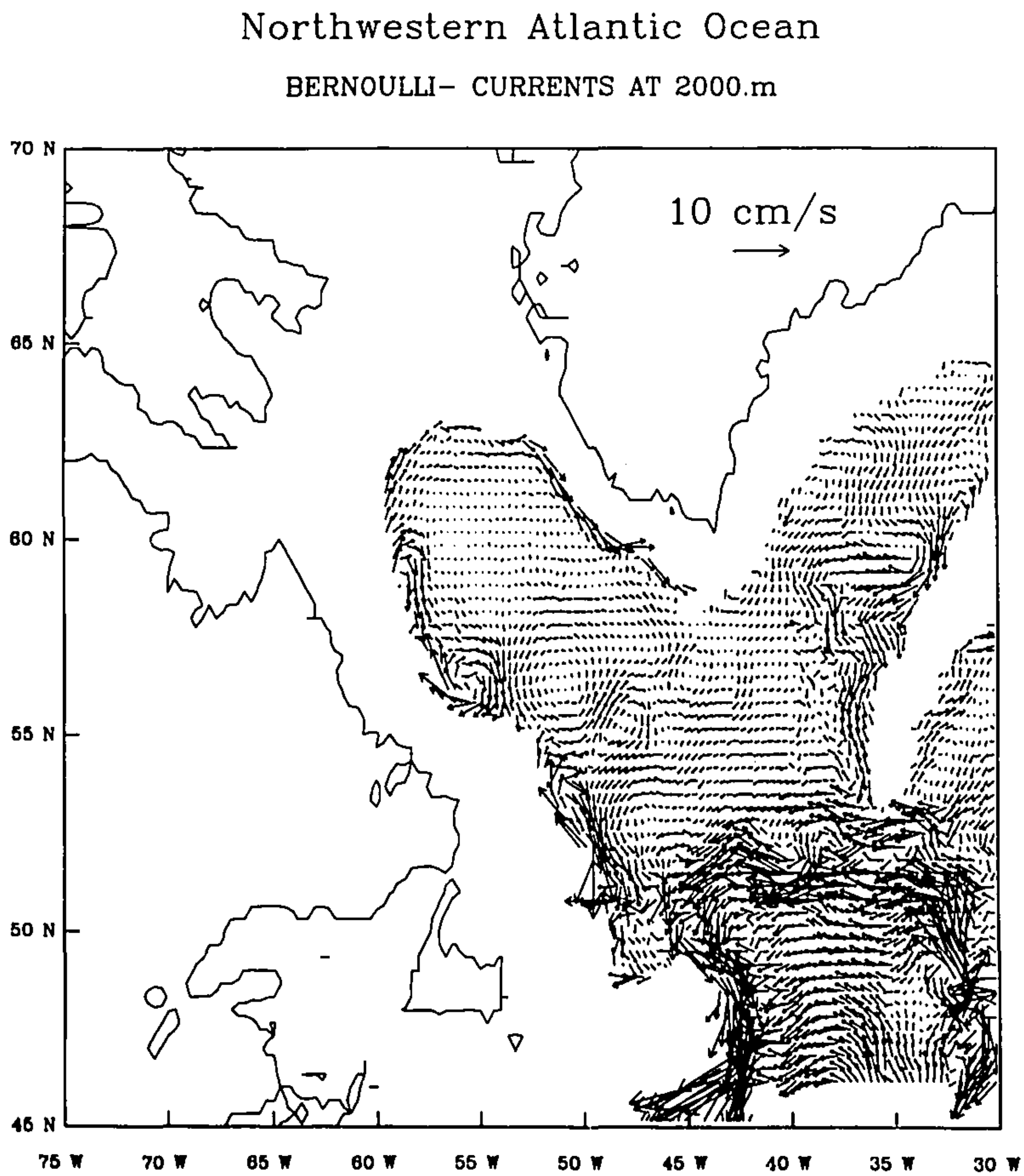

Figure 4.2 cont: c) 2000m,

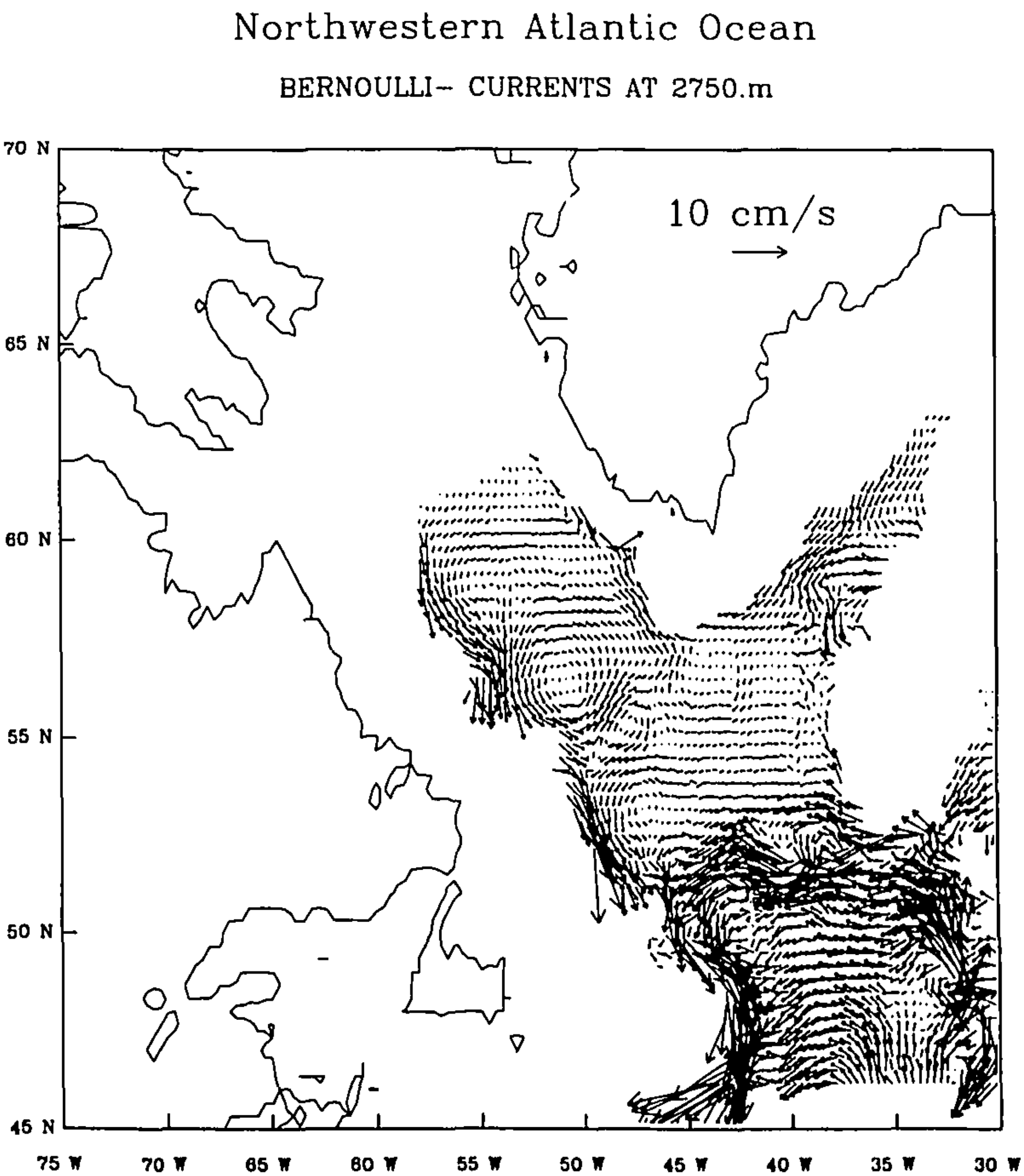

Figure 4.2 cont: and d) 2750m.

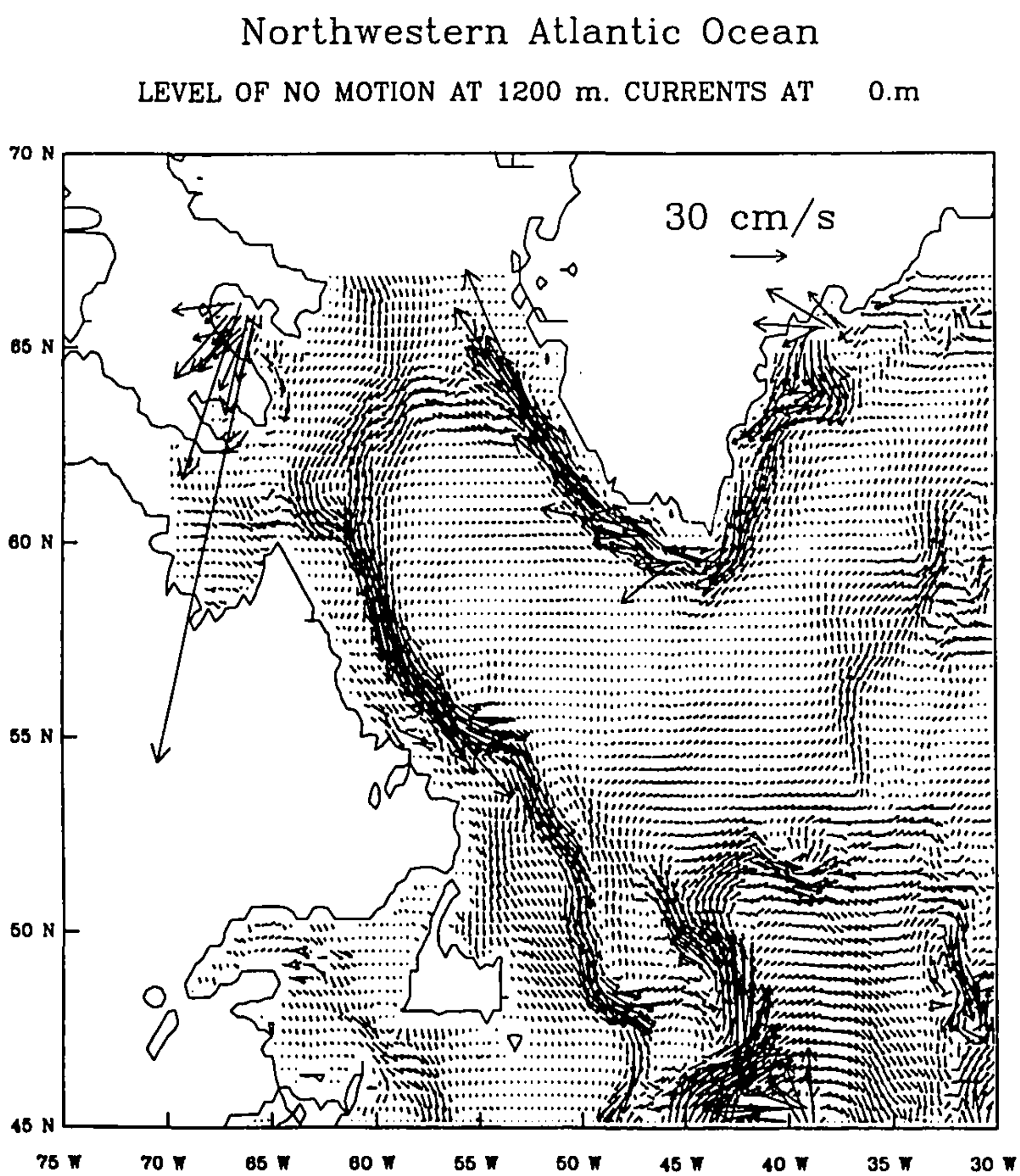

Figure 4.3: Northwestern Atlantic Ocean horizontal currents for summer (1910-89), derived using a level of no motion at 1200m, at a) 0m,

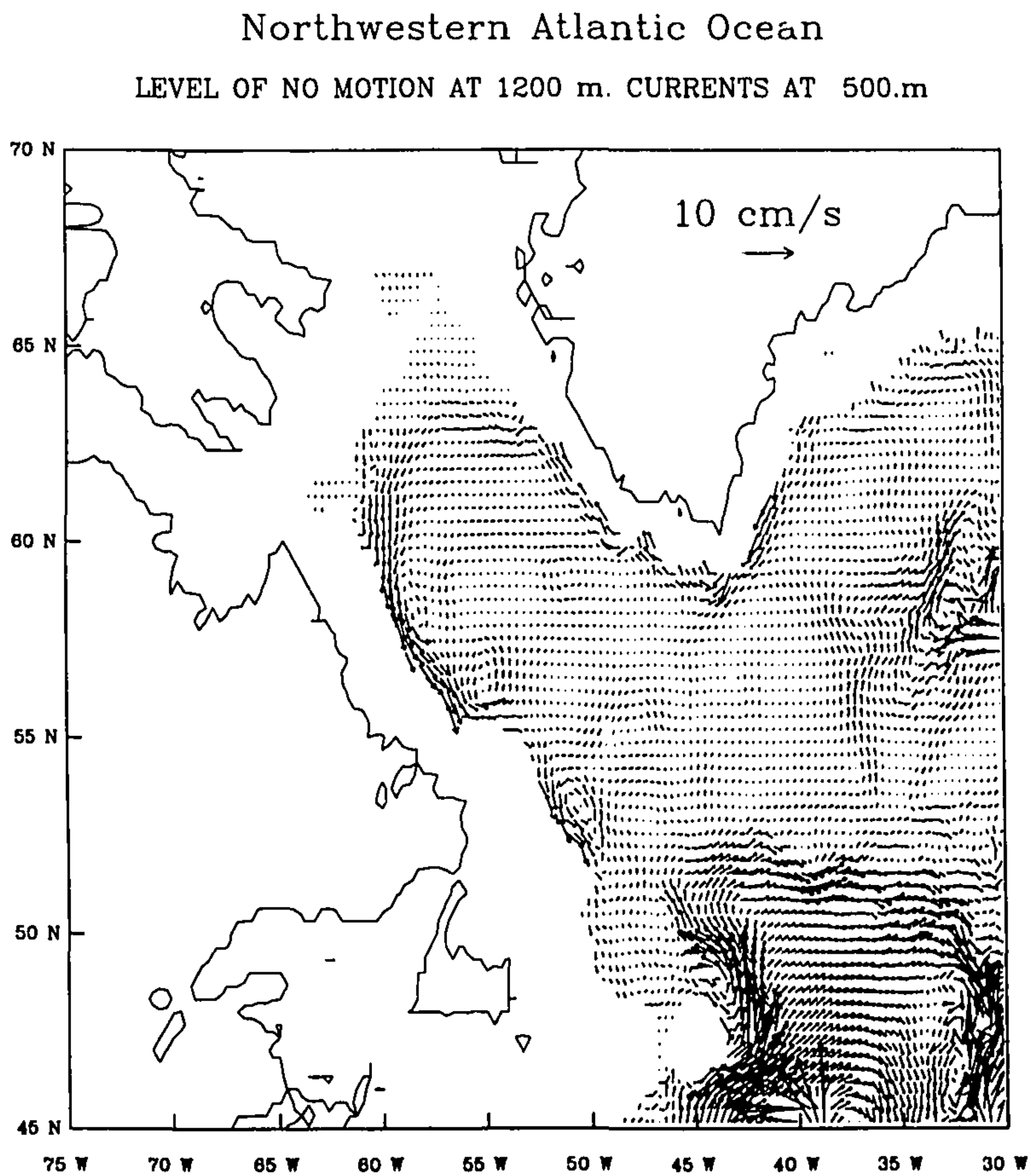

Figure 4.3 cont: b) 500m,

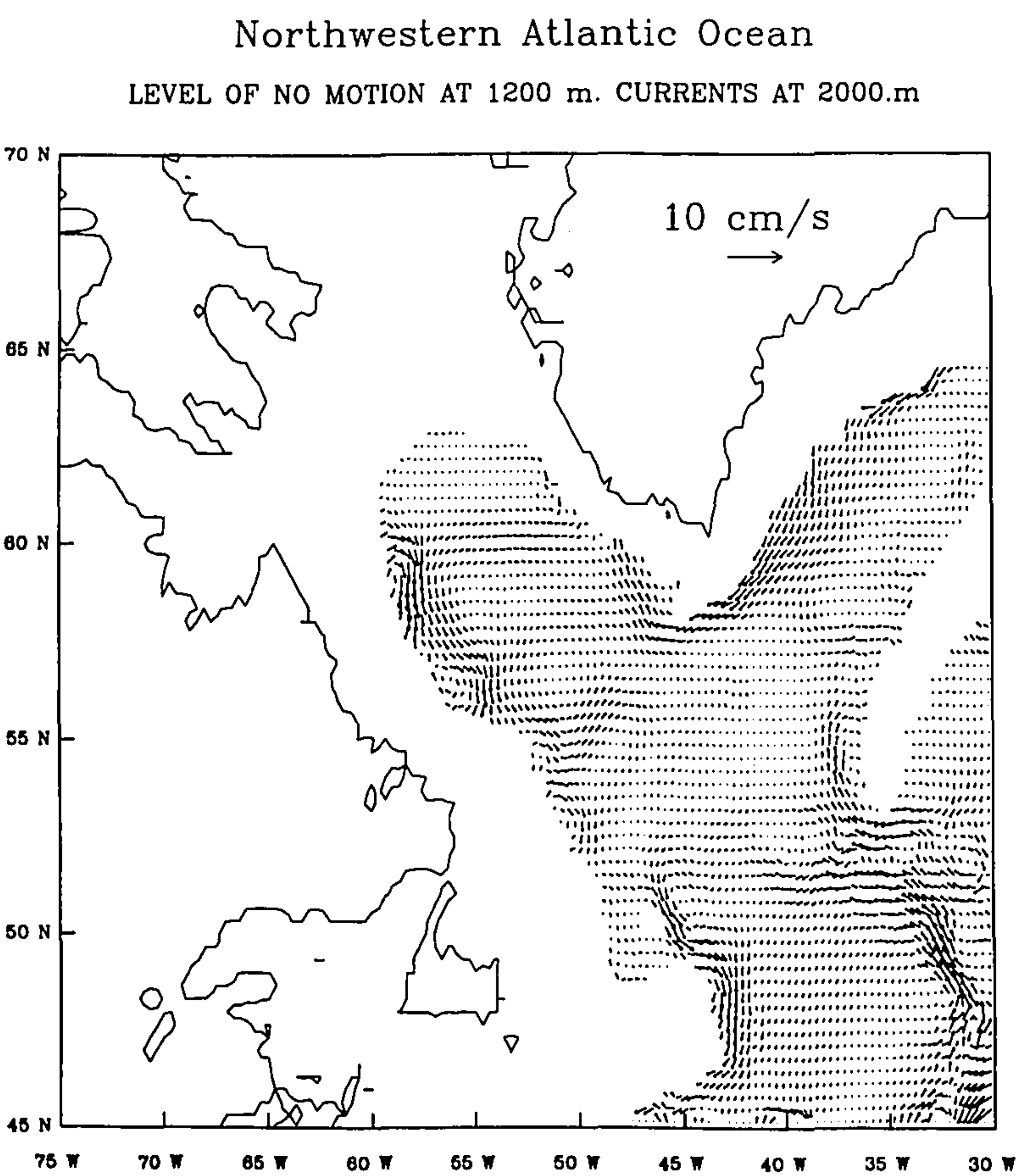

Figure 4.3 cont: and c) 2000m.

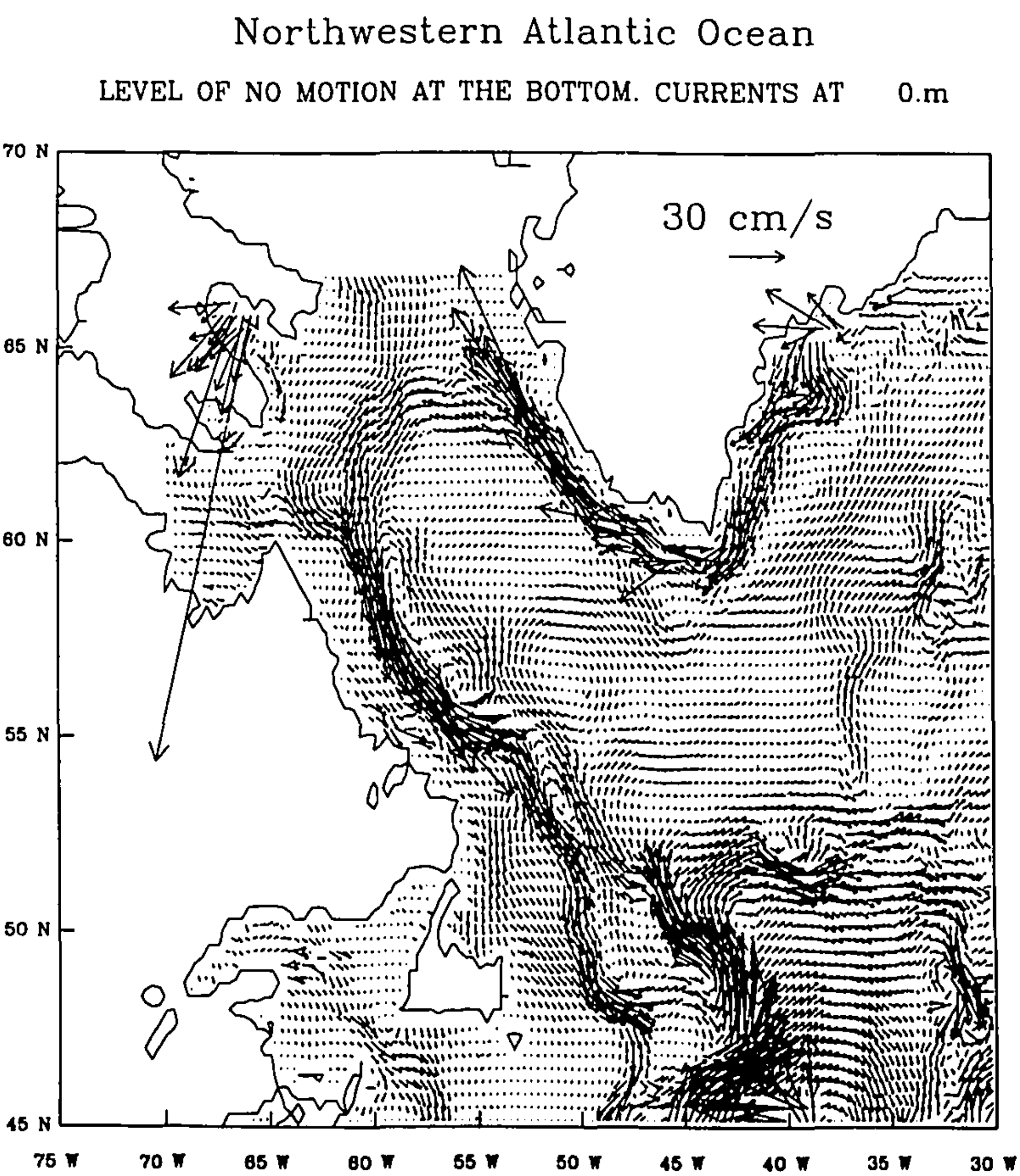

Figure 4.4: Northwestern Atlantic Ocean horizontal currents for summer (1910-89), derived using a level of no motion at the bottom, at a) 0m,

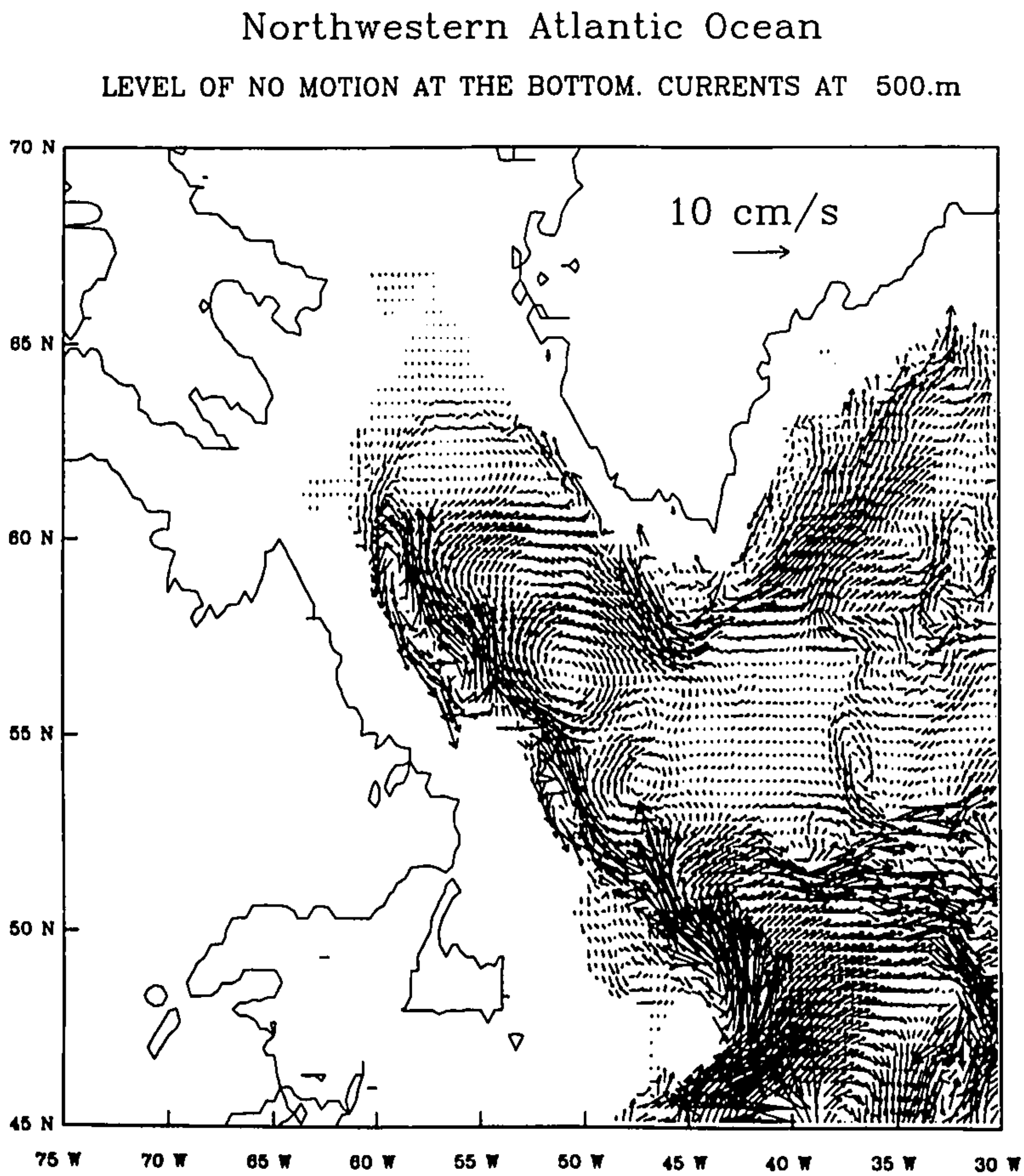

Figure 4.4 cont: b) 500m,

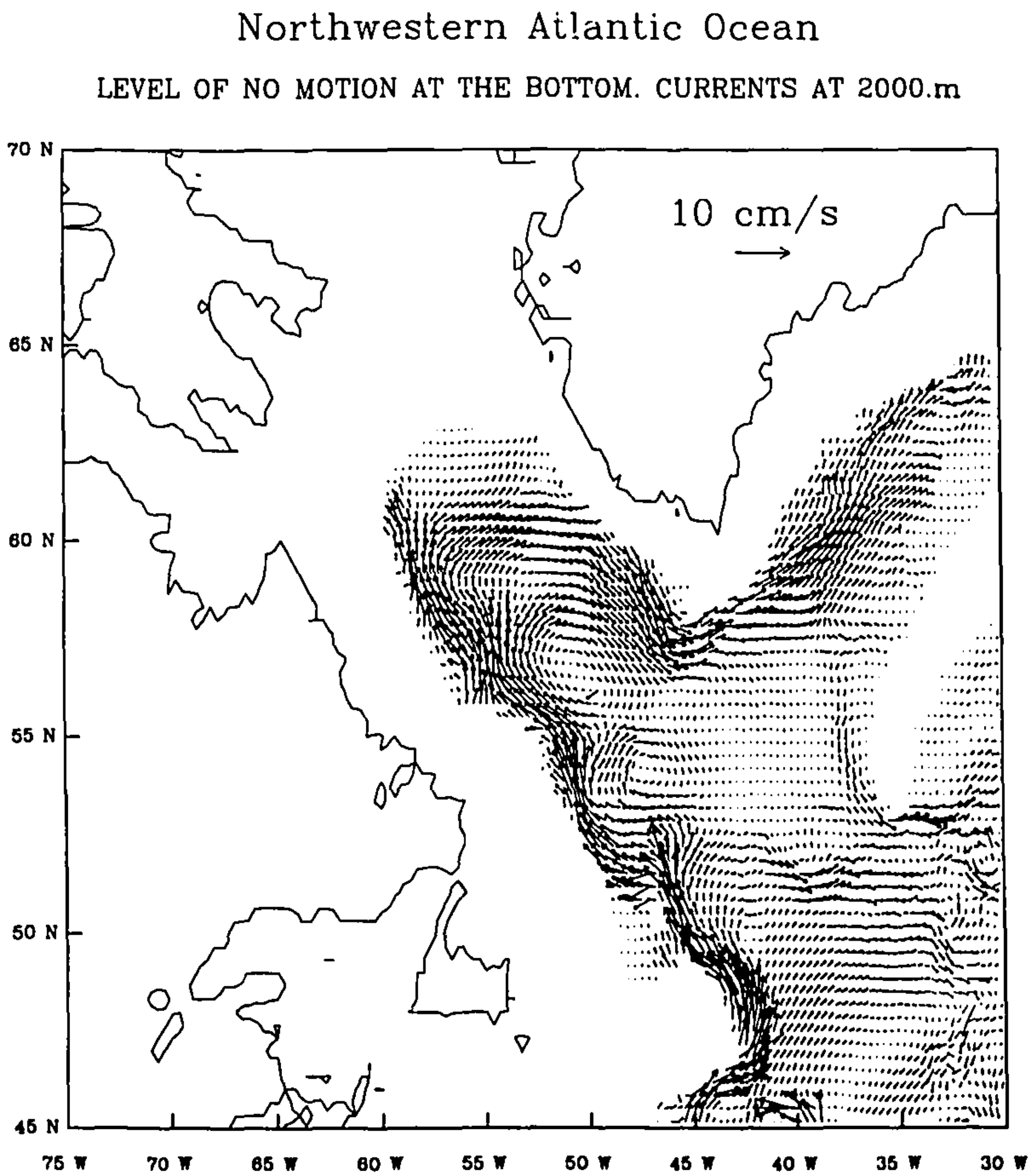

Figure 4.4 cont: and c) 2000m.

CHAPTER 5: THE MELLOR *et al* (1982) METHOD

5.1 The governing equations

Mellor, Mechoso and Keto (1982) successfully used a dynamical method to describe the general circulation in the Atlantic Ocean. The same method, which takes explicit account of the JEBAR, was later used by Greatbatch *et al.* (1991) to study the interpentadal changes of the North Atlantic circulation. In this chapter, this method is described in detail. The time-averaged governing equations used for small Rossby number, frictionless, flow are the horizontal momentum equations under the Boussinesq approximation, the hydrostatic approximation and the equation of continuity, which in spherical coordinates are:

$$-fv = -\frac{m}{\rho_0 R}\frac{\partial P}{\partial \lambda} + \frac{\partial \tau_{z\lambda}}{\partial z} \tag{5.1a}$$

$$fu = -\frac{1}{\rho_0 R}\frac{\partial P}{\partial \phi} + \frac{\partial \tau_{z\phi}}{\partial z} \tag{5.1b}$$

$$\rho g = -\frac{\partial P}{\partial z} \tag{5.1c}$$

$$\frac{m}{R}\frac{\partial u}{\partial \lambda} + \frac{m}{R}\frac{\partial}{\partial \phi}\left(\frac{v}{m}\right) + \frac{\partial w}{\partial z} = 0 \tag{5.1d}$$

where u, v, w, p, ρ, ρ_o, $\rho_o\tau_z$, R, m, f are, respectively, the eastward velocity, northward velocity, vertical velocity, pressure, *in situ* density, Boussinesq reference density, vertical

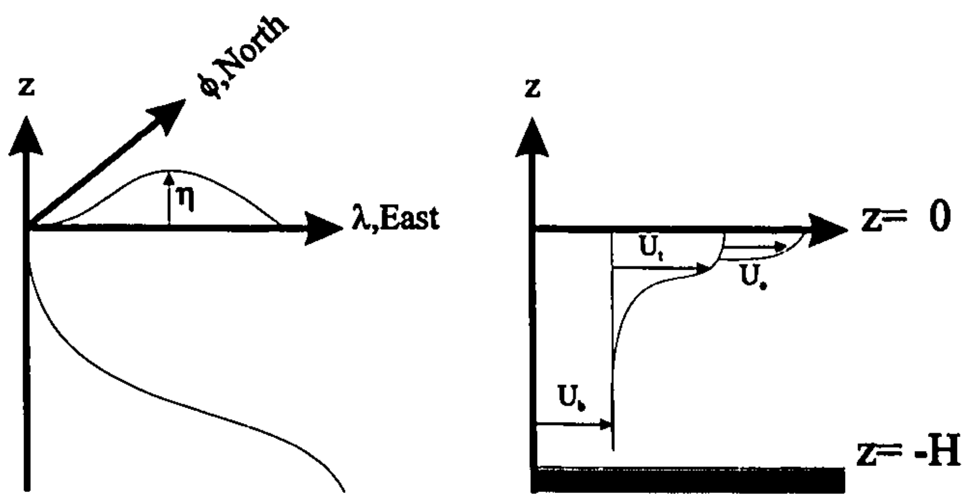

a) b)

Figure 5.1: Schematic diagrams a) of the coordinates used and b) of the three components of the horizontal velocity (redrawn from Mellor *et al* ,1982).

component of Reynolds' stress, Earth's radius, $1/\cos\phi$ (ϕ is the latitude) and the Coriolis parameter. The pressure is obtained by integrating the hydrostatic equation (Eq. 5.1c):

$$P(\lambda,\phi,z) = \rho_0 g \eta(\lambda,\phi,z) + \int_z^0 \rho(\lambda,\phi,z) g\,dz \qquad (5.2)$$

where η is the surface elevation (Fig. 5.1a). The pressure is then substituted into the momentum equations (Eqs. 5.1a and b):

$$-fv = -\frac{m}{R}\left[g\frac{\partial\eta}{\partial\lambda} + \frac{\partial}{\partial\lambda}\frac{1}{\rho_0}\int_z^0 \rho g\,dz\right] + \frac{\partial\tau_{z\lambda}}{\partial z} \qquad (5.3a)$$

$$fu = -\frac{1}{R}\left[g\frac{\partial\eta}{\partial\phi} + \frac{\partial}{\partial\phi}\frac{1}{\rho_0}\int_z^0 \rho g\,dz\right] + \frac{\partial\tau_{z\phi}}{\partial z} \qquad (5.3b)$$

The integral terms of Eqs. 5.3 can be split according to:

$$\int_z^0 f\,dz = \int_{-H}^0 f\,dz - \int_{-H}^z f\,dz$$

and hence the momentum equations can be rewritten as:

$$\begin{aligned}
-fv &= -\frac{m}{R}\left[g\frac{\partial\eta}{\partial\lambda} + \frac{\partial}{\partial\lambda}\frac{1}{\rho_0}\int_{-H}^0 \rho g\,dz\right] + \frac{m}{R}\frac{\partial}{\partial\lambda}\frac{1}{\rho_0}\int_{-H}^z \rho g\,dz + \frac{\partial\tau_{z\lambda}}{\partial z} \\
fu &= -\frac{1}{R}\left[g\frac{\partial\eta}{\partial\phi} + \frac{\partial}{\partial\phi}\frac{1}{\rho_0}\int_{-H}^0 \rho g\,dz\right] + \frac{1}{R}\frac{\partial}{\partial\phi}\frac{1}{\rho_0}\int_{-H}^z \rho g\,dz + \frac{\partial\tau_{z\phi}}{\partial z}
\end{aligned} \tag{5.4}$$

Leibnitz's theorem (Eq. 1.11) is then applied on the second and third terms of the right hand side of Eq. 5.4 which are then rewritten as:

$$\begin{aligned}
-fv &= -\frac{m}{R}\left[g\frac{\partial\eta}{\partial\lambda} + \int_{-H}^0 \frac{\partial}{\partial\lambda}\left(\frac{\rho g}{\rho_0}\right)dz\right] + \frac{m}{R}\int_{-H}^z \frac{\partial}{\partial\lambda}\left(\frac{\rho g}{\rho_0}\right)dz + \frac{\partial\tau_{z\lambda}}{\partial z} \\
fu &= -\frac{1}{R}\left[g\frac{\partial\eta}{\partial\phi} + \int_{-H}^0 \frac{\partial}{\partial\phi}\left(\frac{\rho g}{\rho_0}\right)dz\right] + \frac{1}{R}\int_{-H}^z \frac{\partial}{\partial\phi}\left(\frac{\rho g}{\rho_0}\right)dz + \frac{\partial\tau_{z\phi}}{\partial z}
\end{aligned} \tag{5.5}$$

The density is written as:

$$\rho(\lambda,\phi,z) = \rho_r(z) + \rho'(\lambda,\phi,z) \tag{5.6}$$

where $\rho_r(z)$ is the horizontally-averaged density at each depth and ρ' is the perturbation density. Equation 5.6 is then substituted into Eqs. 5.5 to get:

$$\begin{aligned}
-fv &= -\frac{m}{R}\left[g\frac{\partial\eta}{\partial\lambda} + \int_{-H}^0 \frac{\partial b}{\partial\lambda}dz\right] + \frac{m}{R}\int_{-H}^z \frac{\partial b}{\partial\lambda}dz' + \frac{\partial\tau_{z\lambda}}{\partial z} \\
fu &= -\frac{1}{R}\left[g\frac{\partial\eta}{\partial\phi} + \int_{-H}^0 \frac{\partial b}{\partial\phi}dz\right] + \frac{1}{R}\int_{-H}^z \frac{\partial b}{\partial\phi}dz' + \frac{\partial\tau_{z\phi}}{\partial z}
\end{aligned} \tag{5.7}$$

where the buoyancy (b) is defined as:

$$b \equiv g\,\frac{(\rho - \rho_r)}{\rho_0} \tag{5.8}$$

The equations for the depth-integrated flow are obtained by vertically integrating Eqs. 5.7:

$$-fV = -\frac{mH}{R}\left[g\frac{\partial\eta}{\partial\lambda} + \int_{-H}^{0}\frac{\partial b}{\partial\lambda}dz\right] + \frac{m}{R}\int_{-H}^{0}\int_{-H}^{z}\frac{\partial b}{\partial\lambda}dz'dz + \tau_{0\lambda} \tag{5.9a}$$

$$fU = -\frac{H}{R}\left[g\frac{\partial\eta}{\partial\phi} + \int_{-H}^{0}\frac{\partial b}{\partial\phi}dz\right] + \frac{1}{R}\int_{-H}^{0}\int_{-H}^{z}\frac{\partial b}{\partial\phi}dz'dz + \tau_{0\phi} \tag{5.9b}$$

where $\rho_o(\tau_{0\lambda}, \tau_{0\phi})$ are the eastward and northward component of the wind stress respectively, and U and V are the depth integrated eastward and northward velocity components, defined by:

$$\mathbf{V} = \int_{-H}^{0} \vec{v}\, dz$$

Notice that, in the Eqs. 5.9, the author followed Mellor *et al.* (1982) and the bottom stress was set equal to zero (bottom friction can play a role in shallow regions but is not important for shaping the main features of the circulation which will be discussed in chapter 6; de Young and Greatbatch, personal communication). Using the Leibnitz's theorem (Eq. 1.12) and Eq. 5.10,

$$\int_{-H}^{0}\int_{-H}^{z} b\,dz'dz = -\int_{-H}^{0} z\,b\,dz \tag{5.10}$$

the depth integrated momentum equations (Eqs. 5.9) can be rewritten as:

$$-fV = -\frac{mH}{R}\frac{\partial}{\partial\lambda}\left[g\eta + \int_{-H}^{0} b\,dz\right] - \frac{m}{R}\frac{\partial}{\partial\lambda}\int_{-H}^{0} z\,b\,dz + \tau_{0\lambda} \tag{5.11a}$$

$$fU = -\frac{H}{R}\frac{\partial}{\partial\phi}\left[g\eta + \int_{-H}^{0} b\,dz\right] - \frac{1}{R}\frac{\partial}{\partial\phi}\int_{-H}^{0} z\,b\,dz + \tau_{0\phi} \tag{5.11b}$$

The kinematic bottom pressure and the potential energy are defined respectively as:

$$P_b \equiv g\eta + \int_{-H}^{0} b\,dz \tag{5.12}$$

$$\Phi \equiv \int_{-H}^{0} z\,b\,dz \tag{5.13}$$

which, once substituted into Eqs. 5.11, leads to:

$$f[U,V] = \left[-\frac{1}{R}\frac{\partial\Phi}{\partial\phi} - \frac{H}{R}\frac{\partial P_b}{\partial\phi} + \tau_{0\phi},\ \frac{m}{R}\frac{\partial\Phi}{\partial\lambda} + \frac{mH}{R}\frac{\partial P_b}{\partial\lambda} - \tau_{0\lambda}\right] \tag{5.14}$$

The continuity equation (Eq. 5.1d) can be vertically integrated:

$$\frac{1}{R}\frac{\partial U}{\partial\lambda} + \frac{1}{R}\frac{\partial}{\partial\phi}\left(Vm^{-1}\right) = 0$$

and the following equation is then formed:

$$\frac{1}{R}\frac{\partial}{\partial\lambda}\left(U\frac{f}{H}\right) + \frac{1}{R}\frac{\partial}{\partial\phi}\left(Vm^{-1}\frac{f}{H}\right) = \frac{U}{R}\frac{\partial}{\partial\lambda}\left(\frac{f}{H}\right) + \frac{Vm^{-1}}{R}\frac{\partial}{\partial\phi}\left(\frac{f}{H}\right) \tag{5.15}$$

Equation 5.16a is obtained by substituing Eqs. 5.14 into Eq. 5.15:

$$m\frac{U}{R}\frac{\partial}{\partial\lambda}\left(\frac{f}{H}\right) + \frac{V}{R}\frac{\partial}{\partial\phi}\left(\frac{f}{H}\right) = m\frac{D_1}{R^2} \tag{5.16a}$$

where D_1 is defined as:

$$D_1 = \frac{\partial \Phi}{\partial \lambda}\frac{\partial}{\partial \phi}\left(\frac{1}{H}\right) - \frac{\partial \Phi}{\partial \phi}\frac{\partial}{\partial \lambda}\left(\frac{1}{H}\right) + R\left[\frac{\partial}{\partial \lambda}\left(\frac{\tau_{0\phi}}{H}\right) - \frac{\partial}{\partial \phi}\left(\frac{\tau_{0\lambda}}{H}\right)\right] \tag{5.16b}$$

The volume transport streamfunction (ψ), defined by:

$$U \equiv \frac{1}{R}\frac{\partial \psi}{\partial \phi} \qquad V \equiv -\frac{m}{R}\frac{\partial \psi}{\partial \lambda} \tag{5.17}$$

is then substituted into Eq. 5.16a which leads to:

$$\frac{m}{R^2}\frac{\partial \psi}{\partial \phi}\frac{\partial \xi}{\partial \lambda} - \frac{m}{R^2}\frac{\partial \psi}{\partial \lambda}\frac{\partial \xi}{\partial \phi} = \frac{m}{R^2} D_1 \tag{5.18}$$

where ξ is the planetary potential vorticity (ξ=f/H). Equation 5.18 is equivalent to Eqs. 1.16 and 1.17 (see section 1.3) and shows that the cross-f/H transport is driven by two terms: the JEBAR and the wind forcing. As Mellor *et al.* (1982) found that the field defined by 5.16b is noisy, they substituted Eq. 5.19 into Eq. 5.18:

$$\chi = \psi + \frac{\Phi}{f} \tag{5.19}$$

leading to:

$$\frac{\partial\chi}{\partial\phi}\frac{\partial\xi}{\partial\lambda} - \frac{\partial\chi}{\partial\lambda}\frac{\partial\xi}{\partial\phi} = D_2 \tag{5.20}$$

$$D_2 = -\frac{\partial}{\partial\lambda}\left(\frac{\Phi}{H}\right)\frac{1}{f}\frac{\partial f}{\partial\phi} + R\left[\frac{\partial}{\partial\lambda}\left(\frac{\tau_{0\phi}}{H}\right) - \frac{\partial}{\partial\phi}\left(\frac{\tau_{0\lambda}}{mH}\right)\right] \tag{5.21}$$

By prescribing that the integration is done along ξ=f/H contours, Eq. 5.22 is obtained:

$$\boxed{d\chi = -\frac{D_2}{\left(m^2\xi_\lambda^2 + \xi_\phi^2\right)}\left(\xi_\phi d\lambda - m^2\xi_\lambda d\phi\right) \qquad (5.22)}$$

where ξ_ϕ and ξ_λ are respectively defined by $\partial\xi/\partial\phi$ and by $\partial\xi/\partial\lambda$. Equation 5.22 shows that the change in χ along an f/H contour is determined by the planetary potential vorticity field, the potential energy field and the wind stress field. The total transport is obtained by integrating Eq. 5.22 along f/H contours and then adjusting the integration constants. Mellor *et al* (1982) adjusted their constants by setting the volume transport (Ψ) equal to zero on the eastern boundary. This cannot be done in the Labrador Sea were strong currents are observed at its eastern border. Integrating eastward until the eastern Atlantic coast is not possible as high resolution temperature and salinity fields are not available further eastward. In this analysis the integrating constants were adjusted using transport values on various boundaries (35°W and 30°W, 55°N, 65°N and 45°N). These values were taken from the climatological annual mean transport of Greatbatch *et al* (1991), obtained at 1°x1° resolution using the Mellor *et al* (1982) method. A seasonal correction, calculated using wind torque only (Greatbatch and Goulding, 1989) was also added to our boundary reference values. The density field used by Greatbatch *et al* (1991) was the annual mean obtained from Levitus (1982) and the wind stress fields were those of Hellerman and Rosenstein (1983).

5.2 Determination of bottom velocities

In this section it is illustrated how the bottom velocities are estimated using the Mellor *et al* (1982) method since they will then be used as reference velocities from which the horizontal flow can be derived (as described in section 4.1). Following Fofonoff (1962) and Mellor *et al* (1982), the horizontal velocities are decomposed into three parts: bottom, thermohaline and Ekman velocities, which when vertically integrated give:

$$\mathbf{V} = \mathbf{V}_b + \mathbf{V}_t + \mathbf{V}_w \tag{5.23}$$

The depth integrated thermohaline transport is obtained by integrating vertically Eq. 4.4 with the reference level at the bottom and the reference velocity set equal to zero:

$$\mathbf{V}_t = \frac{g}{f} \int_{-H}^{0} \rho^{-1}(z) \left(\int_{-H}^{z} (\nabla\rho \times \vec{k})\, dz' \right) dz \tag{5.24}$$

The Ekman transport is a function of the wind stress and is given by:

$$\mathbf{V}_w = \frac{1}{f} (\vec{\tau} \times \vec{k}) \tag{5.25}$$

The Hellerman and Rosenstein (1983) wind stress, linearly interpolated onto a 1/3° x 1/3° grid, was used in this analysis. As the wind stress, density and the volume transport streamfunction are known from the Mellor calculation, the bottom velocities can be determined from:

$$\vec{v}_b = \frac{1}{H}\left(\mathbf{V} - \mathbf{V}_t - \mathbf{V}_w\right) \tag{5.26}$$

For the purpose of constructing the three-dimensional velocity field, it is assumed that the wind stress is homogenously distributed as a body force over a mixed layer of 50m depth.

In the next chapter, the Mellor *et al* (1982) method is applied to the summer, warm and cold season climatological mean density fields derived from the objectively analyzed T-S data sets that were discussed in chapter 3. The Mellor *et al* (1982) method is then used in chapter 7 to study the interdecadal variability of the volume transport and the circulation in the northwestern Atlantic Ocean.

CHAPTER 6: THE CIRCULATION OF THE NORTHWESTERN ATLANTIC OCEAN

6.1 The potential energy fields

As shown in the previous chapter, the volume streamfunction (Eq. 5.22) is determined from the potential energy (Eq. 5.13), the surface wind stress (Hellerman and Rosenstein, 1983), the integration path together with some reference transport values which will be discussed in the next section.

The warm and cold season reference densities (ρ_r) used for estimating the buoyancy (b, Eq. 5.8) are shown in Figs. 6.1. The warm surface reference density is ~ 1 kg m^{-3} weaker than the cold season value (Fig. 6.1a) but below 200m the two profiles are nearly identical. The mathematical expression for the potential energy (Eq. 5.13), which contains a z factor in the integral, shows that deep structures are more important than surface ones. As a consequence, suspicious deep T-S objectively analyzed values, like the S~35 psu contours in northern Labrador Sea (Figs. 3.2e and 3.11e) at 2000m in the summer and warm seasons results (due to measurements taken in July 1933), have a large effect on the potential energy. Corrected fields were then produced for the warm season analysis by removing these 1933 salinity observations from the original data set. This was done to improve the comparison with the cold season as seasonal variations in deep waters are probably not real. Although the surface densities are weighted by z~0 and so may appear to contribute weakly to the potential energy, the deep ocean contribution is also reduced by the weak horizontal density gradients which are found there.

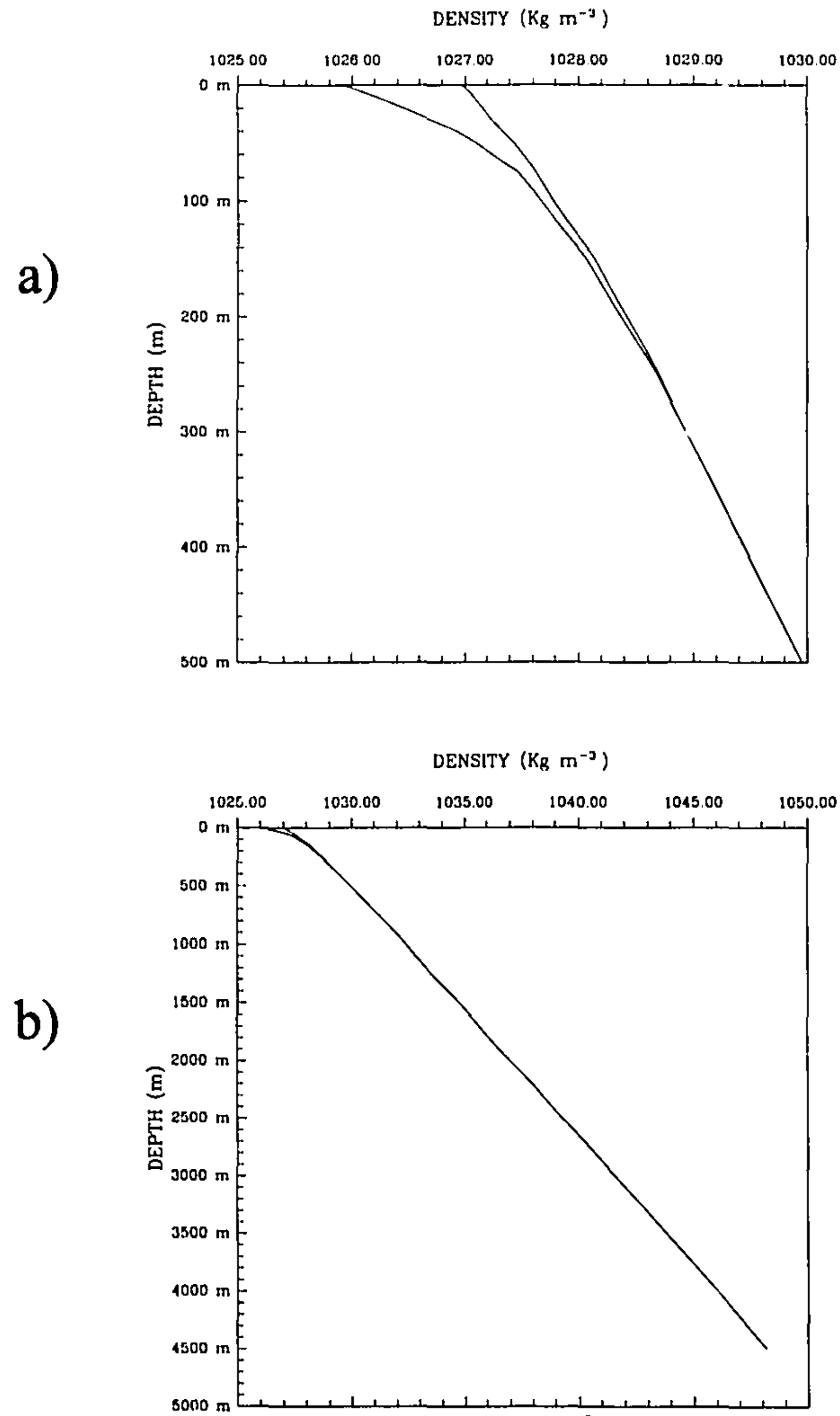

Figure 6.1: Warm and cold season reference density (kg m^{-3}) for a) the top 500m and b) the whole water column.

In order to find what section of the water column contributes the most to the potential energy, the potential energy was split according to:

$$\Phi \equiv \int_{-1500}^{0} zbdz + \int_{-2500}^{-1500} zbdz + \int_{-3500}^{-2500} zbdz + \int_{-5000}^{-3500} zbdz \qquad (6.1)$$

Each term on the right-hand-side of Eq. 6.2 is shown in Figs 6.2 and 6.3 for the warm and cold seasons respectively.

All the warm and cold season potential energy plots show that the domain is divided into two main regions: the NAC region with positive values and the LS-IS region with negative values. This horizontal sign change shows that the LS-IS waters are generally denser than the NAC region waters. The only region for which sign changes are found vertically is the Central LS region where the 1500-2500m layer has positive potential energy values in both the warm and cold seasons results (Figs. 6.2b and 6.3b). The vertical distribution of potential energy is different in the two regions: in the LS-IS region the potential energy is relatively homogeneously distributed over the whole water column whereas in the NAC region ~50% of the total potential energy is contained in the top 1500m.

Although large T-S variations were found between the cold and warm seasons in the top 1500m layer, these seasonal changes did not lead to major differences between the potential energy fields (Figs 6.2a and 6.3a) presumably because of the surface densities are less weighted in the evaluation of the potential energy. Figure 6.4 shows that in the NAC region, no seasonal

a)

b)

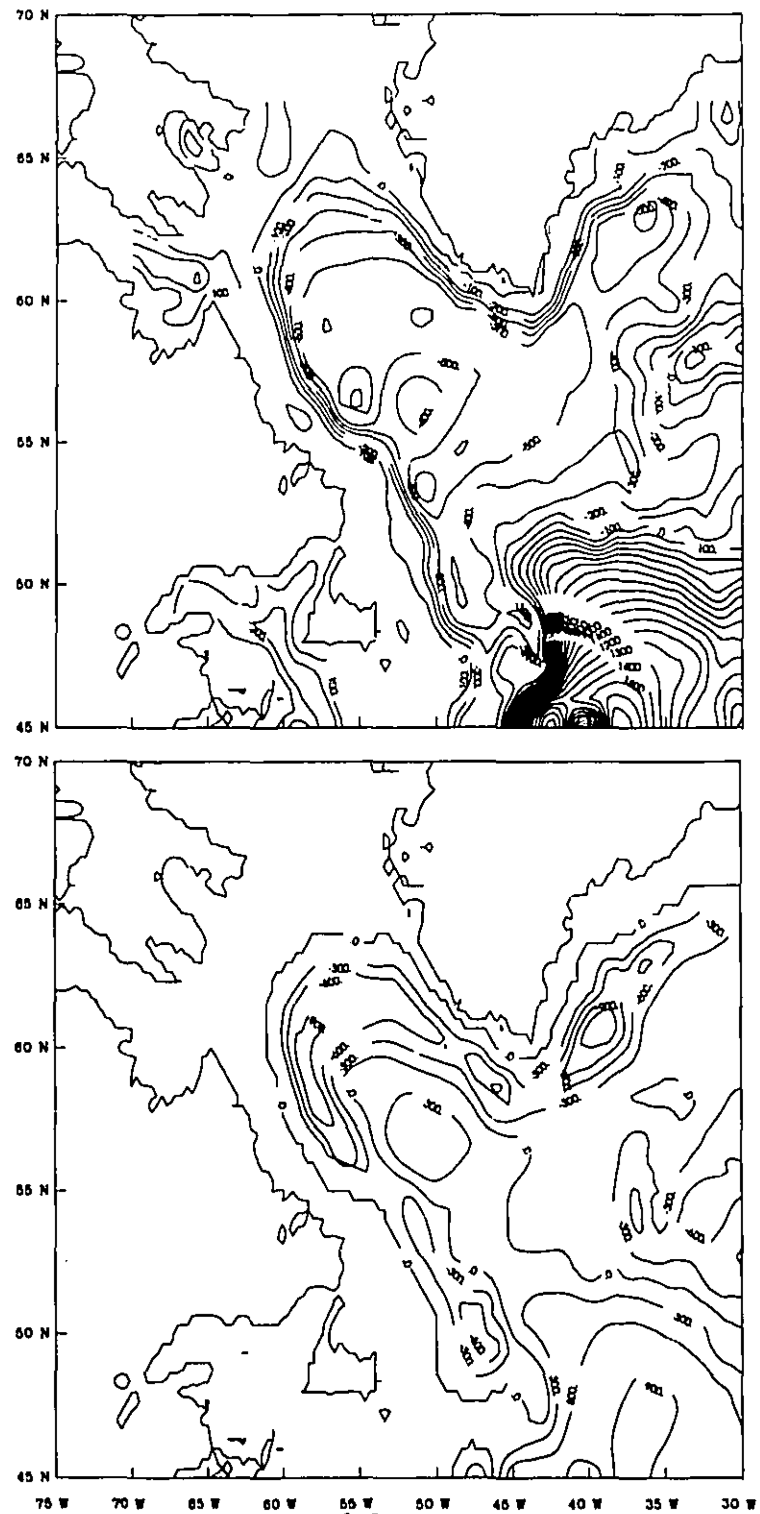

Figure 6.2: Warm season potential energy (m^3s^{-2}) between a) 0-1500m, b) 1500-2500m,

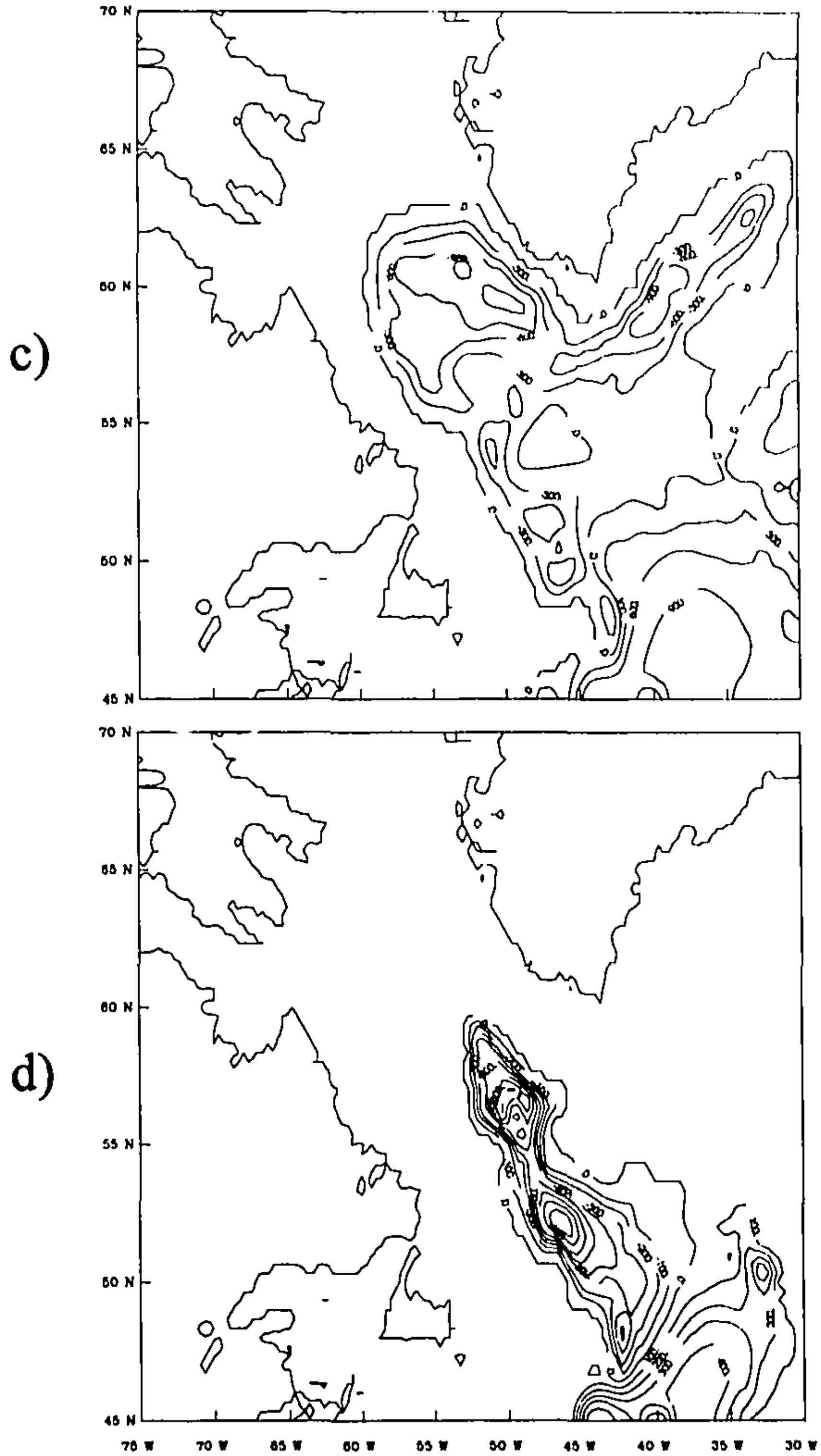

Figure 6.2 cont: c) 2500-3500m and d) 3500-5000m.

a)

b)

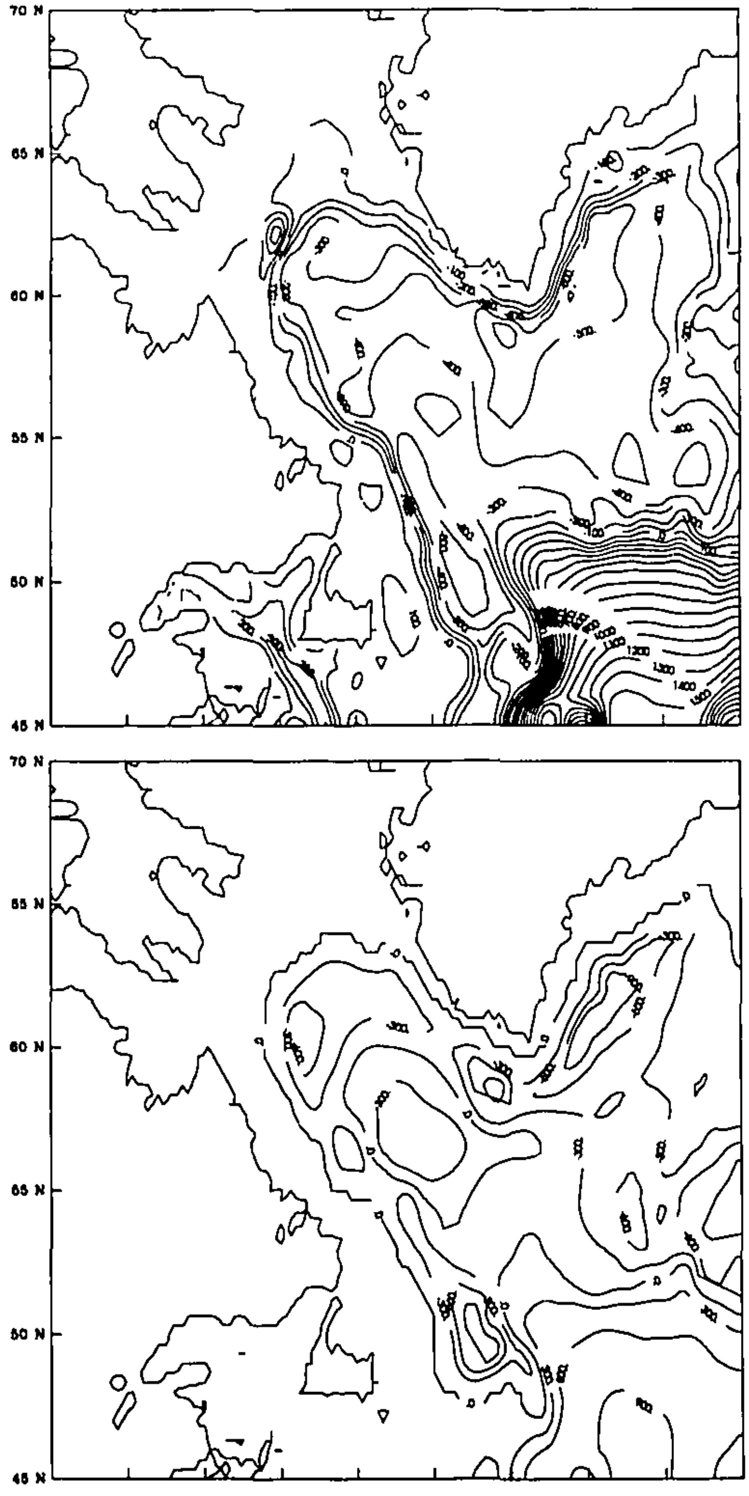

Figure 6.3: Cold season potential energy (m^{2}s^{-2}) between a) 0-1500m, b) 1500-2500m,

c)

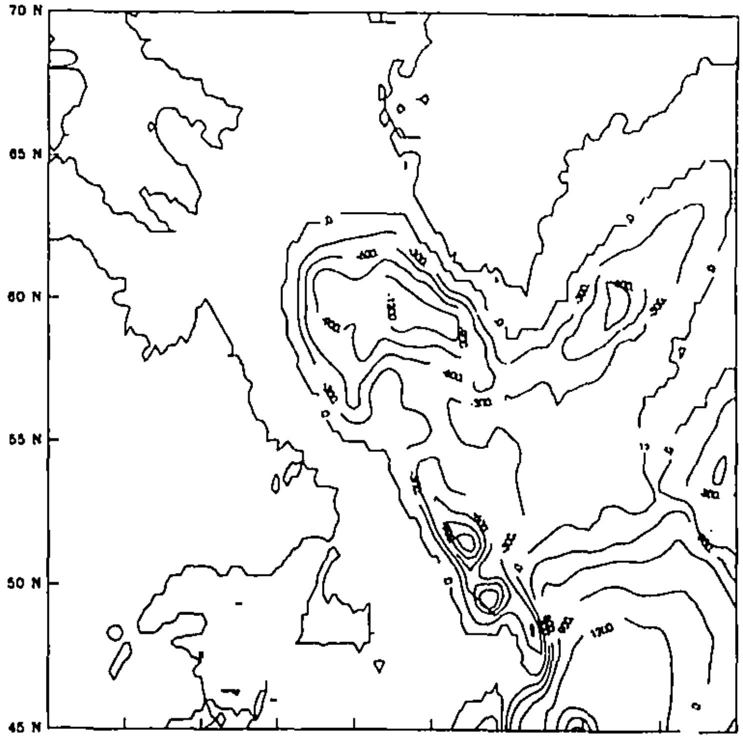

d)

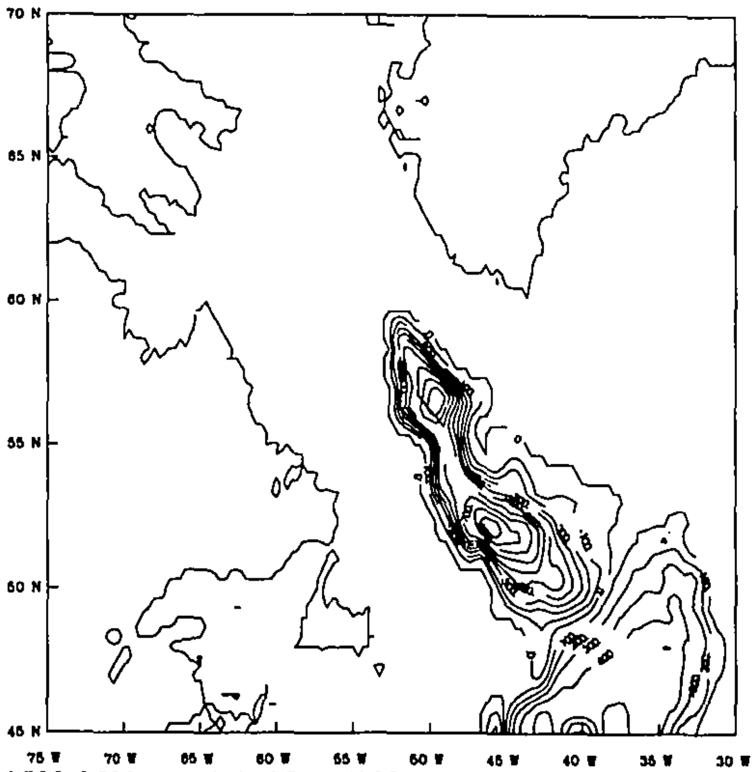

Figure 6.3 cont: c) 2500-3500m and d) 3500-5000m.

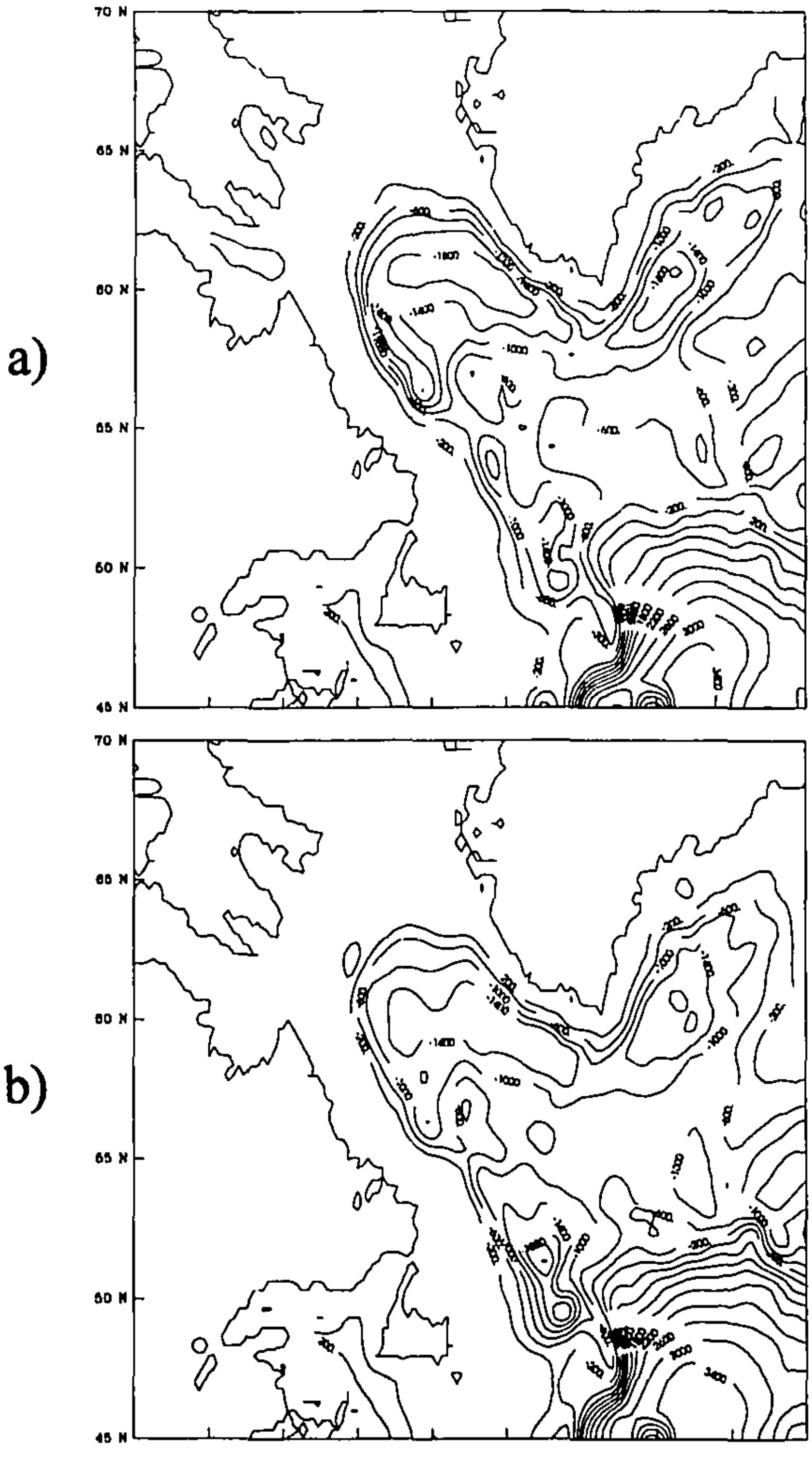

Figure 6.4: Total potential energy (m^3s^{-2}) for the a) warm and b) cold seasons.

variations of the potential energy are seen and that the largest seasonal variations are found ~300 nautical miles northeast of Newfoundland and in the northern LS. The summer potential energy field is shown in Fig. 6.5a and is very similar to the warm season potential energy field (Fig. 6.4a).

6.2 The integration path, the reference tranport values and the wind stress fields

The integration paths for the Mellor *et al* (1982) method are the planetary potential vorticity contours (ξ=f/H) and are shown in Fig. 6.5b. These are followed (Eq. 5.22) until they intersect one of the reference boundaries where the integrating constant adjustments are done. As mentioned earlier, these reference values are the transports taken from the climatological annual mean calculation of Greatbatch *et al* (1991), obtained at 1°x1° resolution using the Mellor *et al* (1982) method, to which a seasonal correction calculated using wind torque only (from Greatbatch and Goulding, 1989) was added.

The choice of the reference boundaries is critical for the determination of the interior volume streamfunction for two reasons: the first reason is that, along the boundary, topographic gradients should be as small as possible, so that coarser resolution studies of Greatbatch and Goulding (1989) and Greatbatch *et al* (1991) provide adequate reference values along f/H lines. The second reason is that in the real ocean, information propagates in the Northern hemisphere with shallow water on the right. This must be reflected in the choice of integration path (planetary potential vorticity lines) and hence the reference boundary should be approached such that the larger values of f/H (shallow water or large f) are kept on the left of the integrating path.

a)

b)

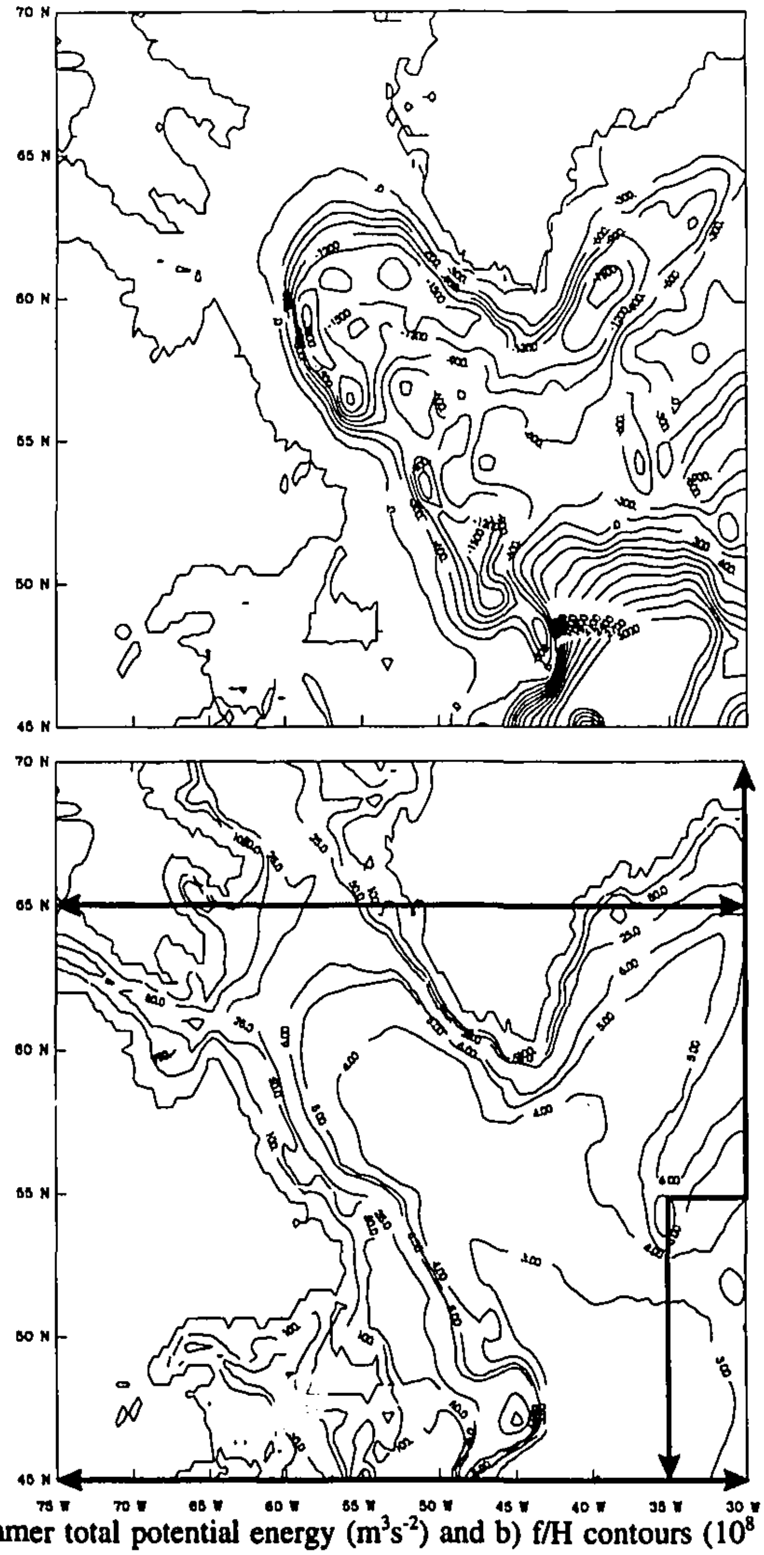

Figure 6.5: a) Summer total potential energy (m^3s^{-2}) and b) f/H contours (10^8 $m^{-1}s^{-1}$).

The reference boundaries were therefore chosen (see arrows on Fig. 6.5b) to be 30°W between 55°N and 70°N, 55°N between 30°W and 35°W, and 35°W between 45°N and 55°N. The northern and southern reference boundaries were defined as 65°N and 45°N, respectively. The kink in the eastern reference boundary was incorporated to improve the circulation in the region of Reykjanes Ridge. Without this kink the eastern reference boundary was intercepted twice by a range of f/H contours, in the Reykjanes Ridge region, and minor problems arose. The reference boundary transport values for summer are shown in Figs. 6.6. The warm and cold seasons reference values are not presented as only a ~ 1Sv difference is found between these set of values and as the warm seasons reference values are very close to the summer ones.

The integration paths were chosen such that they tried first to intersect the eastern reference boundary; if the integration path did not intersect that reference boundary then it tried to intersect the northern reference boundary; if it once more failed it tried to intersect the southern reference boundary at 45°N.

The summer, warm and cold season wind stress fields (from Hellerman and Rosenstein, 1983) which are used in the Mellor *et al* (1982) method are shown in Figs. 6.7. On the eastern side of Greenland, the wind blows from the northeast whereas on the western side the wind blows from the north-northwest sector, and in the southern part of the domain, the wind blows from the west. The main difference between the warm (Fig. 6.7b) and cold (Fig. 6.7c) wind stress fields is the strength of the wind field-the cold season winds being much stronger than the warm season winds. Other minor seasonal differences can be seen such the cyclonic feature in the

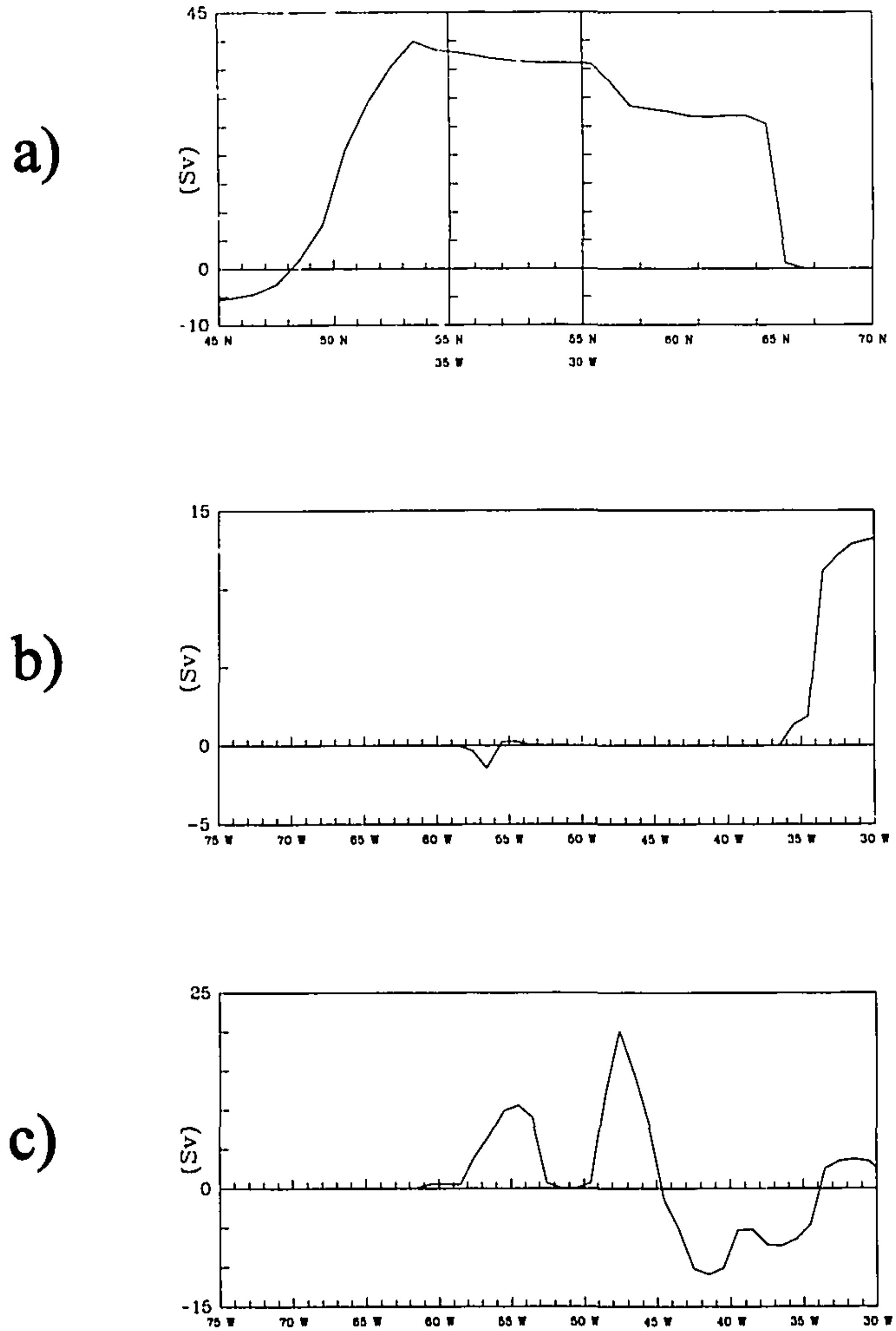

Figure 6.6: Summer reference transport values used in the Mellor *et al* (1982) method for a) the eastern boundary, b) the 65°N northern boundary and c) the 45°N southern boundary.

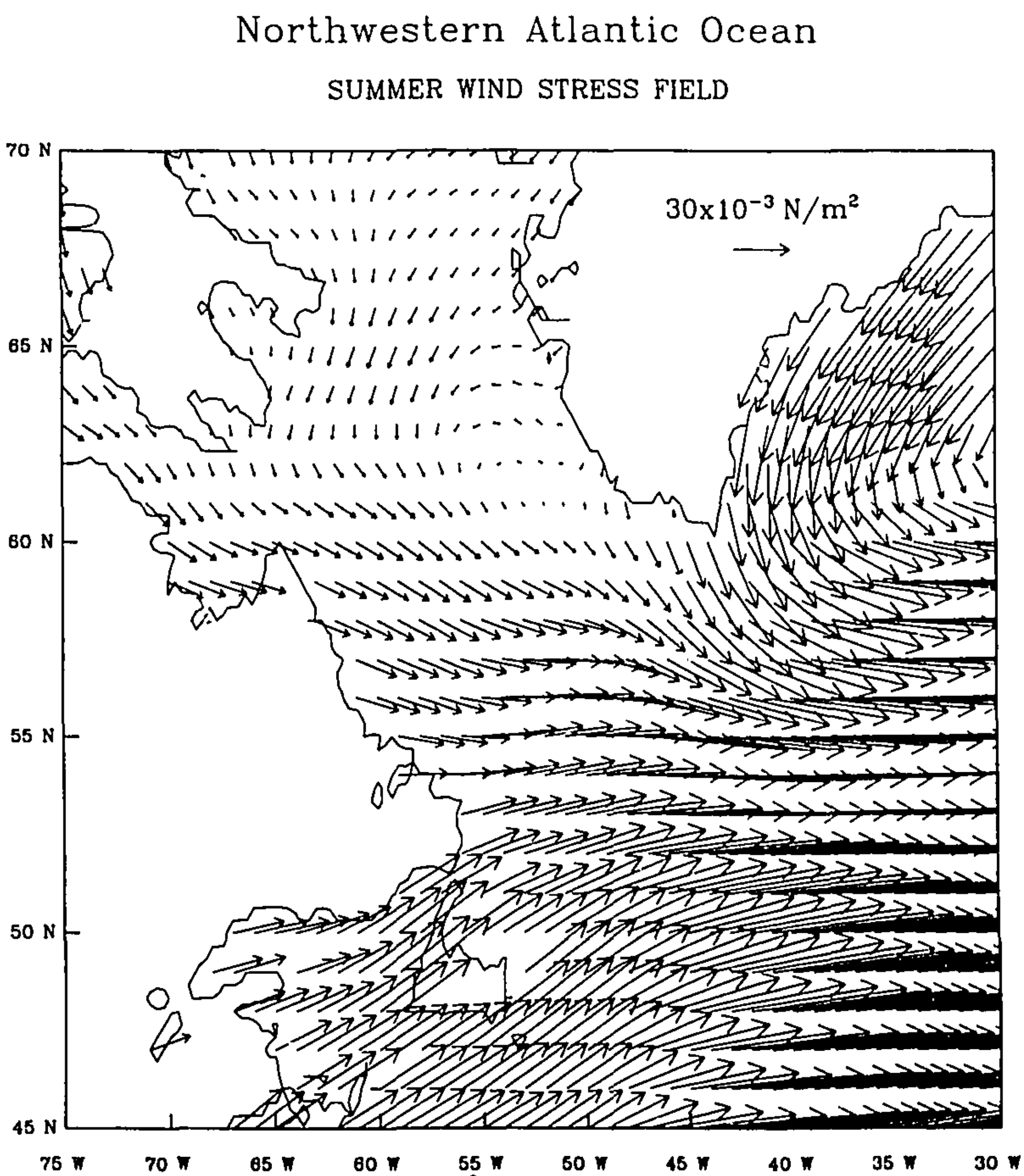

Figure 6.7: Wind stress field (N/m^2) for a) summer,

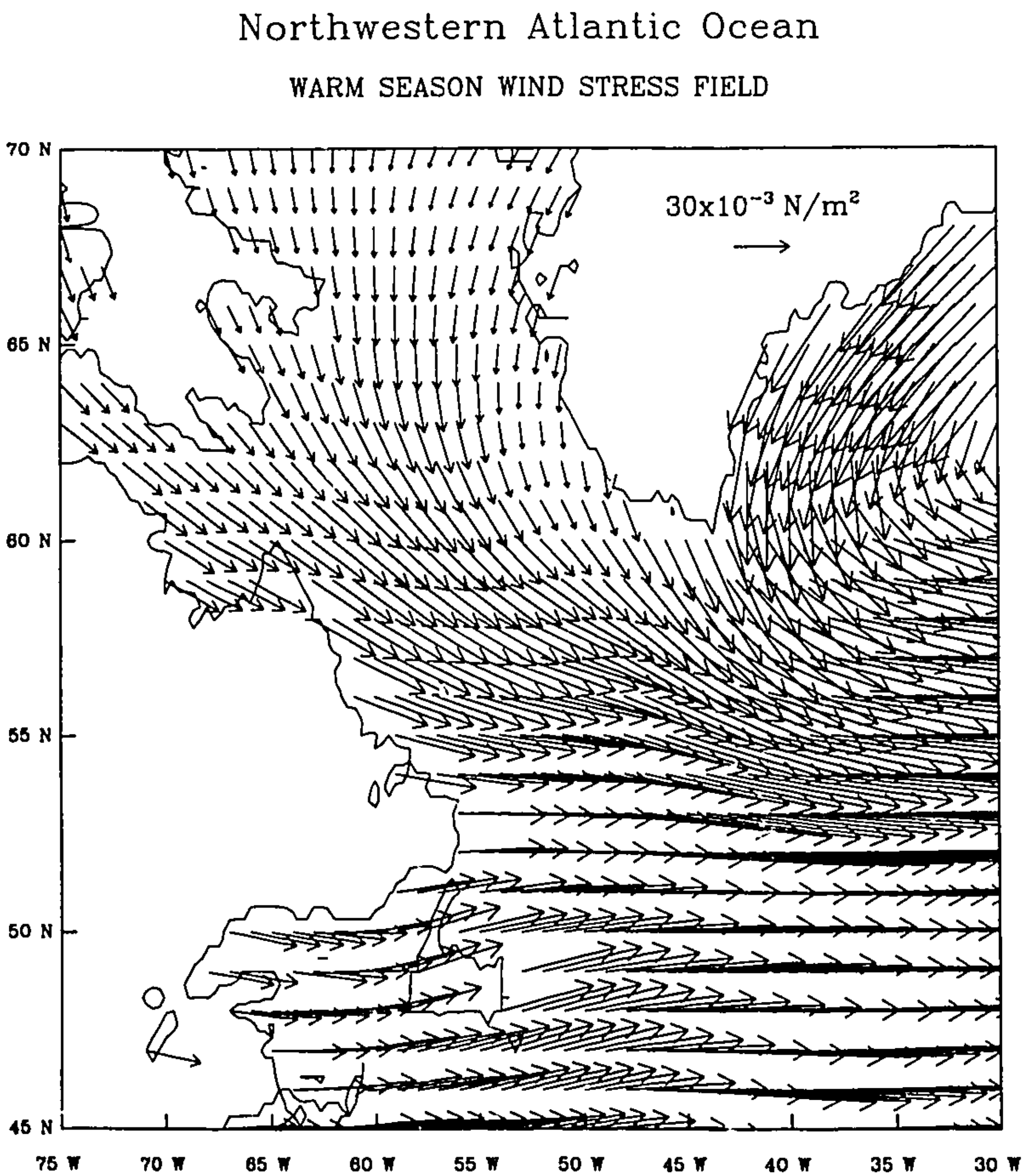

Figure 6.7 cont: b) the warm season,

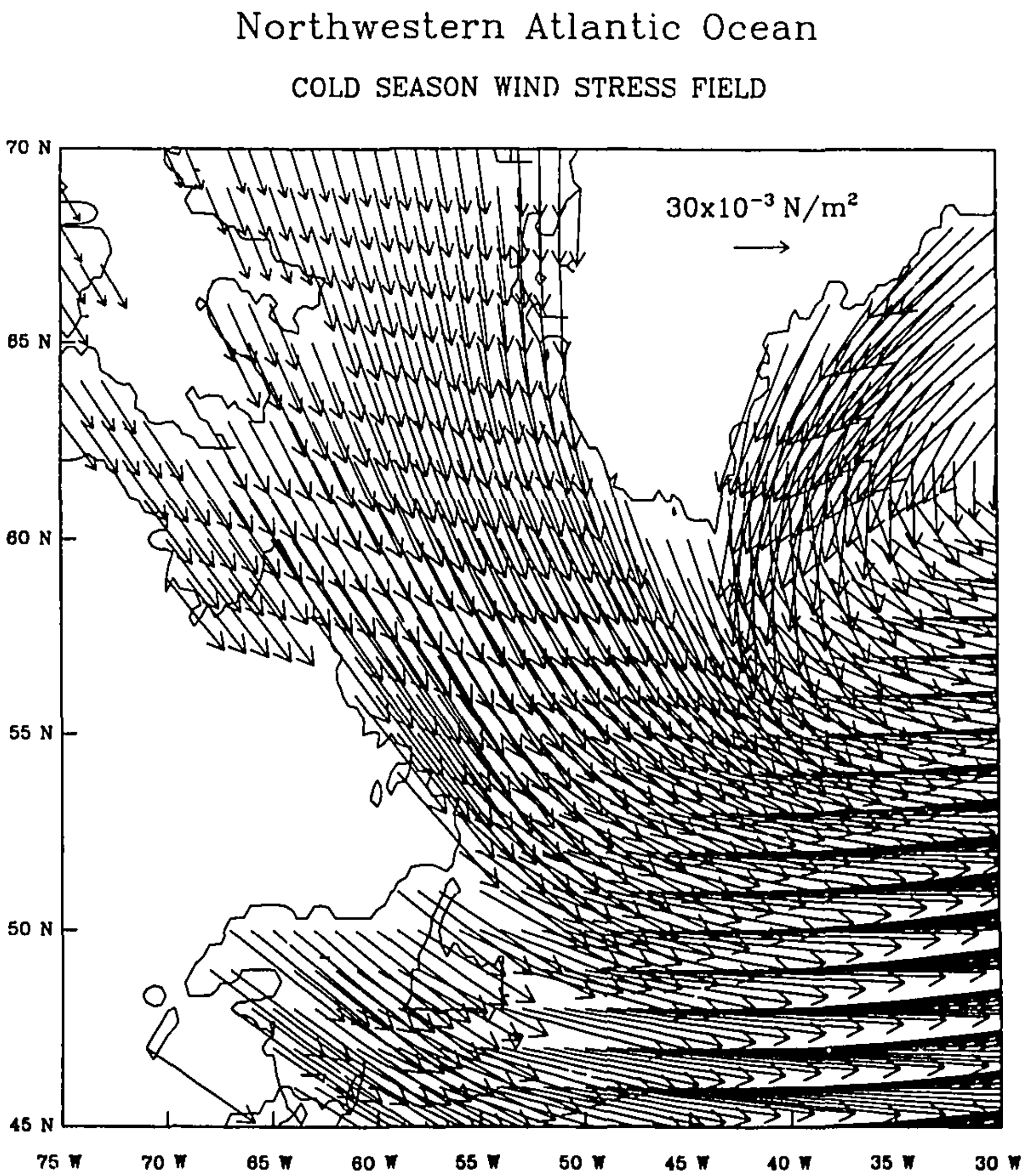

Figure 6.7 cont: and c) the cold season.

summer field (Fig. 6.7a) in the eastern Labrador Sea, and the direction from which the wind blows near the southwestern corner of the domain (compare Figs. 6.7 a,b and c).

For each gridpoint, the interior volume transport was evaluated from both the potential energy at the gridpoint location and the χ value evaluated on the reference boundary at the intersection of the integration path (ξ=f/H). The whole field was smoothed using a 9 point filter and the holes (gridpoints for which the f/H line did not connect to a reference boundary) were filled-up by using the IMSL interpolation scheme of Akima (1978). The Akima interpolator was not applied to the Flemish Cap region as it was found to create suspicious transport gradients. The transport in the Flemish Cap planetary potential vorticity island region was therefore left undetermined.

6.3 The summer volume transport streamfunctions

Results for the volume streamfunction are shown in Fig. 6.8a. A maximum transport of 48.8 and 46.1 Sv were obtained for the Labrador Sea and the Irminger Sea, respectively. These values are closer to the 53 Sv estimated by Ivers (1975) than the 16 Sv estimated by Swallow and Worthington (1969) using a 1200m level of no motion.

The results also show evidence of cross-isobath transport in the Labrador Sea off the Labrador coast (see also the salinity fields of Figs. 3.2a-d). Equations 5.16 can be rewritten as $J(\Psi,\xi)=J(\Phi,1/H)$ + WIND, where J is the Jacobian operator, which shows that the cross-f/H transport is due to both the JEBAR (see also Mertz and Wright, 1992) and

a)

b)

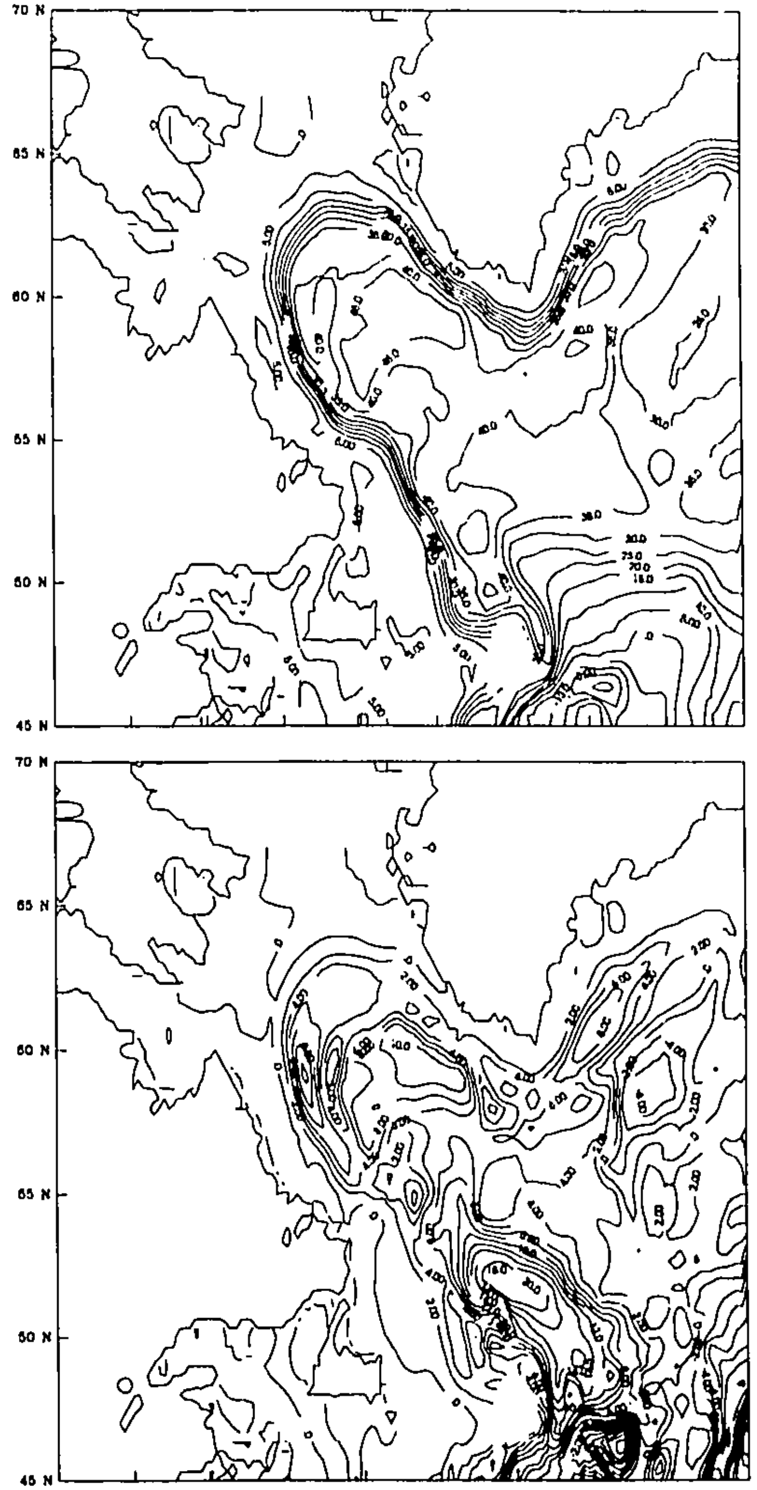

Figure 6.8: Summer diagnosed streamfunction transport (Sv); a) total streamfunction, b) volume transport due to the local JEBAR term,

c)

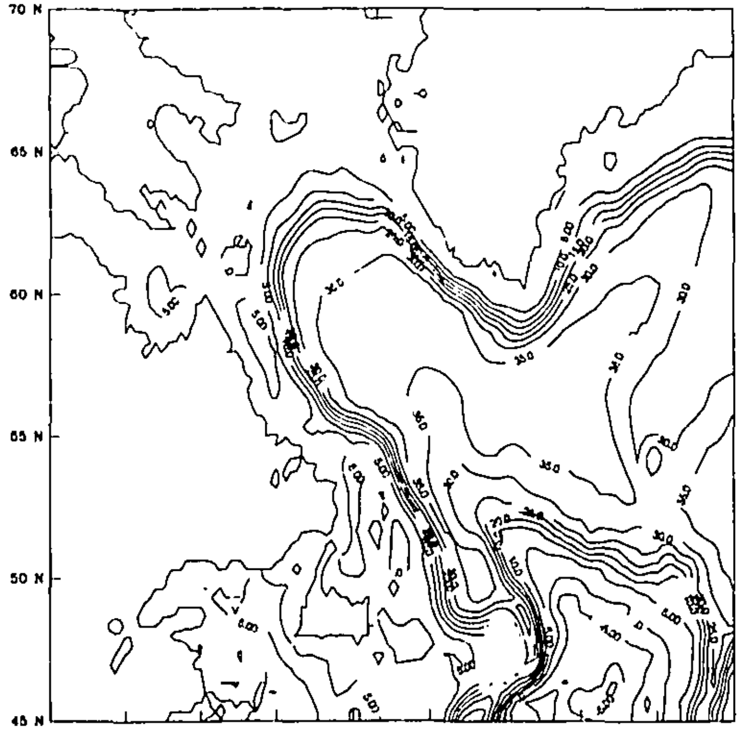

d)

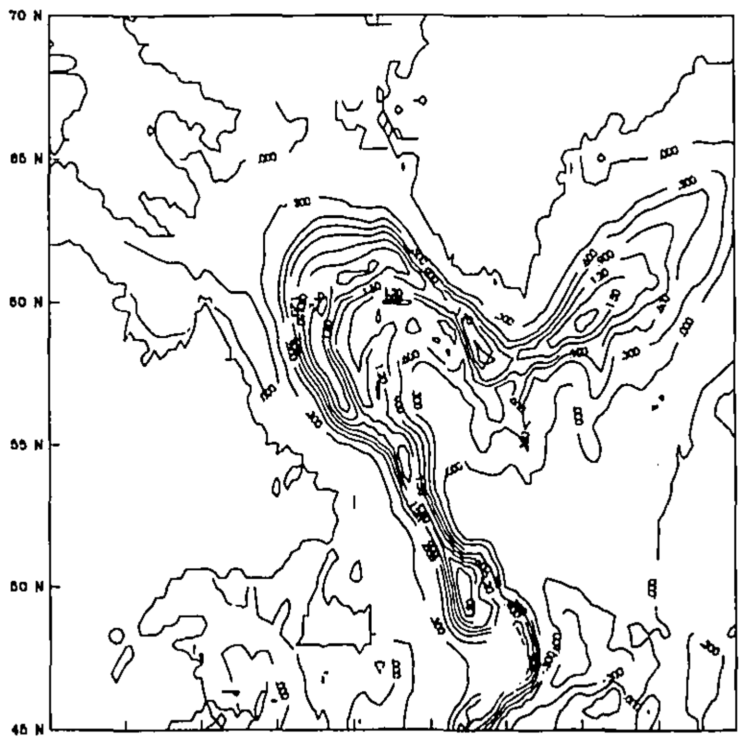

Figure 6.8 cont: c) volume transport inferred by the boundary values and d) volume transport due to local wind forcing. Contour intervals are 5, 2, 5 and 0.3 Sv.

the wind terms. By overlapping the potential energy field (Fig. 6.5a) and the topography map (Fig. 1.1), one can see that the JEBAR term should be large in the northern Labrador Sea and in the western Irminger Sea. These are indeed the regions where cross-isobath transport (see Fig. 6.8a) was diagnosed. The transport in shallow water and near the Labrador coast is less than 5 Sv. This is supplemented by a further 35 Sv on the Labrador slope.

One question that needs to be addressed concerns the importance of volume transport specified along the reference boundaries in the evaluation of the transport inside the whole domain. To address this question, the Mellor *et al* (1982) method was reapplied without any windstress and with the boundary reference volume transports set equal to zero in order to find the local JEBAR contribution to the total transport. The resulting streamfunction is presented in Fig. 6.8b. There are four regions where the diagnosed volume transport is relatively large: (i) in Labrador Sea (on the Labrador side: at 57°W and 59°N and on the Greenland side: at 51°W and 60°N), (ii) southeast of Flemish Cap, (iii) north of Flemish Cap near the Labrador Sea entrance and (iv) southeast of Cape Farewell. These are the regions where the potential energy contours cross the isobaths. This local JEBAR effect is an important contribution to the total transport of the LC in both the northern and the southern Labrador Sea, but is less important near the Cape Farewell area where the inflow along the eastern reference boundary is mainly responsible for the 10-35 Sv transport. The importance of this inflow can be better seen in Fig. 6.8c which shows the streamfunction obtained when both the potential energy and the windstress are set to zero. This figure illustrates that the general shape of the streamfunction contours comes from the transport specified at the reference boundaries.

The contribution to the total transport due to local windstress forcing was similarly calculated by setting the boundary reference volume transports and the JEBAR term equal to zero. The results (Fig. 6.8d) show that the local wind forcing is not an important contribution for driving transport through the Labrador Sea emphasising the importance of remote forcing through the reference boundaries.

6.4 The three-dimensional current structure

As shown in section 5.2, the volume transport streamfunction, the density and the wind stress fields can be combined together to estimate the bottom currents (Eqs. 5.23-5.26). The ocean bottom can then be used as a reference level for which the reference velocity is known and hence, the absolute currents can be estimated (Eq. 4.4).

The bottom currents from the summer analysis, estimated using Eq. 5.26, are shown in Fig. 6.9a. The most important features are the strong currents (5-15 cm/s) in all slope regions which generally follow the isobaths. The absolute currents at various depths, obtained from the summer analysis, are shown in Fig 6.9b-6.9g. These results suggest that: (i) water flows into Hudson Strait on the South shore of Baffin Island and out of Hudson Strait on the north shore Québec; (ii) a portion of the inner branch of the LC follows the southern coast of Newfoundland and flows into the Gulf of St.-Lawrence

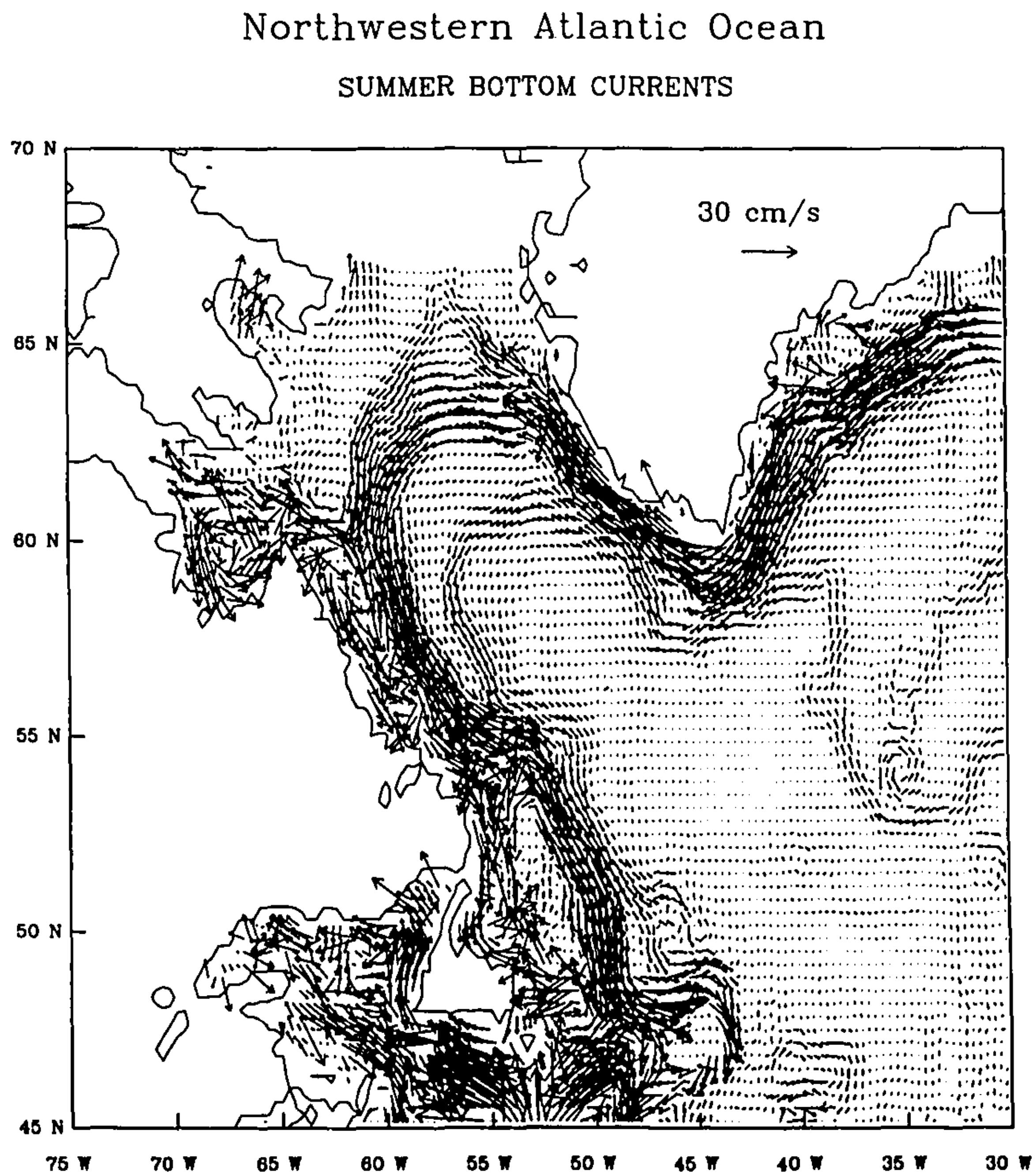

Figure 6.9: Northwestern Atlantic Ocean horizontal currents for summer (1910-89), derived using the Mellor *et al* (1982) method, at a) the bottom of the ocean,

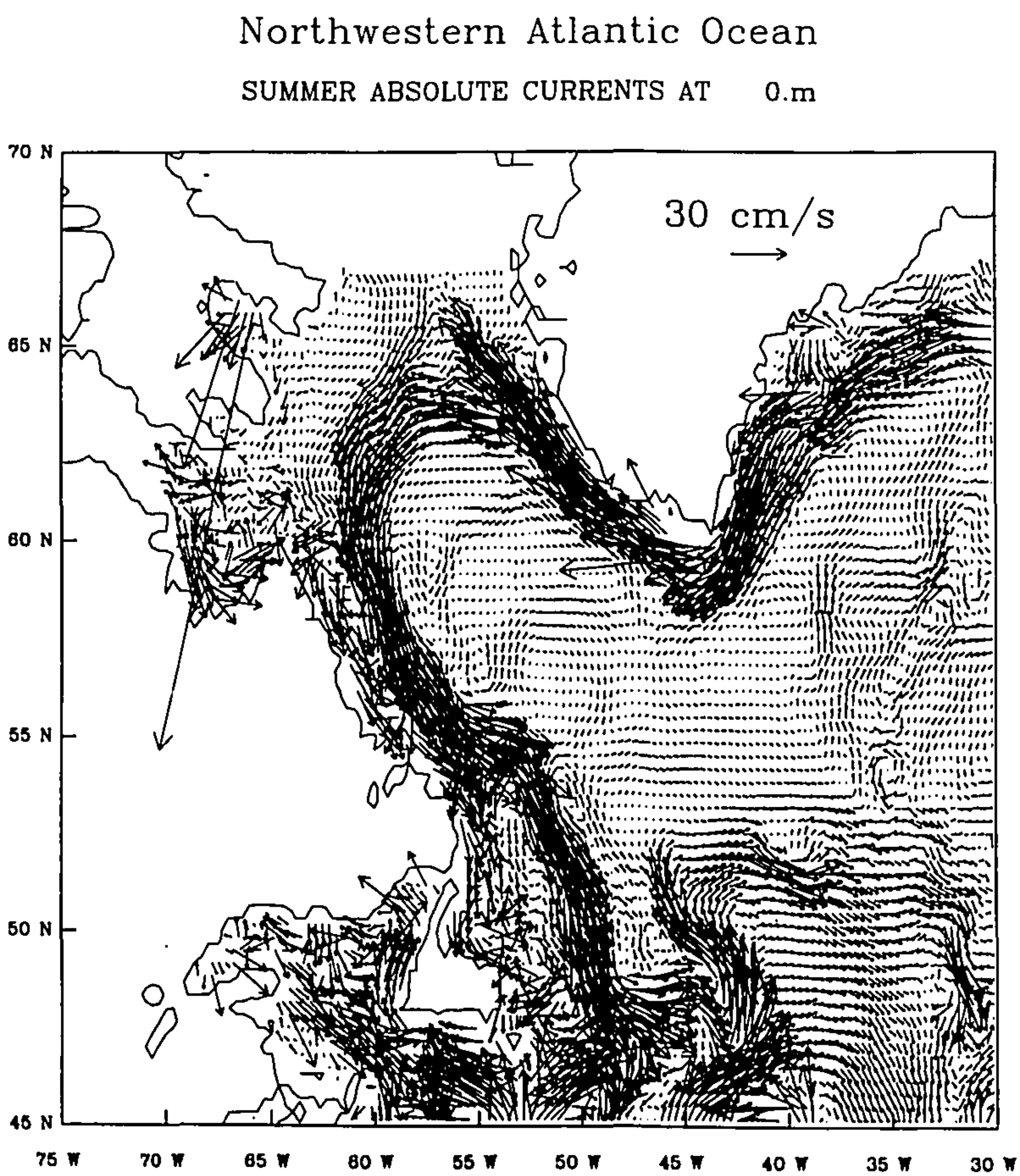

Figure 6.9 cont: b) 0m,

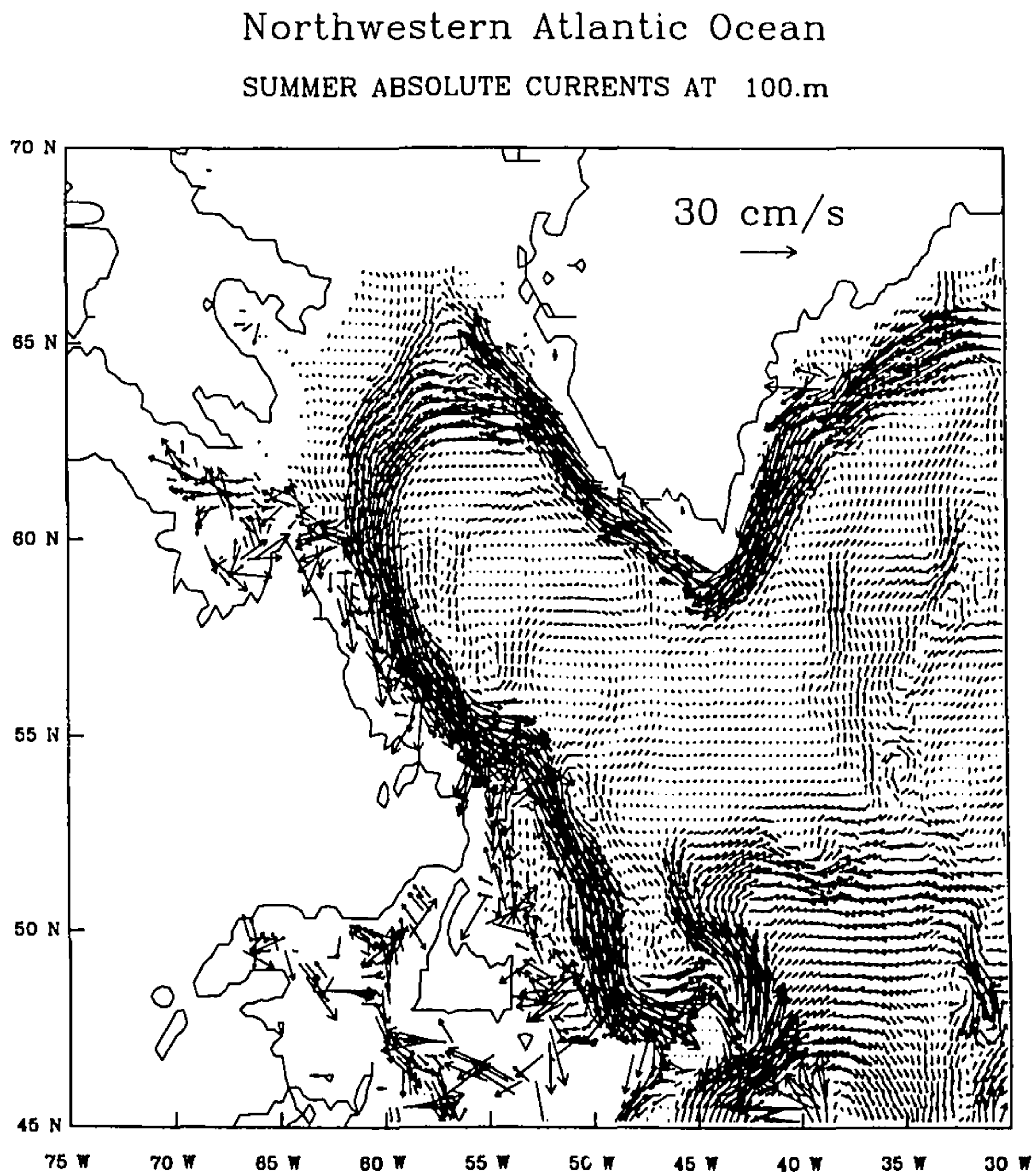

Figure 6.9 cont: c) 100m,

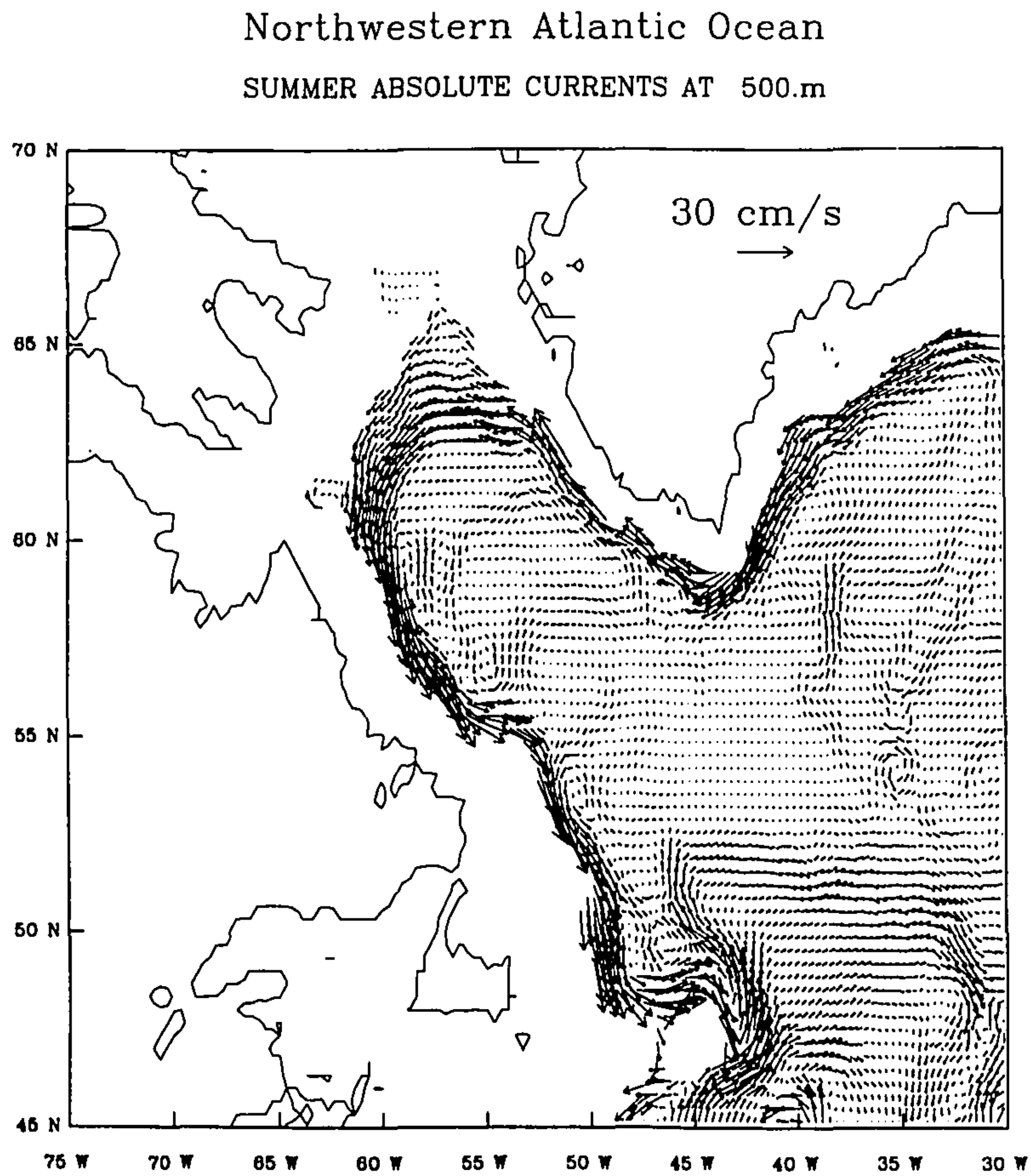

Figure 6.9 cont: d) 500m,

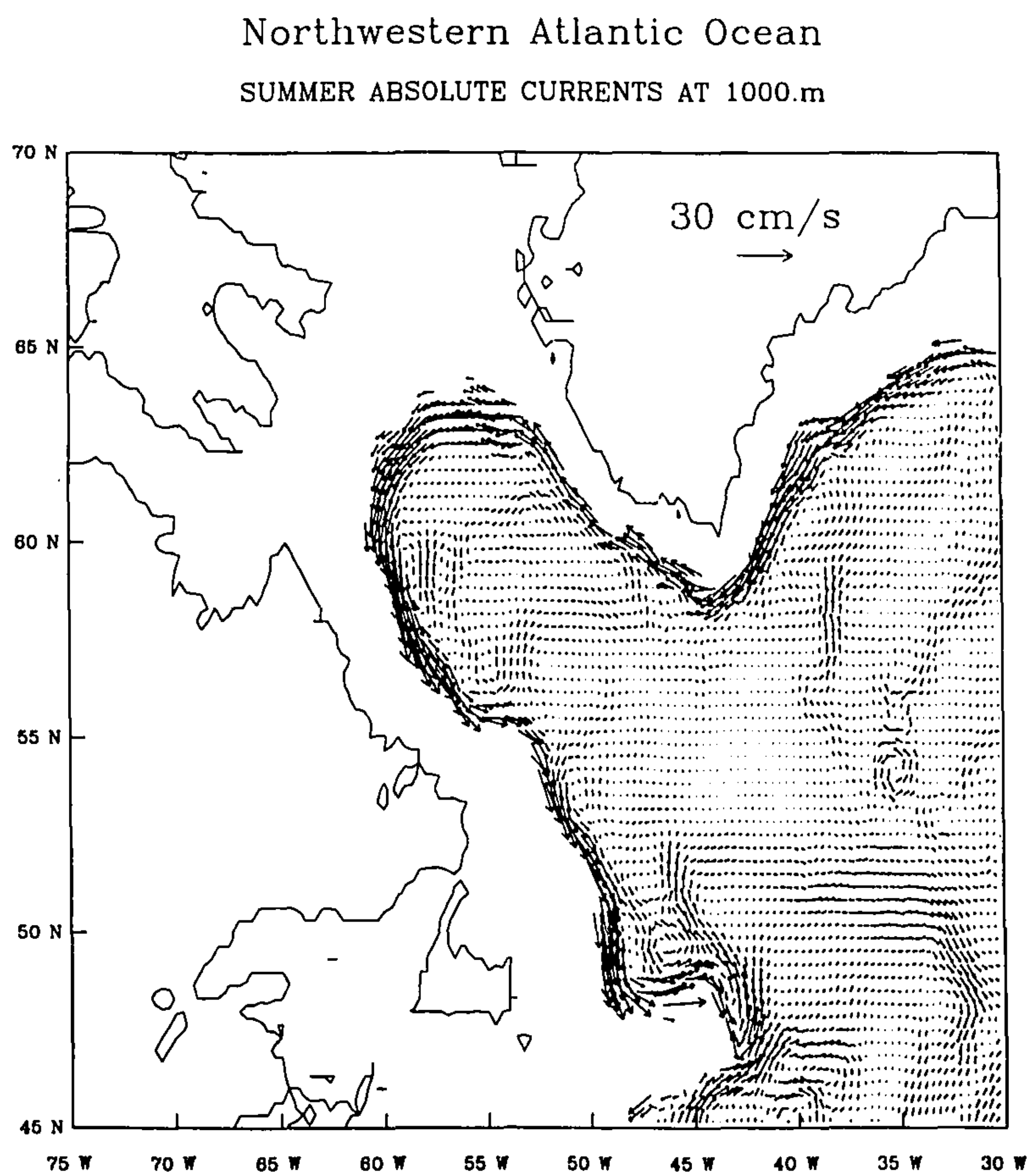

Figure 6.9 cont: e) 1000m,

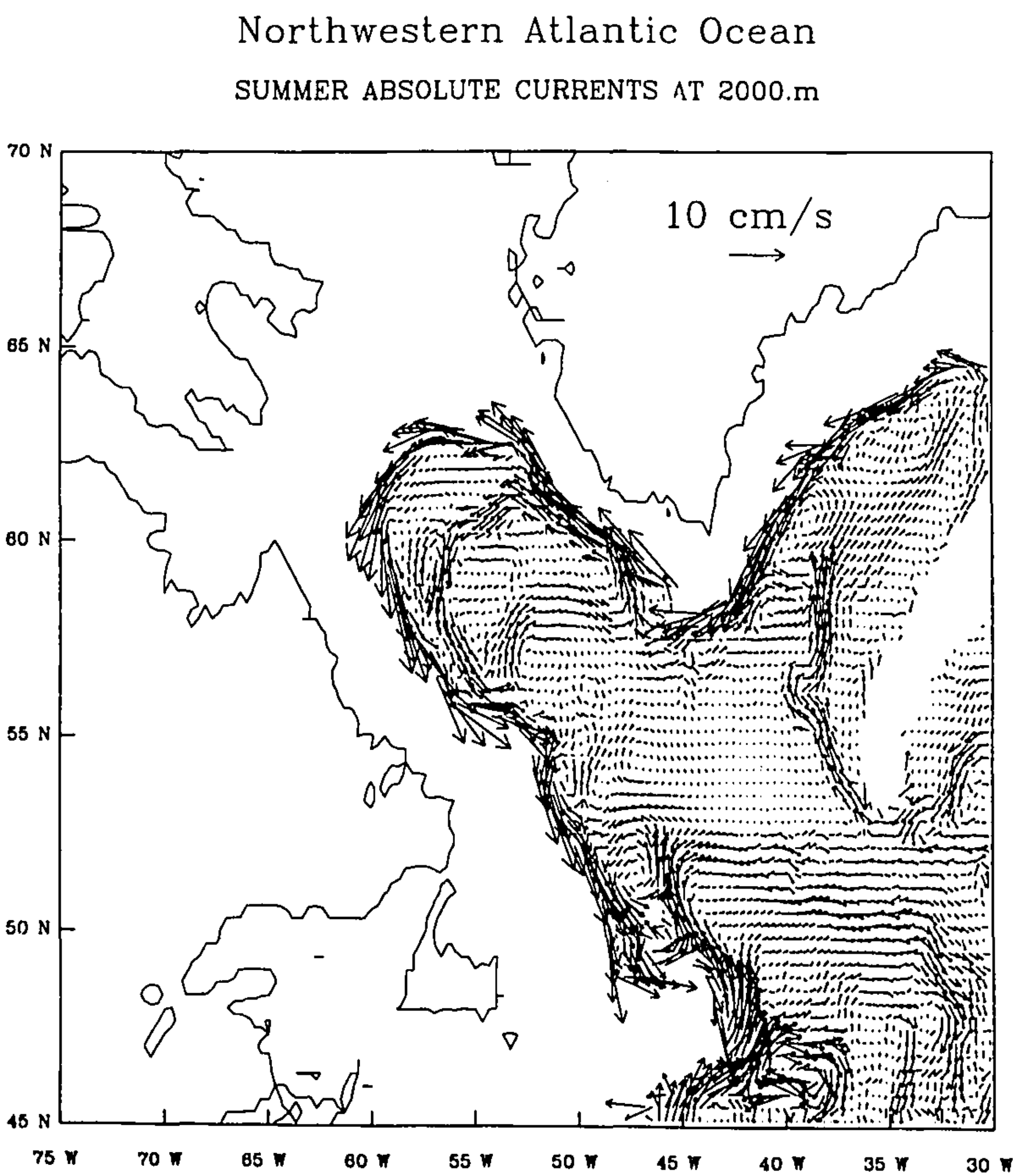

Figure 6.9 cont: f) 2000m,

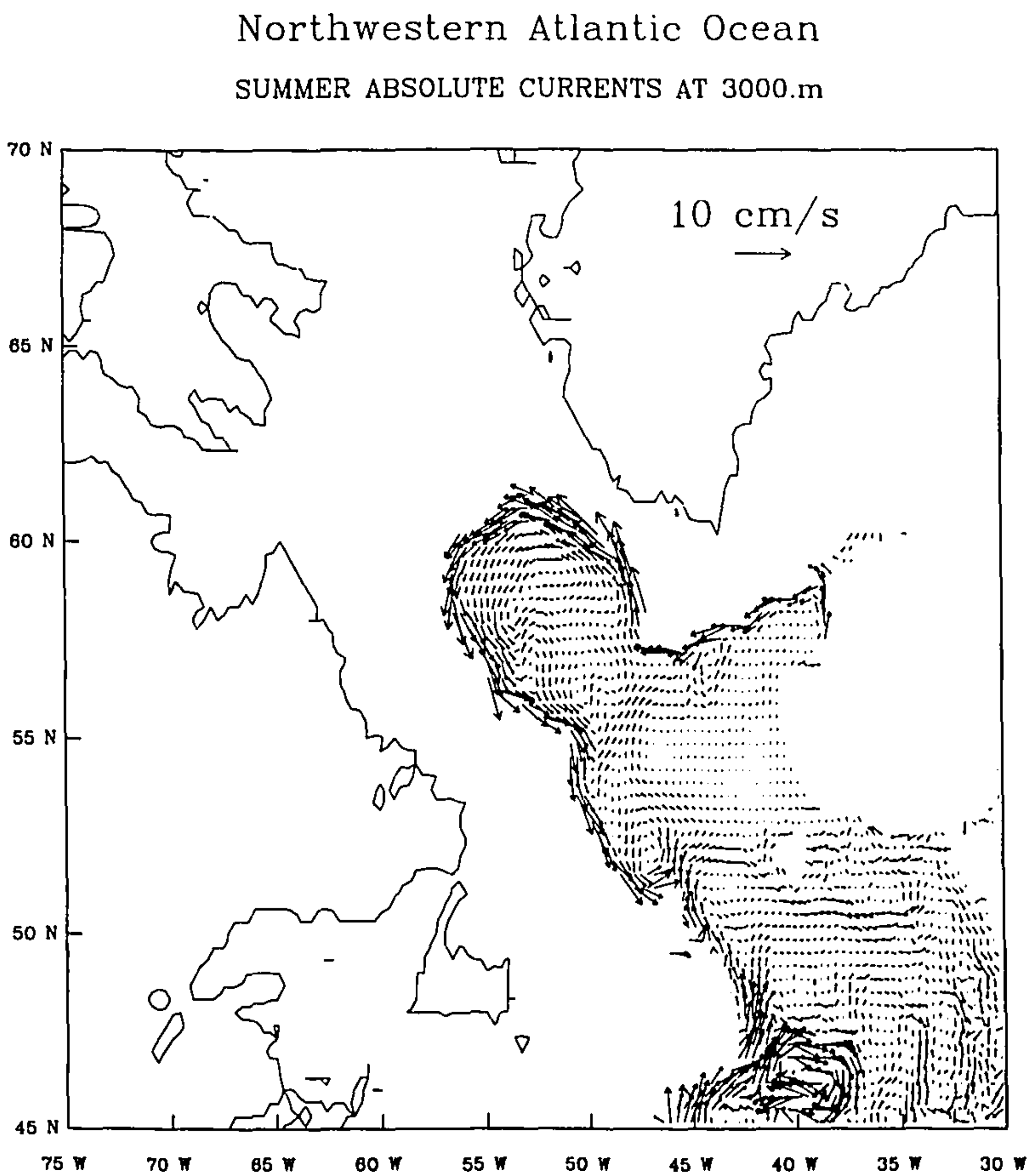

Figure 6.9 cont: and g) 3000m.

and the Gulf of St.-Lawrence water flows out on the western side of Cabot Strait; (iii) the branch of the NAC that flows toward Hamilton bank reaches a depth of 2000m; (iv) near Flemish Cap the currents show a complicated structure where on the western side of Flemish Cap the currents flow southward, and on the eastern side there is some southward flow with stronger northward flow associated with the North Atlantic Current a little further offshore. Figures 6.9b-f suggest that there

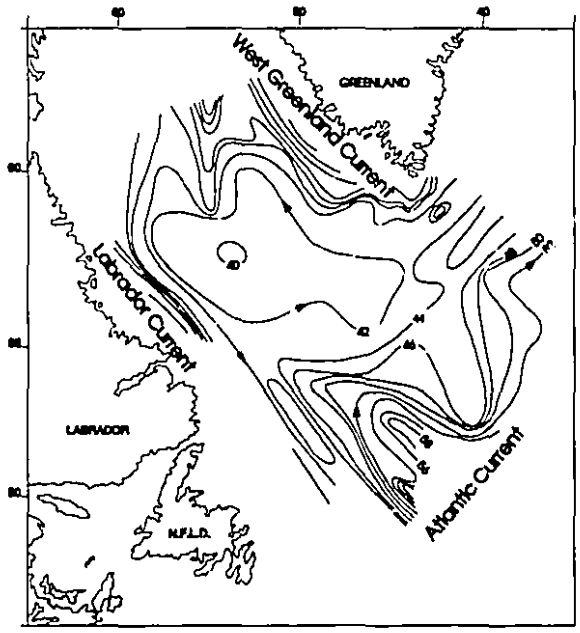

Figure 6.10: Dynamic topography of the sea surface relative to 1000 dbars with contours every 2 dynamic cm. Redrawn from Lazier (1973).

is an anticyclonic circulation in central Labrador Sea. At the surface this anticyclonic circulation is related to the cross-isobath isohalines discussed in chapter 3 and at greater depth with the circular isohalines of Fig. 3.2d (see also the potential energy positive values in Central LS in Fig. 6.5a). Ivers (1975) obtained similar circular isohalines in his Fig. 17 and this cross-isobath flow was also observed by Lazier (1973) in his spring data set (see Fig. 6.10). Notice that although a cross-isobath flow is seen in Fig. 6.10, it is part of the general cyclonic circulation in the Labrador Sea and that Fig. 6.10 does not show an anticylonic circulation in central Labrador Sea.

Dunbar's (1951) surface currents (Fig. 6.11), which are based on measurements

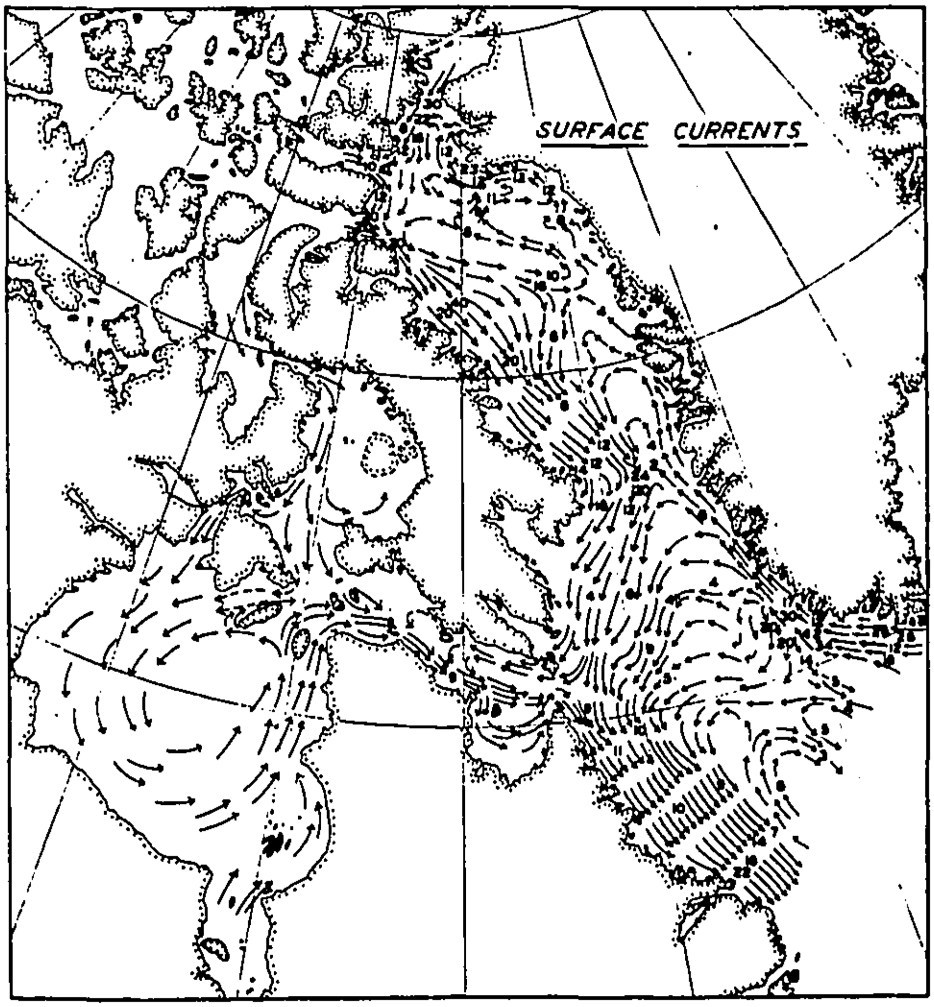

Figure 6.11: Surface currents (cm/s), August-September. The circulation in Baffin Bay, Davis Strait and the LS is taken from Kiilerich (1939), based on the *Godthaab* expedition results of 1928. The Hudson Bay and Hudson Strait circulation is plotted from Hachey (1931 and 1935). Reproduced from Dunbar (1951).

taken in 1928, have many similarities with surface currents shown in Fig. 6.9b. Both figures show generally the same circulation, notice the separation of the WGC, the circulation in Ungava Bay and the cross-shelf current which was discussed above. The cyclonic circulation centered on 57°N and 55°W is also observed in Fig. 6.11.

Figure 6.12a shows the current speed, $(u^2+v^2)^{1/2}$, along 43.67°W (although speed is shown, a sign convention has been introduced such that positive contours are associated with currents directed eastward). This section is nearly parallel to the Cape Farewell-Flemish Cap section discussed in Clarke (1984). Figure 6.12a is similar to Clarke's results (Fig. 1.3) with successive eastward and westward current bands. Clarke evaluated the maximum volume transport to be 33.5 Sv (see his table 2), which is comparable to the 40 Sv of Fig 6.8a. The slight difference is likely due to estimated bottom currents (Fig. 6.9a) which, although small, contribute significantly to the total transport. On the northern side (left in Fig. 6.12a), the EGC speed is of the order of 20-30 cm/s which is comparable to Clarke's estimation. On the other hand, Fig. 6.12a does not show the intense slope currents which are seen on Fig. 1.3. Another discrepancy between Fig. 1.3 and Fig 6.12a is found near the NAC region where he observed, for the NAC, an eastward current speed component of 25 cm/s which is stronger than the value of ~15 cm/s from this analysis (see Figs. 6.9b and 6.12a). Closer to Flemish Cap, a current speed of 30-40 cm/s is diagnosed for the NAC (Fig. 6.9b). Furthermore, the velocity field shown in Fig. 6.12a has been diagnosed from a climatological mean data set, instead of presenting results from a single cruise/station so smaller horizontal temperature and salinity gradients, and hence, through

a)

b)

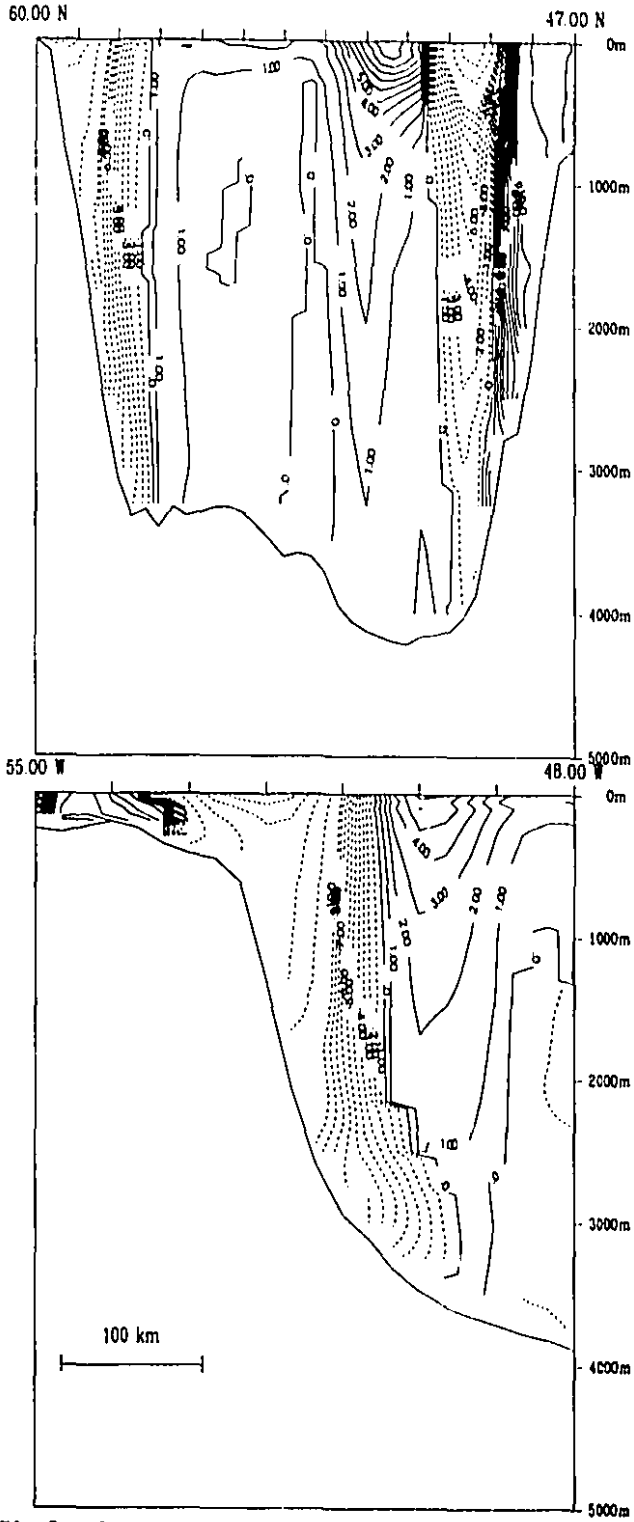

Figure 6.12: Vertical profile for the current speed (cm/s) structure a) along 43.67°W (positive valuc. are for eastward currents), b) along 53.33°N (positive values are for

c)

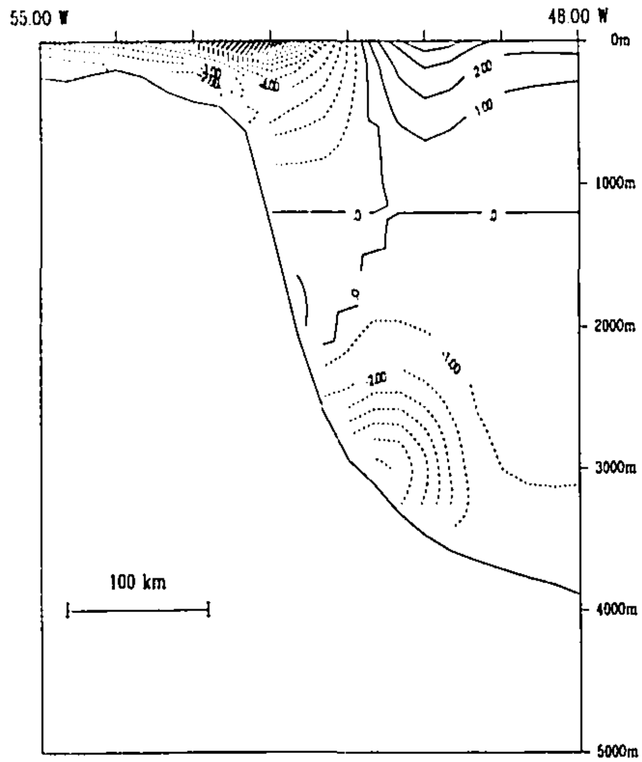

d)

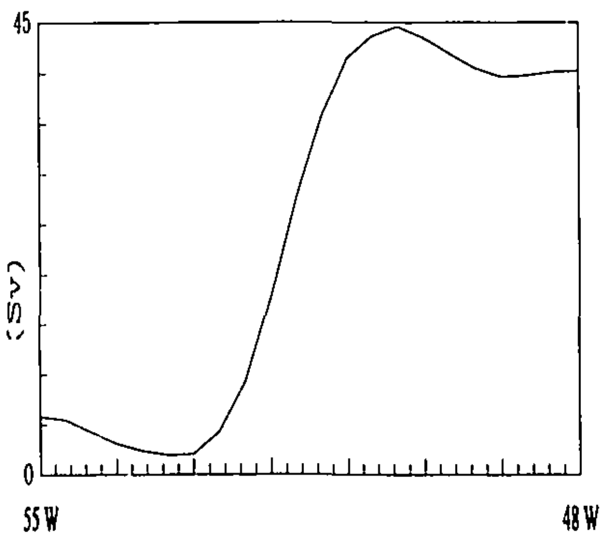

Figure 6.12 cont: northward currents), c) along 53.33°N using a 1200m level of no motion (same sign covention as in b) and d) transport through 53.33°N.

geostrophy horizontal velocities are expected.

Figure 6.12b shows the current speed, $(u^2+v^2)^{1/2}$, along 53.33 °W (same sign convention as Fig. 6.12a but for northward currents). Near Hamilton Bank, the LC splits into two branches (Fig. 6.9b): a weak inshore branch, which follows the Newfoundland coast, and a strong offshore branch (Lazier and Wright, 1993) which flows southward through Flemish pass along the slope of the Grand Banks. Lazier and Wright (1993) present evidence for what they call the *Deep Labrador Current* which flows southward offshore from the shelf break, centered about the 2500m isobath. The annual variations of the LC transport and speed are discussed by Lazier and Wright (1993). They found that the inshore and offshore branches show a baroclinic structure while the deep branch is more barotropic. According to Lazier and Wright (1993), Thompson et al (1986) and Greatbatch *et al* (1990), it seems that the baroclinic regime on the shelf has a buoyancy driven annual cycle whereas the offshore barotropic regime has a wind driven annual cycle. A current speed of 30-50 cm/s is obtained for the LC (Fig. 6.12b). The bottom intensification associated with the DWBU can be better seen in Fig. 6.12c where a maximum current speed of nearly 7 cm/s is observed. However, these values are half those presented by Lazier and Wright (1993) and Clarke (1984), presumably because of the smoothing inherent in the objective analysis procedure.

Figure 6.12d shows the transport through 53.33°N. The total southward transport through the section is about 45 Sv of which about 3 Sv is transported by the continental

a)

b)

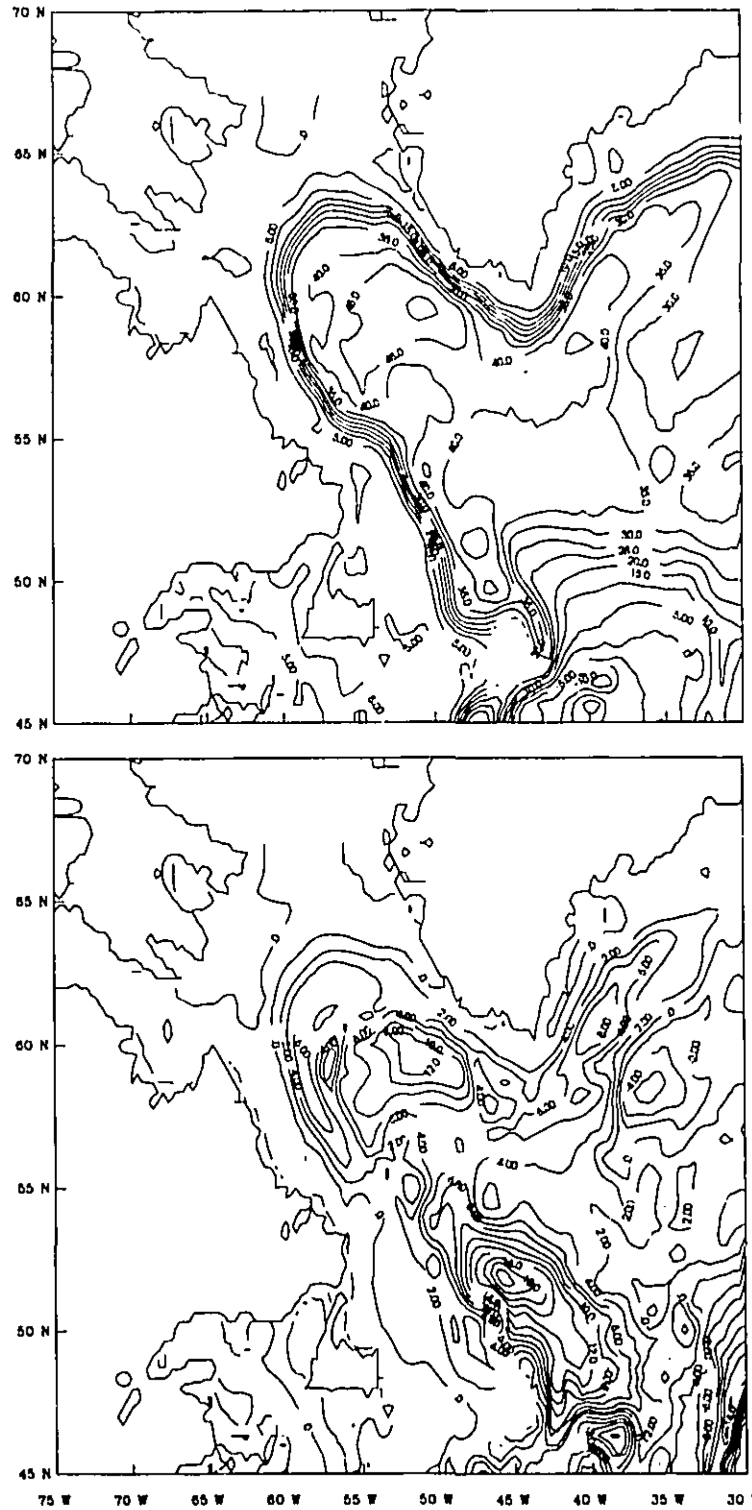

Figure 6.13: Warm season volume transport streamfunctions (Sv); a) total streamfunction, b) volume transport due to the local Jebar term,

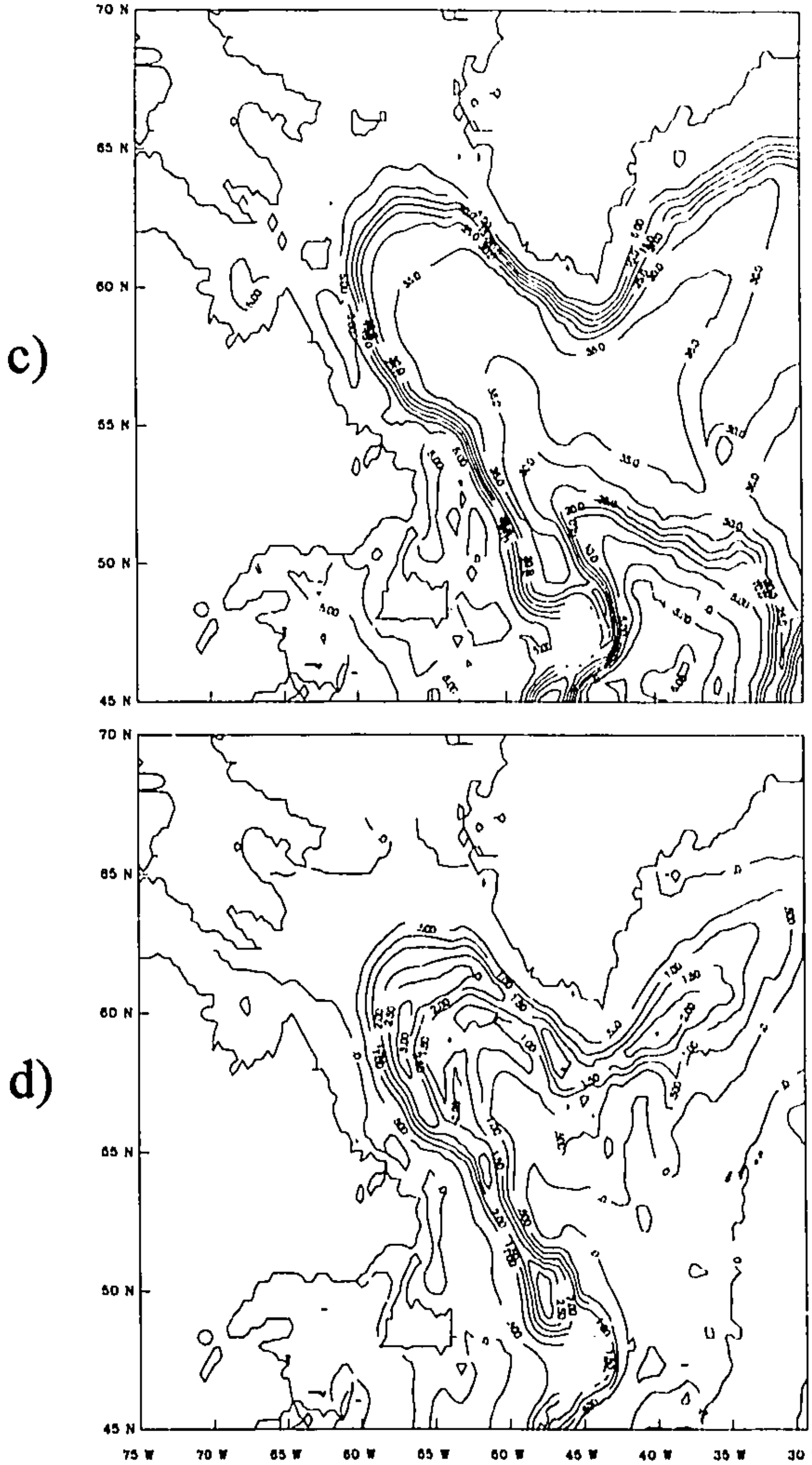

Figure 6.13 cont: c) volume transport inferred by the boundary values and d) volume transport due to the local wind forcing. Contour intervals are 5, 2, 5 and 0.3 Sv.

a)

b)

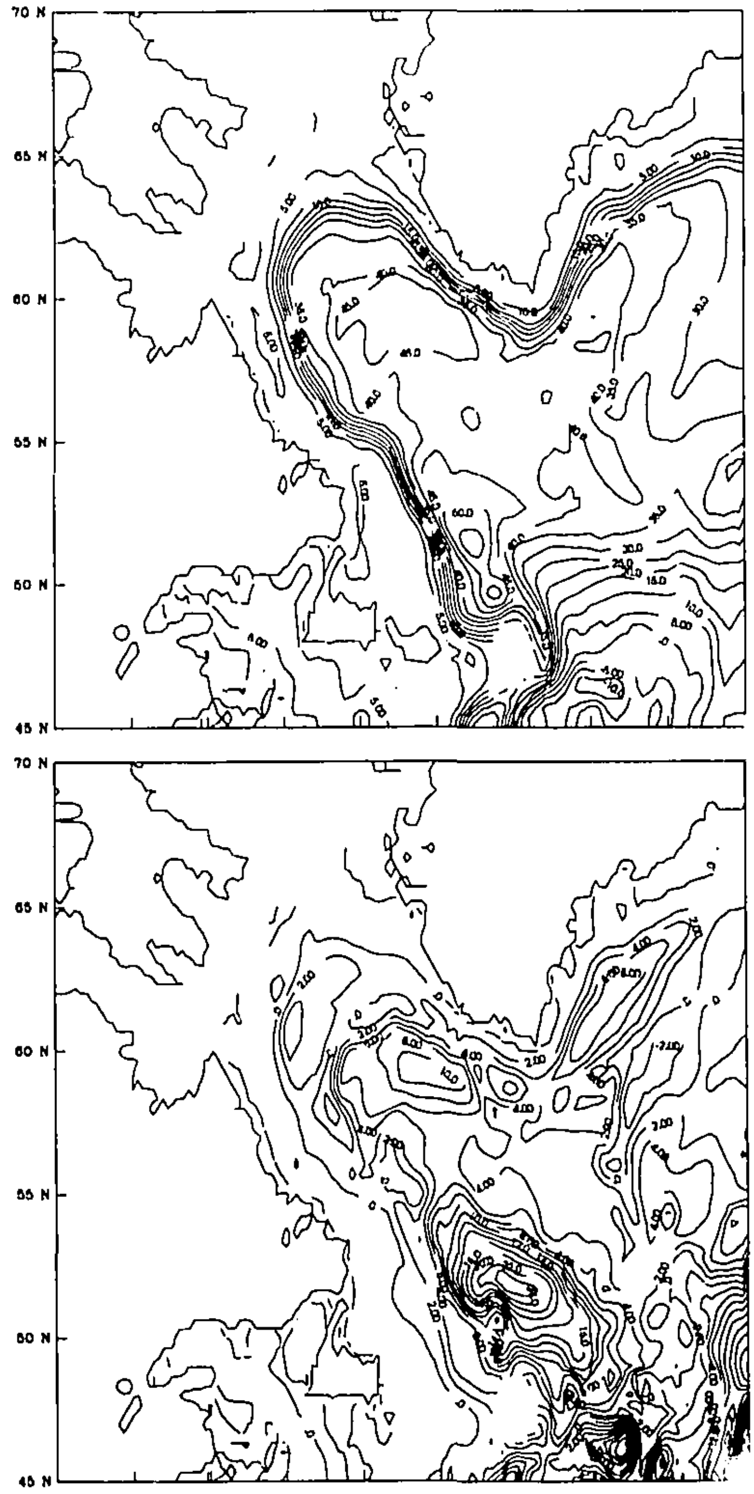

Figure 6.14: Cold season volume transport streamfunctions (Sv); a) total streamfunction, b) volume transport due to the local Jebar term,

c)

d)

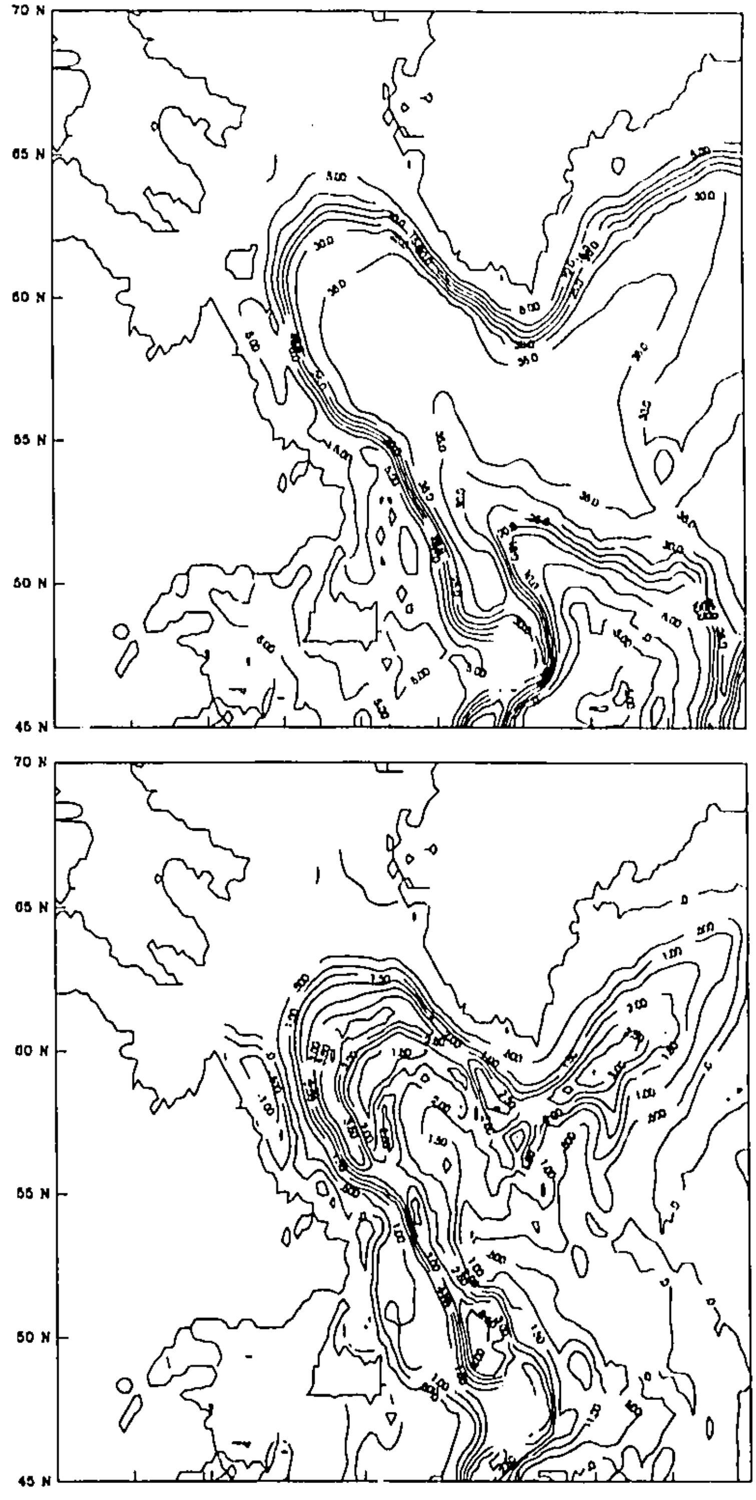

Figure 6.14 cont: c) volume transport inferred by the boundary values and d) volume transport due to the local wind forcing. Contour intervals are 5, 2, 5 and 0.3 Sv.

a)

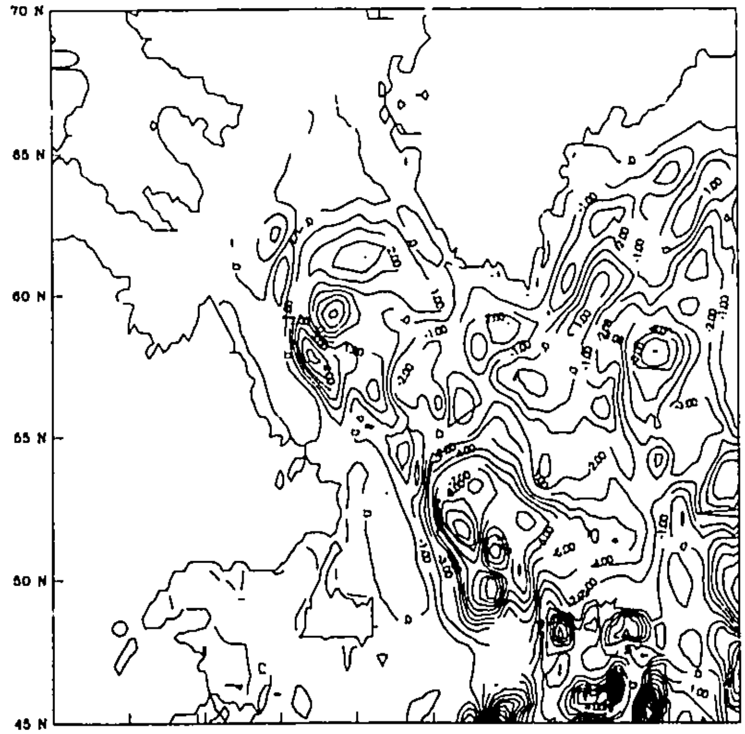

b)

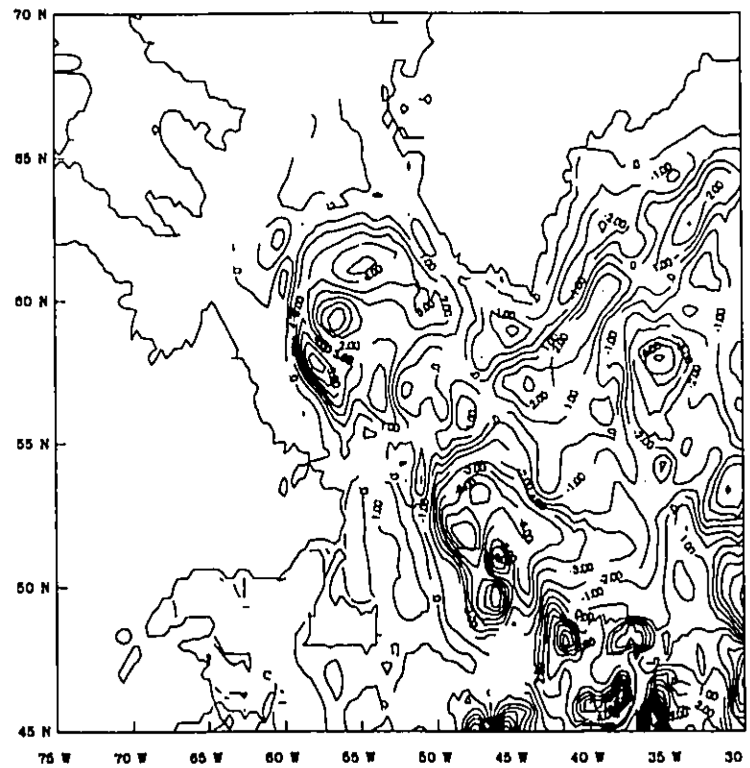

Figure 6.15: Seasonal variability (warm-cold) of a) the total volume transport streamfunction, b) the local Jebar contribution to the total streamfunction,

c)

d)

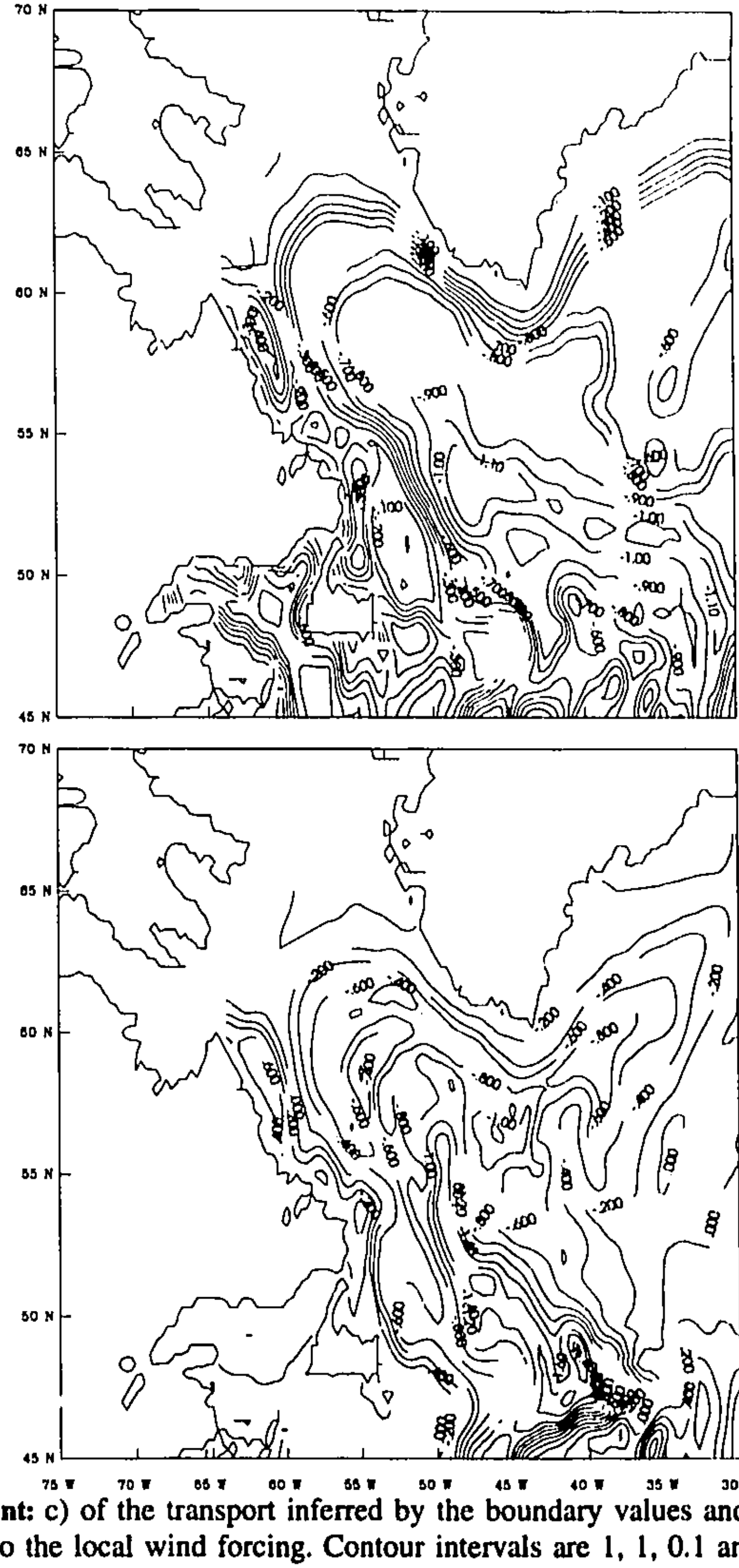

Figure 6.15 cont: c) of the transport inferred by the boundary values and d) of the transport due to the local wind forcing. Contour intervals are 1, 1, 0.1 and 0.2 Sv.

shelf branch of the LC, 16 Sv is carried by the slope branch and the remainder, 27 Sv, by both the deep branch and the DWBU. These results are in general agreement with those of Lazier and Wright (1993).

The summer results, presented in this section and in section 6.4, had shown that both the reference boundary values and the local JEBAR are important for determining the transport in the northwestern Atlantic Ocean. These summer results also shown that the currents flows basically along the f/H contours and the the cross-f/H transport is mainly due to JEBAR.

6.5 The seasonal transport variations

The warm and cold season volume transport streamfunctions (Figs. 6.13 and 6.14) were estimated using the potential energy fields of Figs. 6.4 and with the Hellerman and Rosenstein (1983) wind stress fields shown in Figs. 6.7b and 6.7c. The general structure of the warm season total volume transport streamfunction (Figs. 6.13a) is found to be similar to that of the cold season (Fig. 6.14a), this seems to show that the depth integrated current does not vary much between the two seasons. In fact the current direction is nearly constant during both seasons but its strength varies slightly. The seasonal variations of the current speed will be discussed later.

The volume transport seasonal difference fields are presented in Fig. 6.15. Although relatively noisy, some features should be pointed out. It seems that regions for which the warm season transport exceeds the cold season transport (positive values in Fig. 6.15a) are mostly located near the Labrador and Greenland coasts (near coastal and slope regions) whereas regions for which the cold season transport is larger than the warm season transport (negative values in Fig. 6.15a) are found in deep regions (large values of H) including the central Labrador Sea. On average, a 2-5 Sv seasonal variability is found throughout the domain. In the Labrador Sea, the maximum volume transport found is 50.8 Sv during the warm season and this value drops to 49.9 Sv in the cold season.

The largest seasonal transport variability is found to the northeast of the island of Newfoundland (47°W, 51°N) where a ~11.8 Sv cycle is diagnosed (Fig. 6.15a). The volume transport is 46.1 Sv during the warm season (Fig. 6.13a) and increases to 57.9 Sv in the cold season (Fig. 6.14a). Although such a strong seasonal cycle is questionable, no suspicious T-S structures were found in this area. This region of the domain is found as being the location where the volume transport contribution from JEBAR is the most important : ~20 Sv in the warm season (Fig. 6.13b) and ~25 Sv during the cold season (Fig. 6.14b) which represents ~50% of the total volume transport in that region. Consequently, the seasonal cycle, in this region, is almost entirely due to the local JEBAR term (Figs. 6.15a and 6.15b). This statement can be generalized for the whole domain as the results show that over most of the domain the pattern of the volume transport seasonal variability (Fig. 6.15a) is strongly linked with that of the local JEBAR volume tranport (Fig. 6.15b). The larger transport diagnosed in the Labrador Sea, during the warm season is contradictory to the classical picture of a stronger subpolar gyre during the cold season.

The seasonal transport variability due to seasonal variations in the reference boundary values and in the local wind stress fields account for ~0.5-1.5 Sv each (Figs 6.15c and 6.15d) with, as expected, the strongest transport found during the cold season during which stronger wind stresses are observed. The positive values in Labrador Sea, in Fig. 6.15a, are again due to the seasonal variability of the JEBAR term which dominates the overall seasonal variability.

The seasonal variations of the JEBAR term are due to the seasonality of the buoyancy forcing associated with the convection, the ice formation/melt and the freshwater export from the Hudson and Baffin Bays.

As the seasonal cycle is restricted to near surface and intermediate waters, the seasonal variability of the local JEBAR transport of the the top 1500m was estimated using the potential energy fields shown in Figs. 6.2a and 6.3a (by setting both the wind stress and boundary reference values to zero everywhere). The resulting field was very smooth, contrary to those presented in Figs. 6.15 b-c, showing positive values of 1-3 Sv all over the domain. These positive values indicate that the local JEBAR transport, induced by top 1500m of the water column, is stronger during the warm season.

Lazier and Wright (1993) analyzed current meter data obtained discontinuously from 1978 to 1988 offshore of Hamilton Bank using mooring lines which were oriented across the isobath in that region. Their results show that the maximum current speeds throughout the water column, and the strongest volume transport are found during the cold season from December to March (~6 Sv in February compared to ~2 Sv in September, see their Fig. 17). Figure 6.15a seems to reproduce this feature, although with a weaker signal of ~2 Sv, which is mostly due to the combined seasonal variabilities (~-2 Sv) from the reference boundary values and wind stresses (Figs. 6.15c and d). In the same region the local JEBAR variability field from the top 1500m shows positive values of 1-2 Sv. As in the Hamilton Bank region the overall seasonal variability from the local JEBAR is nearly zero (Fig. 6.15b), this emphasizes the role played by the lower section of the water column which, in that region, must counterbalance the upper 1-2 Sv. The main question is how much reliability can be put into the local JEBAR seasonal variability from the lower section of the ocean. Unfortunately, this question is not answered in this thesis.

6.6 The seasonal current variations

The horizontal surface current fields, for the warm and cold seasons, are presented in Figs. 6.16 a and b, respectively. A comparison between these two figures shows that the direction does not vary much from the cold to the warm season (see also Figs. 6.9), and hence the emphasis in this section will be on the seasonal speed variations. Figure 6.17 shows the seasonal current variations ($\vec{v}_{warm}$- $\vec{v}_{cold}$) for the whole domain at various depths. In Fig. 6.17, vectors in opposite direction to those shown of Figs. 6.9 or 6.16 should be interpreted as the cold season current speeds being larger than the warm season current speeds. At the ocean bottom (Fig. 6.17a) there are very small differences between

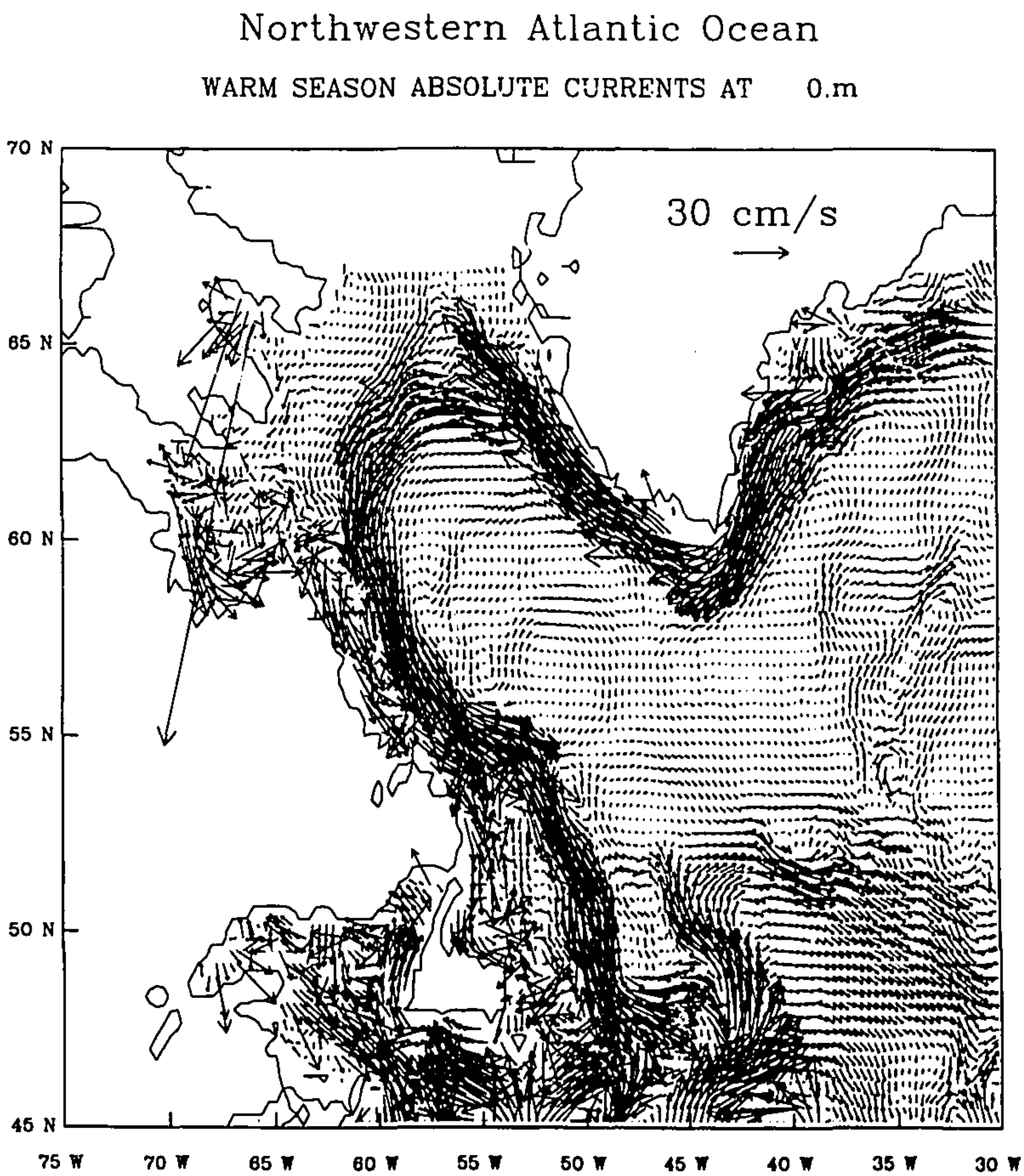

Figure 6.16: Northwestern Atlantic Ocean horizontal currents at surface, derived using the Mellor *et al* (1982) method, for a) the warm season (1910-89),

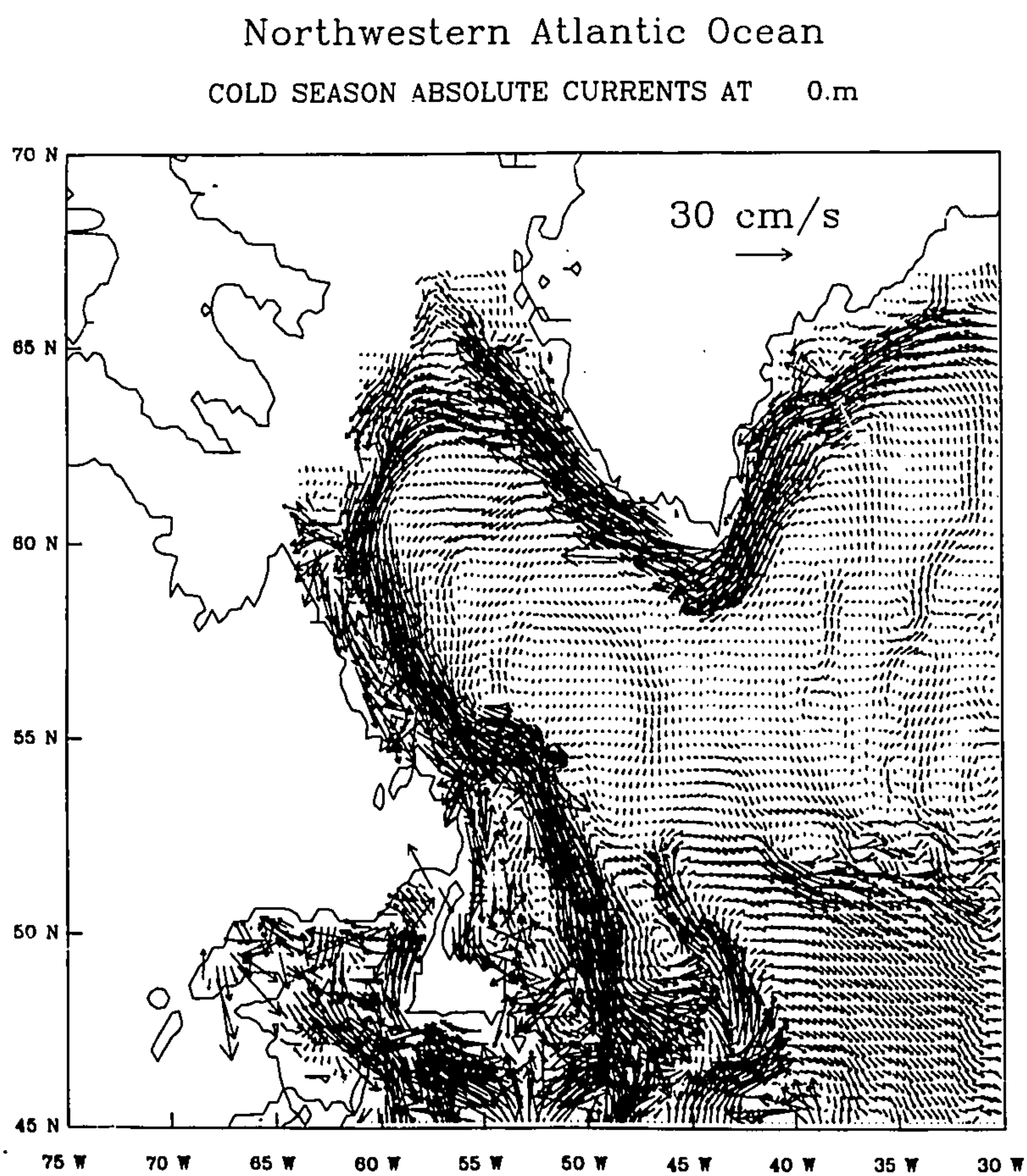

Figure 6.16 cont: and b) the cold season (1910-89).

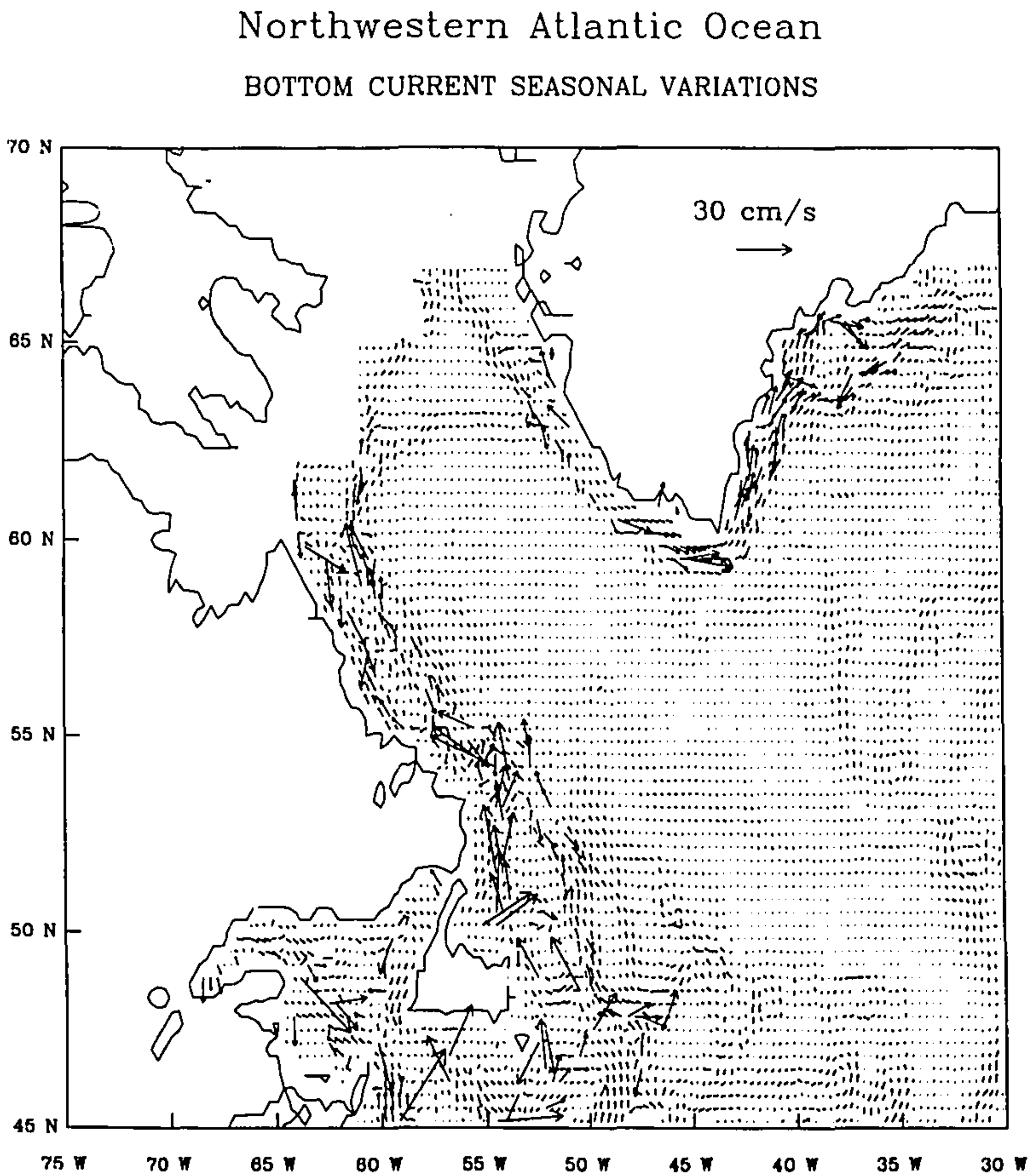

Figure 6.17: Seasonal current variations ($\vec{V}_{warm}$-$\vec{V}_{cold}$) at a) the bottom of the ocean,

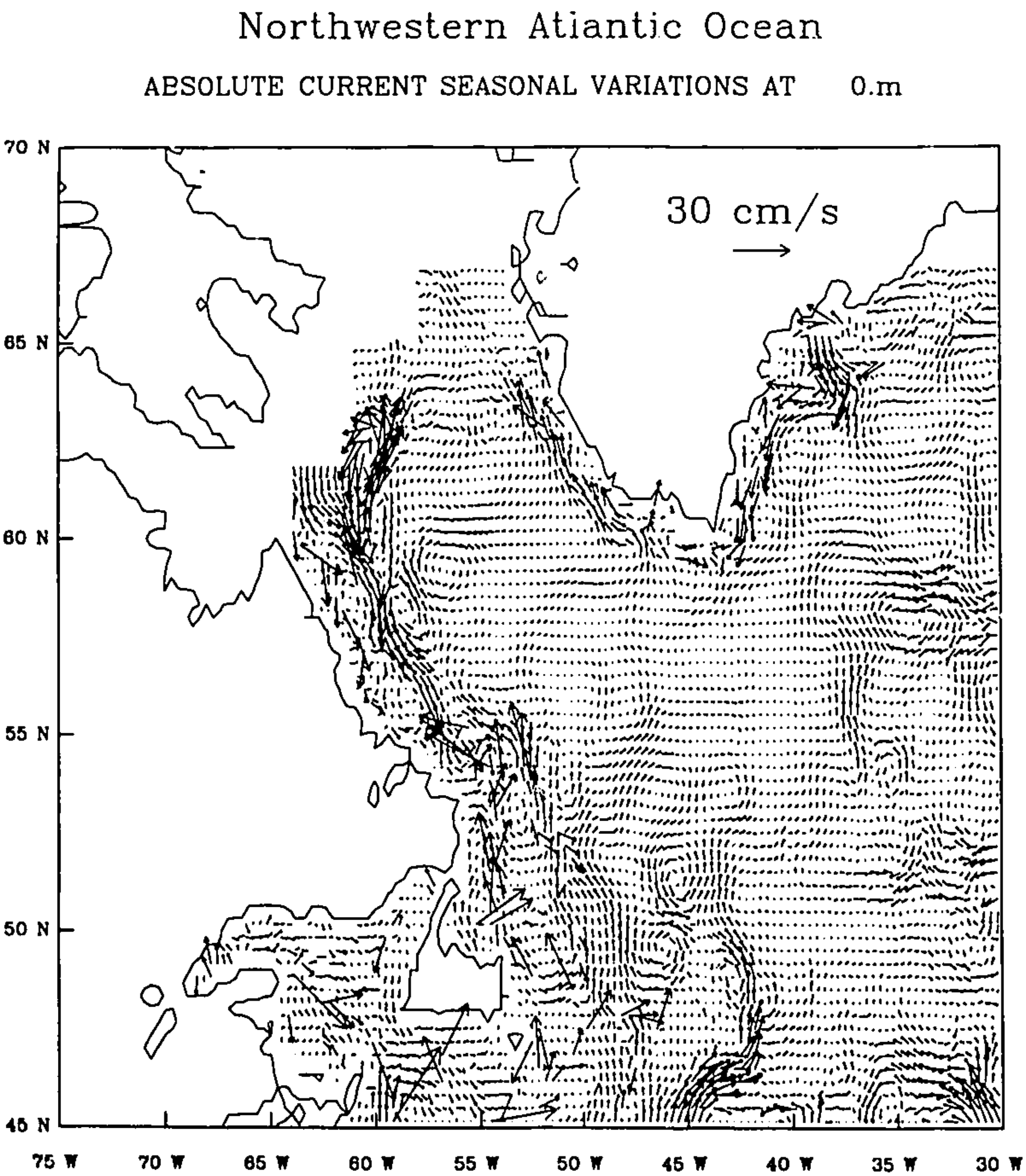

Figure 6.17 cont: b) 0m,

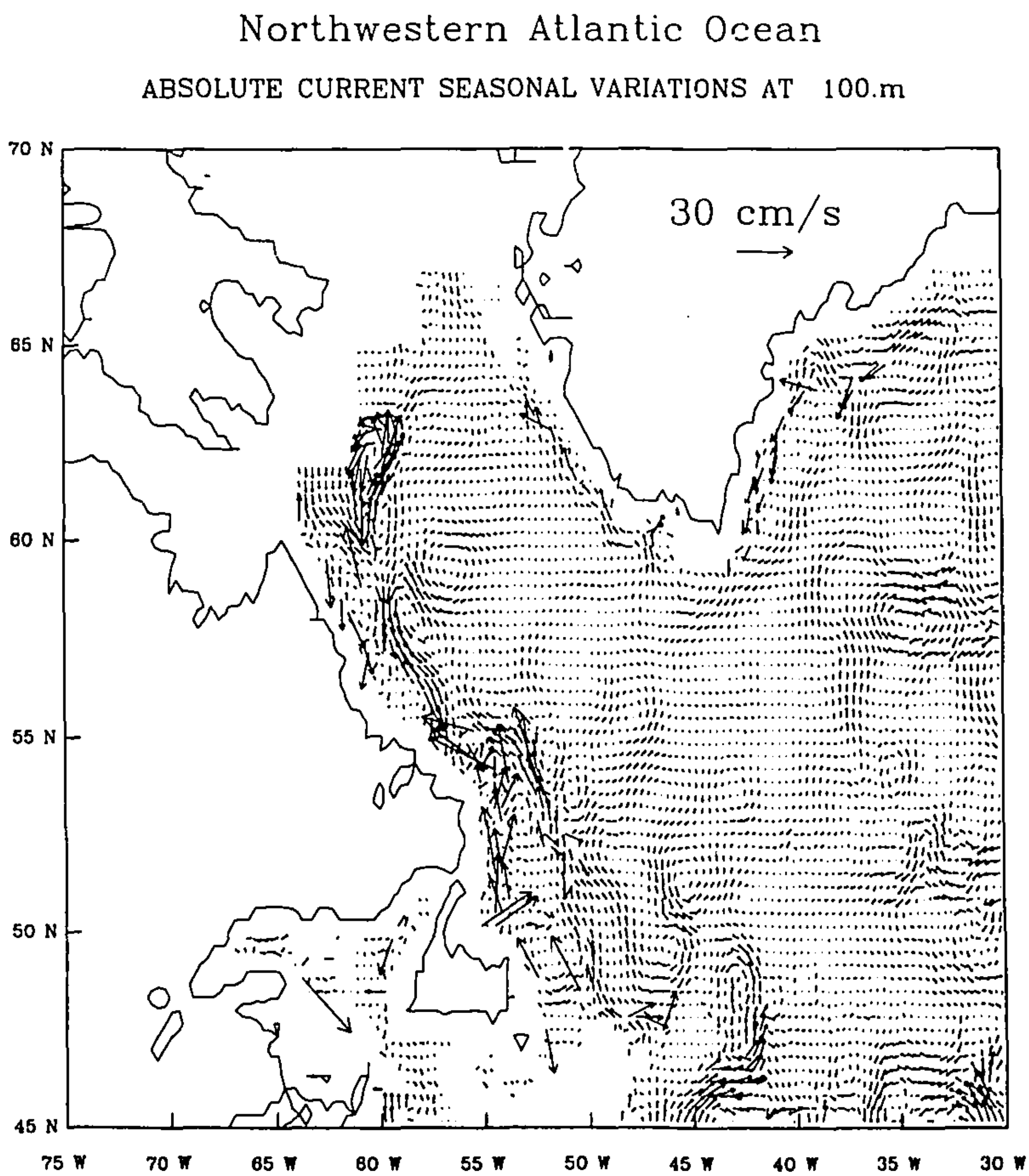

Figure 6.17 cont: c) 100m,

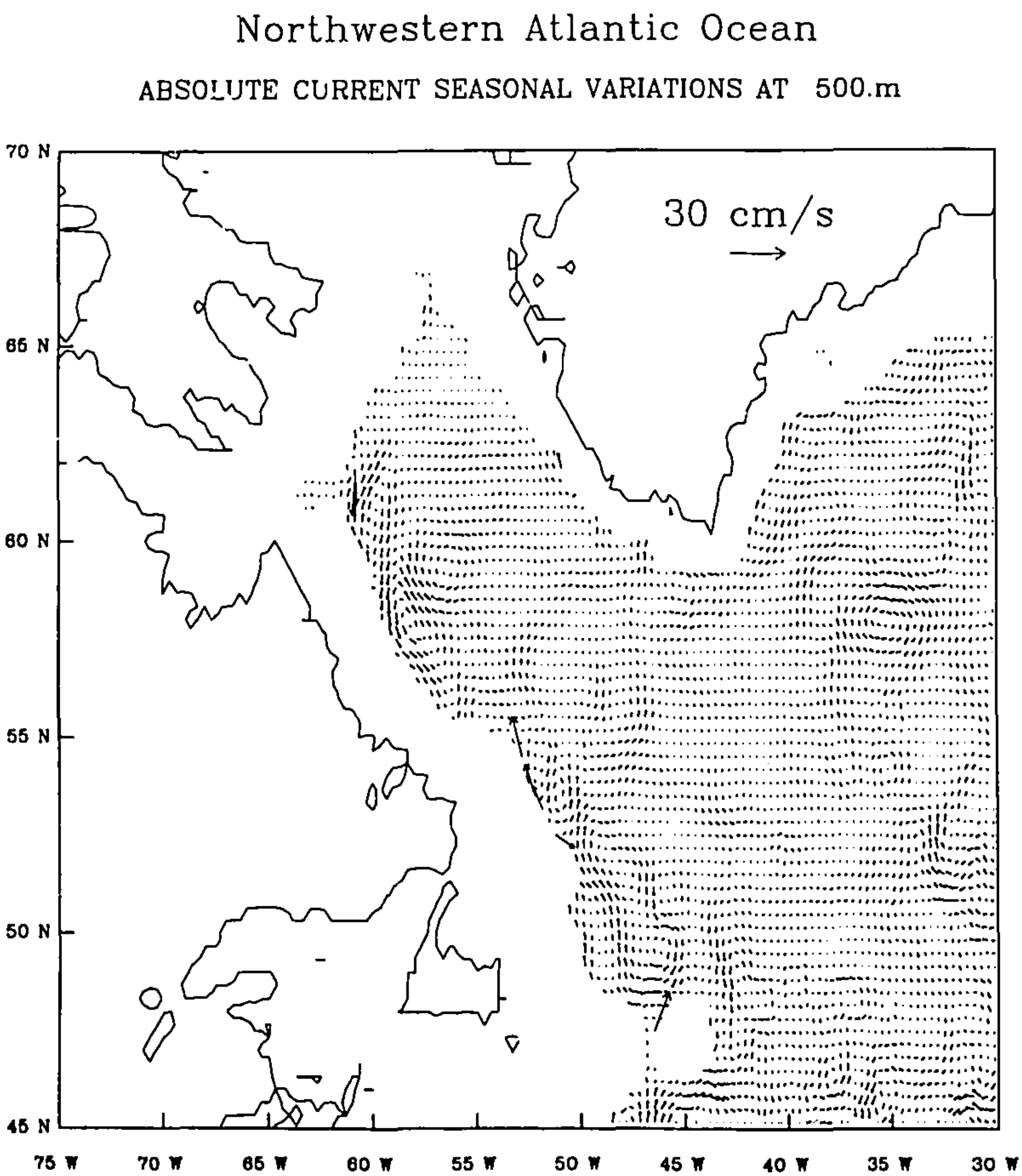

Figure 6.17 cont: d) 500m,

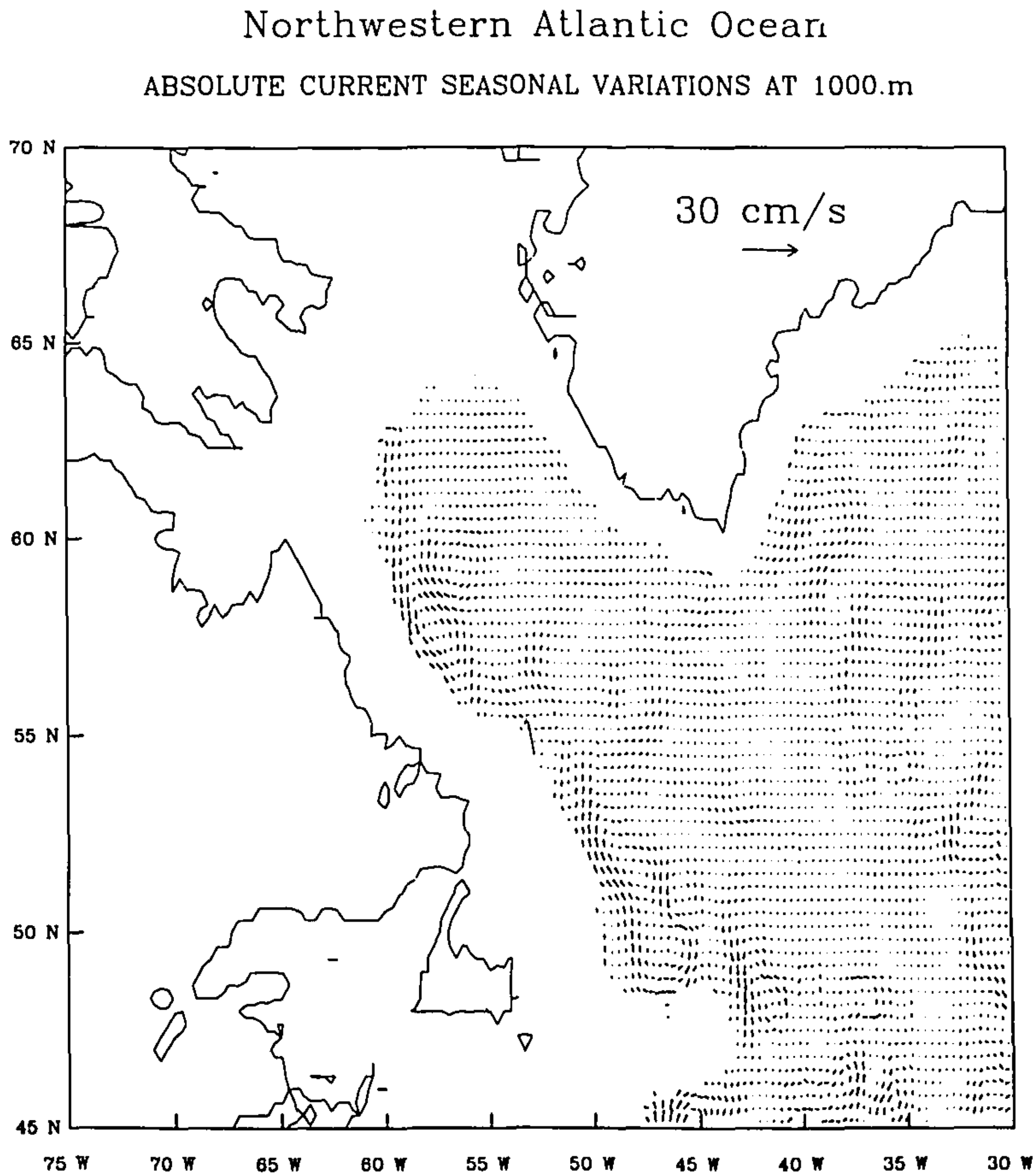

Figure 6.17 cont: e) 1000m,

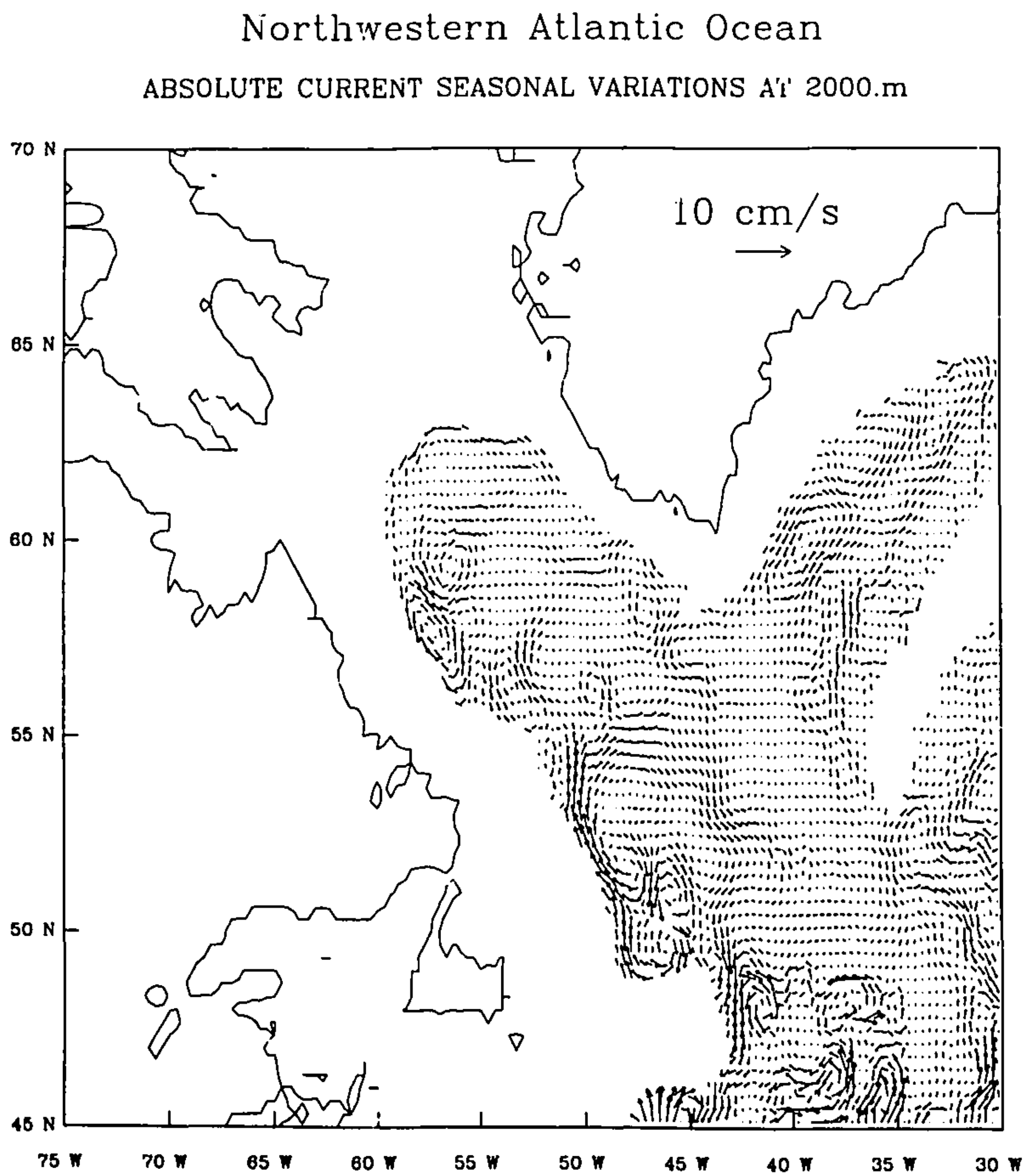

Figure 6.17 cont: f) 2000m,

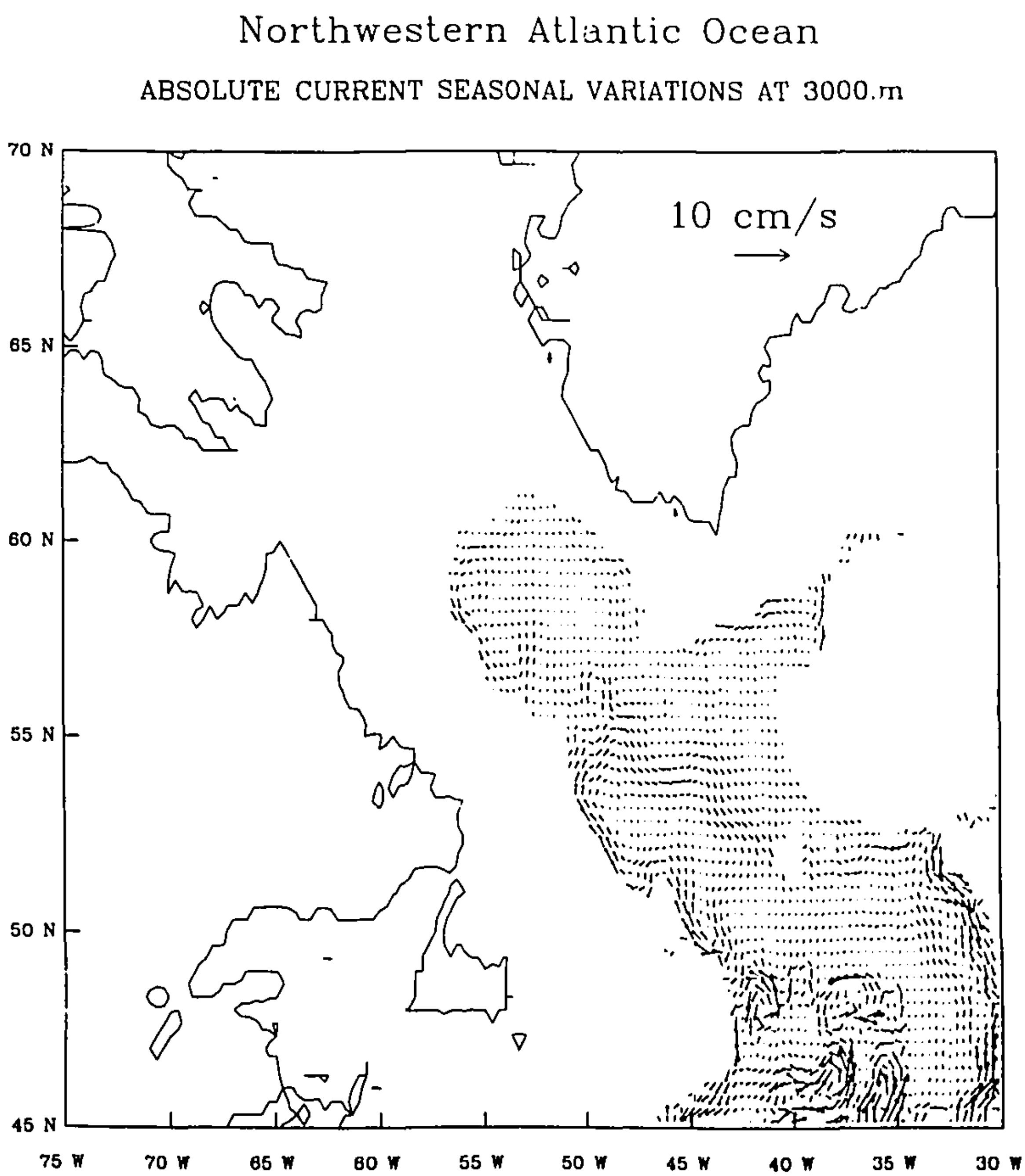

Figure 6.17 cont: and g) 3000m.

the two seasons in central and deep regions. Most of the large vectors are found near coastal regions, in the 0-1000m isobath range. Along the shelf and slope regions of Labrador and Greenland, a stronger bottom circulation is found during the cold season (Fig. 6.17a). The horizontal seasonal current variation fields (Figs. 6.17 b-g) show many eddy structures throughout all the water column. The positions of these eddies were found to be associated with those seen in the volume transport streamfunction seasonal variability field (Fig. 6.15a).

In general, the seasonal current variations fields (Figs. 6.17 b-f) show that the cyclonic circulation around Greenland and along the Labrador Coast is stronger during the warm season. Many of the seasonal variations below ~1000m are thought to be suspicious as the T-S fields (see Chapter 3) do not seem to support large current variations. Notice that the cross-shelf flow discussed in section 6.4 seems to weaken during the cold season and that this weakening can be seen up to ~3000m (Fig. 6.17g). Offshore of the southern Labrador coast, the poleward vectors seen throughout all the water column indicate a stronger circulation during the cold season which is associated with the JEBAR driven circulation discussed in the previous section. Figure 11 of Lazier and Wright (1993) shows some time series of the average along-isobath speed from current meter data which were located near Hamilton Bank (onshore from the other moorings discussed above). These show a broad peak reached in September-October. In general at all depth, the time series presented by Lazier and Wright (1993) in their Fig. 11 show that the along-isobath component of the velocity tends to increase in spring, reaches a broad maximum at the end of the summer and then decreases in the winter. Results of Fig. 6.17 in the coastal regions of Labrador tend to agree with Lazier and Wright (1993).

A vertical section along 53.33°N of the seasonal speed variations between the two seasons is presented in Fig. 6.18a and the seasonal variations of the poleward current component is shown in Fig. 6.18b. These figures show vertical changing sign bands which are associated with the sign changes of the $\Delta\psi$ zonal gradient according to:

$$\Delta V = -\frac{m}{R}\frac{\partial}{\partial\lambda}\Delta\psi \tag{6.1}$$

where:

$$\begin{aligned} \Delta V &= V_{warm} - V_{cold} \\ \Delta\psi &= \psi_{warm} - \psi_{cold} \end{aligned} \tag{6.2}$$

Figures 6.19 show the seasonal variations of the volume transport streamfunction through 53.33°N, offshore of the southern Labrador coast. They illustrate that the local JEBAR term (Fig. 6.19b) dominates the other terms (Figs. 6.19c-d). The zonal gradient of $\Delta\psi$ is positive, on the shelf, up to 53°W (Fig. 6.19a) which implies that ΔV is negative in that region. A negative ΔV in a region where the mean current is southward implies a stronger southward current during the warm season. These negative ΔV values are not seen on Fig. 6.18b which could be due to the bottom friction that was set equal to zero in Eq. 5.9. The sign of the zonal gradient of $\Delta\psi$ switches to negative over the slope near ~53°W so that stronger currents are now diagnosed during the cold season. A speed difference of ~14 cm/s is found near the surface at the shelf break (Fig. 6.18a). Other sign changes

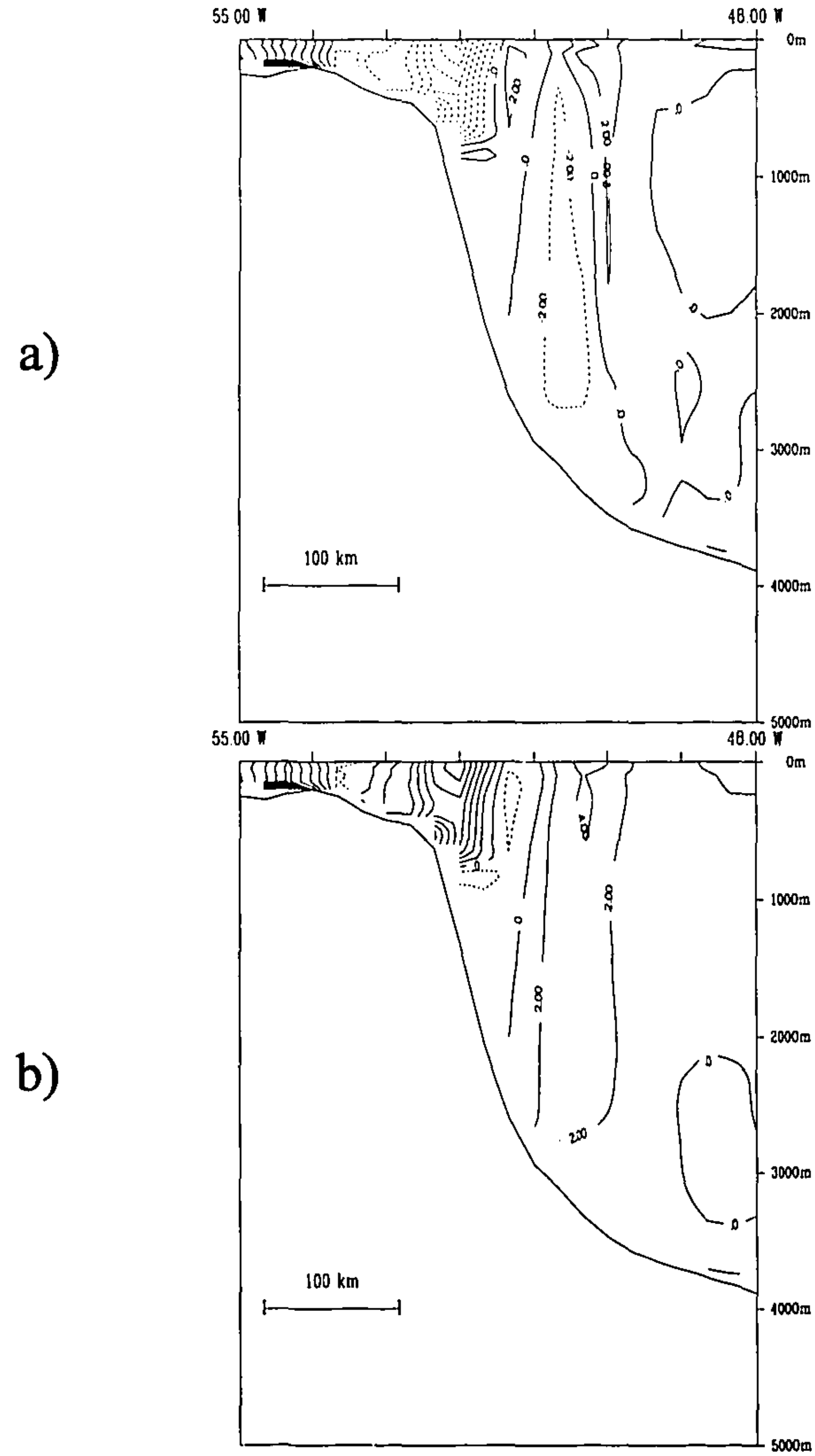

Figure 6.18: Vertical profile along 53.33°N for the seasonal variations (warm-cold) of a) the current speed (cm/s) and b) the northward current component (cm/s).

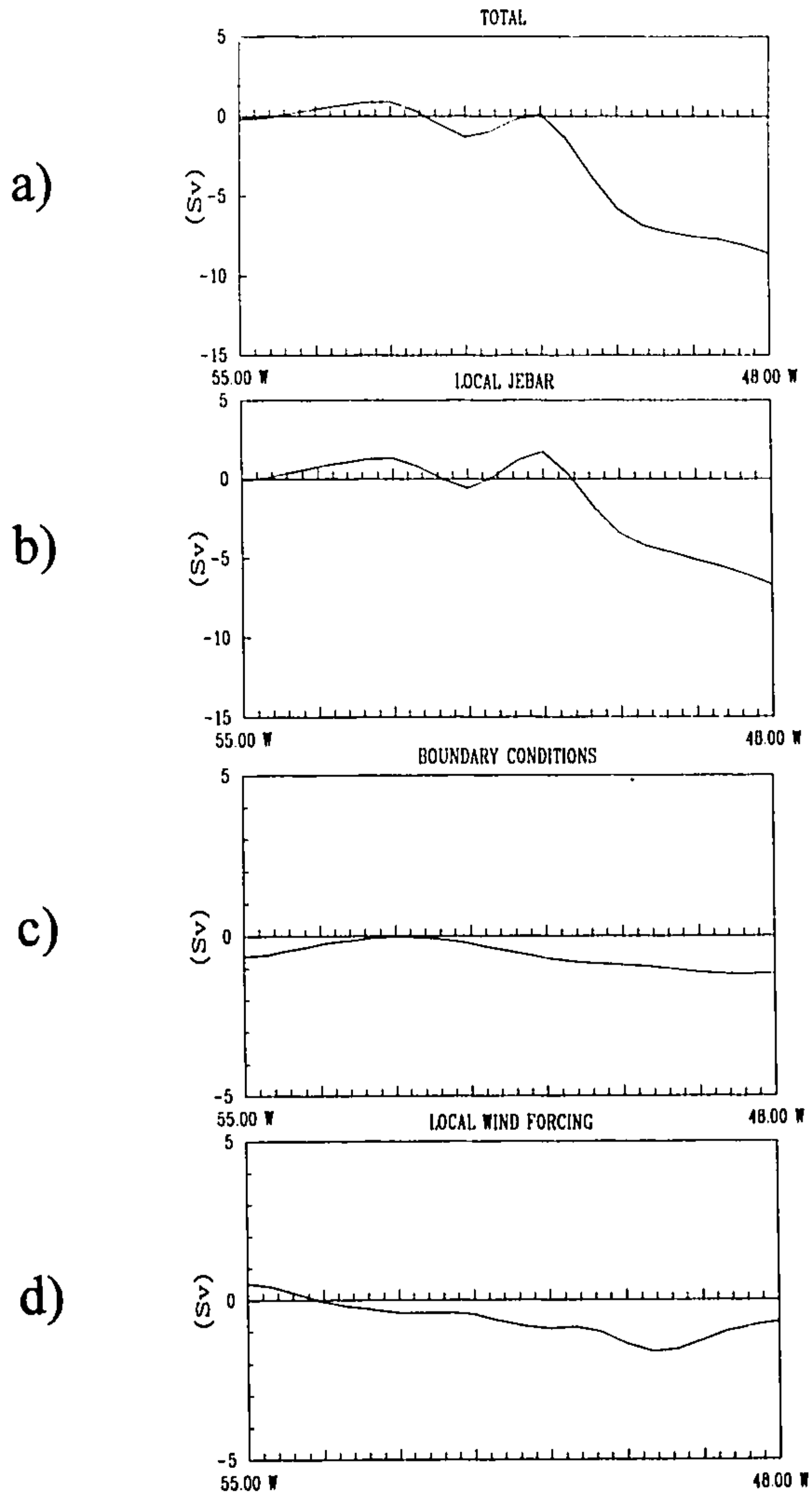

Figure 6.19: Seasonal transport variation (Sv) through 53.33°N (warm-cold) a) total, b) due to the local JEBAR, c) due to the boundary conditions and d) due to the local wind forcing.

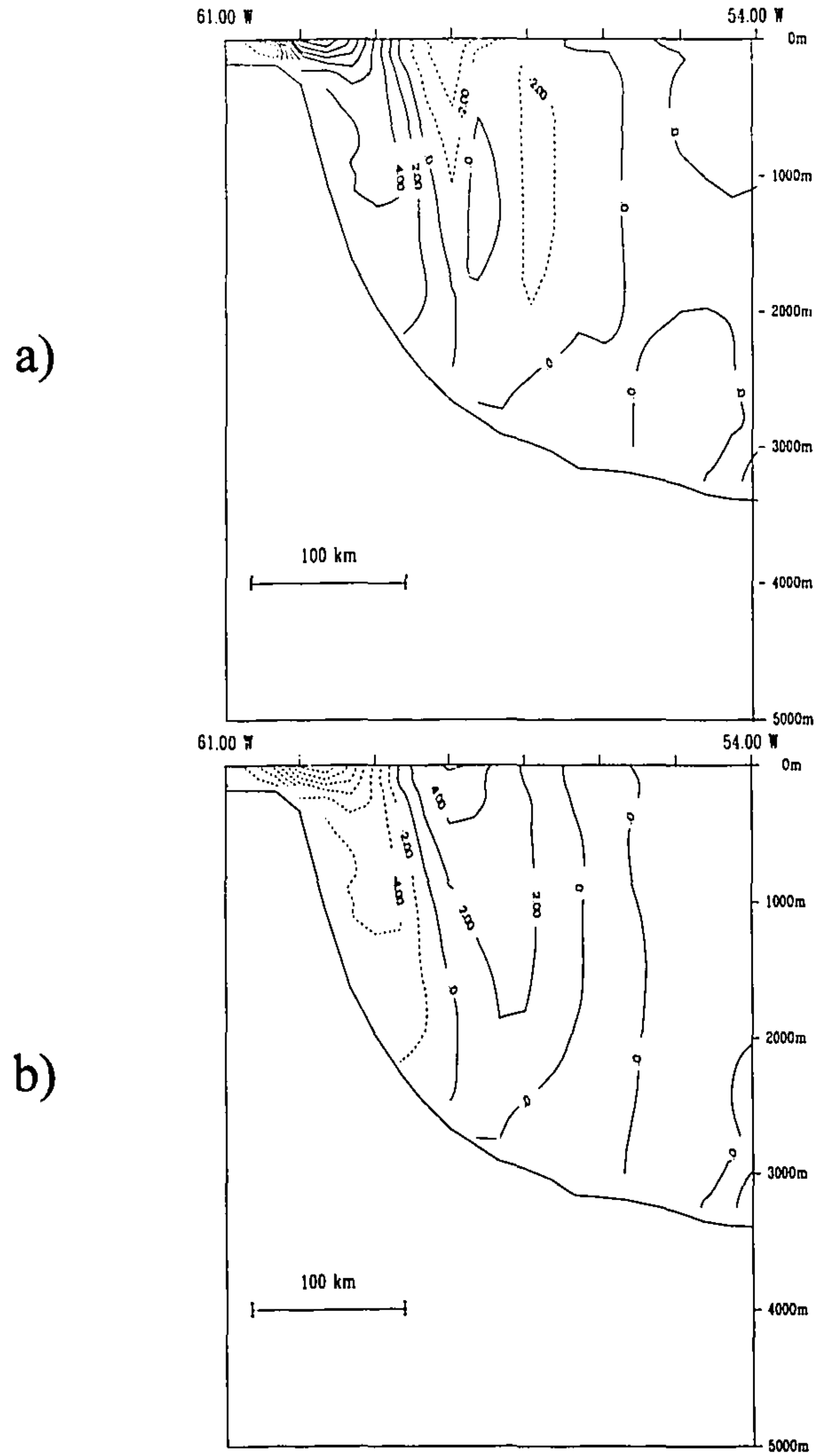

Figure 6.20: Vertical profile along 58.33°N for the seasonal variations (warm-cold) of a) the current speed (cm/s) and b) the northward current component (cm/s).

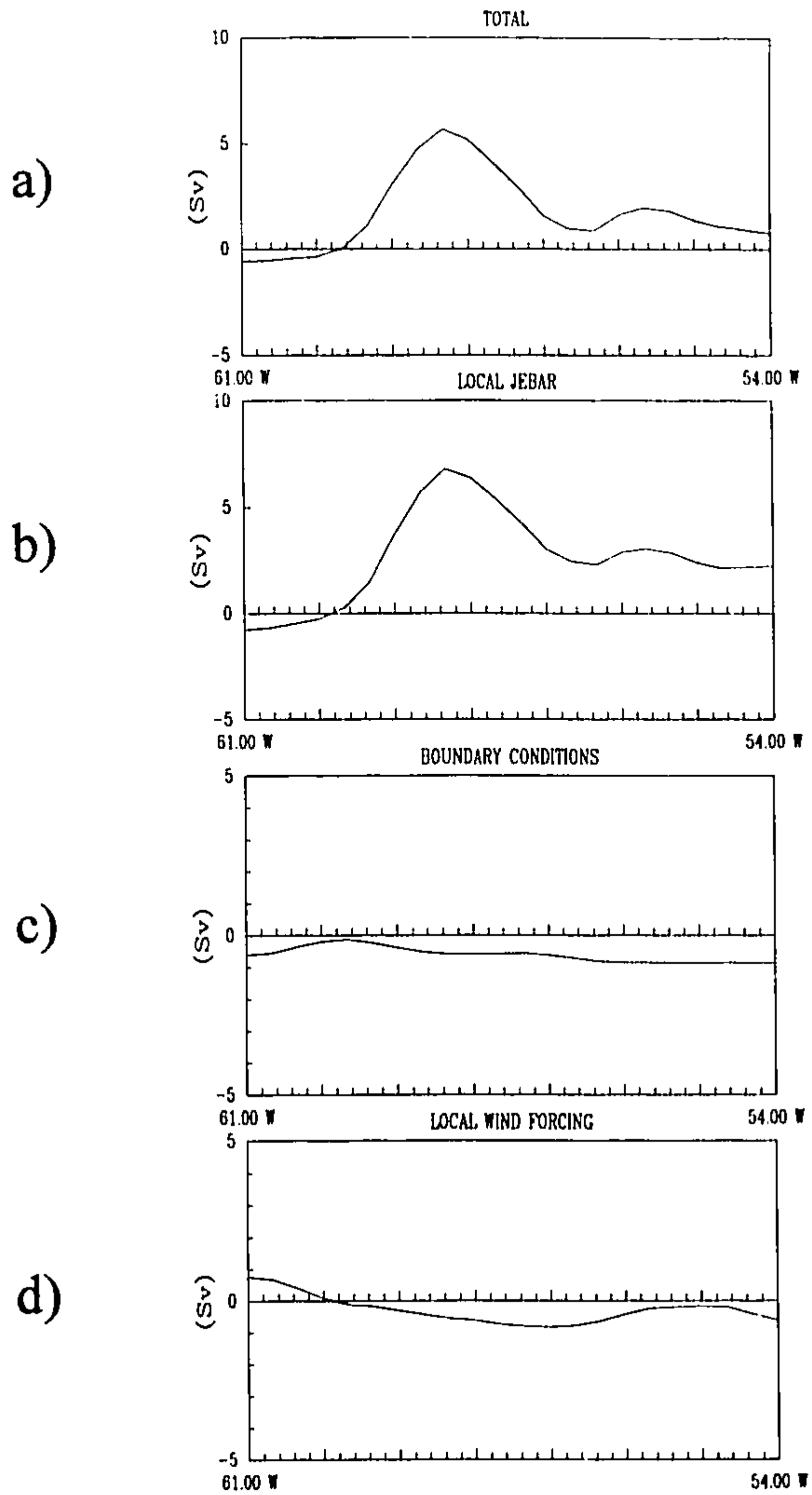

Figure 6.21: Seasonal transport variation (Sv) through 58.33°N (warm-cold) a) total, b) due to the local JEBAR, c) due to the boundary conditions and d) due to the local wind forcing.

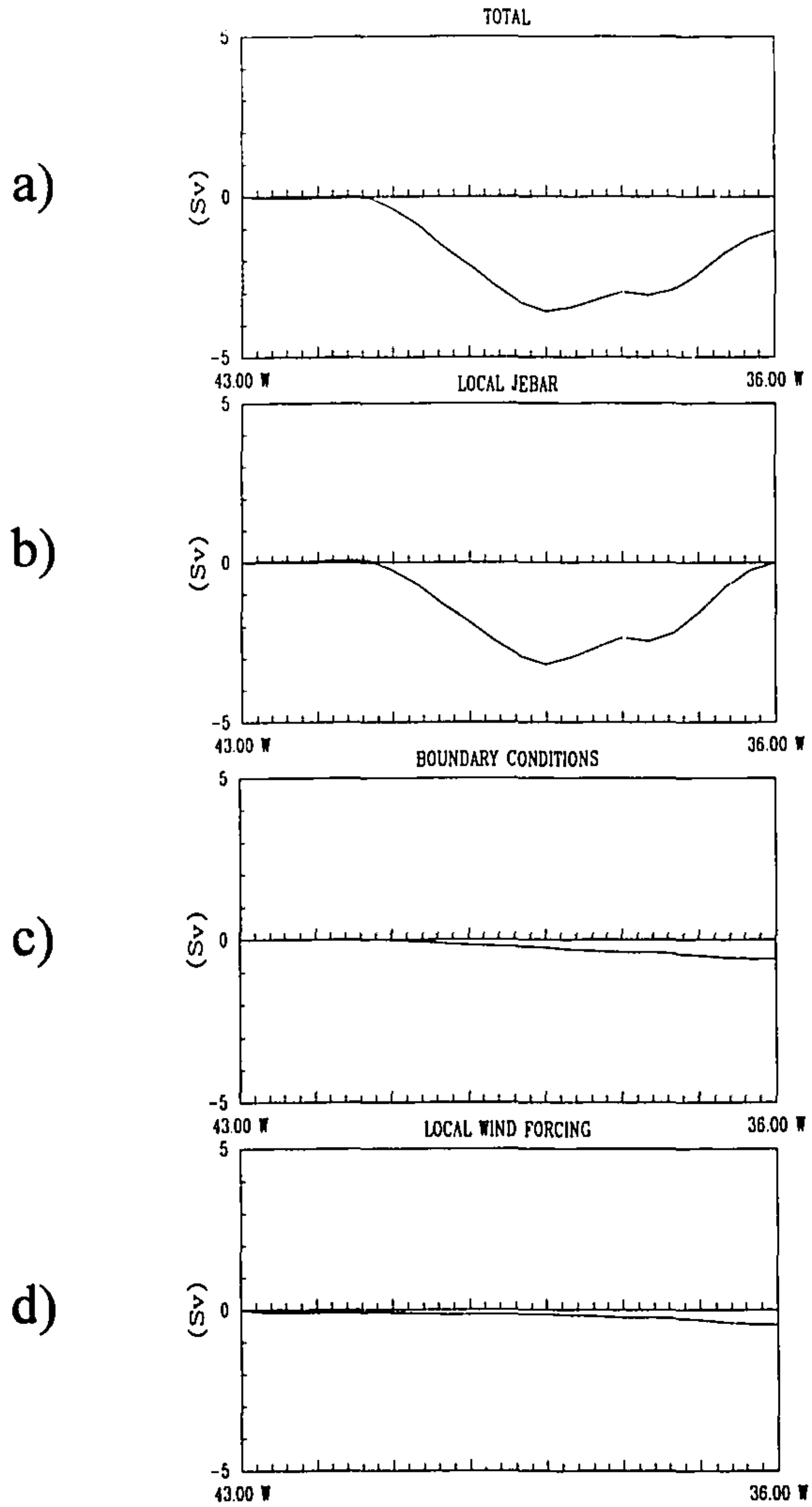

Figure 6.22: Seasonal transport variation (Sv) through 62.67°N (warm-cold) a) total, b) due to the local JEBAR, c) due to the boundary conditions and d) due to the local wind forcing.

a)

b)

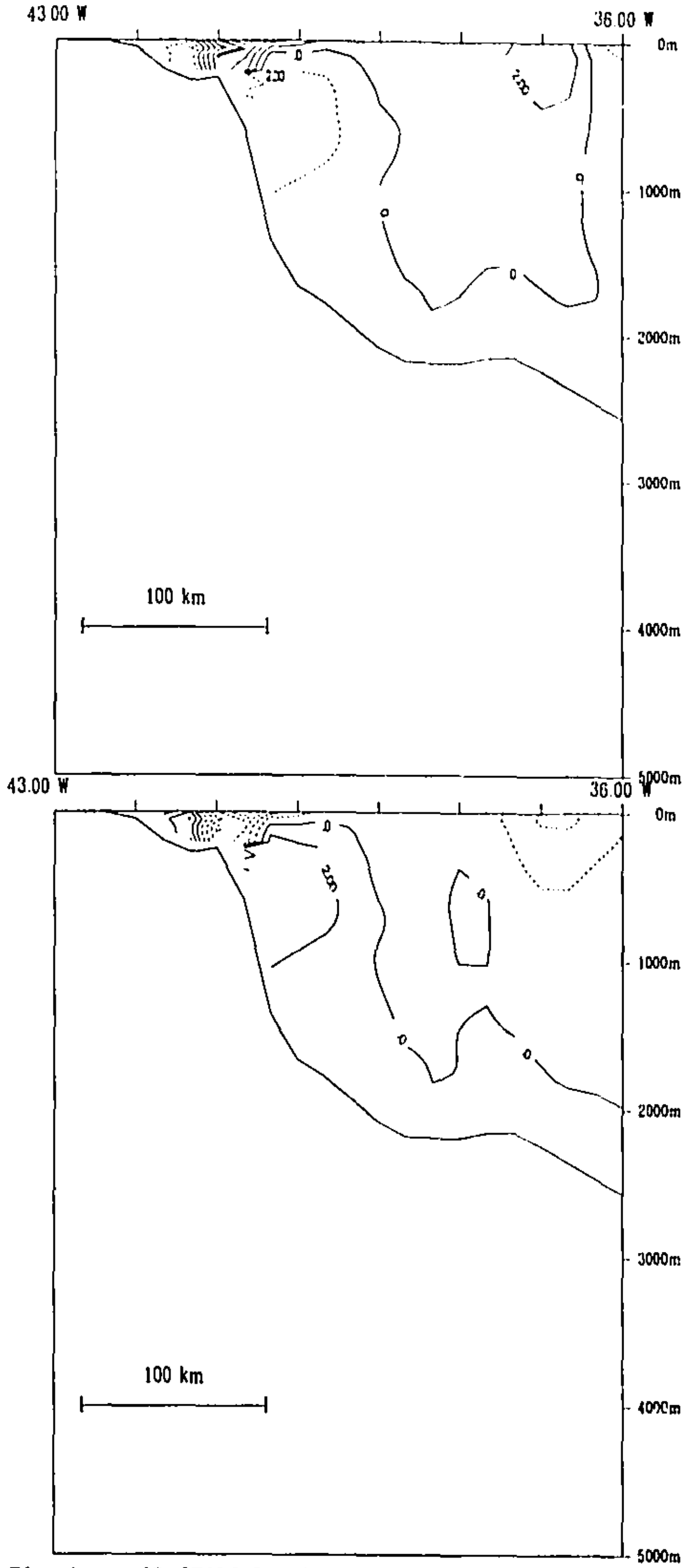

Figure 6.23: Vertical profile along 62.67°N for the seasonal variations (warm-cold) of a) the current speed (cm/s) and b) the northward current component (cm/s).

can be seen near 52°N and 53°N but they are associated with smaller speed differences. In the north of the Labrador Sea, the seasonal speed variation section (Fig. 6.20a) shows a different situation where the strongest currents are found during the warm season on both the shelf and slope regions. The strongest speed difference of ~14cm/s is found in near-surface waters in the bottom slope region. These seasonal speed changes are mostly due to changes in the north-south component of the current (Fig. 6.20b). The negative sign should be interpreted as the $V_{warm}<V_{cold}$ and that V_{warm} is greater in magnitude than V_{cold}. As in the previously discussed region (on southern Labrador coast) the seasonal changes of the volume transport ($\Delta\psi$) are found to be driven by the local JEBAR (Fig. 6.21a-b) with very little influence from the local wind stress field and from the reference boundary values (Fig. 6.21c-d). The zonal gradient of $\Delta\psi$ is found to be positive up to 58.4°W and then negative up to 56.4°W, these sign changes can also be seen in Figs. 6.20.

On the east Greenland coast, the volume transport seasonal variations ($\Delta\psi$) are again found to be driven by the local JEBAR forcing (Fig. 6.22). The zonal gradient of $\Delta\psi$ is negative up to ~39°W which in turn implies that ΔV is positive (Fig. 6.22). The situation in the Irminger Sea is slightly different from that in the Labrador Sea as the currents are found to be stronger in near-surface waters during the warm season and in deeper waters during the cold season (Figs. 6.23). At the shelf break a ~10 cm/s speed difference is found at the surface (Fig 6.23a). Notice that in this region, the seasonal transport variability due to local JEBAR from the top 1500m shows positive 1-2Sv values (warm-cold), which, again, brings up the question as to the reliability of the seasonal

JEBAR from the deeper regions of the ocean.

The results presented in the last two sections of this chapter suggest that JEBAR forcing is mostly driving the seasonal changes in the northwestern Atlantic Ocean. This conclusion implies that the seasonal changes due to seasonal variations in the wind stress field and reference boundary values do not seem to be important in comparison with the changes induced by the local JEBAR term. As mentioned previously, the seasonality of the JEBAR term is very likely linked to the seasonality of convection, ice formation and melt as well as the freshwater advection from Hudson and Baffin Bays.

CHAPTER 7: INTERANNUAL AND INTERDECADAL VARIABILITY OF THE NORTHWESTERN ATLANTIC OCEAN

7.1 Methodology

As mentioned in the introduction, the water mass properties (T-S) of the Atlantic Ocean are subject to long timescale variability; this chapter is an attempt to determine how much variability can be seen in the temperature and salinity fields and the impact of these changes on the circulation. The first step of the analysis is to determine the *warm season* T-S fields for the periods 1950-64 and 1965-81 by applying the objective analysis scheme described in Chapter 2. The differences between the present objective analysis scheme and that which was previously used are: 1) a coarser resolution of 1/2°x1/2°; 2) only two iterations are used with influence radii of 500 and 200 km; and 3) the first guess field (see Eq. 2.1) is the *warm season* 1910-89 analysed T-S field, described in Chapter 3, interpolated onto the coarser grid. The volume transport streamfunctions for these periods are then diagnosed by applying the Mellor *et al* (1982) method as described in Chapter 4.

The last subsection of the thesis contains an attempt to seek shorter time scale climatic changes. The objective analysis is applied in two subregions to determine the T-S changes that occured between various periods. The selected periods are defined as 1959-64, 1967-72, 1975-80 and 1983-88. The two subregions that were chosen are the Hamilton Bank and Flemish Cap regions (see boxes on Fig. 1.1). These were selected because of both their importance to the fishery industries and as the data coverage was good in these regions. This latter analysis is restricted to the warm season although, a resolution of 1/3°x1/3° is once more used.

7.2 The 1950-64 and 1965-81 T-S fields

The positions of the temperature and salinity stations for the 1950-64 and 1965-81 periods were presented in Figs. 2.6 and 2.7 and were already discussed in Chapter 2. The objective analysis was not applied in regions were the lack of data was obvious; these regions are located west of 70°W, north of 67°N and near the southeastern corner of the domain (Figs. 7.1). The Akima (1978) interpolation scheme was not applied in these three regions. Notice that the two periods do not have the same duration since some sections taken in the Irminger Sea during 1981 had to be included in the data set (without these stations the Irminger Sea region could not be objectively analysed for the 1965-81 period). Figures 7.1 show the undetermined gridpoints from the objective analysis at 1000m and 2000m for both periods. The undetermined gridpoints for the 1950-64 period are mostly located in the southern portion of the domain (Fig. 7.1c) with some found offshore from the Labrador coast (Figs. 7.1a and c); for the 1965-81 periods they are mainly found in Reykjanes Ridge region (Figs. 7.1 b and d).

The filtered and interpolated T-S fields at the surface, 500m, 1000m and 2000m are presented in Figs. 7.2 and 7.3, respectively. The T-S fields do not differ radically from those presented in Chapter 3 for the 1910-89 warm season analysis – the same strong gradients are found over the slope (Figs. 7.2 and 7.3). At the surface, the most noticeable feature is the weakening of the cross-shelf isohaline in the Labrador Sea during both the 1950-64 and the 1965-81 analyses (see Fig. 7.2 a-b and Fig. 3.11a), although they are apparent at subsurface levels (eg. Figs. 7.2c and 7.2d). The difference fields (1965-81 analysis minus 1950-64 analysis) for the salinity and temperature are shown in Figs. 7.4 and 7.5 (hereafter, $\Delta S=S_{1965\text{-}81}-S_{1959\text{-}64}$ and $\Delta T=T_{1965\text{-}81}-T_{1959\text{-}64}$, T being the *in situ* temperature). These figures show large and smooth structures.

At the surface, in offshore regions, negative ΔS values are found over most of the domain with values from -0.6 to -0.1 psu (Fig. 7.4a). These negative values are likely associated with the *Great Salinity Anomaly* which was discussed in Chapter 1. Positive ΔS values from 0-0.8 psu are found in coastal regions, along the Labrador and east Greenland coasts. Positive ΔS values can also be seen in these same regions in Levitus's (1989a – Fig. 14) at a depth of 250m. Notice that Levitus used shorter periods (1955-59 and 1970-74) which are a susbet of this analysis. In deeper waters the sign of ΔS switches to positive (Figs. 7.4 b-d). The same sign change is also seen in the results of Levitus (1989a – see his Fig 11). At a depth of 2000m, ΔS values of 0.02 psu are found in the Labrador Sea (Fig. 7.4d). In Fig. 7.4c, the contours found near 35°W and 50°N are probably spurious and created by the interpolator while filling up the undetermined gridpoints in that region (Fig. 7.1a) in the 1950-64 period.

At the surface, the ΔT field shows a more complicated structure than the ΔS fields (Fig. 7.5a), three positive regions can be seen in the Irminger Sea, in northern Labrador

Sea and in the NAC region (Fig. 7.5a). The maximum values found in these regions are: ~3°C in the NAC region as well as in the Irminger Sea and ~0.6°C in the northern Labrador Sea. Negative ΔT values are found otherwise, with values from -3°C to -1°C (Fig. 7.5a). At a depth of 500m and 1000m, positive ΔT values (~0.2-0.4°C) are found in the whole Labrador Sea while negative ΔT values are still found near the eastern border and in the NAC region (Fig. 7.5 b-c). Notice that Levitus (1989a) also found negative ΔT values near the position of our eastern border (see his Fig. 10). At a depth of 2000m, almost no temperature variations are found (Fig. 7.5d).

These ΔT and ΔS sign changes between the near-surface waters and intermediate waters are likely associated with the deep water formation through convection in the Labrador Sea. During the later period, Lazier (1980) has reported that the deep water formation weakened during the *G.S.A* years. If deep water formation is suppressed, then the cold and fresh surface waters are not mixed with the warmer and saltier intermediate waters. These ΔT and ΔS sign changes with depth are very likely the signature of the *G.S.A*. which was advected in the northwestern Atlantic Ocean during the 1965-81 period.

7.3 The 1950-64 and 1965-81 volume transport streamfunctions

The volume transport streamfunctions, for the 1950-64 and 1965-81 periods, were estimated using the Mellor *et al* (1982) method as described in Chapter 4. The wind stress fields used in this analysis (Figs. 7.6) are the *annual mean* fields derived from the Comprehensive Ocean-Atmosphere Data Set (COADS) for the 1950's and 1970's (see Da

Silva, 1991). The $1°\times1°$ wind stress field was interpolated onto the $1/2°\times1/2°$ grid using the Akima (1978) interpolation scheme. The reference boundary values used for the eastern, northern and southern borders were obtained from the *annual mean* results of Greatbatch *et al* (1991) for the 1954-59 and 1970-74 pentads. As in the summer and seasonal analyses, a 9-point filter was applied and holes were filled up using the Akima (1978) interpolator. Notice the interpolator was once more not applied for Flemish Cap.

The volume transport streamfunctions are presented in Figs. 7.7. A comparison between the 1950-64 period streamfunction (Fig. 7.7a) and the one for 1965-81 period (Fig. 7.7b) shows that the transport over most the domain seems to be weaker during the later period. The volume transport interdecadal variability ($\Delta\psi$ where $\Delta\psi$ is defined as $\psi_{1965\text{-}81}$-$\psi_{1959\text{-}64}$) field (Fig. 7.9a) shows that the cyclonic circulation is weaker by 5-6 Sv in the Labrador Sea and by 4 Sv in the Irminger Sea. These values are in quite good agreement with the weakening of the subpolar cyclonic gyre diagnosed by Greatbatch *et al* (1991) between the 1950-64 and 1965-81 pentads (see their Fig. 4b). Some positive $\Delta\psi$ can be seen in the northeast of Newfoundland (+8 Sv) and in the Irminger Sea (+6Sv). The pattern of the interdecadal variability due to the local JEBAR (Fig. 7.8b) is similar to that of the total interdecadal variability (Fig 7.8a) which shows that the interdecadal variability is mostly driven by the local JEBAR. About 50-70% of the total weakening is due to the decrease, during the second period, of the volume transport induced by the local JEBAR. The remaining 30-50% is due to the variability of the boundary reference values (Fig. 7.8c). Notice that the appearance of closed contours on Fig. 7.8c is due to the smoothing and the plotting package which were used. As in the seasonal analysis, the local wind effect is found not to be very important here (Fig. 7.8d). The fact that the variability from the reference boundary values and from local wind stress field contribute less than that induced by the local JEBAR is important, as both the wind stress fields and the reference boundary values were set up for the pentadal analysis of Greatbatch *et al* (1991), and not for the longer periods studied in this analysis.

The interdecadal changes discussed above are likely associated with data taken during the *G.S.A.* years. Dickson *et al* (1988) has presented a simple scenario where a negative salinity anomaly is advected around the subpolar gyre. Mysak *et al* (1990) showed that a more complex situtation occured where the negative salinity anomaly is linked with ice conditions that are conditioned by other factors, like winter air temperature and river runoff. Also, Mysak *et al* (1990) associated interdecadal variations in river runoff with atmospheric changes through a teleconnection pattern.

The Labrador and Greenland Seas are the two regions where the deep water is expected to be formed. As Dickson *et al* (1990) reported no large variations in the water mass properties of the DSOW, which was sampled from June 1987 to July 1989, this is perhaps an indicator that the source of interdecadal variability is within the Labrador Sea.

7.4 The T-S fields in the subregions

The two subregions studied in this section are the Hamilton Bank (50°W-57°W and

52°N-57°N) and Flemish Cap (42°W-55°W and 45°N-50°N) regions (see Fig 1.1). The objective analysis was applied onto a 1/3°x1/3° grid (as in the previous analysis) and only two iterations were used with influence radii of 500km and 200km. Notice that the first guesses for the objective analysis (see Eq. 2.1) were also the 1910-89 *warm season* T-S fields. The periods studied in this section are those mentioned in section 7.1, but as the data coverage varies from one period to another, not all the water column can be objectively analysed. The top 1500m were objectively analysed for the 1959-64 and 1967-72 periods whereas for the 1975-80 period, the analysis was restricted to the top 500m due to a poor data coverage. For the 1983-88 period, the top 2750m were objectively analysed but the analysis was restricted to the temperature data because of the mysterious lack of salinity data in the 80's (see Fig. 2.1). Notice that the fields were then filtered and interpolated using the same procedures as before.

The salinity and *in situ* temperature fields, for both subregions at surface and 500m and for all periods, are shown in Appendix 1. In order to simplify the comparisons between the periods, the following definitions are introduced:

$$\begin{aligned} \Delta F_1 &= F_{1967-72} - F_{1959-64} \\ \Delta F_2 &= F_{1975-80} - F_{1967-72} \\ \Delta F_3 &= F_{1983-88} - F_{1975-80} \end{aligned} \qquad (7.1)$$

where F can either be the *in situ* temperature or the salinity (T, S).

Figures 7.9 present the $\Delta_1 S$ field for the Hamilton Bank region at the surface and at 500m. These figures show that in offshore regions surface waters tend to be fresher by 0.9 to 0.4 psu during the second period (1967-72, *G.S.A.* years) while onshore surface waters are saltier during the later period (Fig. 7.9a). The sign of $\Delta_1 S$ switches to positive in deeper waters (Fig. 7.9b) where saltier water (+0.02 psu) are found during the 1967-72 period. The surface $\Delta_1 T$ field (Figs. 7.10a) shows that colder *in situ* temperature are found during the *G.S.A* period with the temperature being colder by 0.2°C to 3°C over most the Hamilton Bank region. At a depth of 500m (Fig. 7.10b) a sign change is found (compare to the surface field), and the *in situ* temperature is now warmer during the *G.S.A* years by 0.2°C to 0.6°C. The $\Delta_2 S$ fields (Figs. 7.11) show that the sign of the salinity difference is almost exactly the opposite to that of $\Delta_1 S$ (Fig. 7.9) at both the ocean surface and in deeper waters. This suggests as the *G.S.A.* vanishes the salinity conditions prior to the G.S.A were recovered. The same situation is observed for $\Delta_2 T$ at 500m (Fig. 7.12b) with values of -0.6°C to -0.4°C. At the surface, the temperature is still found to decrease in the coastal and offshore regions (Fig. 7.12a) with $\Delta_2 T$ values of -1.5°C to -0.4°C. Notice that some positive $\Delta_2 T$ values are seen on Fig. 7.12a. The $\Delta_3 T$ field shows relatively weak temperature variations in deep waters (Fig. 7.13b). In near surface waters $\Delta_3 T$ (Fig. 7.13a) shows a more complex pattern with, in coastal regions, the temperatures still decreasing (-2°C to -1°C) while offshore and in slope regions the temperature trend is positive with values of +1°C.

Figures 7.14 show the $\Delta_1 S$ field for the Flemish Cap region. These figures show almost the same pattern as for the Hamilton Bank region: a negative trend for the salinity

(-1.0 to -0.2 psu) in near surface waters (Fig. 7.14a) associated with a positive salinity trend in deeper waters (Fig 7.14b). Notice in the southeastern corner (in the NAC region) the positive $\Delta_1 S$ values (+1.4 psu) in both near surface waters and intermediate waters (Fig. 7.14b). In near surface waters, the $\Delta_1 T$ field (Figs. 7.15a) shows a negative temperature trend west of 49°W and a positive temperature trend (+1°C to +7°C) is seen east of this longitude. In intermediate waters, the $\Delta_1 T$ field (Fig. 7.15b) shows positive values everywhere with values up to +6°C in the NAC region. Both the $\Delta_2 S$ (Figs. 7.16) and the $\Delta_2 T$ fields (Figs. 7.17) show that the trends observed between the 1959-64 and 1967-72 periods tend to reverse during the 1975-80 period. Notice that a cooling is still found at the surface near the northwestern corner of the region (Fig. 7.17a). The $\Delta_3 T$ field for the surface waters (Figs. 7.18a) shows negative temperature trends near the Flemish Cap area (with values of ~-2°C) and near the island of Newfoundland. Fig. 7.18a also shows positive temperature trends to the southwest and to the east of Flemish Cap (~2-3°C). In intermediate waters, only positive values are found (Fig. 7.18b).

In sections 7.2 and 7.3 of this chapter, the T and S and volume transport streamfunctions for longer periods were diagnosed. The subregion results, which were discussed above, show that shorter time scale variability can be found and that it is associated with relatively large T and S signals. The results of both sections 7.2 and 7.4 show that the variability of the upper ocean is often opposite to that found in deeper waters. This feature can be explained by mixing of water masses through convection.

The decrease of northern cod stock is a major problem in Canada. Dunbar (1993) mentioned that although overfishing is often pointed out as the main cause for this problem, perhaps the focus should be more on the interdecadal variability of the near-surface water temperatures as the cod stock cannot be renewed under cold temperature conditions. Figure 1 from Dunbar (1993) shows a good correlation between the amount of cod caught and the SST. Notice that the SST trends from Dunbar (1993) are similar to that shown on Fig. 1.8. As the surface temperature trends found in both the Hamilton Bank and Flemish Cap subregions (Fig. 7.13a and 7.18a) are negative, it is tempting to speculate that the decrease of the cod stock in 1990s could be associated with these colder than normal ocean temperatures.

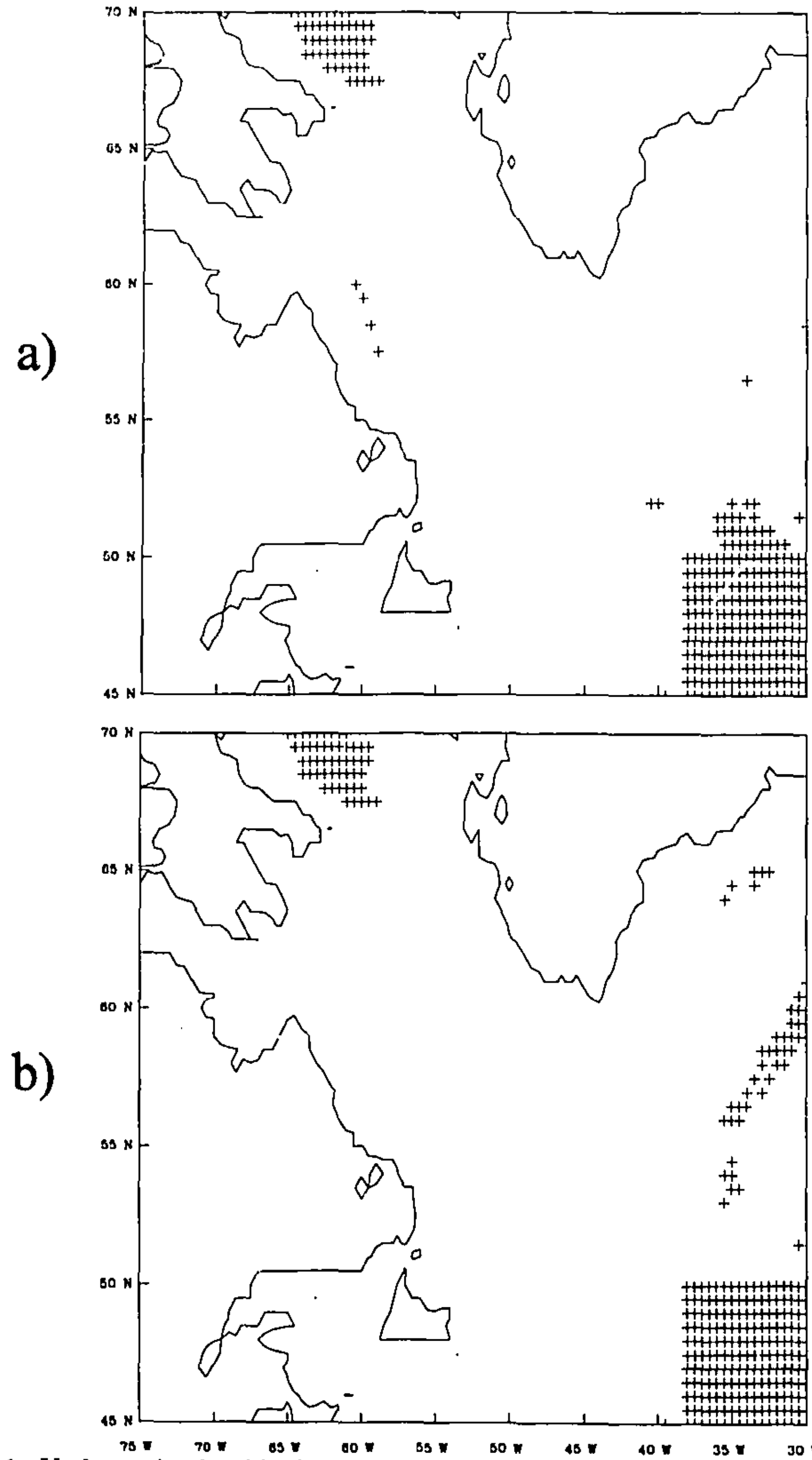

Figure 7.1: Undetermined gridpoints from the objective analysis: a) for the 1950-64 analysis at 1000m, b) for the 1965-81 analysis at 1000m,

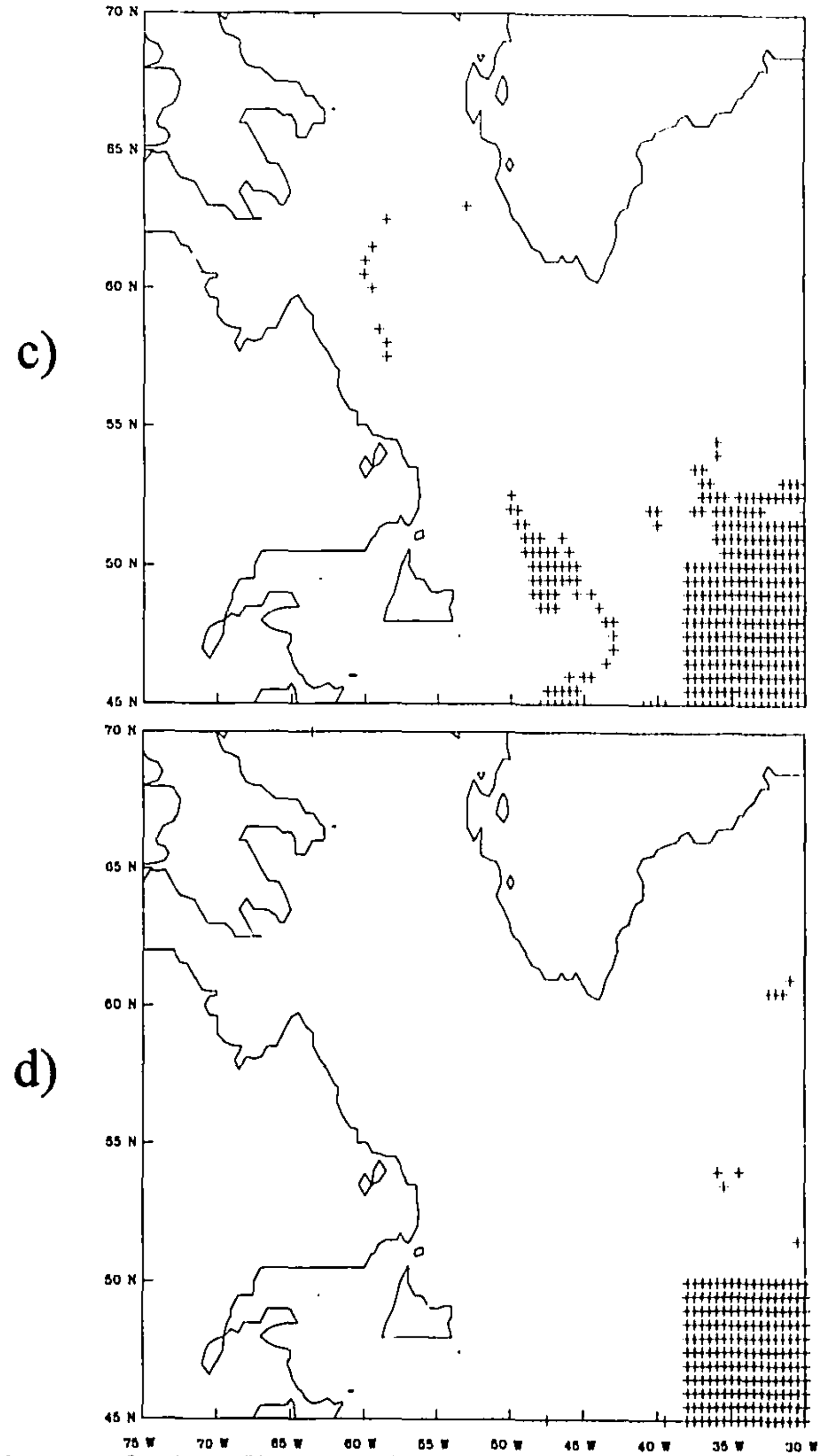

Figure 7.1 cont: c) for the 1950-64 analysis at 2000m and d) for the 1965-81 analysis at 2000m.

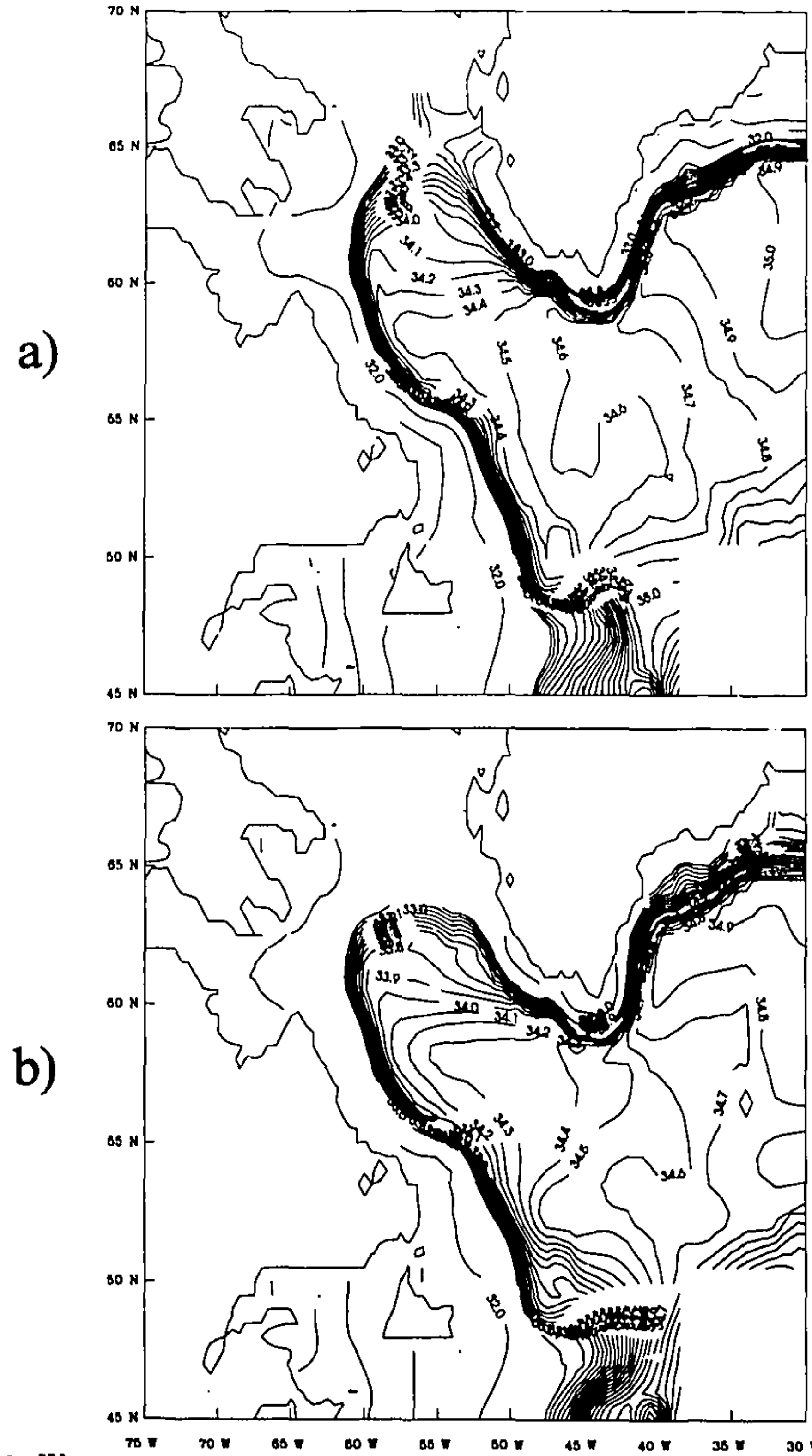

Figure 7.2: Warm season salinity (psu) of the northwestern Atlantic Ocean for a) the 1950-64 analysis at 0m, b) the 1965-81 analysis at 0m,

c)

d)

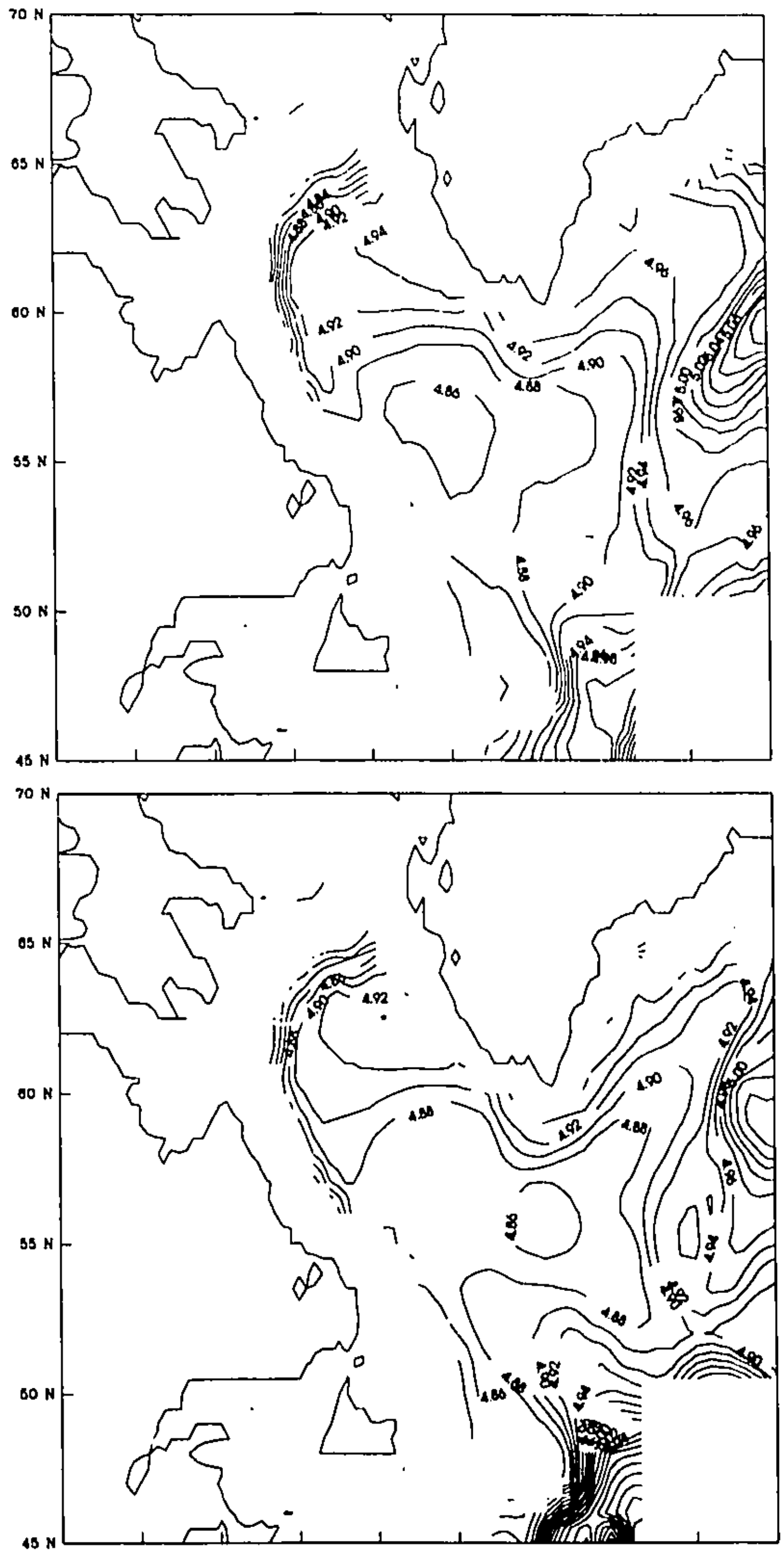

Figure 7.2 cont: c) the 1950-64 analysis at 500m (true salinity=30+reported salinity), d) the 1965-81 analysis at 500m (true salinity=30+reported salinity),

e)

f)

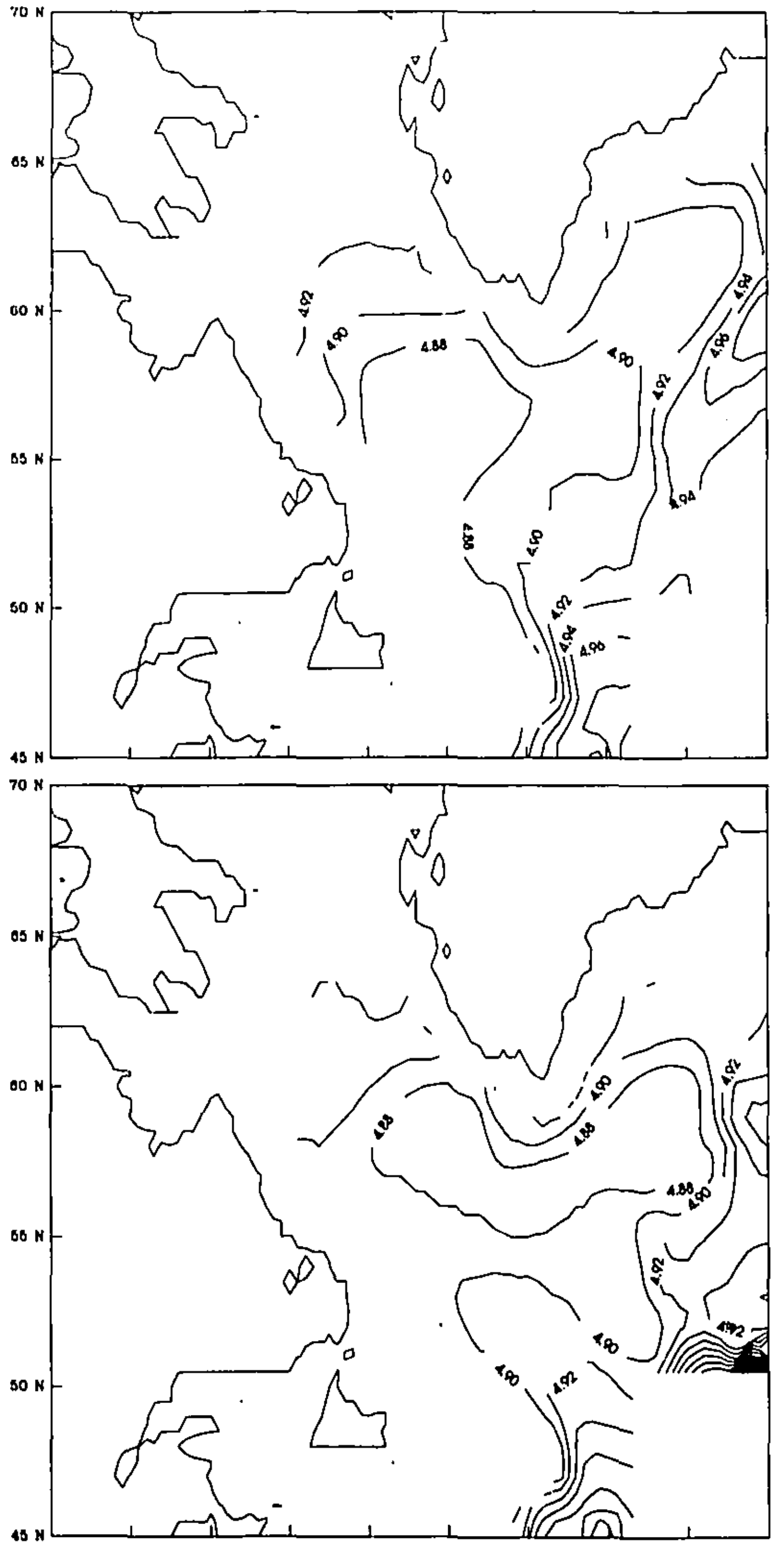

Figure 7.2 cont: e) the 1950-64 analysis at 1000m (true salinity=30+reported salinity), f) the 1965-81 analysis at 1000m (true salinity=30+reported salinity),

g)

h)

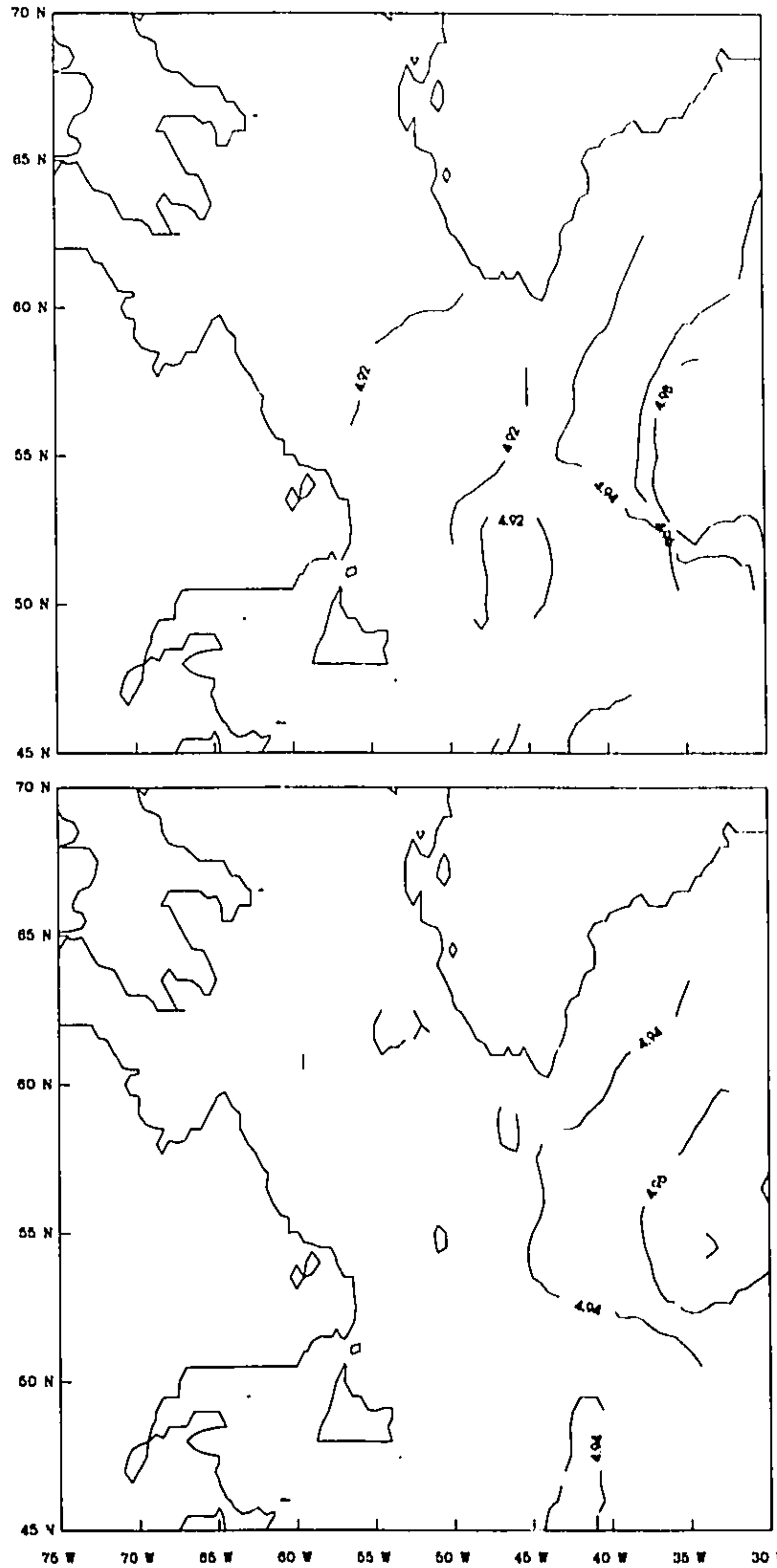

Figure 7.2 cont: g) the 1950-64 analysis at 2000m (true salinity=30+reported salinity) and h) the 1965-81 analysis at 2000m (true salinity=30+reported salinity).

a)

b)

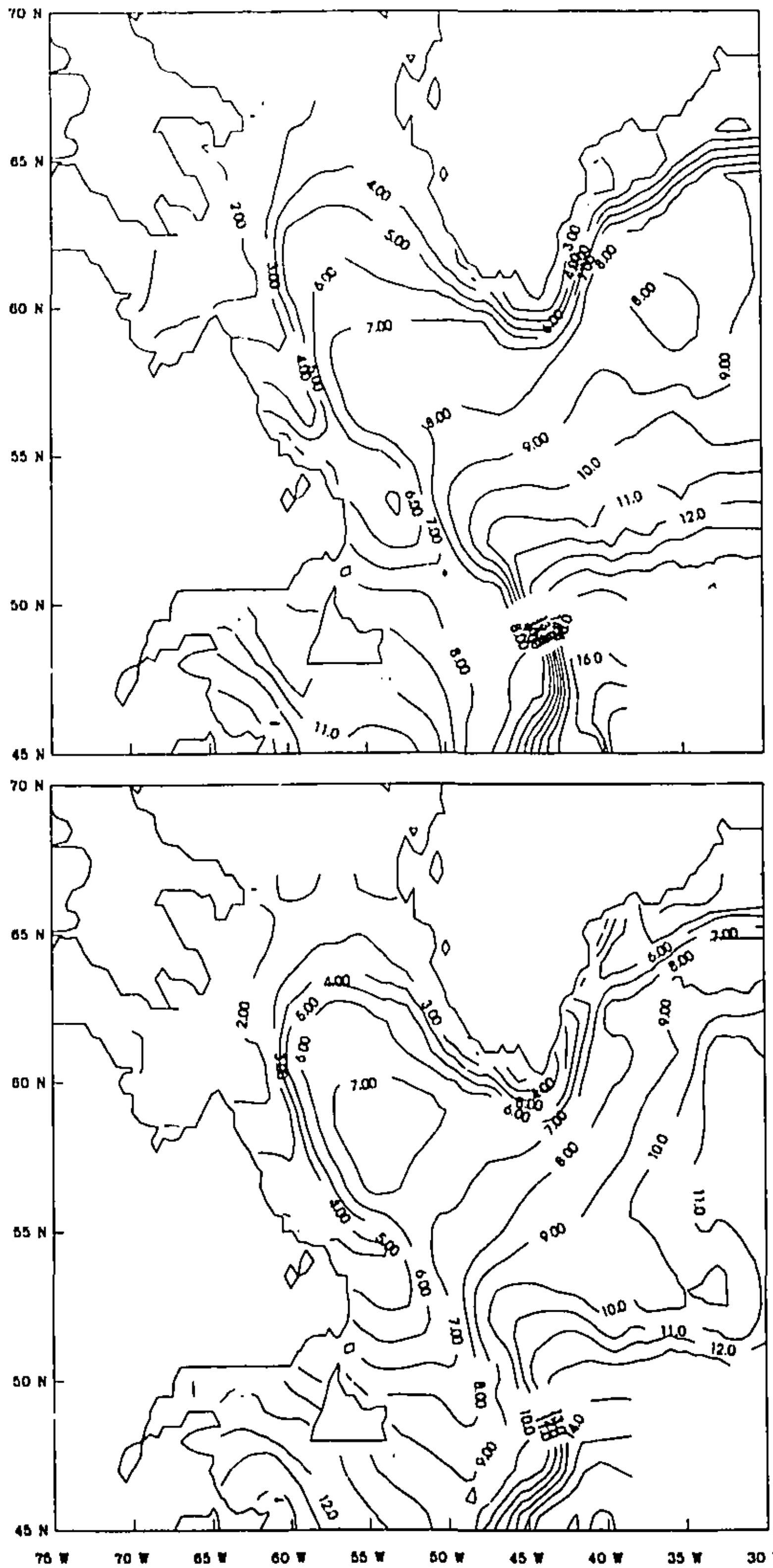

Figure 7.3: Warm season in situ temperature (°C) of the northwestern Atlantic Ocean for a) the 1950-64 analysis at 0m, b) the 1965-81 analysis at 0m,

c)

d)

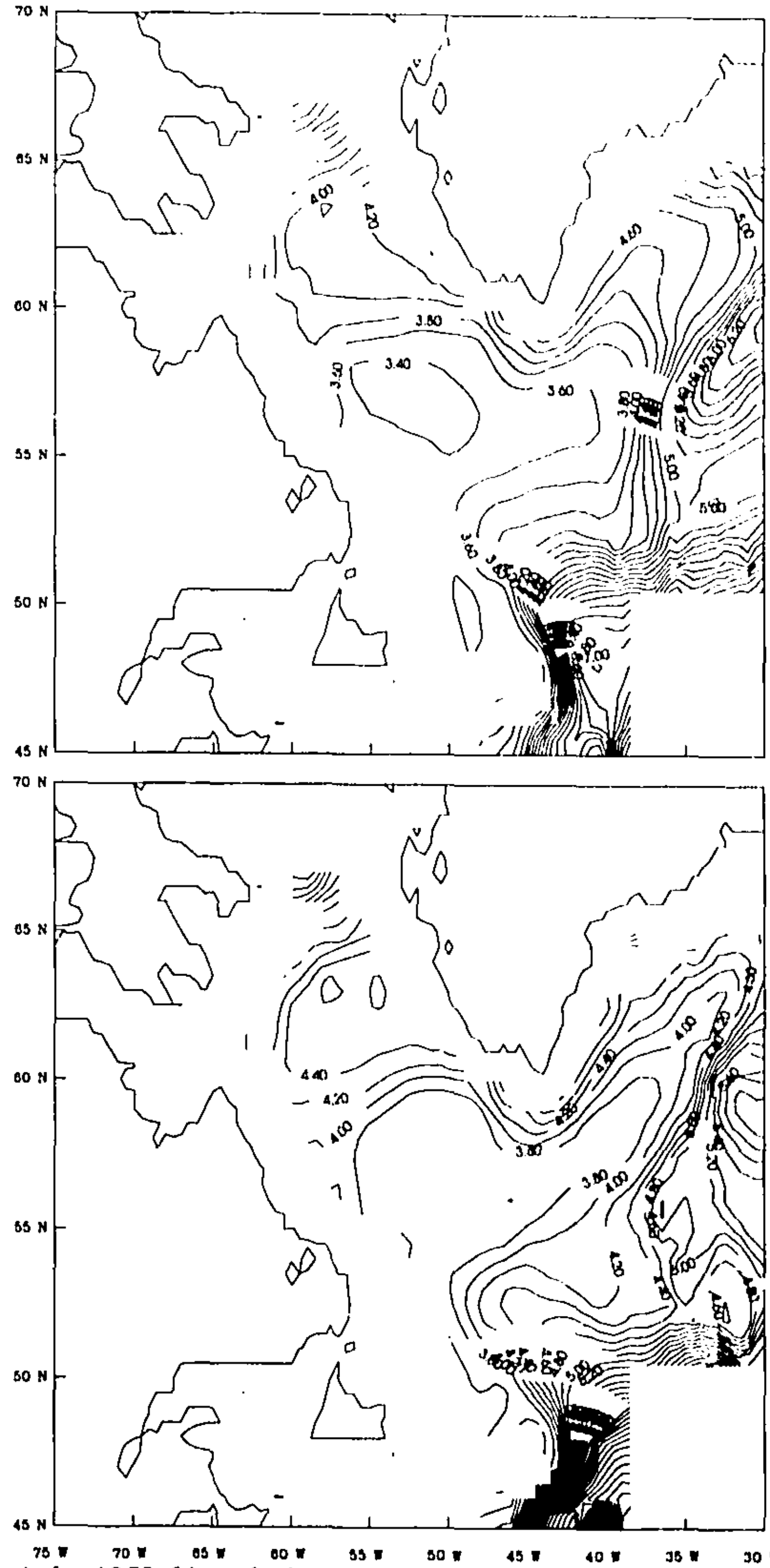

Figure 7.3 cont: c) the 1950-64 analysis at 500m, d) the 1965-81 analysis at 500m,

e)

f)

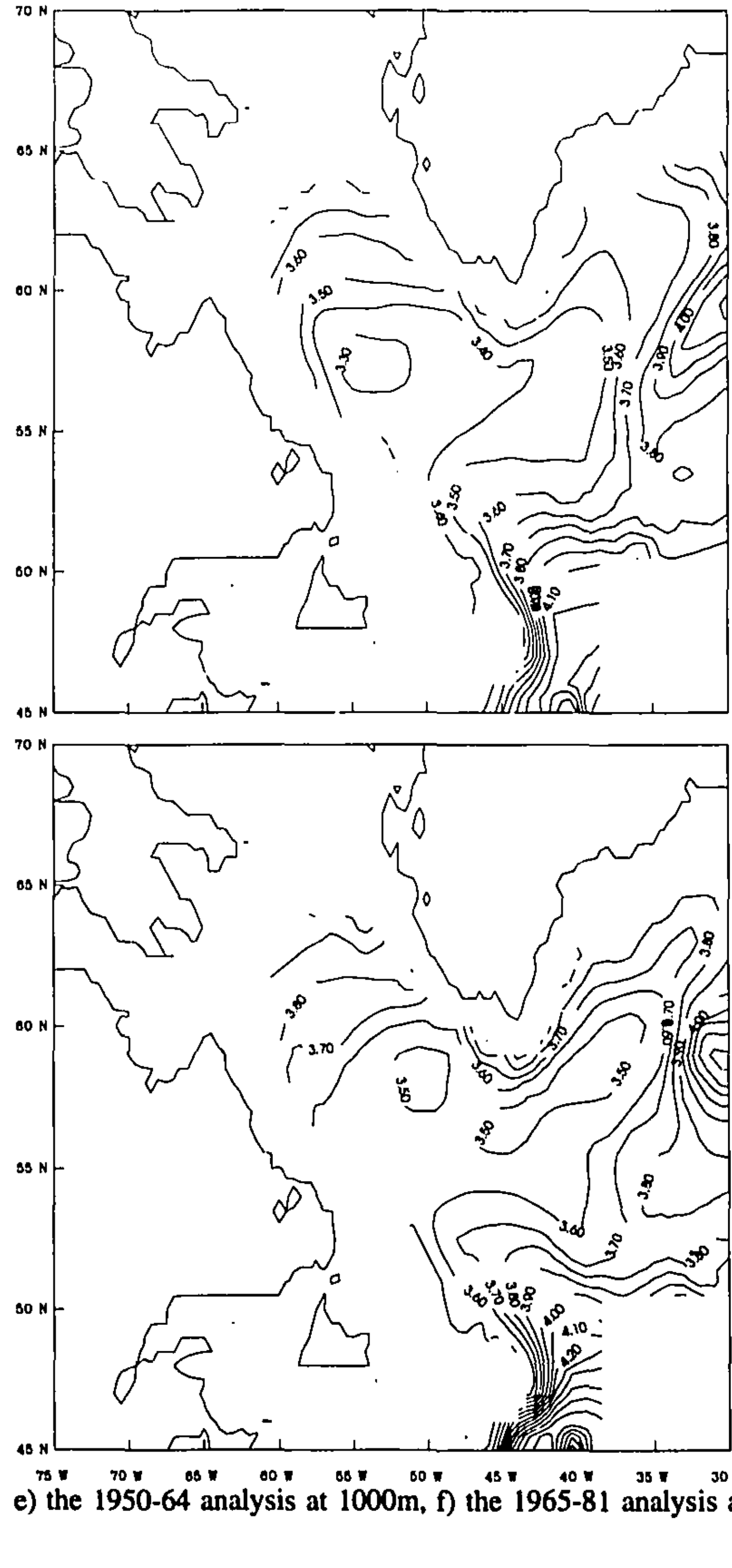

Figure 7.3 cont: e) the 1950-64 analysis at 1000m, f) the 1965-81 analysis at 1000m,

g)

h)

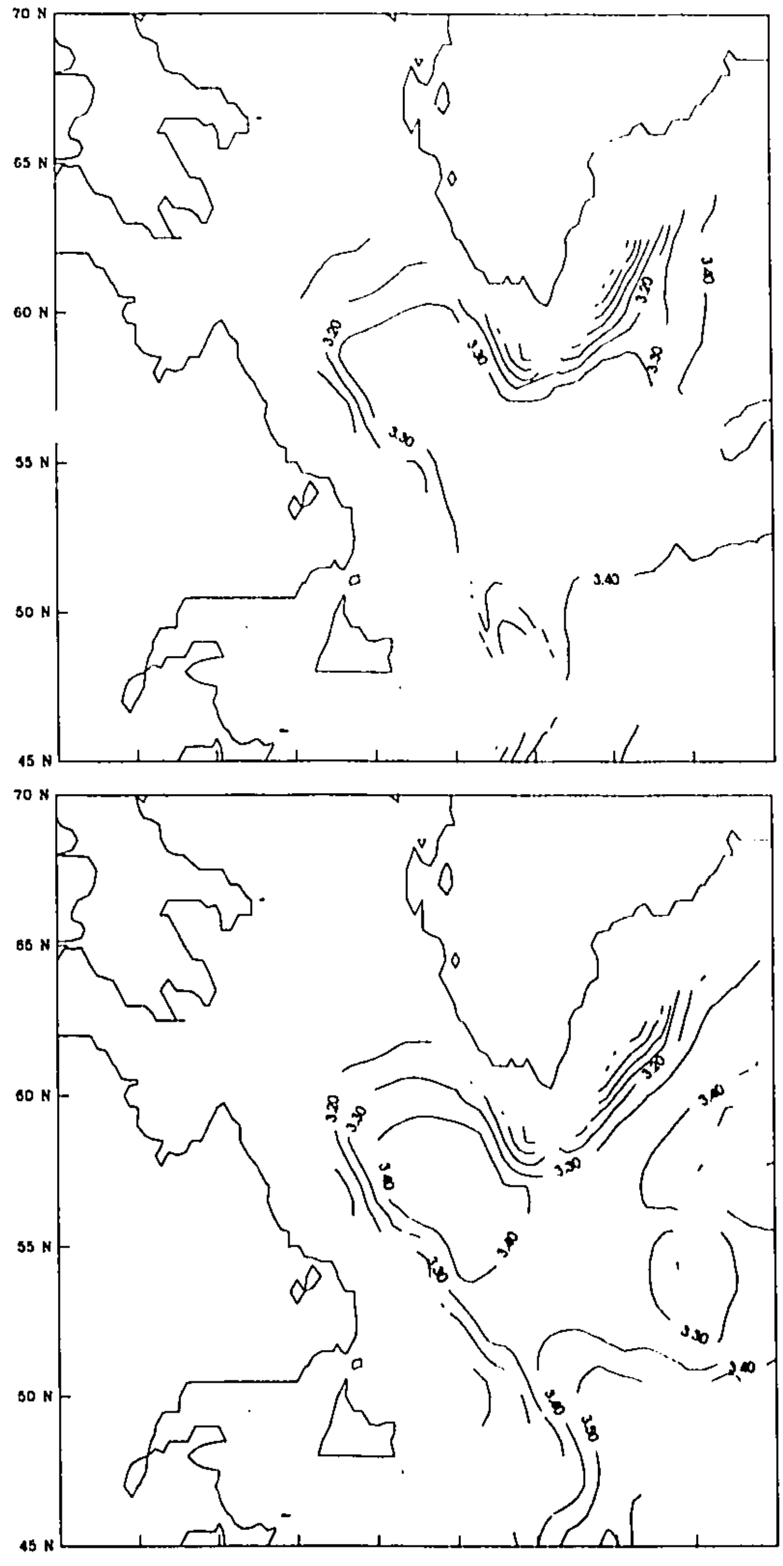

Figure 7.3 cont: g) the 1950-64 analysis at 2000m and h) the 1965-81 analysis at 2000m.

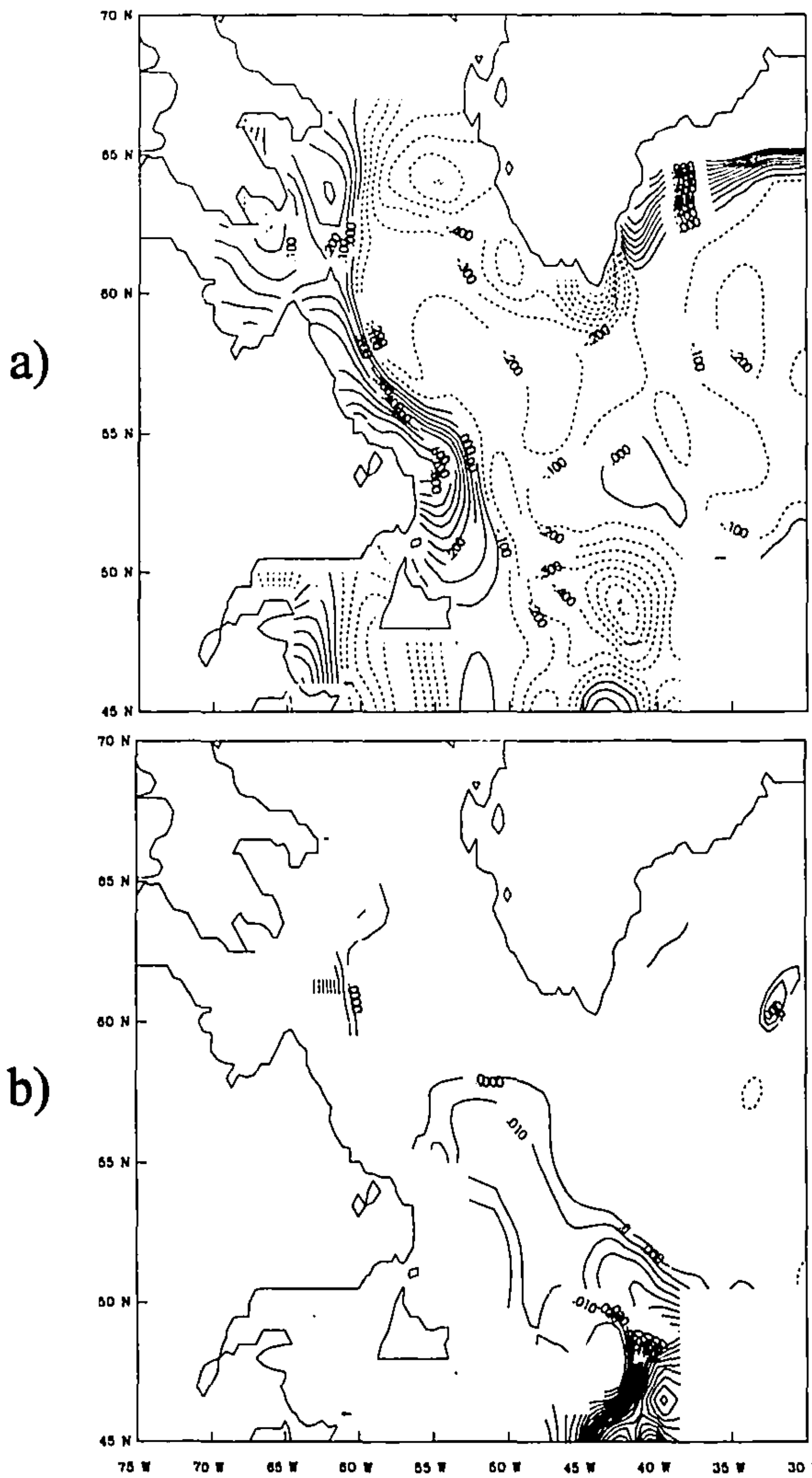

Figure 7.4: Salinity interdecadal variations (psu), (1965-81)-(1950-64), at a) 0m, b) 500m,

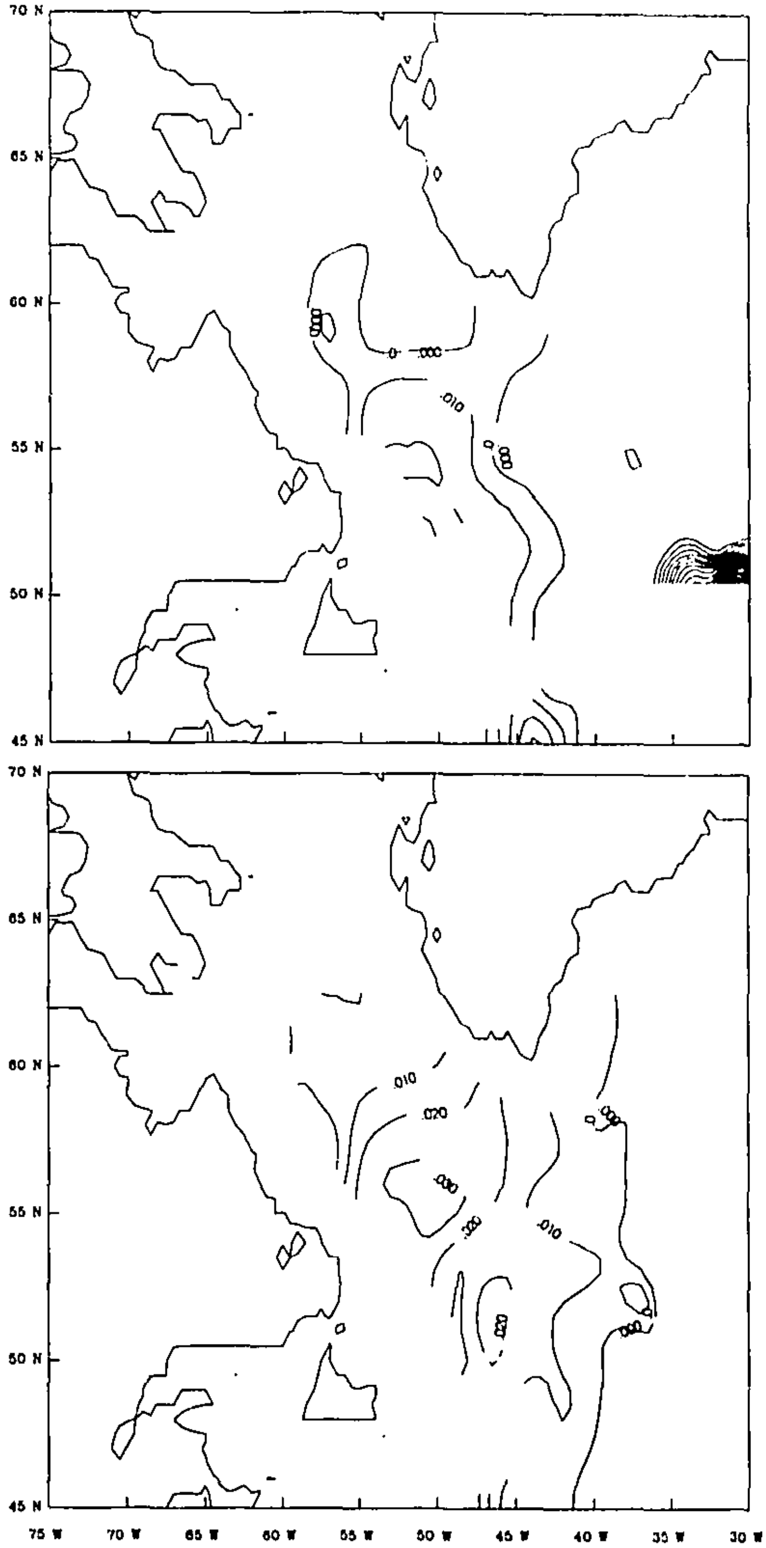

c)

d)

Figure 7.4 cont: c) 1000m and d) 2000m.

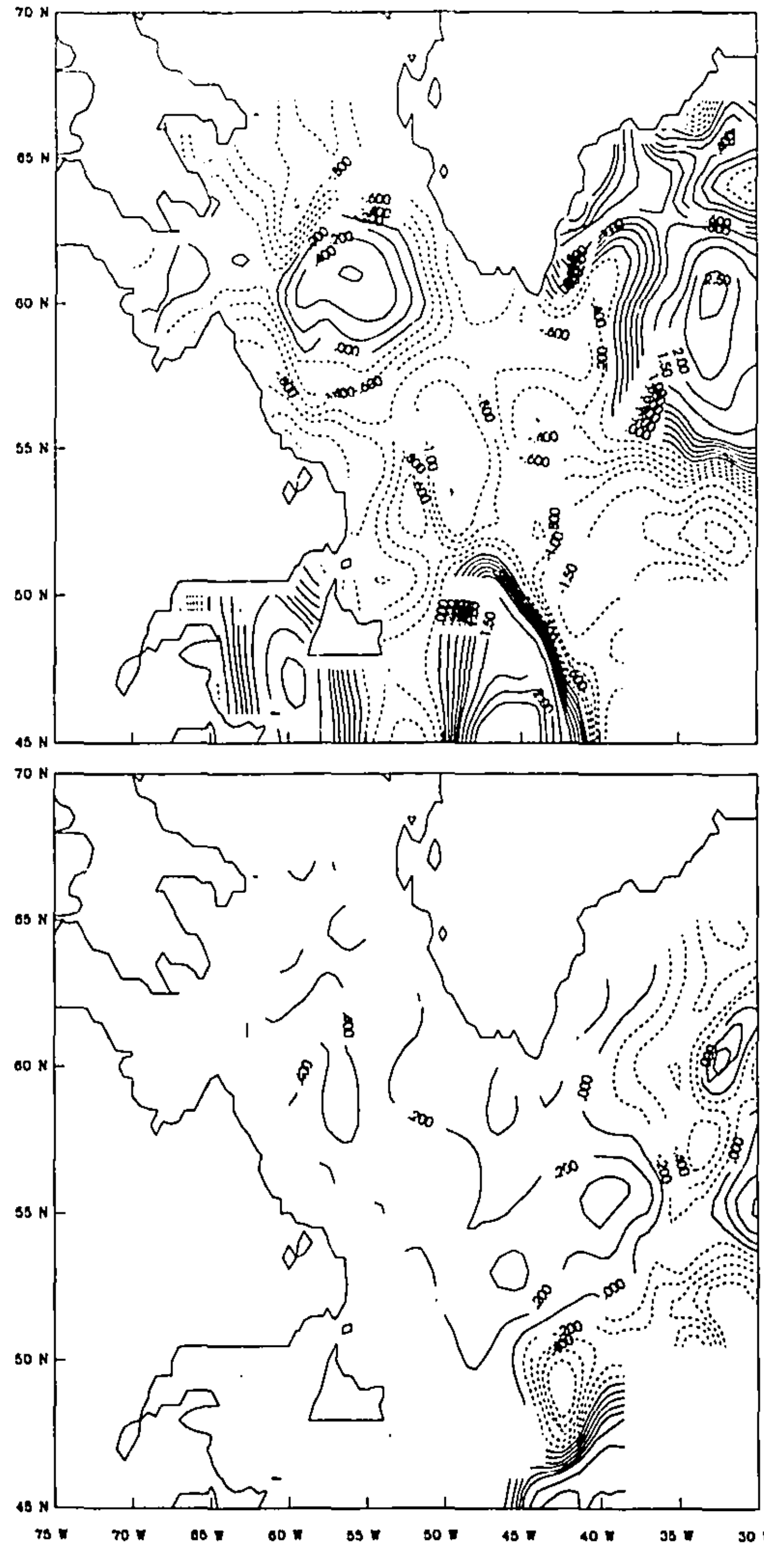

Figure 7.5: Temperature interdecadal variations (°C), (1965-81)-(1950-64), at a) 0m, b) 500m,

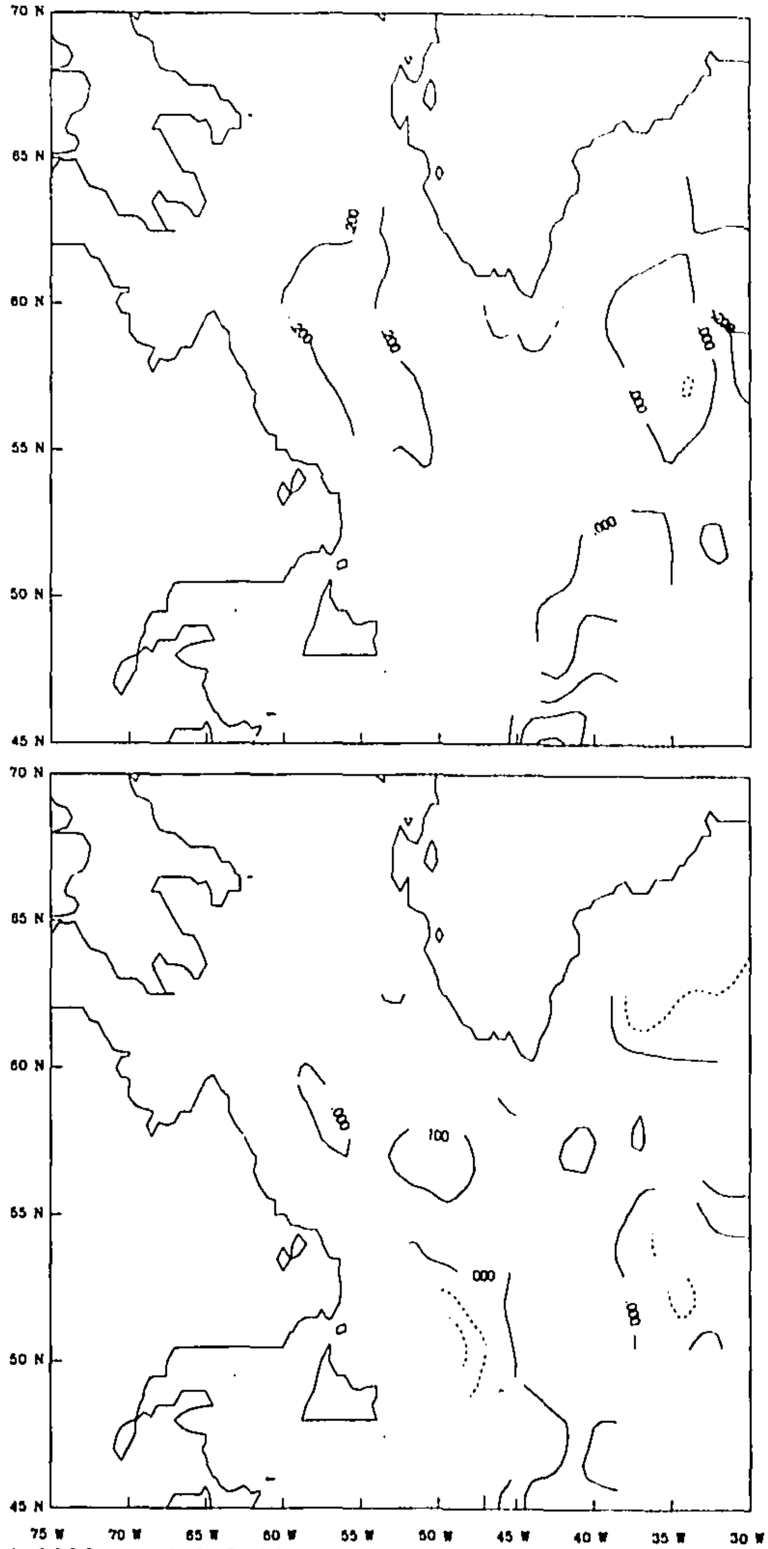

c)

d)

Figure 7.5 cont: c) 1000m and d) 2000m.

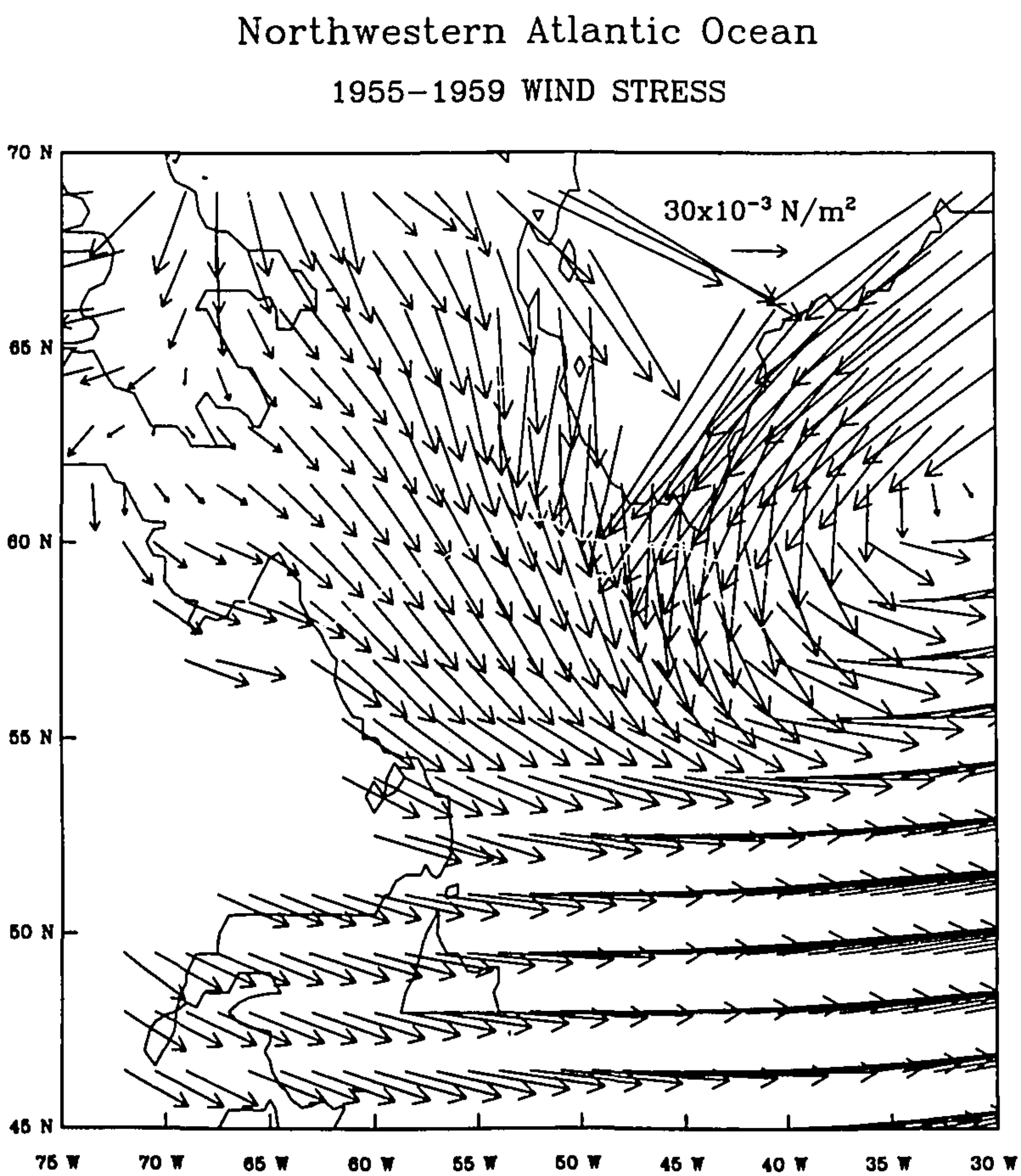

Figure 7.6: Annual mean wind stress field (N/m^2) for a) the 1955-59 period,

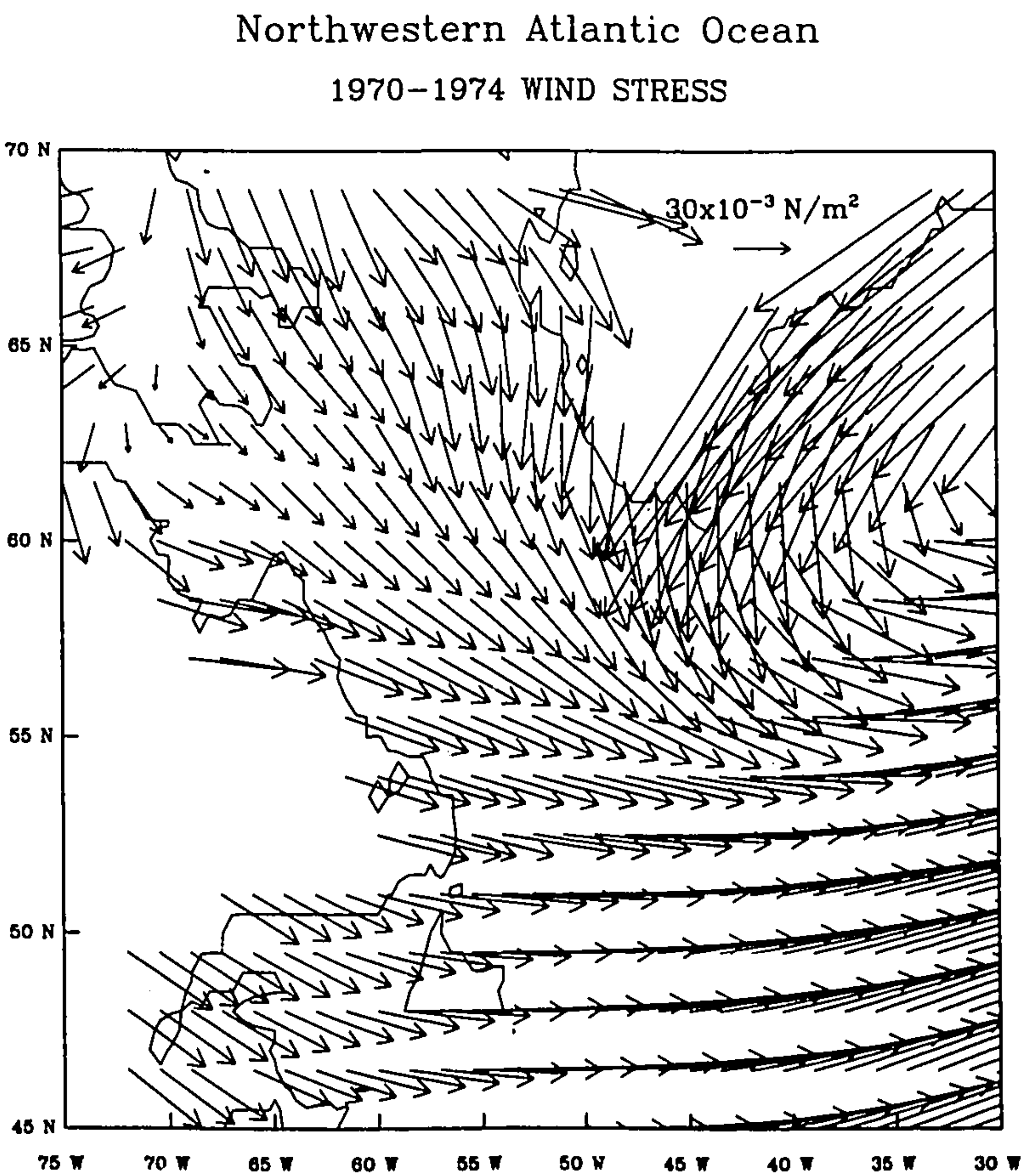

Figure 7.6 cont: and b) the 1970-74 period (from Da Silva, 1991).

a)

b)

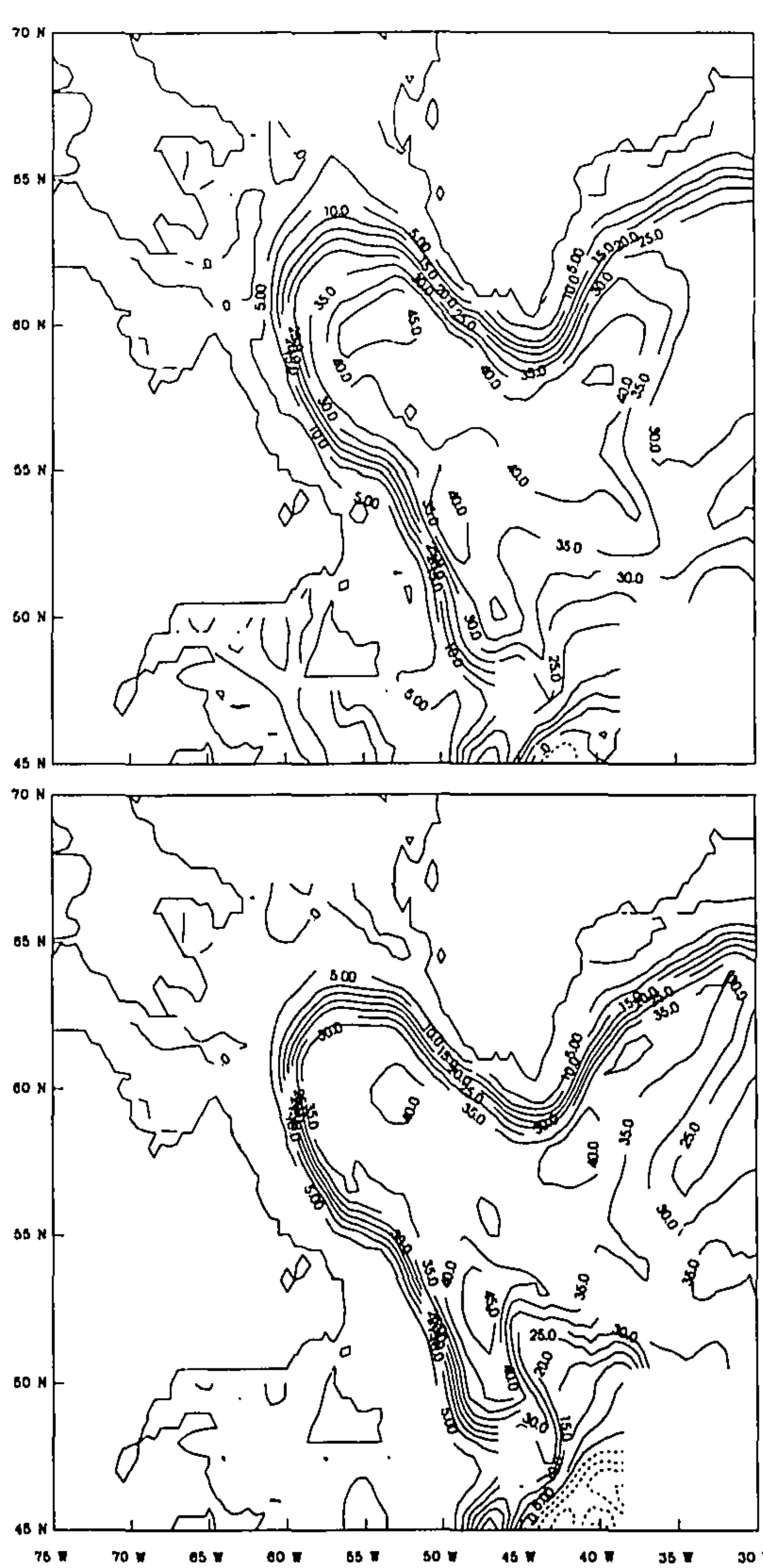

Figure 7.7: Warm season volume transport streamfunctions (Sv) for a) the 1950-64 analysis, b) the 1965-81 analysis.

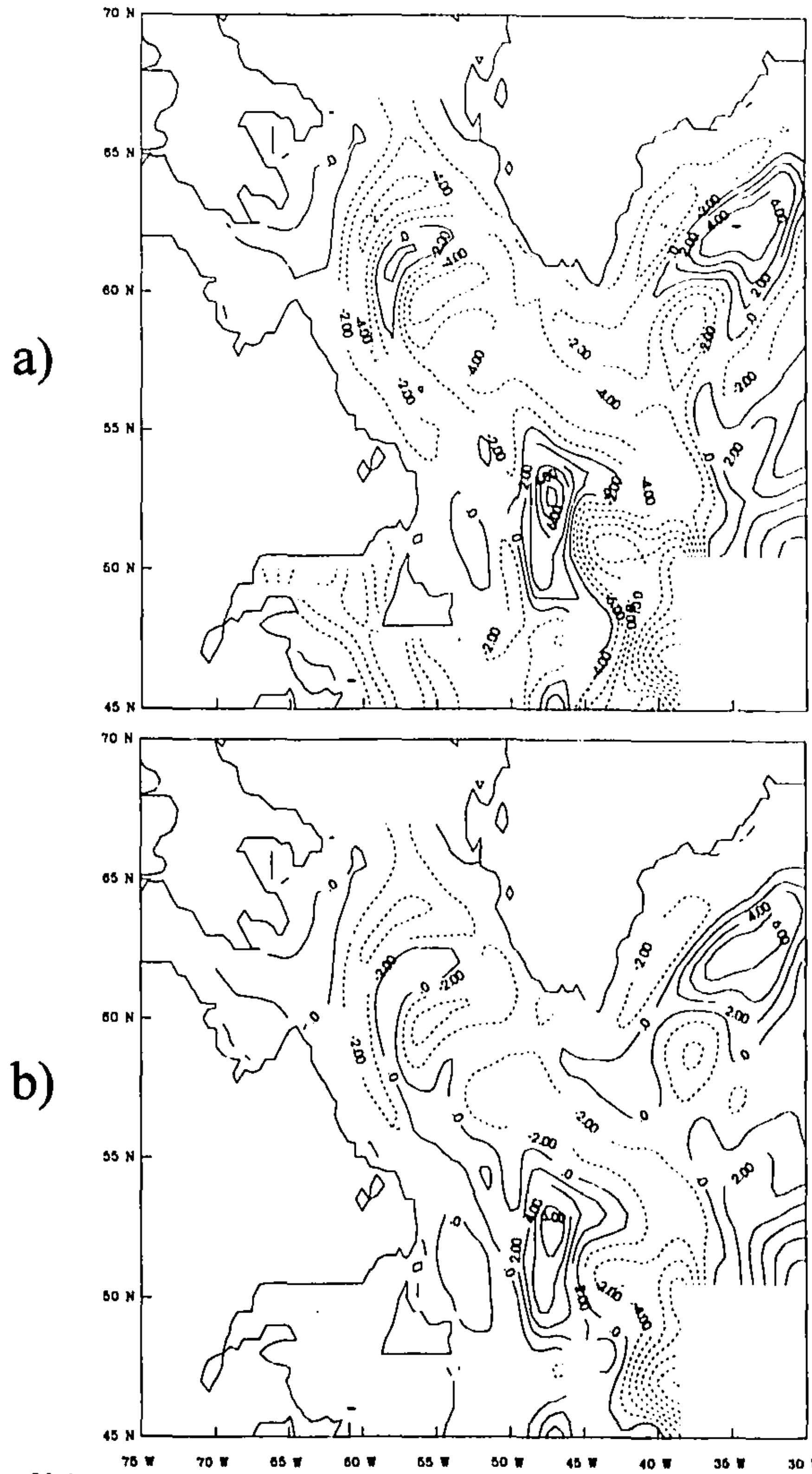

Figure 7.8: Volume transport interdecadal variations (Sv), (1965-81)-(1950-64), a) total streamfunction, b) volume transport due to the local JEBAR term,

c)

d)

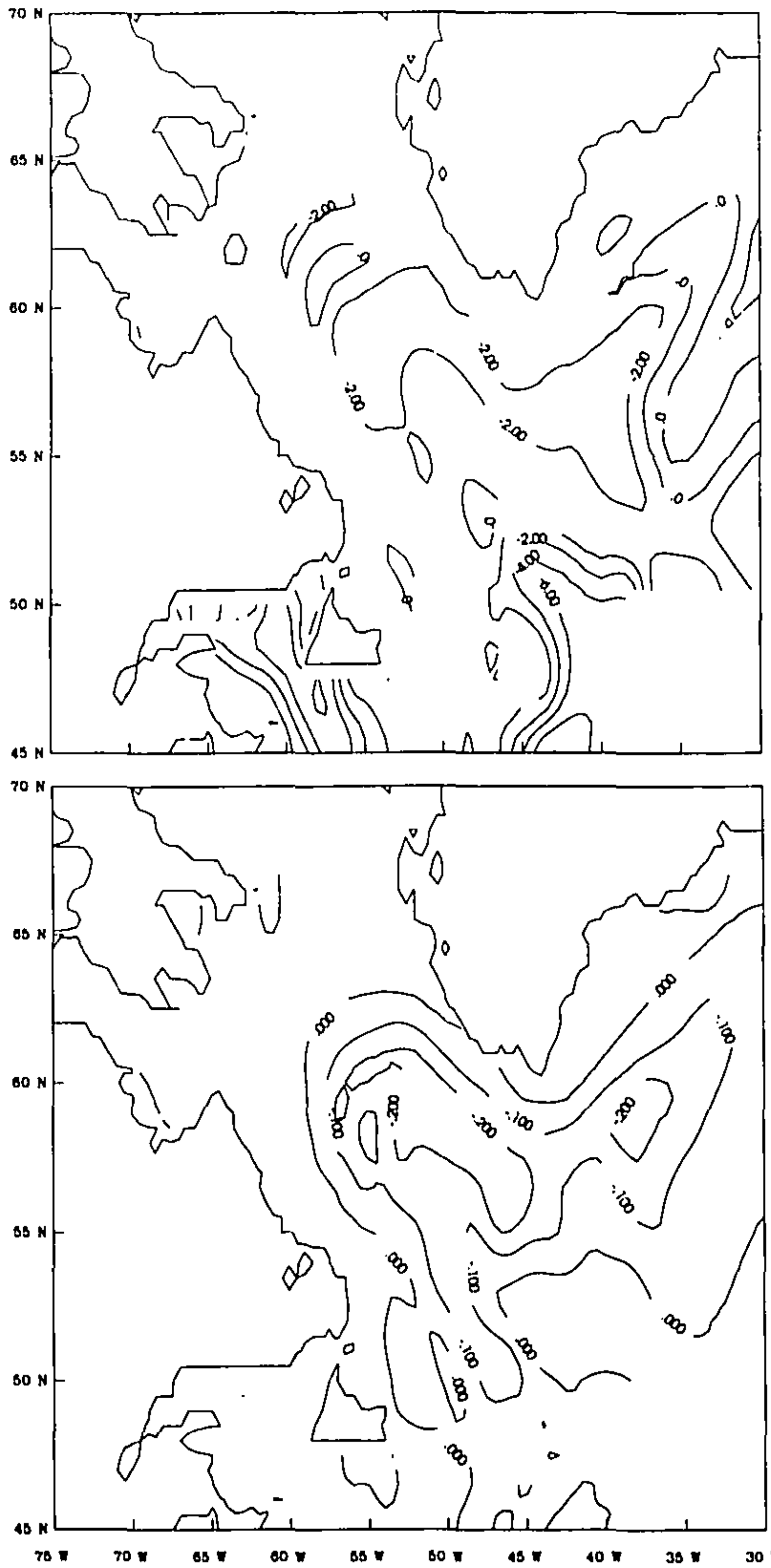

Figure 7.8 cont: c) volume transport inferred by the boundary values and d) volume transport due to the local wind forcing.

a)

b)

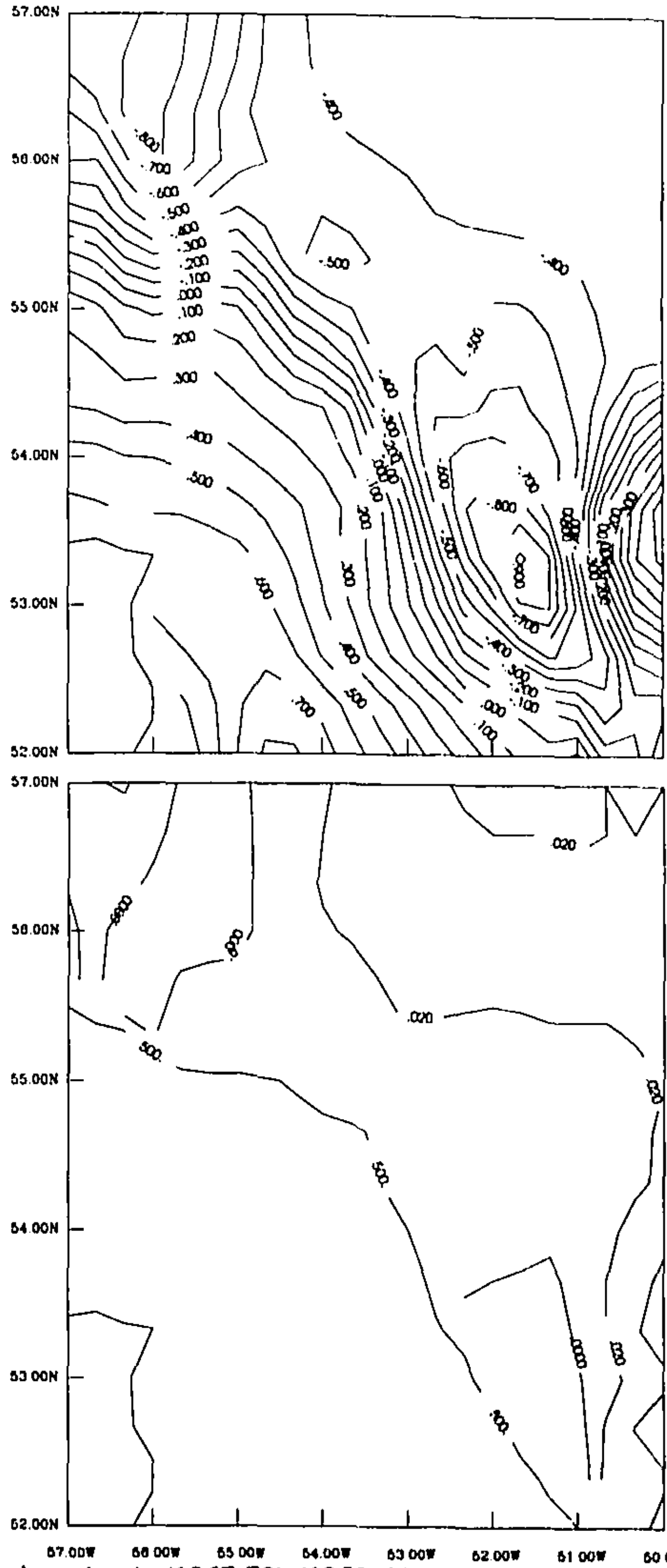

Figure 7.9: Salinity variations (psu), (1967-72)-(1959-64), at a) 0m and b) 500m for the Hamilton Bank subregion.

a)

b)

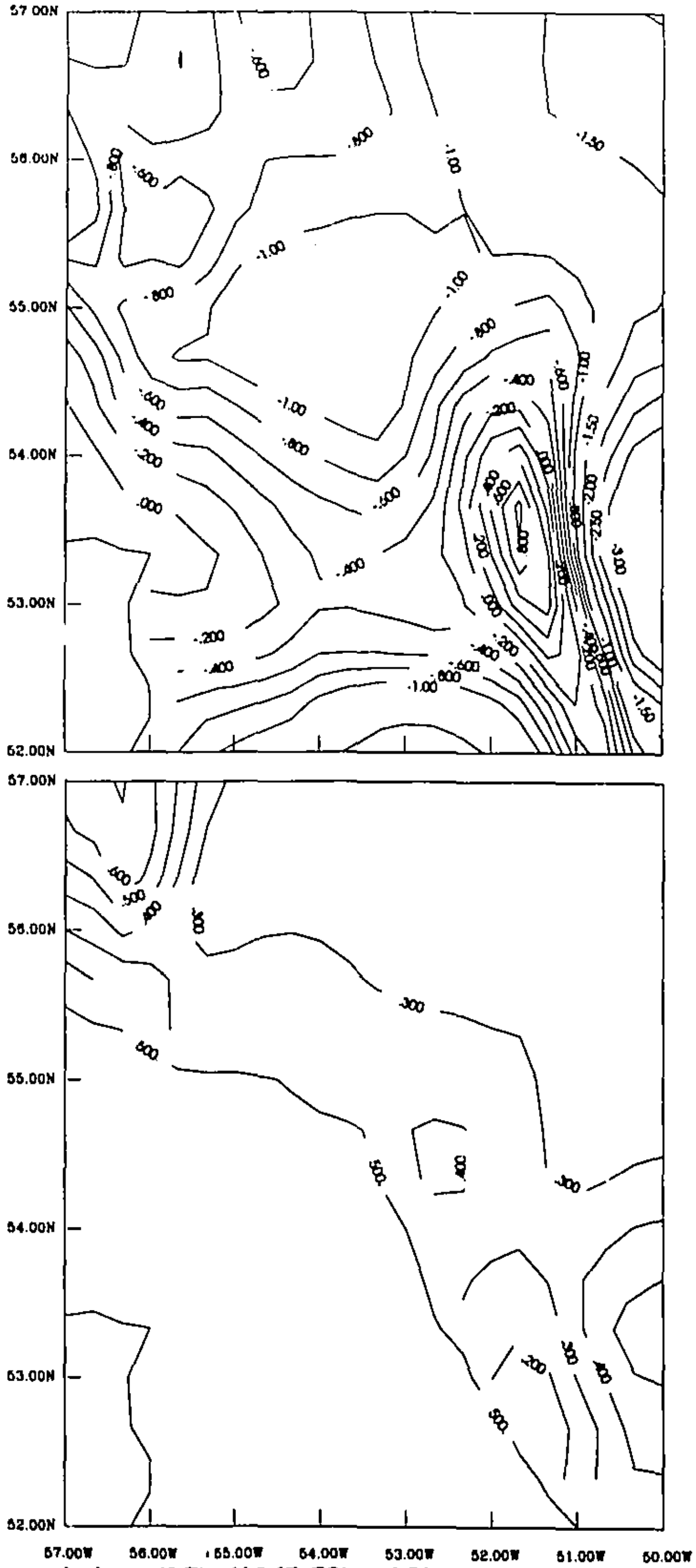

Figure 7.10: Temperature variations (°C), (1967-72)-(1959-64), at a) 0m and b) 500m for the Hamilton Bank subregion.

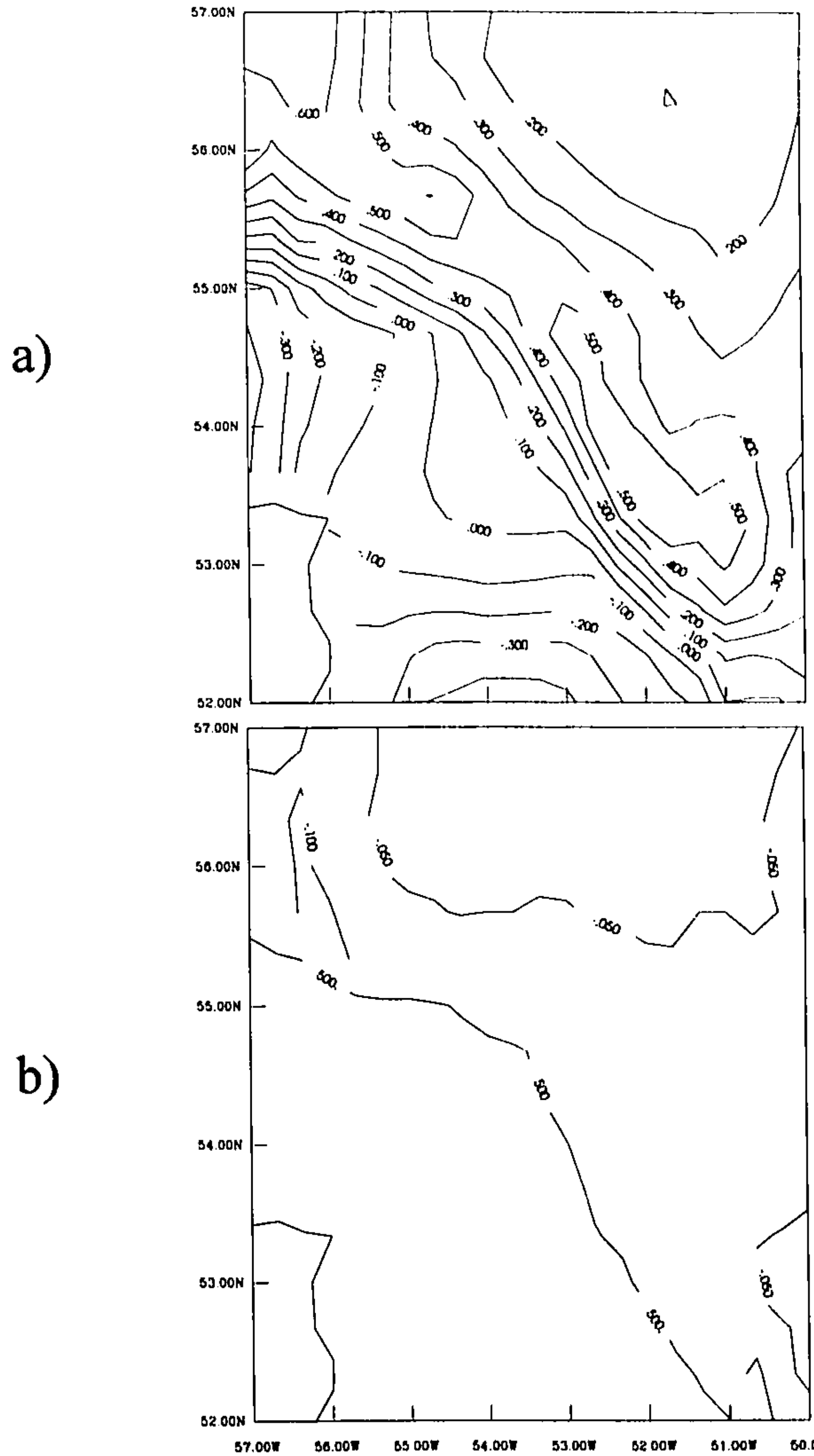

Figure 7.11: Salinity variations (psu), (1975-80)-(1967-72), at a) 0m and b) 500m for the Hamilton Bank subregion.

a)

b)

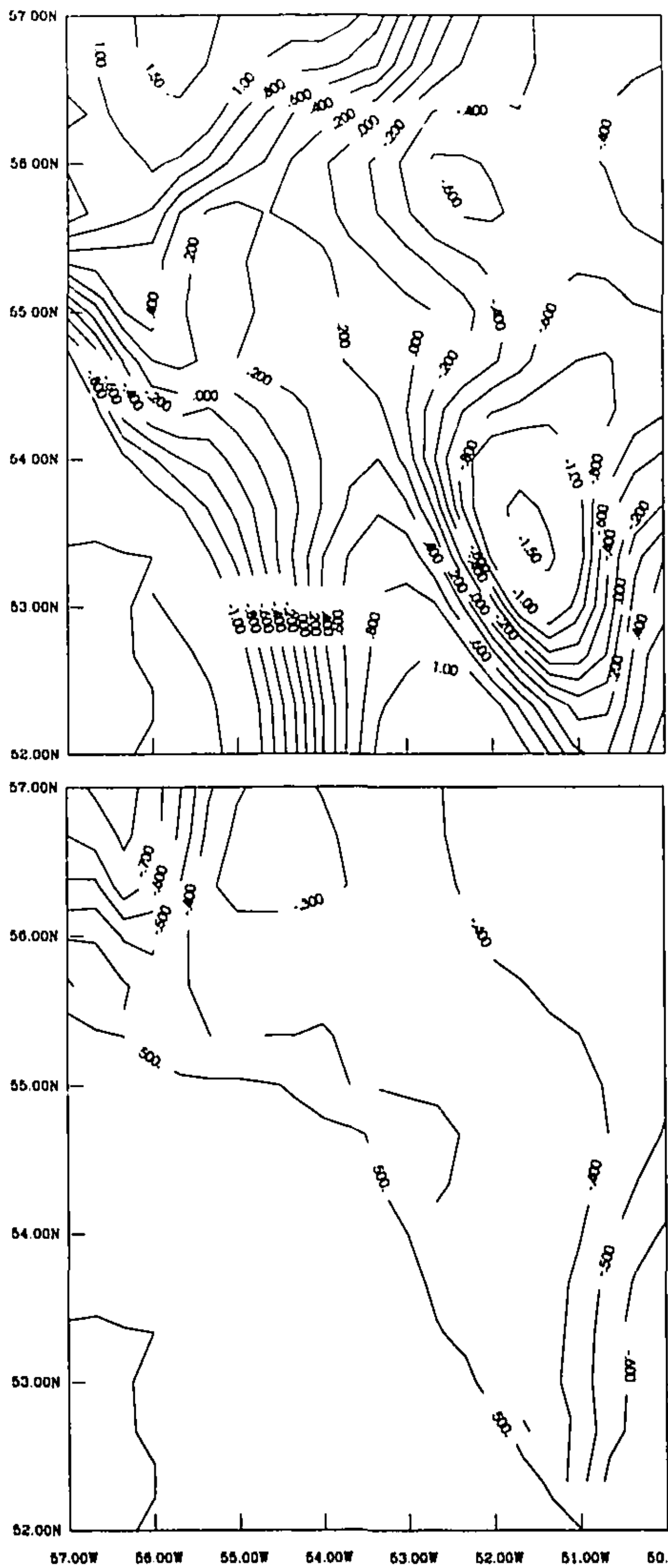

Figure 7.12: Temperature variations (°C), (1975-80)-(1967-72), at a) 0m and b) 500m for the Hamilton Bank subregion.

a)

b)

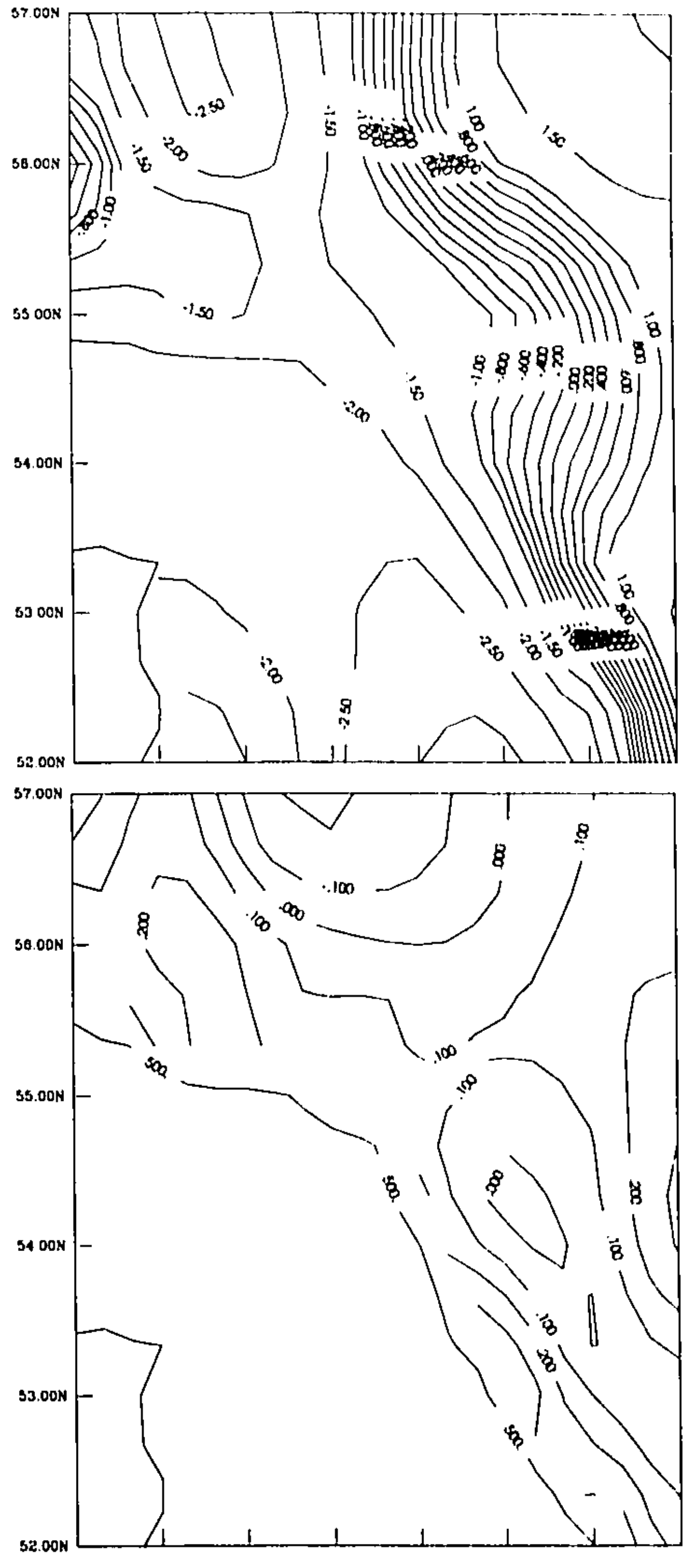

Figure 7.13: Temperature variations (°C), (1983-88)-(1975-80), at a) 0m and b) 500m for the Hamilton Bank subregion.

a)

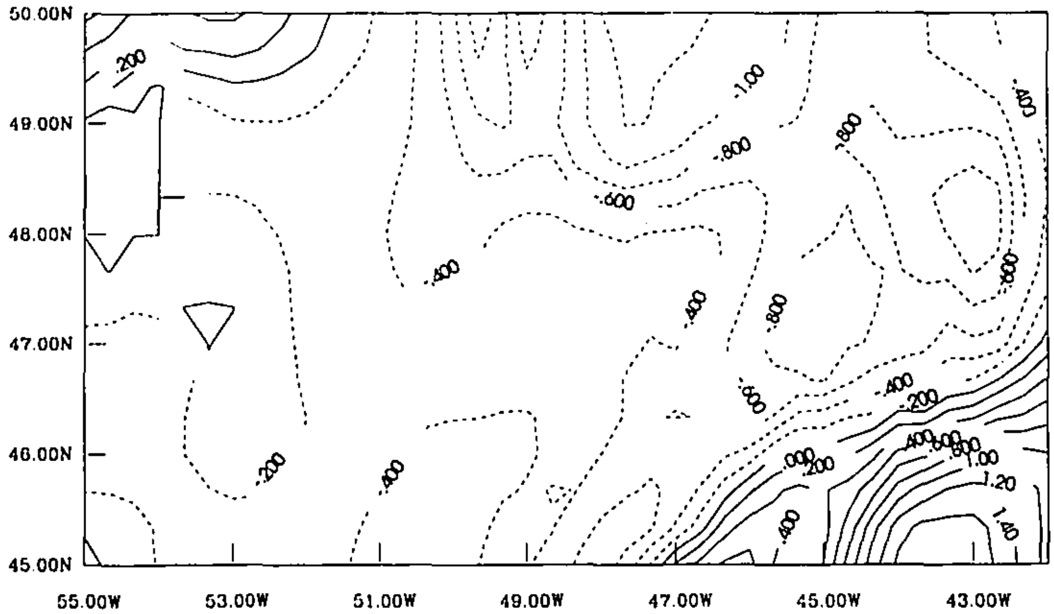

b)

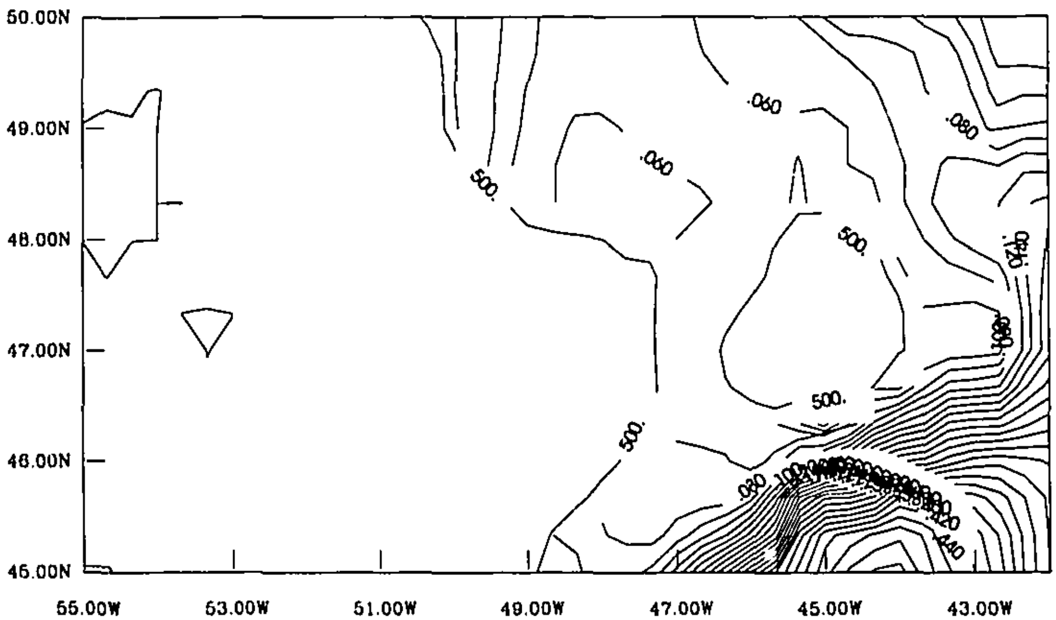

Figure 7.14: Salinity variations (psu), (1967-72)-(1959-64), at a) 0m and b) 500m for the Flemish Cap subregion.

a)

b)

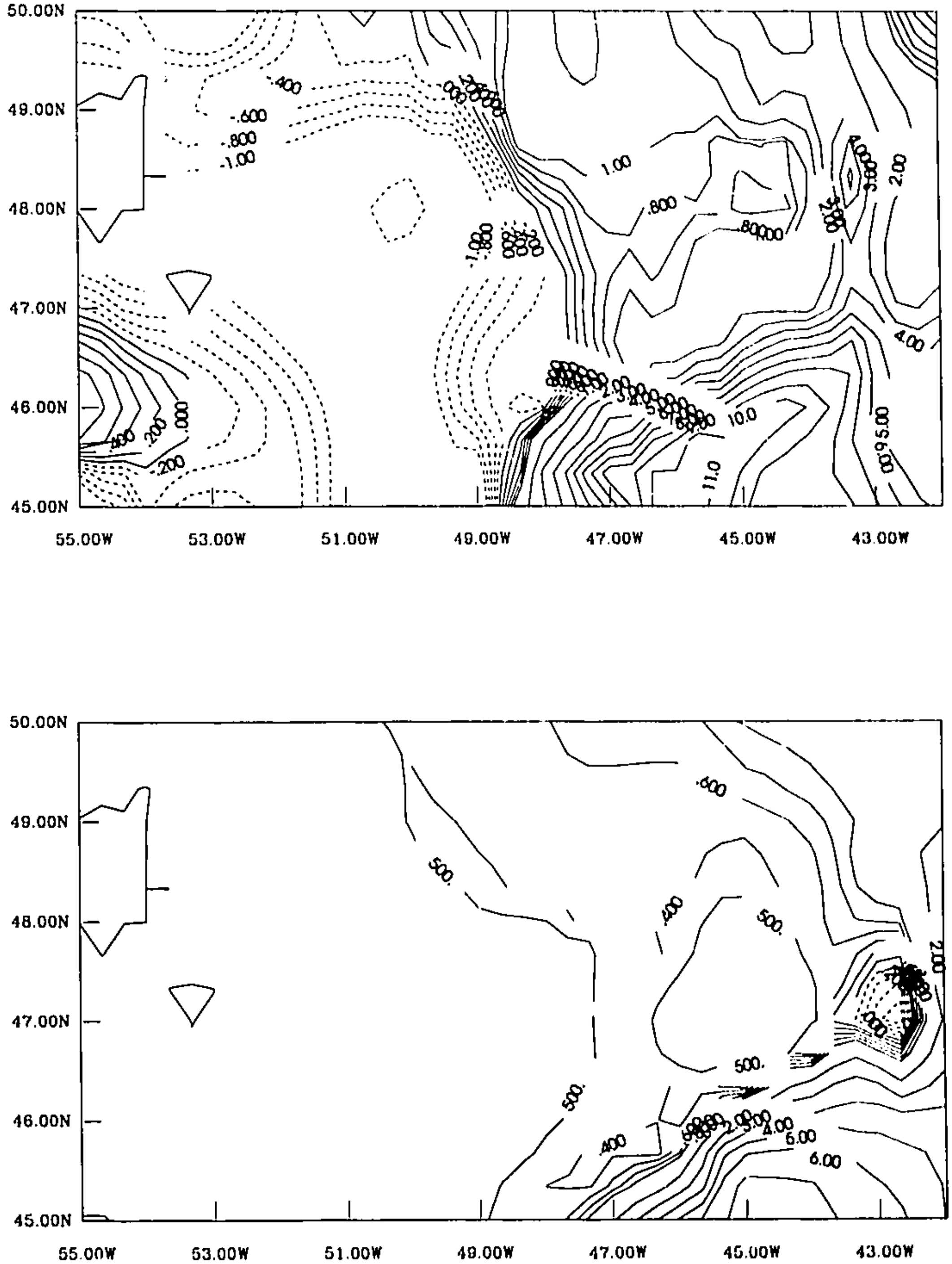

Figure 7.15: Temperature variations (°C), (1967-72)-(1959-64), at a) 0m and b) 500m for the Flemish Cap subregion.

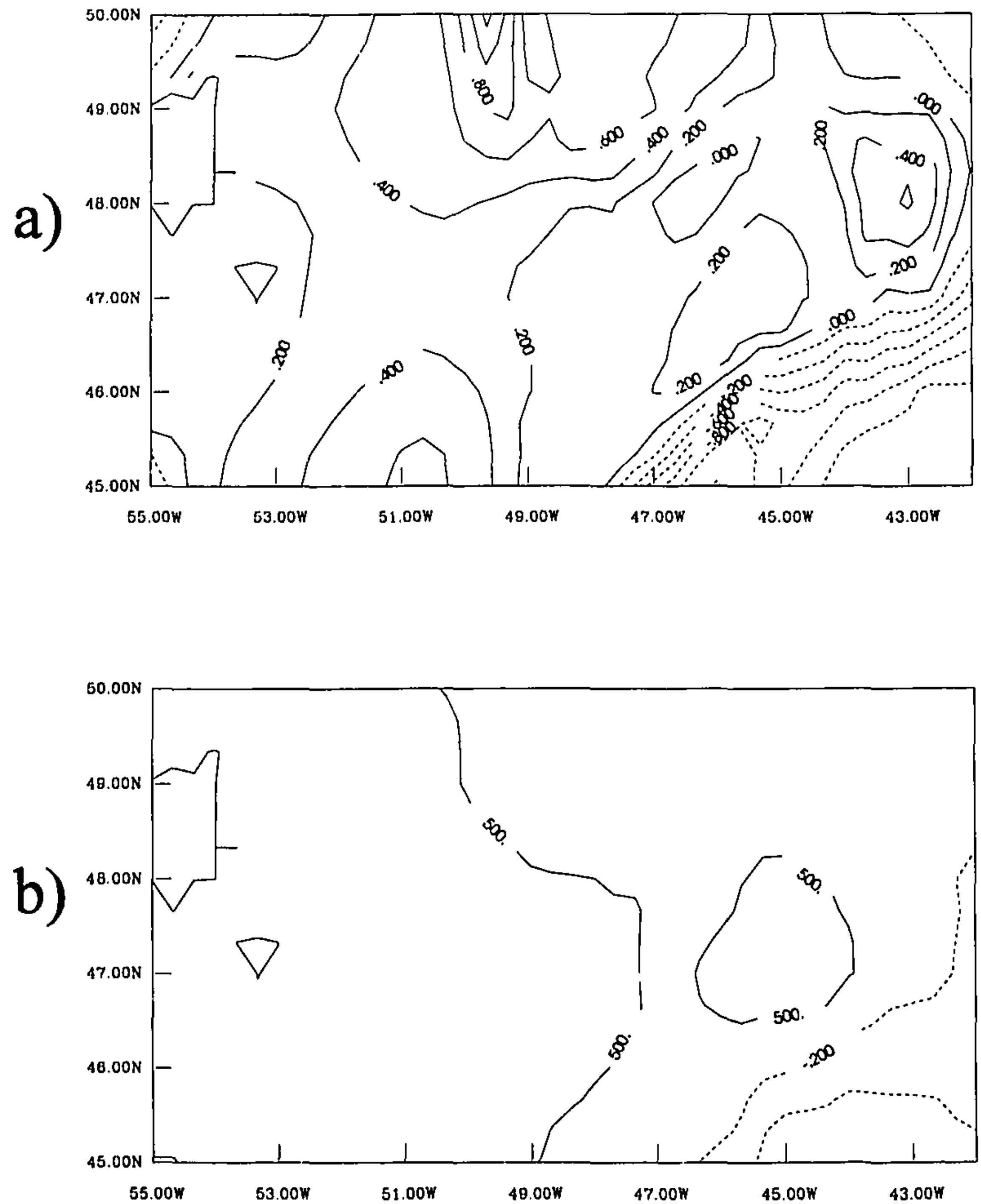

Figure 7.16: Salinity variations (psu), (1975-80)-(1967-72), at a) 0m and b) 500m for the Flemish Cap subregion.

a)

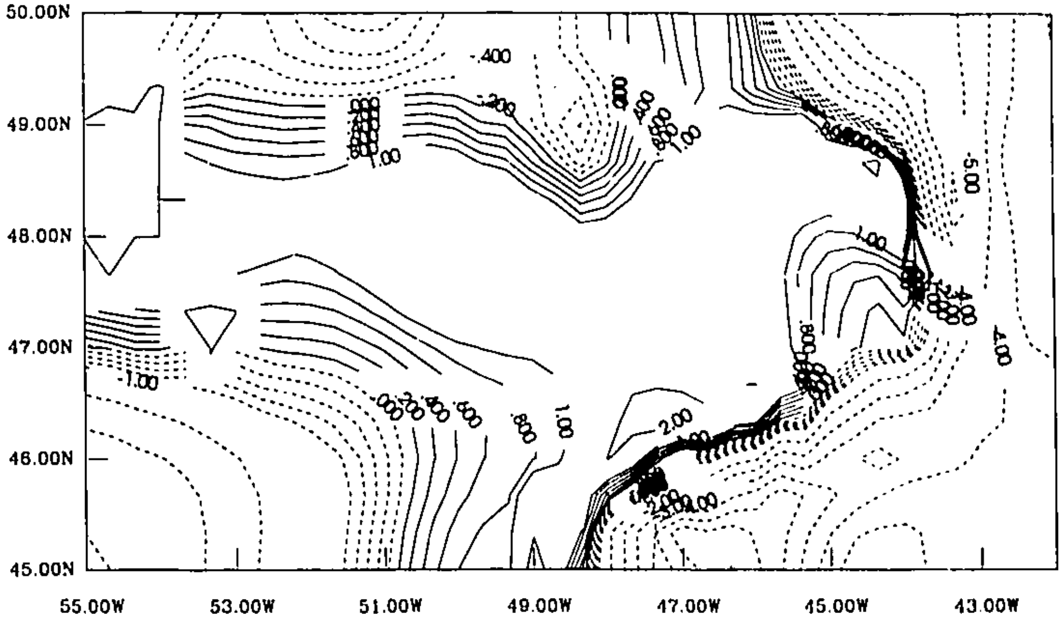

b)

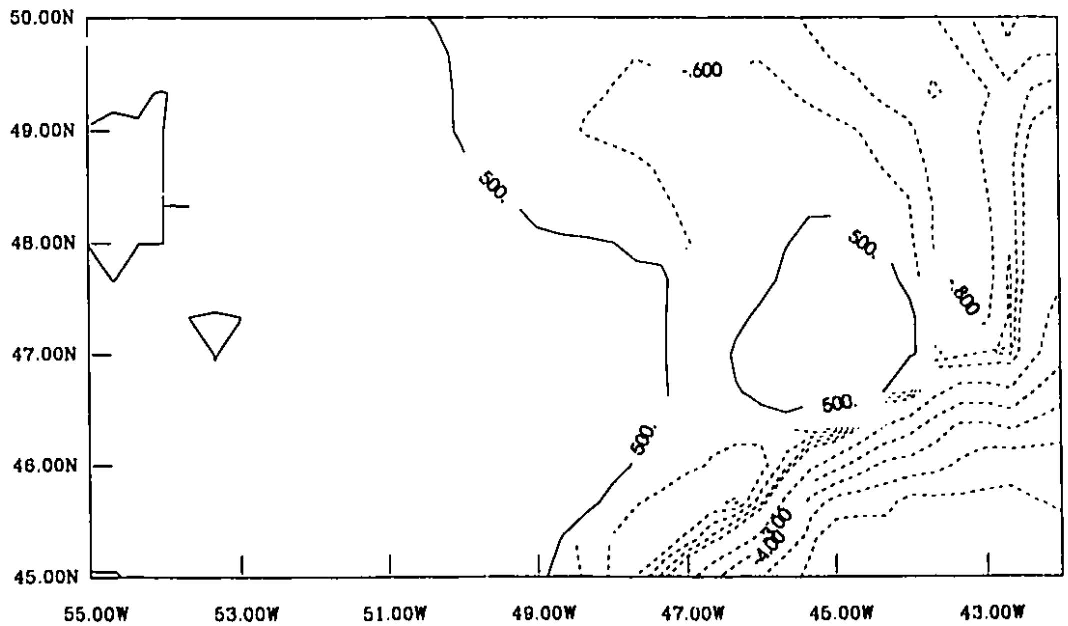

Figure 7.17: Temperature variations (°C), (1975-80)-(1967-72), at a) 0m and b) 500m for the Flemish Cap subregion.

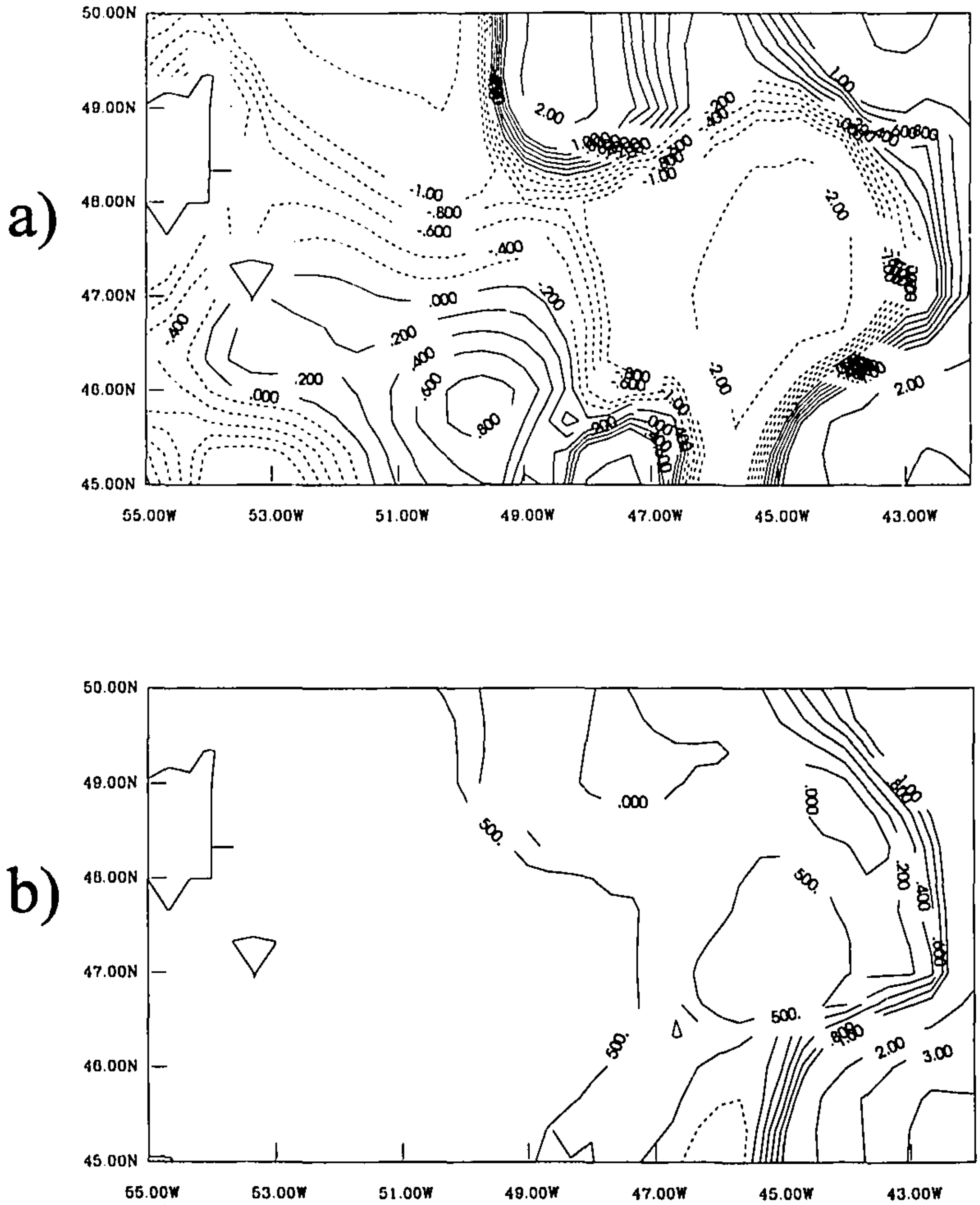

Figure 7.18: Temperature variations (°C), (1983-88)-(1975-80), at a) 0m and b) 500m for the Flemish Cap subregion.

CHAPTER 8: DISCUSSION AND CONCLUSION

In this thesis, the circulation of the northwestern Atlantic Ocean was diagnosed using the Mellor *et al* (1982) method. The emphasis was first toward estimating the mean (1910-89) summer mean circulation, then the seasonal and interdecadal variability were studied. The density field was computed from gridded temperature and salinity values obtained by applying a modified version of the Levitus (1982) objective analysis scheme with much higher resolution (1/3°x1/3° or 1/2°x1/2° versus 1°x1° used in Levitus, 1982). The data set used was from MEDS, supplemented by a subset of NODC data from J. Reid and by the 1980's data from Fukumori and Wunsch (1991). The original Levitus (1982) scheme was modified such that it allowed a better representation of the density gradients associated with fronts over the slope region. The 1910-1989 temperature and salinity fields obtained using this scheme are probably slightly biased toward the mean conditions that occurred during the second half of this century due to the time distribution of observations.

Bogden *et al* (1993) recently undertook a detailed diagnostic calculation of the North Atlantic Ocean. They showed, using the dynamic equations (5.1) together with specified vertical velocities at the top and bottom of the water column, that the velocities (u,v,w and hence Ψ) can be determined up to an arbitrary function of f/H. The velocity (and hence transport) can then be determined everywhere along an f/H contour if one value of $\mathbf{u} \times \nabla$ f/H is known on that contour. Mellor *et al* (1982) specified the transport on the eastern boundary as Ψ=0. Notice that Bogden *et al* (1993) applied the Ψ=0 condition when the 1000m isobath was encountered whereas Mellor *et al* (1982) used the 500m isobath. The results presented in this thesis reveal a strong dependance of the transport on the specified reference values which can be viewed as a weakness of this analysis; as the problem of the reliability of these values arises. Nevertheless, I am able to draw the conclusion that the circulation of the Labrador Sea is largely determined by dynamics external to the region. This statement follows from the analysis of the local wind and JEBAR forced circulation (Figs. 6.8, 6.13 and 6.14).

The current structure of the northwestern Atlantic ocean was also studied by Provost and Salmon (1986, hereafter P&S). Their analysis was based on data from 11 sections occupied between March 12 and May 12 1966. The main differences between P&S and the results presented in this thesis (Figs. 6.9), concern the cross-isobath flow and the NAC. The cross-isobath flow in the Labrador Sea did not seem to be observed consistently throughout the water column in their spring analysis (perhaps due to unresolved dynamics in their diagnostic model). In some of their figures (e.g., Figs. 7 and 16), the NAC appeared only in the upper 500m of the water column. This contradicts the results presented in Chapter 6 (see Figs. 6.9e-f), which show a deep NAC flowing northward along the eastern edge of Flemish Cap and then turning eastward. This deep NAC is also seen in Bogden *et al* (1993) (see their Figs. 22 and 23). Notice that P&S did show a deep NAC (see their Fig. 8) but their circulation in the Labrador Sea at 2000m flowed in the wrong direction. Figure 6.9 shows an NAC which extends throughout all the water column whereas Bogden *et al* (1993) analysis shows currents reversing direction between 2000 and 3500m (compare their Figs. 23 and 25 at 40°W and 50°N). It is possible that the barotropic component of the NAC shown in Fig. 6.9 may be overestimated so that it deep component (> 2000m) flows in opposite direction to that of Bogden *et al* (1993) and P&S (1986), but in the same direction as that of Mellor *et al* (1982, see their Fig.15). It thus appears that further work is still needed to better represent the deep northwestern Atlantic current characteristics as the results from different analysis differ slightly. Furthermore, at a depth of 1000m in the Labrador Sea, the Bogden *et al* (1993) current field looks suspicious as the LC flows poleward (see their Fig. 22).

It should be noted that P&S used only data from within the Labrador Sea, so that their analysis did not take into account dynamics external to the region of interest (at least explicitly), which was found to be important. Their best solution was obtained while adding the conservation of potential density (see their Eq. 4.21) as a constraint to their inverse method (see their Figs. 13 and 16). Their circulation pattern (see their Figs. 16) shows no sign reversal for the current direction in the Labrador Sea and is in good agreement with my Figs. 6.9. It seems that adding this constraint is somehow equivalent to infer the transport through the eastern boundary. One important conclusion of this thesis is that my results tend to show the importance of the external forcing (see sections 6.2 and 6.5) in comparison with the internal forcings (local JEBAR and wind).

In this analysis the method of Mellor *et al* (1982) is followed by neglecting the bottom friction in Eq. 5.9. The circulation obtained around the Grand Banks is not consistent with observations e.g. see the poleward currents on Fig. 6.9b. Perhaps bottom friction could be of importance in shallow regions with strong currents. Note that adding bottom friction to Eq. 5.9 would preclude the use of the Mellor *et al* (1982) method. A study of the circulation in the Grand Banks area is currently undertaken by de Young and Greatbatch using a model which explicitly takes into account the bottom friction. Furthermore, adding friction permits solving circulation for the planetary potential vorticity islands (closed f/H contours).

The Bernoulli method (Killworth, 1986) was also used on the data set described in section 3. The results obtained were not satifying as they showed a sign reversal in much of the deep current structure (LC, WGC and EGC). The currents derived from the Bernoulli method were similar to those obtained assuming a bottom level of no motion (both show deep currents flowing in the wrong way, see Figs. 4.2c and 4.4c) which seems to indicate that the Bernoulli method cannot resolve the barotropic transport properly. This is most likely due to the small difference in potential density between the surface and bottom waters (see Figs. 3.6 and 3.9) in the domain of interest. Killworth and Bigg (1988) also stated that the Bernoulli method failed in weakly stratified regions. Nevertheless, this calculation was undertaken as it was suggested (Killworth and Bigg, 1988) that this technique was useful in regions of strong currents. Indeed, the surface current structure obtained using the Bernoulli method was quite reasonable

It was found, from this analysis, that neither the local wind stress field nor the local JEBAR could explain the mean strength of the volume transport streamfunction in the Labrador Sea, the reference boundary used largely determined the mean magnitude of the interior transport. This analysis also suggests that the seasonal and interdecadal transport variability is largely driven by the local JEBAR term. Furthermore it was shown that the magnitude of both seasonal and interdecadal transport variability was about 2-6 Sv. But this thesis does not answer the question as to how much of this JEBAR is real. For the seasonal analysis, it was found that the local JEBAR variability field for the top 1500m was smooth with values of 1-3 Sv (warm-cold), whereas the total JEBAR field (Fig. 6.15a) was more noisy. This shows that that the local JEBAR variability of the deep ocean is important for estimating the total seasonal variability of the volume transport, which is contrary to the fact that the seasonal cycle is mostly a near surface event.

Throughout all thesis the local wind stress contribution to the total volume transport streamfunction has been presented as uncoupled from the local JEBAR contribution (Eqs. 5.16). Perhaps one should consider the possibility that the wind could push away the isopycnals at the surface from the isobaths which then feeds back on the transport through the local JEBAR. This could be the case for the nearly 12 Sv seasonal variability found in the northeast of Newfoundland (Fig. 6.15a), which was attributed to the local JEBAR (Fig. 6.15b), as the wind blows perpendicular to the isobaths in a region where strong horizontal density gradients are found (Fig. 1.1, Figs. 3.11, Figs. 3.12 and Figs. 6.7).

Analyses like those of Kushnir (1994) and Deser and Blackmon (1993) restrict their attention to the ocean surface. The results presented in Levitus (1989a) and in this thesis tend to show that the surface trends (warming, cooling, freshning, etc) are not necessarly representative of the situation that occurs in deeper waters (sections 7.2 and 7.4). For example, the sign change between the surface and deeper waters (see Figs 7.10, 7.11 and 7.12) during the *G.S.A.* years shows that while a freshning and cooling occured in near surface waters, the opposite is found in deeper waters. The mechanism for explaining this situation is the disappearance of *deep water formation* during the *G.S.A.* years (Lazier, 1980). This disappearance (weakening) implies that the fresh and cold surface waters are not mixed with the warmer and saltier deep waters, such that these deep waters appear to be warmer and saltier during the *G.S.A.* years. The subregion analysis (section 7.4) reveals that variability at time scales smaller than those studied in section 7.2 and 7.3 exist but their associated transport variablity cannot be diagnosed due to a lack of data.

The collapse of the fisheries industry in eastern Canada is due to a dramatic decrease of the cod stock in this region. The interdecadal analysis shows that the water mass properties vary from one pentad to another. Dunbar (1993) suggested that the observed decrease in the cod stock is perhaps linked with *natural* climate cycles in such a way that the cod population decreases when colder than normal temperature conditions occur in near surface waters. The reason for this is that cod eggs and young cod cannot develop below a temperature of 2°C (Dunbar, 1993). Negative surface temperature trends can be found during the *G.S.A.* years during which the deep water formation was suppressed. Recent data from the coastal regions off Newfoundland also show a dramatic decrease in SST during the 1990s.

One of the most important characteristics of my diagnosed climatological mean circulations (1910-1989 summer, warm and cold seasons) is the JEBAR driven cross-isobath flow. Associated with this flow is the transport of relatively cold, fresh West Greenland and Labrador shelf waters into the central Labrador Sea. Based on this analysis, I suggest that the path by which the fresh *G.S.A.* anomaly entered the central Labrador Sea was via the cross-shelf flow off Labrador. In addition, I further suggest that any future variations in this cross-shelf flow or the temperature and salinity properties associated with it, may once more alter the properties of the Labrador Sea deep convection and hence the climate of the North Atlantic.

REFERENCES

Akima H., A method for bivariate interpolation and smooth surface fitting for irregularity distributed data points, *ACM Transactions on Mathematical Software*, 4(2), 148-159, 1978.

Bogden P.S., R.E. Davis and R. Salmon, The North Atlantic circulation: combining simplified dynamics with hydrographical data, *Journal of Marine Research*, 51,1,1-52, 1993.

Bryan K., A numerical method for the study of the circulation of the world ocean, *J. of Comp. Phys.*, 4, 347-376, 1969.

Bryden H.L., New polynomials for thermal expansion, adiabatic temperature gradient and potential temperature of sea water, *Deep Sea Res.*, 20, 401-408, 1973.

Clarke, R.A, Transport through the C[illegible] Farewell-Flemish Cap section, *Rapport Procès-Verbaux Réunion Conseil International Exploration Mer*, 185, 120-130, 1984.

Clarke, R.A. and J.-C. Gascard, The formation of the Labrador Sea Water: Part I large-scale processes, *J. Phy. Oceanogr*, 13, 1764-1768, 1983.

Cox M.D., A primitive equation three dimensional model of the ocean, *GFDL Ocean Group Technical Report No.1*, 1984.

Cressman, G.P., An operational objective analysis sytem, *Mon. Weath. Rev.*, 87, 367-74, 1959.

Daley, R, *Atmospheric Data Analysis*, Atmospheric & Space Sciences Series, Cambridge University Press, Editors: Houghton-Rycroft-Dessler, Cambridge, 456 pp., 1991.

Da Silva A.M., Estimates of monthly mean wind stress from monthly pseudo-stress, winds and wind standard deviations, Dept. of Geophysics, University of Wisconsin, Milwaukee, U.S.A, 1991.

Deser, C., and M.L., Blackmon, Surface climate variations over the North Atlantic ocean during winter: 1900-1989, *Journal of Climate*, 6, 1743-1753, 1993.

Dickson, R.R., J. Meincke, S.A. Malmberg and A.J. Lee, The "Great Salinity Anomaly" in the North Atlantic 1968-1982, *Prog. in Oceanogr.*, 20, 103-151, 1988.

Dickson, R.R, E.M. Gmitrowicz and A.J. Watson, Deep water renewal in the northern North Atlantic, *Nature*, 344, 848-850, 1990.

Dunbar M.J., Eastern arctic waters, **Fish. Res. Board of Canada**, 88, 131 pp., 1951.

Dunbar M.J., Marine Climate and the Newfoundland Northern Cod, *Centre for Climate and Global Change Research Quaterly*, vol. 4, 1, McGill University, 1993.

Fofonoff, N.P, Dynamics of ocean currents. *The Sea*, Vol 1, M.N. Hill, editor, Interscience Publishers, New-York, 323-395, 1962.

Fukumori, I. and C. Wunsch, Efficient representation of the North Atlantic hydrographic and chemical distributions, *Prog. Oceanogr.*, 27, 111-196, 1991.

Fukumori, I., F. Martel and C. Wunsch, The hydrographic of the North Atlantic in the early 1980's: An atlas., *Prog. Oceanogr.*, 27, 1-110, 1991.

Greatbatch R.J. and A. Goulding, Seasonal variations in a linear barotropic model of the North Atlantic driven by the Hellerman and Rosenstein wind stress field, *J. Phys. Oceanogr.*, 19, 572-595, 1989.

Greatbatch R.J., B. DeYoung, A. Goulding and J. Craig, On the influence of local and North Atlantic wind forcing on the sesonal variation of sea level on the Newfoundland and Labrador Shelf, *J. Geophys. Res.*, 95, 5279-5289, 1990.

Greatbatch R.J., G. Fanning, A. Goulding and S. Levitus, A diagnosis of interpentadal circulation changes in the North Atlantic, *J. Geophys. Res.*, 96, 22009-22023, 1991.

Hachey H.B., Biological and oceanographic conditions in Hudson Bay. 6. The general hydrography and hydrodynamics of the water of the Hudson Bay region. *Contr. Can. Biol.*, N.S., 7 (9), 91-118, 1931.

Hachey H.B., The circulation of Hudson Bay water as indicated by drift bottles, *Science*, 82 (2125), 275-276, 1935.

Hellerman, S. and M. Rosenstein, Normal monthly wind stress over the world ocean with error estimates, *J. Phys. Oceanogr.*, 13, 1093-1104, 1983.

Holland W.R., Baroclinic and Topographic Influences on the Transport in Western Boundary Currents, Geophys. Fluid Dyn., 4, 187-210, 1973.

Holland, W.R. and A.D. Hirschman, A numerical calculation of the circulation of the North Atlantic Ocean, *J. Phys. Oceanogr.*, 2, 336-354, 1972.

Huthnance J.M., Slope currents and "Jebar", *J. Phys. Oceanogr.*, 14, 795-810, 1984.

Ivers, W.D, *The deep circulation in the northern North Atlantic with especial reference to the Labrador Sea*, Ph.D. Thesis, University of California at San Diego, 179pp., 1975.

Ikeda M., Decadal oscillations of air-ice-ocean system in the northern hemisphere, *Atmos.-Ocean*, 28, 106-139, 1990.

Kiilerich A.B., A theoretical treatment of the hydrographical observation material. Godthaab Expedition, **Medd. om Grönl**, 78 (5), 1-149, 1939.

Killworth, P.D, A Bernouilli inverse method for determining the ocean circulation, *J. Phys. Oceanogr.*, 16, 2031-2051, 1986.

Killworth, P.D. and G.R. Bigg, An intercomparison of inverse methods using an eddy resolving general circulation model, *J. Phys. Oceanogr.*, 18, 987-1008, 1988.

Krauss, W, The North Atlantic Current, *J. Geophys. Res.*, 91, 5061-5074, 1986.

Kushnir, Y, Interdecadal variations in the North Atlantic sea surface temperature and associated atmospheric conditions. *Journal of Climate*, 7, 141-157, 1994.

Lazier, J.R.N, The renewal of the Labrador Sea water, *Deep-Sea Res.*, 20, 341- 353, 1973.

Lazier, J.R.N, Oceanographic conditions at O.W.S Bravo 1964-1974, *Atmos.-Ocean*, 18, 227-238, 1980.

Lazier, J.R.N., Seasonal variability of temperature and salinity in the Labrador Current. Journal of Marine Reseach, 40, 341-356, 1982.

Lazier, J.R.N. and D.G. Wright., Annual velocity variations in the Labrador Current, *J. Phys. Oceanogr.*, 23, 4, 659-678, 1993.

Lee, A.J., *NORWESTLANT Surveys: Physical oceanography*, ICNAF Special Publ., 7, Part 1, 31-54, 1968.

Lee, A. and D. Ellet., On the water masses of the Northwest Atlantic Ocean, *Deep Sea Res.*, 12, 129-142, 1967.

Leetma A. and A.F. Bunker, Updated charts of the mean annual wind stress, convergences in the Ekman Layers, and Sverdrup transports in the North Atlantic, *Journal of Marine Research*, 36, 311-322, 1978.

Levitus, S., Climatological Atlas of the World Ocean. NOAA Prof. Pap, 13, Natl. Oceanic and Atmos. Admin., Washington D.C. 1982.

Levitus, S., Interpentadal variability of temperature and salinity at intermediate depths of the North Atlantic ocean, 1970-1974 versus 1955-1959, *J. Geophys. Res.*, 94, 6091-6131, 1989a.

Levitus, S., Interpentadal variability of salinity in the upper 150m of the North Atlantic ocean, 1970-1974 versus 1955-1959, *J. Geophys. Res.*, 94, 9679-9685, 1989b.

Levitus, S., Interpentadal variability of temperature and salinity in the deep North Atlantic, 1970-1974 versus 1955-1959, *J. Geophys. Res.*, 94, 16125-16131, 1989c.

Levitus, S., Interpentadal variability of steric sea level and geopotential thickness of the North Atlantic ocean, 1970-1974 versus 1955-1959, *J. Geophys. Res.*, 95, 5233-5238, 1990.

Levitus, S. and A. Oort, Global analysis of oceanographic data, *Bull. Amer. Meteor. Soc.*, 58, 1270-1284, 1977.

Mercier, H., Determining the general circulation of the ocean: a non linear inverse problem, *J. Geophys. Res.*, 91, 5103-5109, 1986.

Mercier, H., A study of the time averaged circualtion in the western North Atlantic by simultaneous nonolinear inversion of hydrographic and current meter data, *Deep Sea Res.*, 36, 297-313, 1989.

Mercier, H, M. Ollitrault and P.Y. Le Traon., An inverse model of the North Atlantic general circulation using Lagrangian float data. *J. Phys. Oceanogr.*, 23, 689-715, 1993.

McCartney, M.S. and L.D. Talley, The Subpolar Water Mode of the North Atlantic, *J. Phy. Oceanogr.*, 12, 1169-1187, 1982.

Mellor, G.L., C.R. Mechoso and E. Keto, A diagnostic calculation of the general circulation of the Atlantic Ocean, *Deep-Sea Res.*, 29, 1171-1192, 1982.

Mertz, G. and D.G. Wright, Interpretation of the JEBAR term, *J. Phys. Oceanogr.*, 22, 301-305, 1992.

Munk W. H., On the wind-driven ocean circulation, *J. Meteorol.*, 7, 79-93, 1950.

Myers R.A. Helbig J.A. and Holland D., Seasonal and interannual variability of the Labrador Current and the West Greenland Current, *ICES* C/M 1989/C:16, 18pp, 1989.

Mysak L.A. and Manak D.K., Arctic sea-ice extent and anomalies 1953-1984, *Atmos.-Ocean*, 27, 376-405, 1989.

Mysak, L.A., D.K. Manak and R.F. Marsden, Sea-ice anomalies in the Greenland and Labrador Seas during 1901-1984 and their relation to an interdecadal climate cycle, *Clim. Dyn.*, 5, 111-133, 1990.

Pedlosky J., Geophysical Fluid Dynamics, Springer-Verlag, New-York, 624 pp., 1979.

Petrie B., J.W. Loder, S. Akenhead and J. Lazier, Temperature and salinity variability on the eastern Newfoundland shelf: the annual harmonic, *Atmos.-Ocean*, 29, 14-36, 1991.

Provost, C. and R. Salmon, A variational method for inverting hydrographic data, *J. Mar. Res.*, 44, 1-34, 1986.

Sarkisyan, A.S. and V.F. Ivanov, The combined effect of baroclinicity and bottom relief as an important factor in the dynamics of ocean currents. Izv. Acad. Sci. USSR, *Atmosp. Oceanic Phys.*, 173-188 (AGU translation), 1971.

Seeman, R.S. Objective analysis accuracies of statistical interpolation and successive correlation schemes, *Aust. Met. Mag.*, 31, 225-240, 1983.

Smith, E.M., F.M. Soule and O. Mossby, The Marion and General Greene Expeditions to Davis Strait and Labrador Sea, *Bulletin of the U.S. Coast Guard*, 19, 259 pp, 1937.

Stommel H. and F. Schott, The beta spiral and the determination of the absolute velocity field from hydrographic station data, *Deep-Sea Res.*, 24, 325-329, 1977.

Swallow, J.G. and L.V. Worthington, Deep currents in the Labrador Sea, *Deep-Sea Res.*, 16, 77-84, 1969.

Talley L.D. and M.S. McCartney, Distribution and circulation of the Labrador Sea, *J. Phy. Oceanogr.*, 12, 1189-1205, 1982.

Thompson, K.R., J.R.N. Lazier and B. Taylor, Wind-forced changes in Labrador Current transport, *J. Geophys. Res.*, 91, 14, 261-268, 1986.

Weaver A.J. and E.S. Sarachik, Evidence for decadal variability in an ocean general circulation model: An advective mechanism, *Atmos.-Ocean*, 29, 197-231, 1991.

Worthington, L.V., *On the North Atlantic circulation*, Johns Hopkins Oceanogr. Studies, 6, Johns Hopkins University Press, Baltimore and London, 110 pp, 1976.

Wunsch, C., The North Atlantic general circulation west of 50°W determined by inverse methods, *Rev. of Geophys. and Sp. Phys.*, 16, 583-620, 1978.

APPENDIX 1

a)

b)

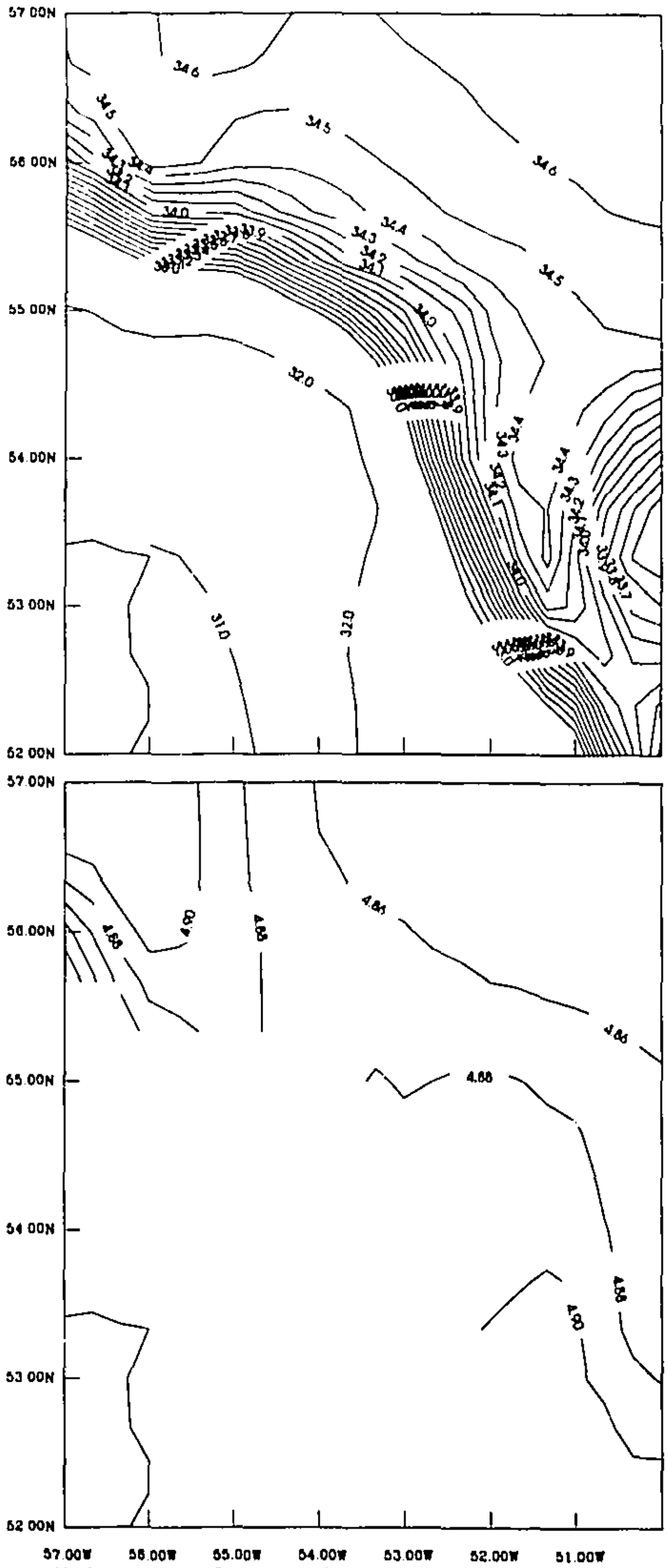

Figure A1.1: Warm season salinity (psu), for the 1959-64 period, at a) 0m and b) 500m (real value = 30 + reported value) for the Hamilton Bank subregion.

a)

b)

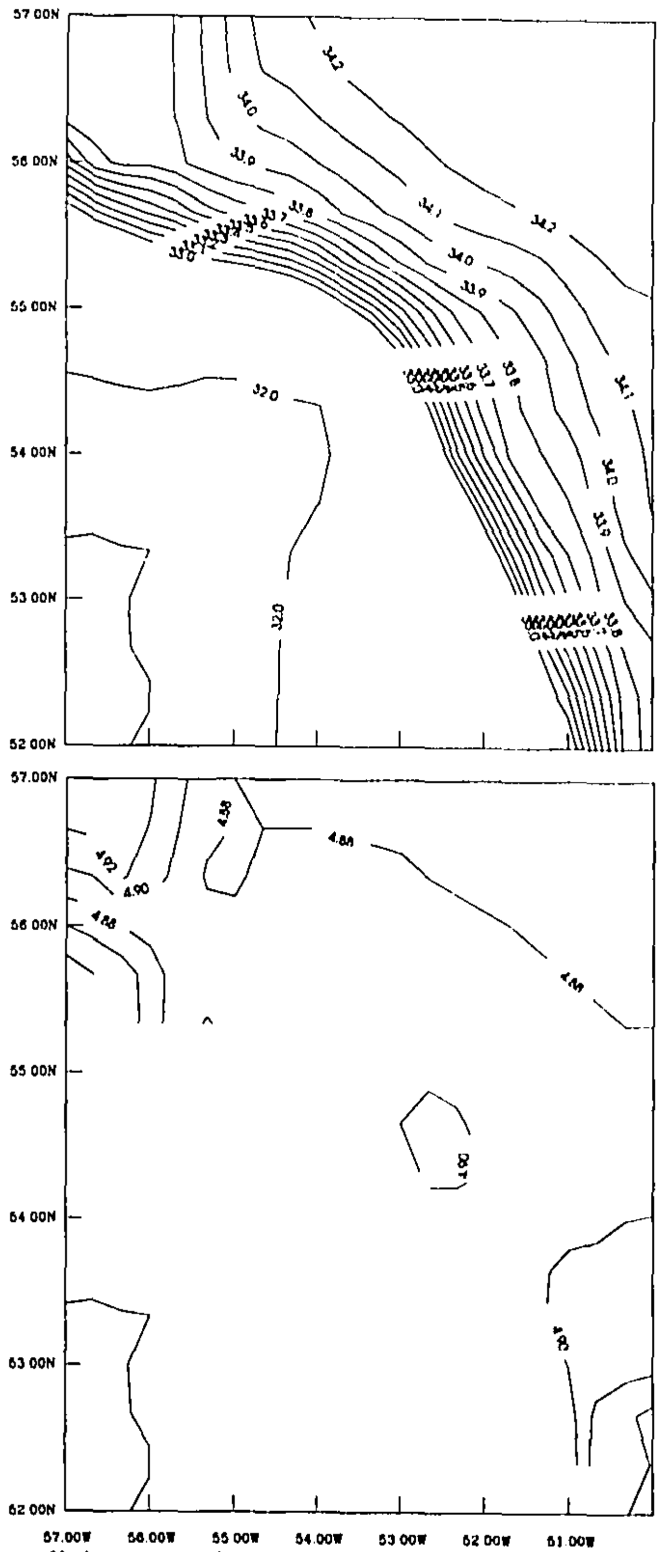

Figure A1.2: Warm season salinity (psu), for the 1967-72 period, at a) 0m and b) 500m (real value = 30 + reported value) for the Hamilton Bank subregion.

a)

b)

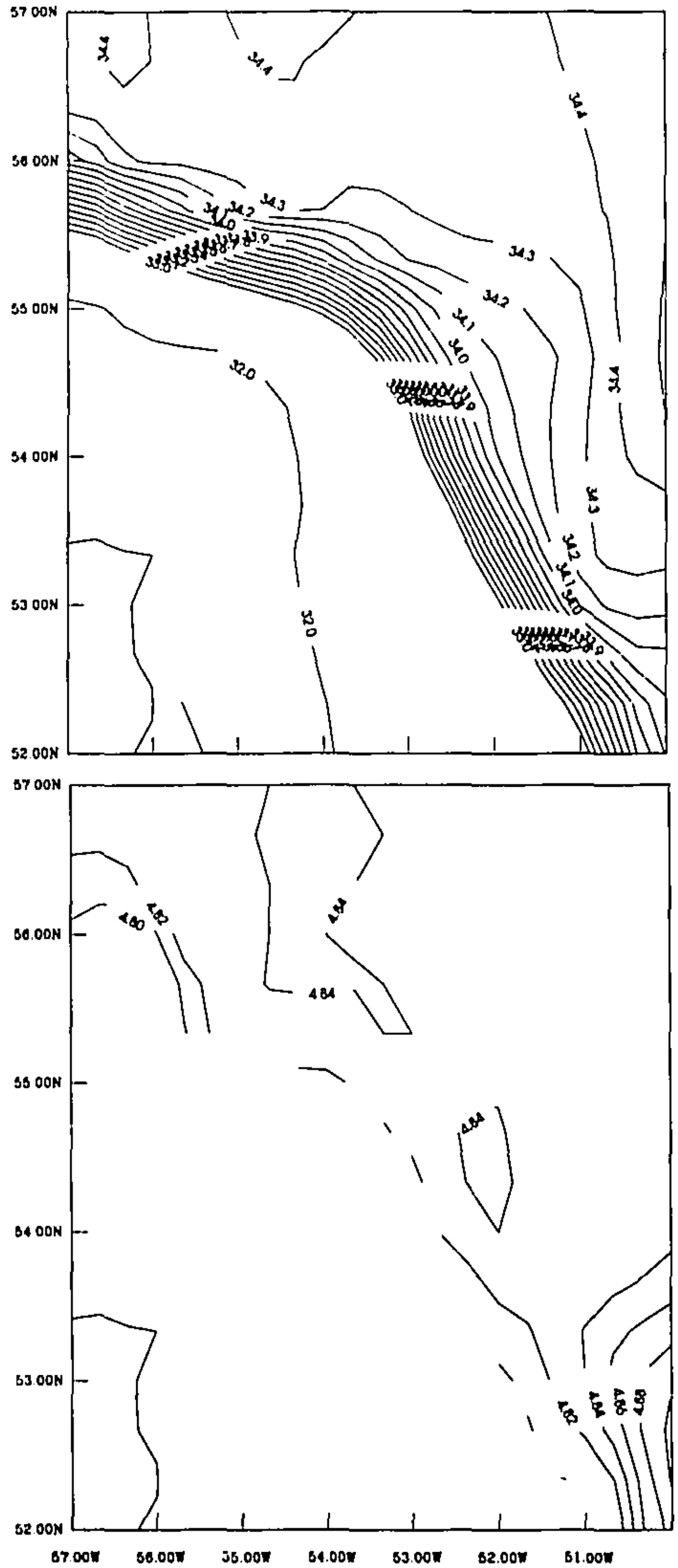

Figure A1.3: Warm season salinity (psu), for the 1975-80 period, at a) 0m and b) 500m (real value = 30 + reported value) for the Hamilton Bank subregion.

a)

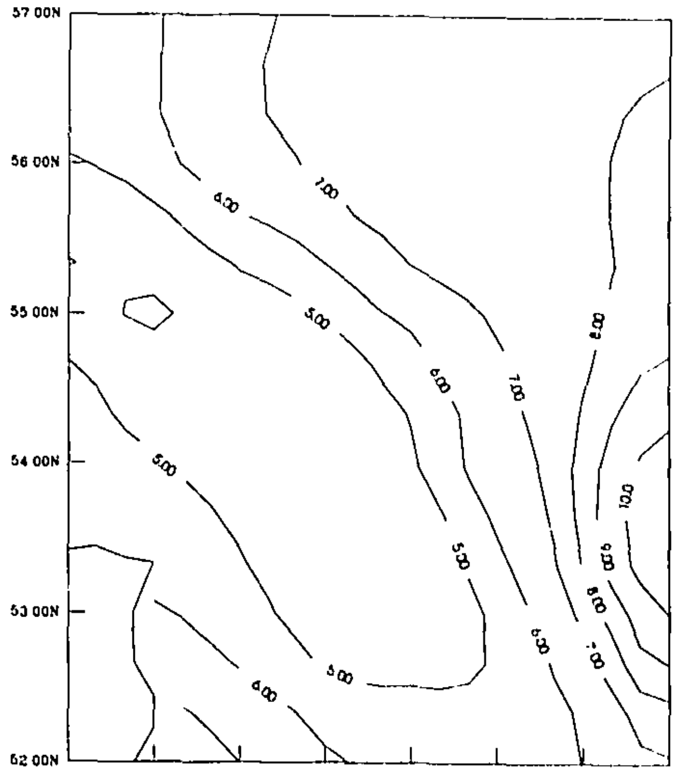

b)

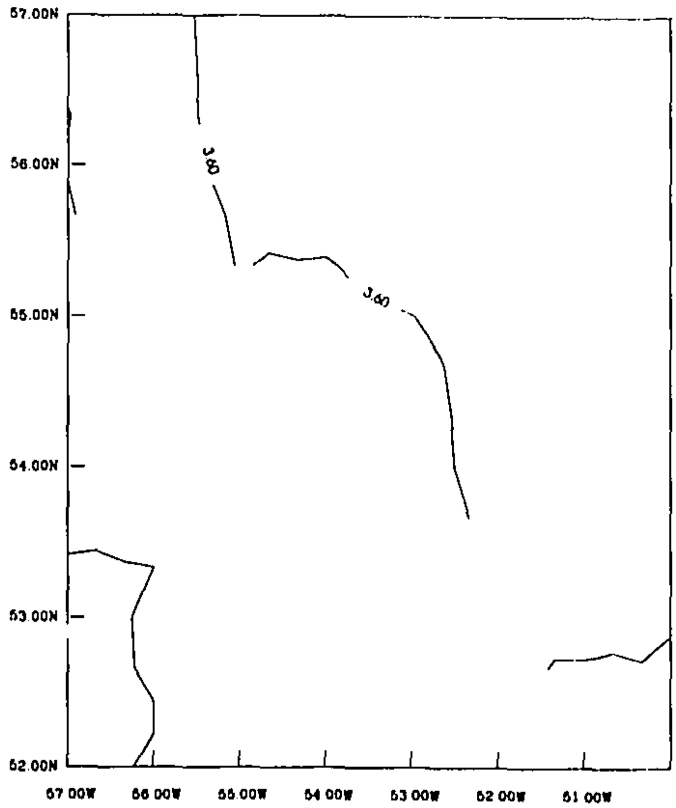

Figure A1.4: Warm season *in situ* temperature (°C), for the 1959-64 period, at a) 0m and b) 500m for the Hamilton Bank subregion.

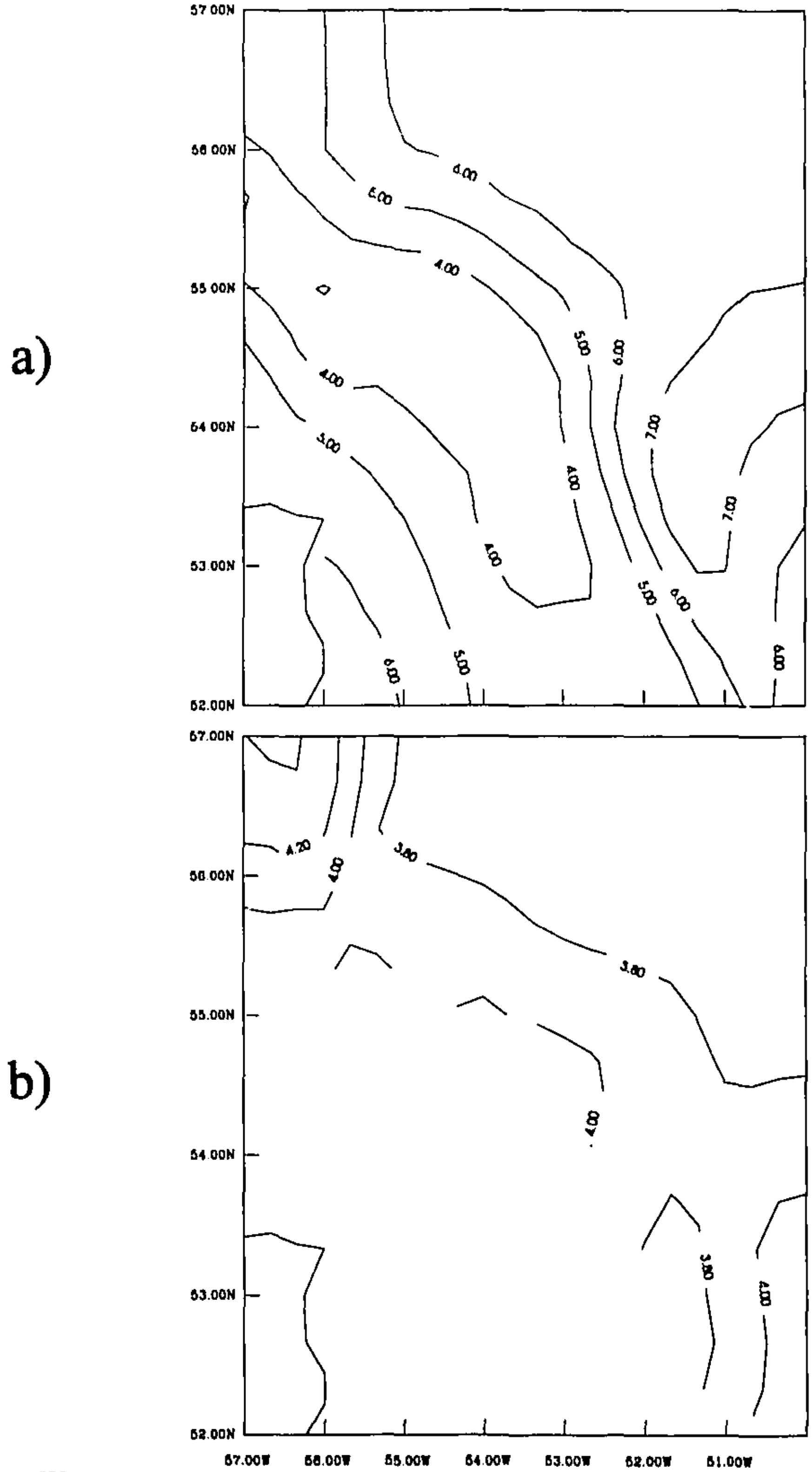

Figure A1.5: Warm season *in situ* temperature (°C), for the 1967-72 period, at a) 0m and b) 500m for the Hamilton Bank subregion.

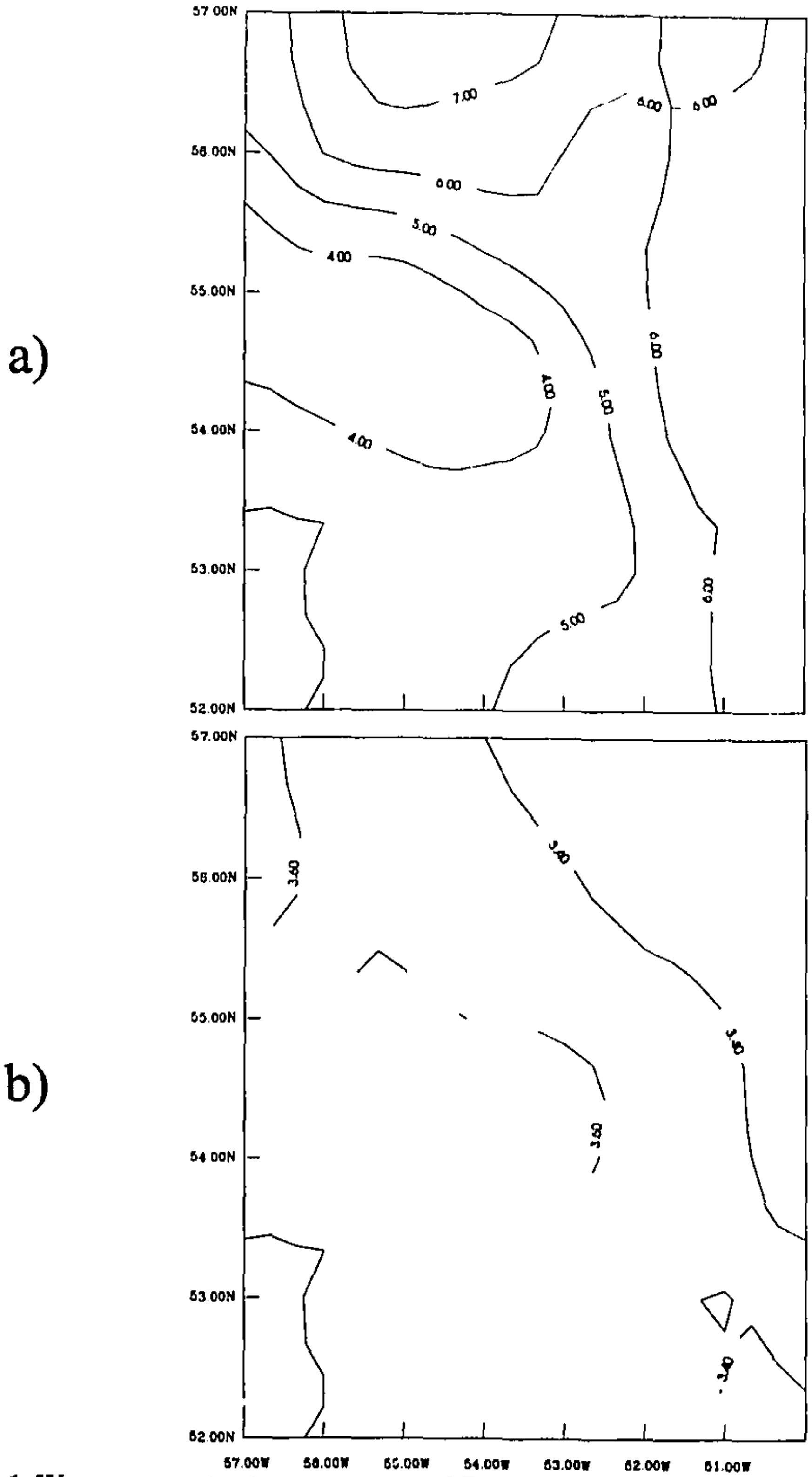

Figure A1.6: Warm season *in situ* temperature (°C), for the 1975-80 period, at a) 0m and b) 500m for the Hamilton Bank subregion.

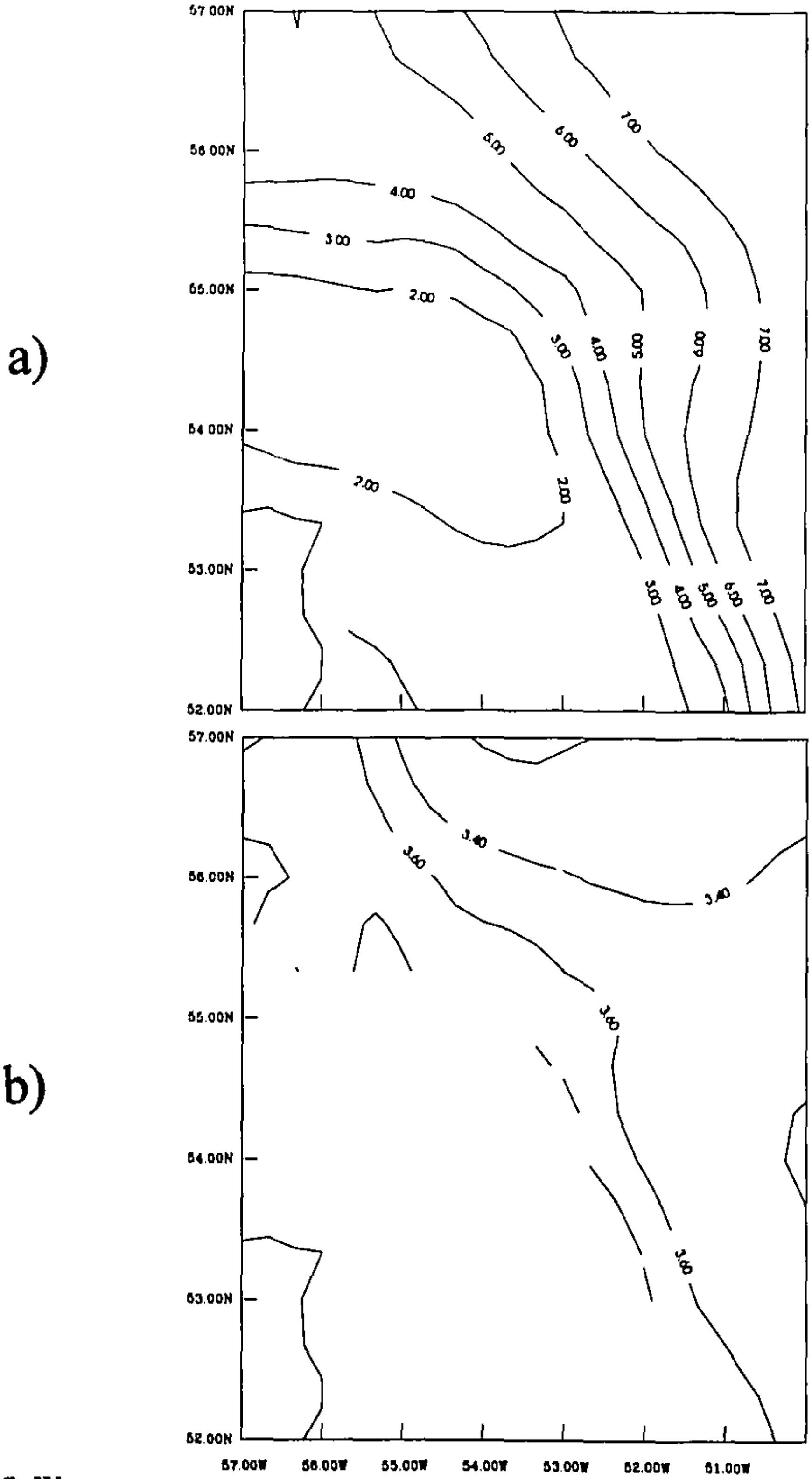

Figure A1.7: Warm season *in situ* temperature (°C), for the 1983-88 period, at a) 0m and b) 500m for the Hamilton Bank subregion.

a)

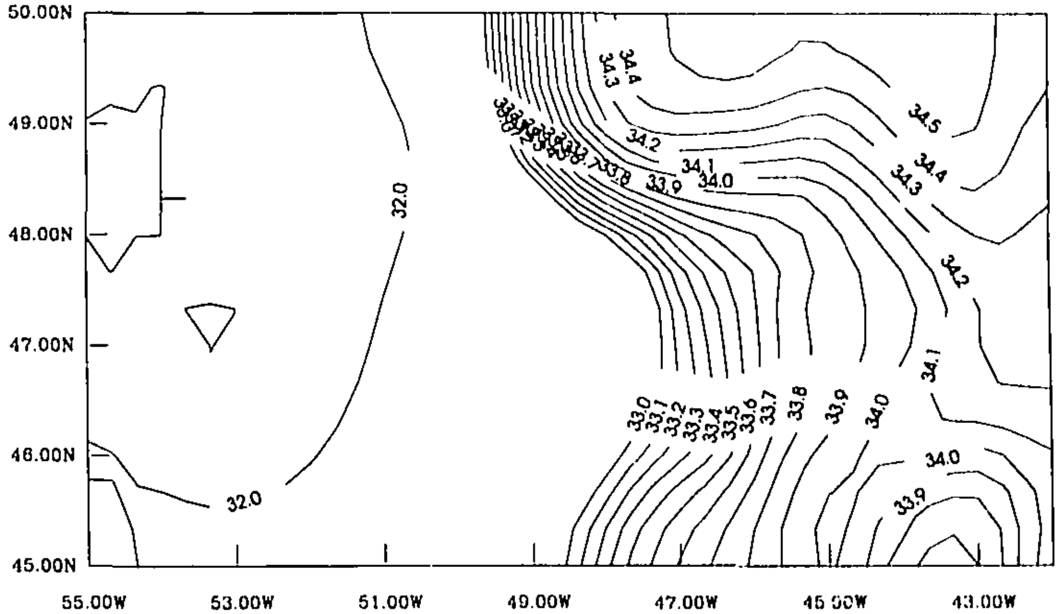

b)

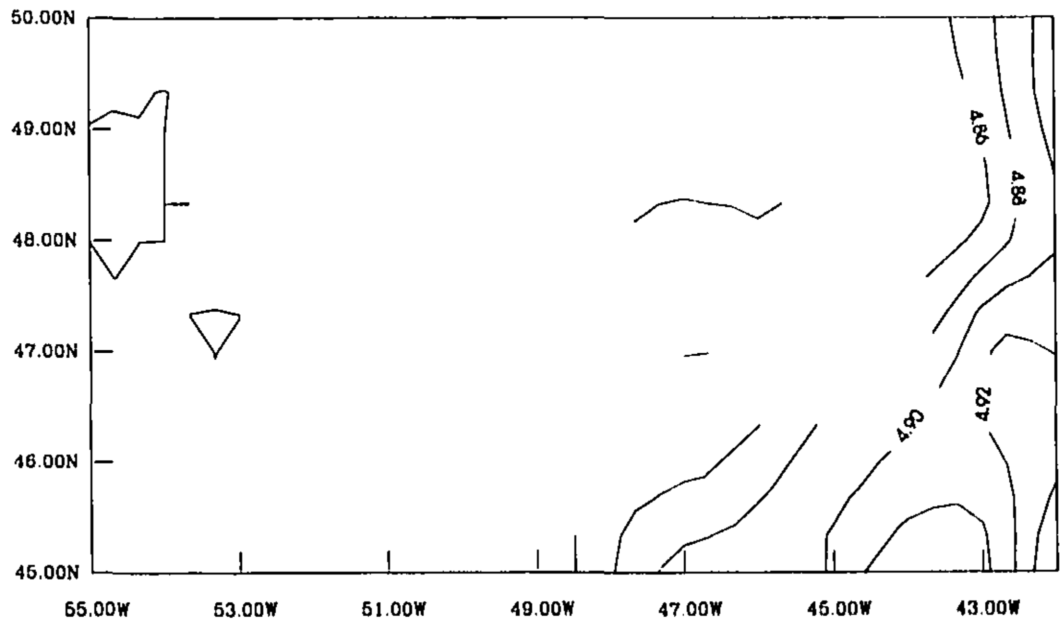

Figure A1.8: Warm season salinity (psu), for the 1959-64 period, at a) 0m and b) 500m (real value = 30 + reported value) for the Flemish Cap subregion.

a)

b)

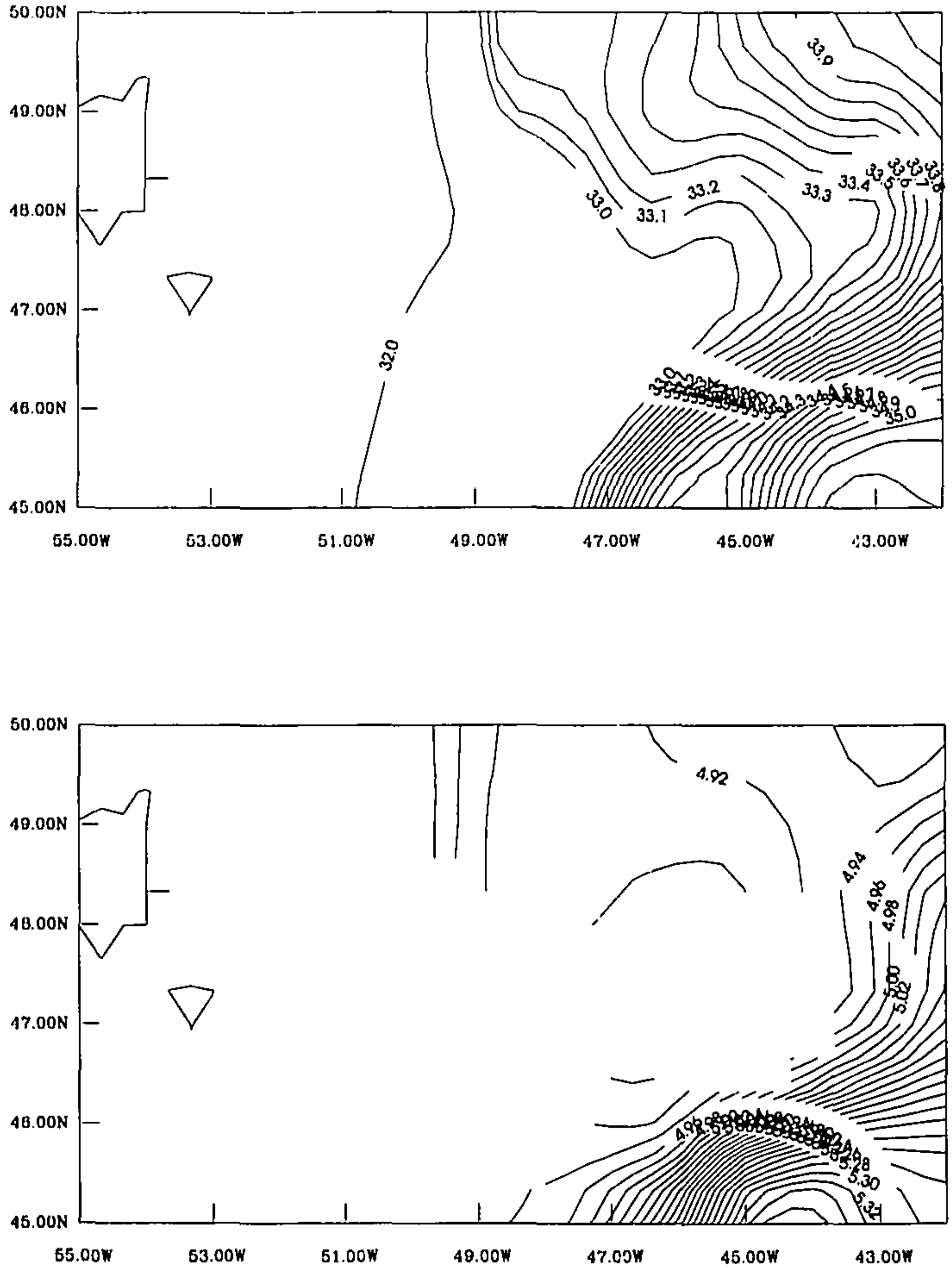

Figure A1.9: Warm season salinity (psu), for the 1967-72 period, at a) 0m and b) 500m (real value = 30 + reported value) for the Flemish Cap subregion.

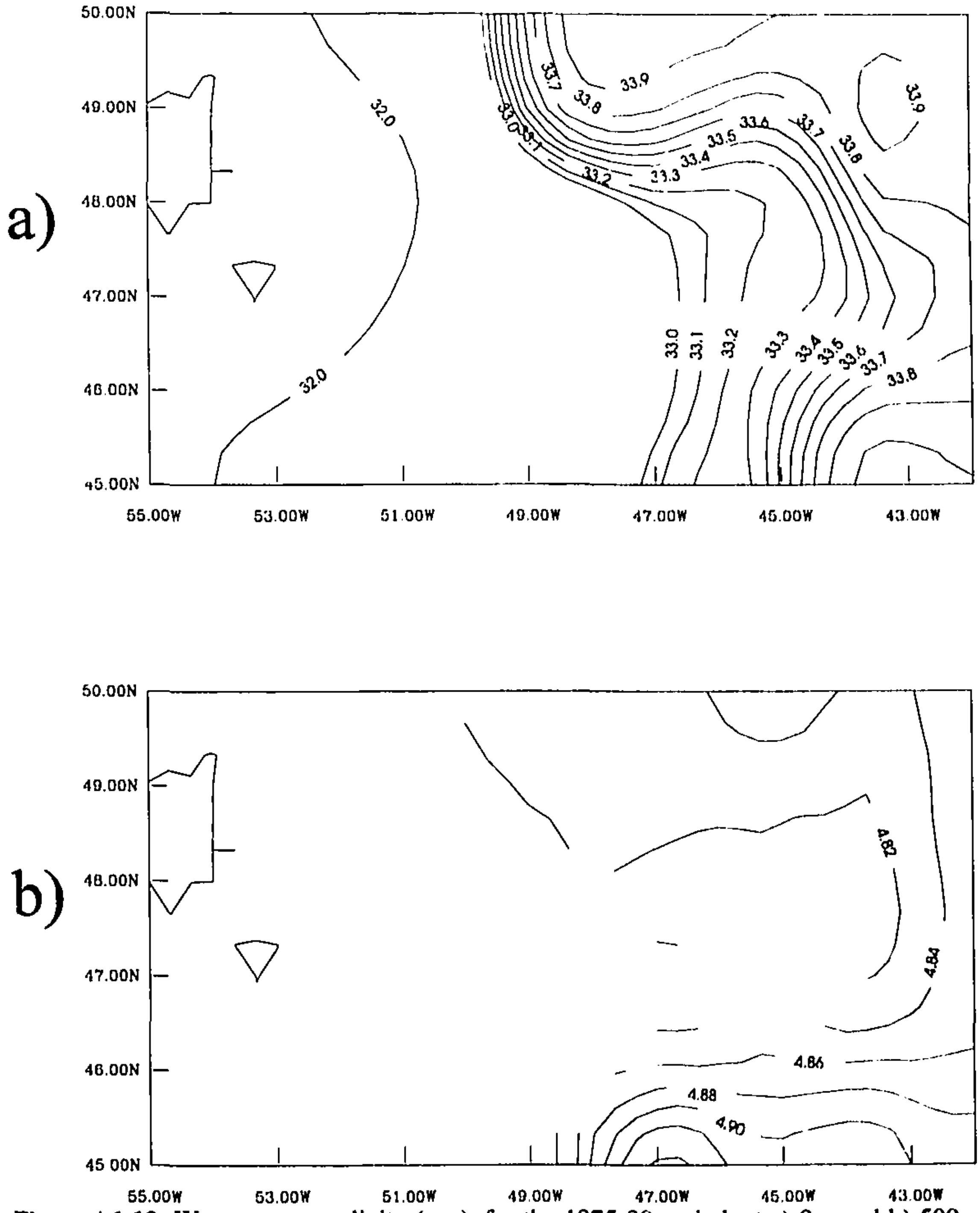

Figure A1.10: Warm season salinity (psu), for the 1975-80 period, at a) 0m and b) 500m (real value = 30 + reported value) for the Flemish Cap subregion.

a)

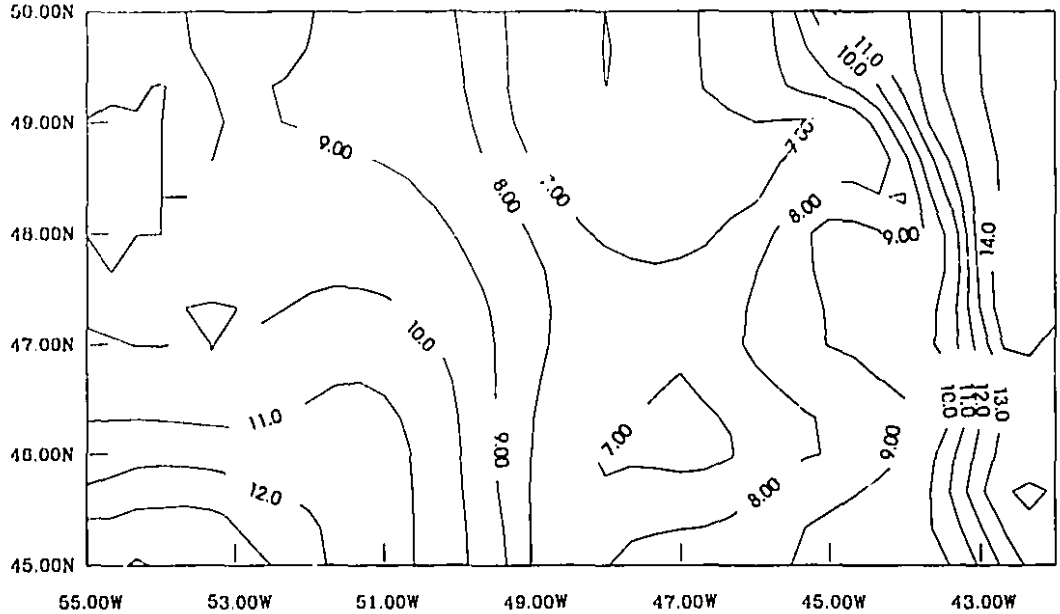

b)

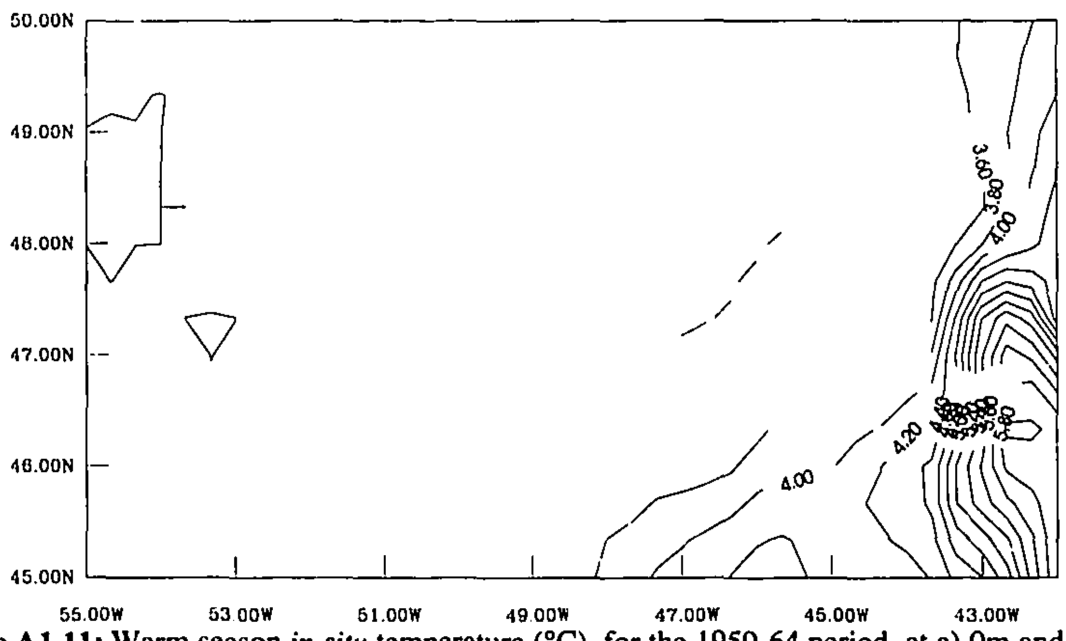

Figure A1.11: Warm season *in situ* temperature (°C), for the 1959-64 period, at a) 0m and b) 500m for the Flemish Cap subregion.

a)

b)

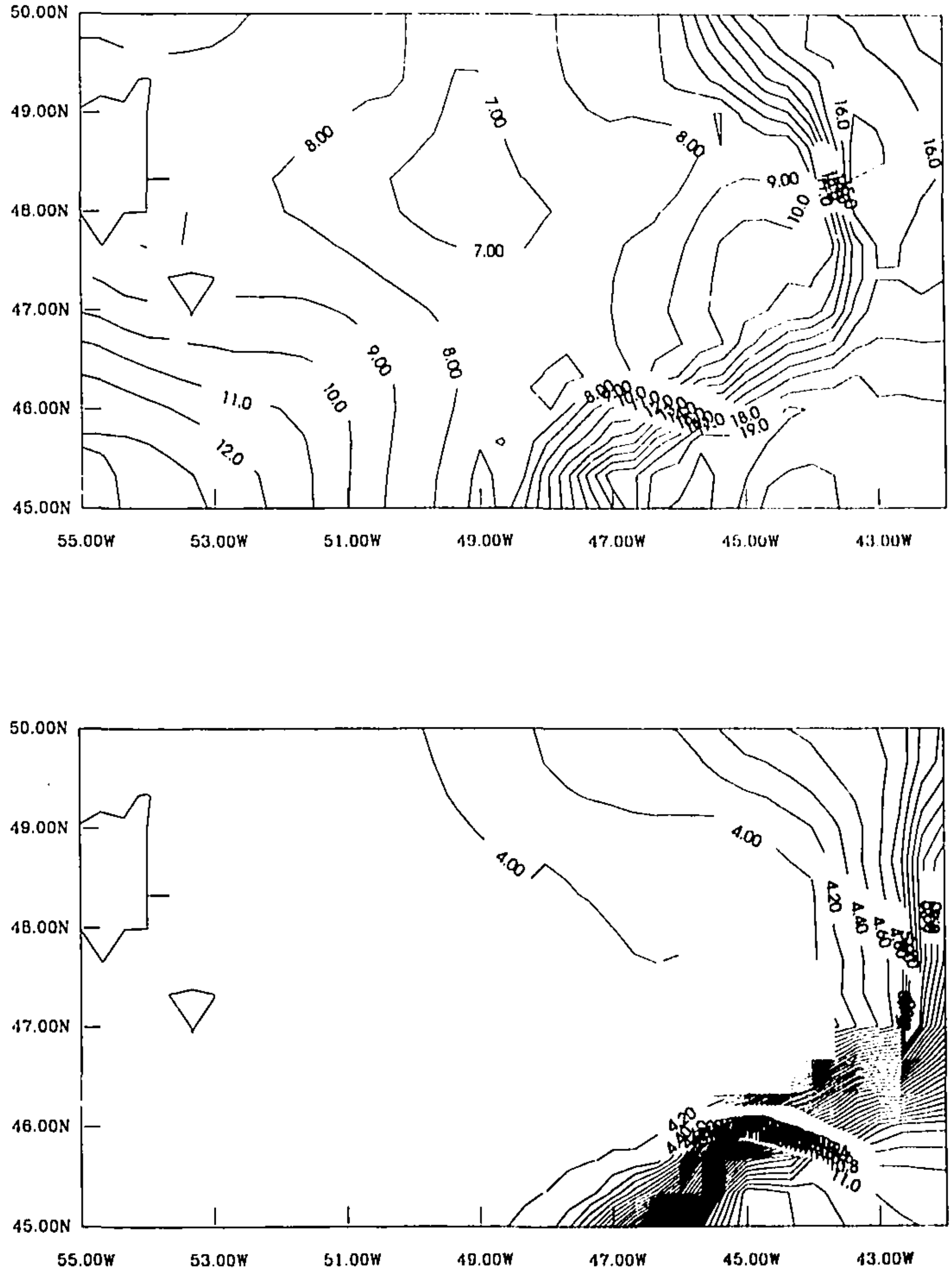

Figure A1.12: Warm season *in situ* temperature (°C), for the 1967-72 period, at a) 0m and b) 500m for the Flemish Cap subregion.

a)

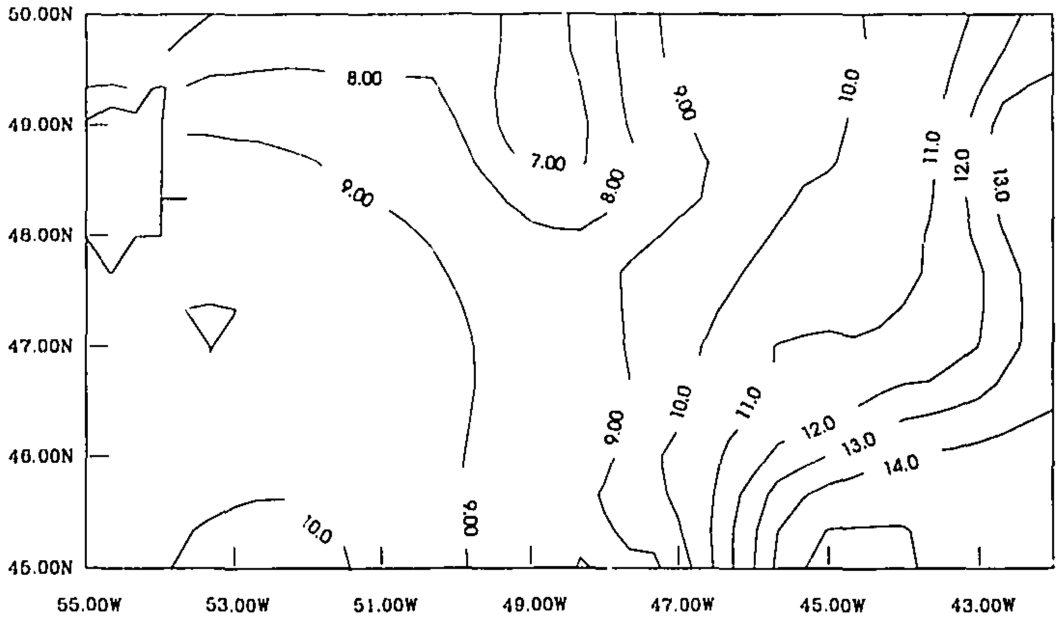

b)

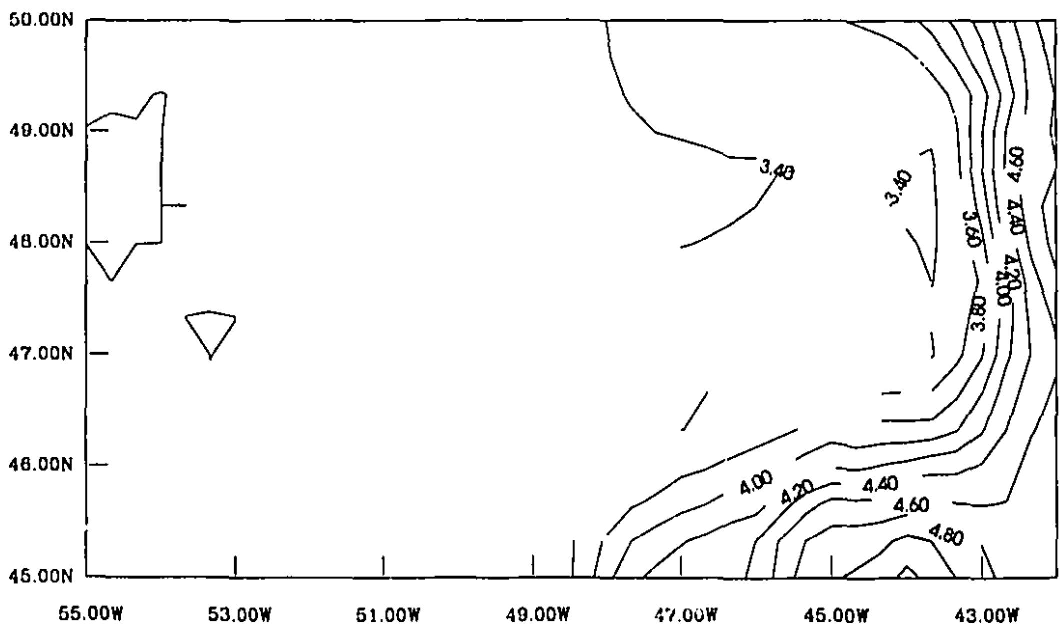

Figure A1.13: Warm season *in situ* temperature (°C), for the 1975-80 period, at a) 0m and b) 500m for the Flemish Cap subregion.

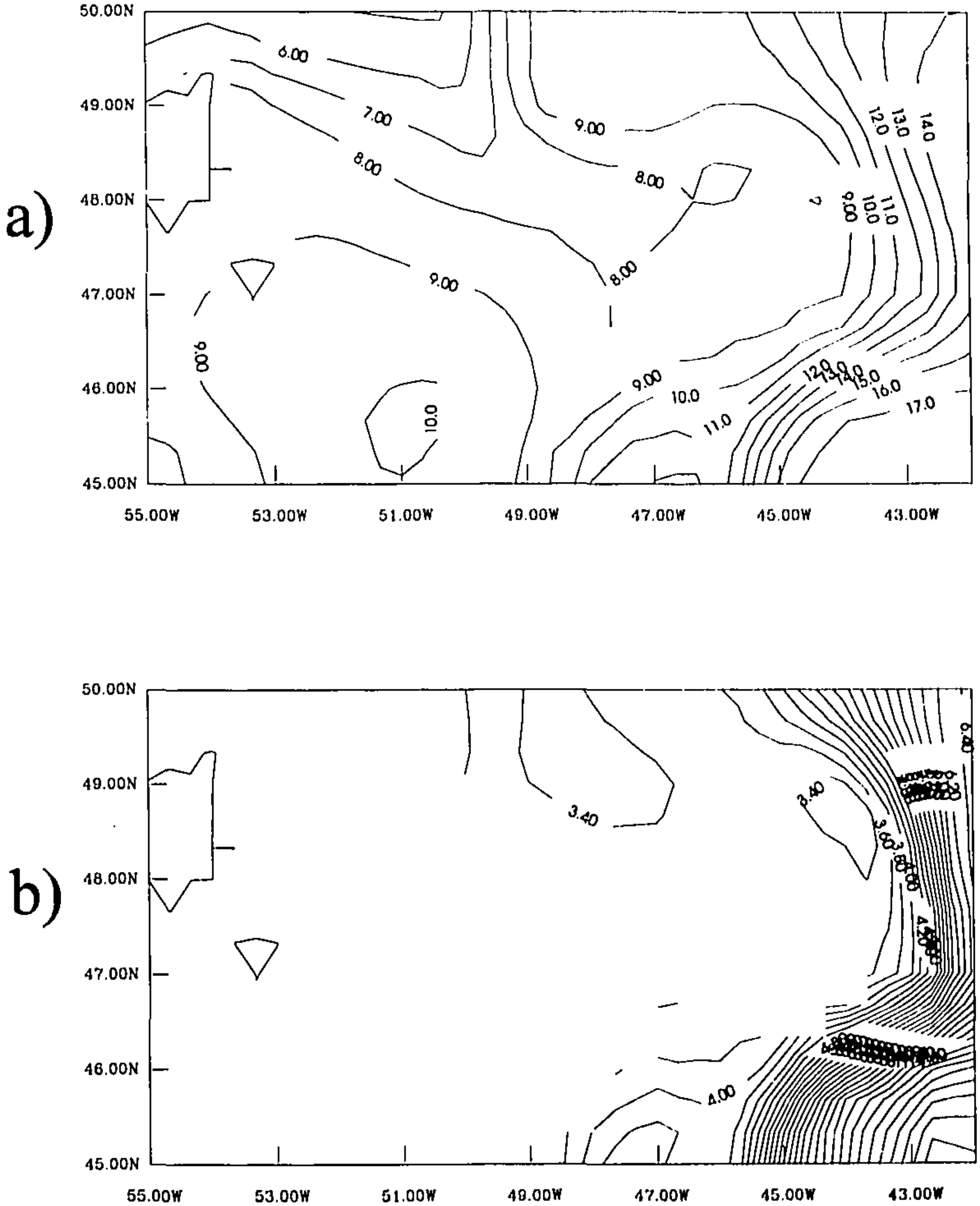

Figure A1.14: Warm season *in situ* temperature (°C), for the 1983-88 period, at a) 0m and b) 500m for the Flemish Cap subregion.